Spectro Imagerie terahertz de tissues biologiques : application à la détection de cancers du sein

Amel Al-Ibadi

THESIS

Submitted for the degree of Doctor

Department of Physics Sciences and Engineering (SPI)

École doctorale Sciences Physiques et de l'Ingénieur (SPI)

At UNIVERSITY OF BORDEAUX

Presented by

Amel Al-Ibadi

Entitled

Terahertz Imaging and Spectroscopy of biomedical tissues

Application to breast cancer detection

Defense: 30 th April 2018

Proposed to be presented in front of the examination panel

M. J. Louis Coutaz	Professor	IMEP-LHAC	President
Mme. D. Coquillat	CNRS Senior Researcher	L2C MONTPELLIER	Referee
M. G. Gallot	CNRS Senior Researcher	LOB	Referee
M. T. Zimmer	Professor	IMS	Member
M. P. Mounaix	CNRS Senior Researcher	IMS	Thesis director
M. J.P. Guillet	Associate Professor	IMS	Thesis co-director
M. P. Balcou	CNRS Senior Researcher	CELIA	Invited
M. G. Mac Grogan	Professor	Institut Bergonié	Invited

ABSTRACT IN ENGLISH

Terahertz Imaging and Spectroscopy of biomedical tissues
Application to breast cancer detection

The objective of the research reported in this thesis was to develop spectroscopy and imaging tools for medical applications. The goal is to determine the potential and the efficiency of terahertz spectroscopy and imaging in detecting cancer regions and distinguishing between diseased and healthy tissue in breast cancer in women. Terahertz spectroscopy is a non-contact, non-ionizing technique to obtain fast results, compared with standard clinical analysis. The experimental studies are divided in to two main sections:

Section I:

This part focuses on THz spectroscopy using accurately controlled THz radiation that passes through or that is reflected by samples at frequencies in the terahertz bandwidth. Several types of materials were used as phantoms for analysis: solids (silica, Teflon, sapphire, and glass), liquids (methanol, water, and alcohol), and biological tissue (cancer, fiber, and fatty), as well as a mixture (water-methanol). The refractive indices, absorption coefficients, and complex dielectric functions were first calculated then fitted to the Debye model. The biological tissues appeared heterogeneous in thickness and uneven surfaces, making it difficult to extracting accurate information, due to THz artefact in reflection THz spectroscopy. The signals were processed as follows: THz signals were reflected from the interference between the air/sample, air/window, water/window, and window/window measured as a baseline signal to estimate and improve the signal-noise ratio in THz spectroscopy measurements of dielectric materials. The advantage of this method was its accuracy, simplicity, and easy application for a reflection system with an incident angle. Measuring the refractive indices and absorption coefficients of samples with tumor and healthy tissues revealed that tumor regions present differences than normal tissue when the THz beam propagated through it.

Section II:

The second part of this study focused on THz imaging for breast cancer detection, in both transmission and reflection modes. The sections used included paraffin-embedded, fresh, formalin-fixed, and block tissues. Three image processing methods were used: slices, automated, and manual procedure. Moreover, the images obtained in time domain and frequency domain were analyzed to describe and identify the different breast tissue regions under study and determine the contrast between healthy and diseased tissue. The amount of water, which caused strong absorption of THz radiation over the frequency range may be one of the contrast origin. Cancer tissue has a higher water content than fiber or fatty tissues, making it possible to discriminate accurately between cancer, fiber, and fatty regions on THz images.

ABSTRACT IN FRENCH

Application de la spectro- imagerie térahertz pour la détection du cancer du sein

Les travaux de cette thèse consistent à développer des outils de spectroscopie et d'imagerie térahertz pour des applications médicales. L'objectif est de déterminer le potentiel et l'efficacité de la spectroscopie térahertz et de l'imagerie dans la détection des régions cancéreuses et la distinction entre les tissus malades et sains pour le cancer du sein chez les femmes. La spectroscopie térahertz est une technique sans contact, non ionisante pour obtenir des résultats rapides, comparée à l'analyse clinique standard. Les études expérimentales sont divisées en deux sections principales :

Section I :

Cette partie se concentre sur la spectroscopie en utilisant un rayonnement THz. La maîtrise de cette technique permet de travailler en mode réflexion ou transmission avec des fréquences dans la bande passante térahertz. Plusieurs types de matériaux ont été utilisés comme fantômes pour la calibration de l'expérience : des solides (silice, téflon, saphir et verre), des liquides (méthanol, eau et alcool) et des tissus biologiques (cancer, fibres et gras), ainsi qu'un mélange (eau-méthanol). Les indices de réfraction, les coefficients d'absorption et les fonctions diélectriques complexes ont d'abord été mesurés et extraits puis fittés avec un modèle de Debye. Les tissus biologiques sont apparus hétérogènes en épaisseur et avec des surfaces qui peuvent être irrégulières, ce qui rend difficile l'extraction d'informations précises, en raison d'artefacts induits. Les signaux ont été traités en suivant un protocole rigoureux : Les mesures sont effectuées sur un support parfaitement caractérisé en transmission pour réduire les incertitudes sur la phase lors des mesures en réflexion. Les signaux THz réfléchis aux interfaces entre l'air / échantillon, air / fenêtre, eau / fenêtre et fenêtre / fenêtre sont utilisés comme signal de base pour estimer et améliorer le rapport signal-bruit dans les mesures de spectroscopie. L'avantage de cette méthode est sa précision, sa simplicité et sa facilité d'application pour un système de réflexion avec un angle d'incidence. La mesure des indices de réfraction et des coefficients d'absorption des échantillons avec des tissus tumoraux et sains a révélé que les régions tumorales présentent des différences significatives par rapport au tissu normal lors de l'interaction tissu-rayonnement térahertz.

Section II :

La deuxième partie de cette étude porte sur l'imagerie THz pour la détection du cancer du sein, à la fois dans les modes de transmission et de réflexion. Plusieurs types d'échantillons ont été étudiés. Les coupes utilisées comprenaient des tissus inclus en paraffine, des tissus frais sortis du bloc opératoire, fixés au formol et des blocs. Pour cela le spectromètre a été déplacé à l'hôpital. Plus de 50 échantillons ont été ainsi inspectés. Trois

méthodes de traitement d'image ont été utilisées : le découpage, l'automatisation et le tri d'images manuel. De plus, les images obtenues dans le domaine temporel et dans le domaine fréquentiel ont été analysées pour décrire et identifier les différentes régions du tissu mammaire étudiées et déterminer le contraste entre le tissu sain et le tissu malade. La quantité d'eau différentielle présente dans les tissus malades peut être l'une des origines de contraste. En effet, le tissu cancéreux possède une teneur en eau plus élevée que celle des fibres ou des tissus adipeux normaux, ce qui permet de discriminer les régions cancéreuses, fibreuses et graisseuses sur les images THz.

ACKNOWLEGEMENTS

First of all, I would like to thank the fellowship program between Iraq and France, which supports this program at the University of Bordeaux, and everyone that has made this fellowship possible.

I would like to express special thanks to my research supervisors, Patrick Mounaix and Jean-Paul Guillet for giving me this wonderful opportunity to work with them. Their kind advice and encouragement during my three-year PhD study have brought me to where I am today. Their willingness to give so generously of their time has been very much appreciated. Without their help, this research would not have been possible.

I would like to thank my committee: Dominique Coquillat, Guilhem Gallot, Coutaz Jean Louis, Thomas Zimmer, Philippe Balcou, and Gaetan MacGrogan, for agreeing to evaluate my work.

Next, my thanks go to the laser group: Dean, Frederic D, Fredric F, Hugo, Mingming, and Jean Baptiste for their help and for providing a pleasant working environment. Special thanks to the Bergonié Cancer institute and all the technical staff for their help with this work.

In the last year of this study, I was privileged to work with my colleague, Quentin, who was always there to discuss, explain concepts, and provide encouragement, while learning together.

I want to thank from my heart Ayad ALjuwaed, Naseer Alfatlawi, Corinne El Khoueiry, and Zaineb Jebri, who were always ready to provide help and support, as well as for all the ideas they suggested during my PhD study.

My special thanks go to Nahlah Al Jubouri for being more than a friend and sister, as well as encouraging, supporting, and sharing all my successes and difficult times.

I would also like to thank Aquitaine Traduction for their help in correcting the grammar of my manuscript and making it more readable.

Finally, heartfelt thanks to my family: my father, who has supported me all my life, and encouraged me to achieve his dream of obtaining a PhD. My mother has always surrounded me with her warmth, as have my sisters: Luma, Nuha, and Suha. My brothers: Faisel, Yarup, and Nazar, have been incredibly supportive to me during this period. Without them, I would have never achieved this personal challenge. All my family and friends deserve thanks for helping me and always believing me.

Amel Al-Ibadi

30 April 2018

TABLE OF CONTENT

LIST OF FIGURES

CHAPTER 1

This Chapter introduces the basic physics of coherent terahertz (THz) radiation. In addition, it describes the characteristics of THz radiation and its effects on biological tissue in medical applications. Then, it presents THz waves and study targets, such as teeth, burns, eyes, and tumors. Finally, it summarizes some THz spectroscopy and imaging studies using these techniques as medical tools to detect different types of cancer in various organs.

1. Introduction and background

1.1. Introduction

Terahertz (THz) belongs to the "electromagnetic spectrum" of radiation, in a frequency band from 0.3 to 10 terahertz (1 THz = 10^{12} Hz) [1]. This corresponds to wavelengths between 1 mm (at 0.3 THz) and 30 µm (at 10 THz). Terahertz radiation occupies a middle area between microwaves and infrared light waves in the electromagnetic radiation family, as shown in Figure 1. THz radiation, also known as T-ray or far-infrared radiation thus bridges the technological gap between two regions:

- lower frequencies used for electronic communication
- and higher frequencies used for optics communication.

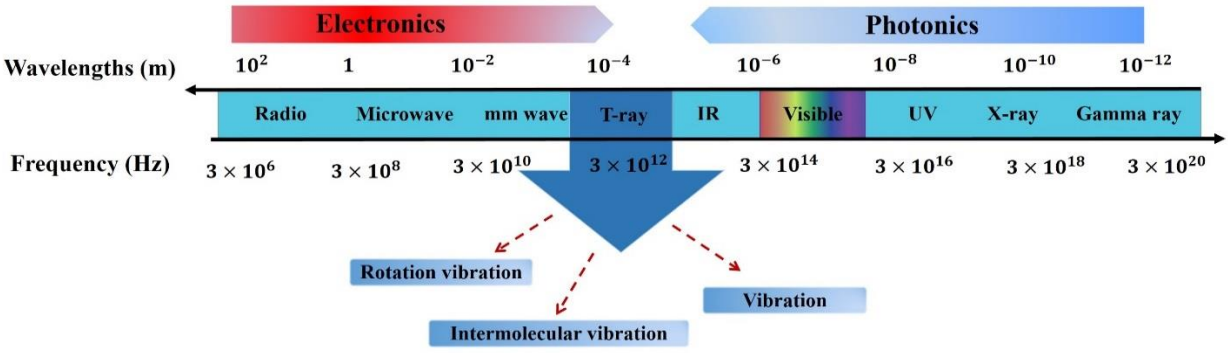

Figure 1: Diagram of the electromagnetic radiation spectrum, showing the location of terahertz (THz) radiation.

THz radiation has several properties: it probes the collective motion of atoms and has the potential to provide both chemical and structural information, through the excitation of intramolecular and intermolecular vibration modes [2]. For example, the double-helix structure in DNA can be probed directly by THz radiation [3].

Terahertz radiation is also known to be highly attenuated by water molecules, as the absorption coefficient in water is reported to lie between 100-1000 cm^{-1} [4]. Moreover, water is one of the main constituents of biological tissues and the penetration depth of low power THz radiation typically ranges from a few hundred microns in high water-content tissues (such as muscle) to several millimeters in adipose tissue, which is very encouraging for future medical applications [5]. In addition, the properties of terahertz radiation include non-ionization, propagation along straight lines, and good penetrating power in non-conducting materials [6] such as clothing, paper, cardboard, wood, masonry, plastic, and ceramics.

These properties make it useful in numerous areas of study, including;

- Biomedical studies, including teeth, artificial skin models [7], healthy skin, and basal cell carcinoma, both in vitro and in vivo [8], as well as liver [9] and breast cancer [10], where it is capable of identifying differences between normal and diseased tissue on the basis of their fundamental properties [11]. We review these studies in later sections.
- In particular, the high sensitivity of THz waves to the water content in tissue has been identified as one of the key differentiators for characterizing freshly excised tissue. As illustrated in previous studies [12], the hydration characteristics of biological samples can be accurately quantified using THz waves. In other studies [13], bound water and absorbed formalin were observed to be critical factors for differentiating diseased from healthy tissue in freshly excised and formalin-fixed samples. Furthermore, THz radiation excites rotational and vibrational modes in some biological molecules and has already demonstrated its good tissue differentiating abilities [7].
- Food inspection [14], [1].
- Non-destructive evaluation of mural paintings [15] [16] and, more generally, art science,
- Standoff screening of hidden weapons [17].
- In addition, due to the noninvasive properties of THz radiation, THz spectroscopy and imaging techniques can be useful for detecting illicit drugs by their spectral fingerprints [18].

While it may be argued that IR, MRI, and optical systems are capable of generating higher-resolution images, it has been observed that THz imaging offers greater contrast, an important requirement for distinguishing between substances [4]. In fact, this contrast is instrumental in the THz applications for detecting various tumors, such as breast cancer, as it provides higher resolution and clearer margins between cancerous and fibroglandular or fatty regions [19]. Therefore, THz technology has also been studied in medical applications and the next section discusses the effect of THz radiation on biological tissue.

1.2. THz imaging and biological tissues

1.2.1. Terahertz radiation in the biological domain

Biological tissues are strongly heterogeneous systems with a cellular organization between those of cells and complete organs. A tissue is an ensemble of similar cells of the same origin that fulfil a specific function, often by means of biological networks, involving highly-specific, sequential interactions of molecular complexes.
THz spectroscopy is a powerful tool for transmitting an electric field and directly accessing the amplitude and phase, to extract the absorption coefficient and dispersion properties, thanks to the generation of coherent THz signals. Therefore, THz spectroscopy and imaging techniques are being developed to determine and analyze the complex refractive indices of various materials, such as biological tissue [20].

- Frequency: ν = 1 THz = 1000 GHz,
- Period: $\tau = 1/\nu$ = 1 ps,
- Wavelength: $\lambda = c/\nu$ = 300 μm,
- Wavenumber: $k = 1/\lambda$ = 33.3 cm^{-1} ,
- Photon energy: $h\nu$ = 4.41 meV,
- Temperature: $T = h\nu/k_B$ = 48 K,

Where c is the speed of light in vacuum, h is Plank's constant, and k_B is Boltzmann's constant.
These parameters of THz radiation, which result in numerous advantages, including:

- A THz pulse source produces single- or low-multiple-cycle oscillations, with the range frequency of each pulse between 0.3 and 10 THz, and peak power up to 10 MW/m [21]. This radiation does not cause ionization in living tissue and is not, therefore, harmful, thus providing an efficient means of analyzing the spectral properties of biological tissues [22].
- THz radiation emissions may have different characteristics: when the photons all move together at the same time in phase, producing is highly temporally and spatially coherent THz radiation, ideal for accurate acquisition of the optical properties of samples.
- Moreover, THz radiation offers strong penetration power in non-polar substances and may thus be used for detecting optical properties.
- THz waves are also strongly absorbed by polar molecules of liquids (such as water), so THz spectroscopy is useful for studying material structures by analyzing the various phases of biological tissues, such as skin, muscle, fat, and other tissues under examination [23]. As tumor cells contain more water than healthy tissue and terahertz radiation attenuates differently in water, the reflection off a tumor is less intense than the surrounding regions [24].

- In addition, THz wavelengths can easily penetrate most dielectric materials, such as heterogeneous biological tissue, to a much greater depth than visible or near-infrared light, as the longer THz wavelengths are less susceptible to effects like low (Rayleigh) scattering, thus providing strongly enhanced contrast, whereas scattering tends to produce blurred images.

For example, when a THz beam passes through living tissue such as liver, heart muscle, kidney, pancreas, breast, and fat, significant differences between the absorption and refractive index of the THz radiation and tissue are measurable. After the beam passes through and interacts with tissue, the reflection or transmission of the THz pulses produce valuable information on the molecular structure of the biological tissues [25], used to produce images. Water is used to illustrate the behavior of substances with low atomic numbers, such as air and fat and fiber tissues that contribute to their strong interaction with THz radiation [22]. The absorption coefficient and refractive index of fatty tissue is lower than that of kidney and liver tissues, since fatty tissues contain hydrocarbon chains and relatively few polar molecules [26]. Therefore, THz waves are extremely sensitive to hydration levels and their non-ionizing nature makes them safe for assessing biological samples.

The biological effects of electromagnetic waves may be divided into thermal and non-thermal effects, as THz radiation is low energy and non-ionizing, so its vibration and rotational levels overlap with those of biological macromolecules, resulting in the non-thermal biological effects. Many findings from studies of the biological effects of THz radiation have confirmed that it has no effect on the differentiations of human keratinocytes or neurons at a power of 0.45 J/cm^2 [27]. In addition, THz radiation has not been found to have any significant effect in terms of genotoxicity or alterations in cell-cycle kinetics in blood cells, morphology, adhesion, proliferation, and differentiation of human epithelial and embryonic stem cells, as well as the chromosomes of human lymphocytes [28].

The demonstrated sensitivity of THz waves to biological tissue raised the possibility of using THz waves as a fully-developed diagnosis and analysis tool, for identifying, as well as detecting, human diseases. Indeed, THz spectroscopy and imaging may facilitate faster diagnosis without needing biopsies for pathological inspection. THz spectroscopy and imaging for bio-medical applications were developed through experiments utilizing state-of-the-art THz spectroscopy and imaging apparatus. Various bio-chemical compounds, human tissues healthy and diseases were investigated by THz spectroscopy and imaging. Scanning, reflection, and transmission measurements from THz spectroscopy were used to extract the optical properties of examination samples. Several THz frequency applications in medicine, used to analyze teeth, burns, eyes, and cancer, are presented in the following sections.

1.2.2. Terahertz imaging of teeth

Teeth are composed of four dental tissues. Three of them, enamel, dentin, and cementum, are hard tissues. The fourth is the pulp, a soft, non-calcified, tissue at the center of the tooth that contains nerves, blood vessels and connective tissue. The structure of a healthy tooth is illustrated Figure 2.

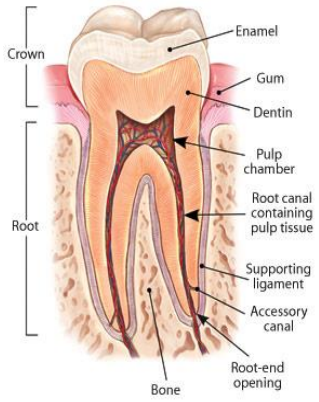

Figure 2: Cross-section showing the multi layers in a tooth and its internal structure.

The enamel is a hard, calcified tissue covering the dentin in the crown of a tooth. As it contains no living cells, tooth enamel cannot repair damage from decay or wear. The anatomical crown is the visible part of the tooth. The gums consist of soft tissues that cover and protect the roots and cover teeth that have not yet erupted. The pulp chamber is the space occupied by the soft tissue in the center of the tooth, containing nerves, blood vessels, and connective tissue. The neck is the area where the crown joins the root. Dentin is the part of the tooth beneath the enamel and cementum. It contains small hollow tubes or canals.

X-rays are used extensively in medical fields, especially in diagnostic applications. Similarly, X-rays are the primary diagnosis imaging technology used to diagnose tooth disease. However, it is an ionizing radiation with possible detrimental effects on human health [29]. Digital radiography is a type of X-ray imaging that uses digital X-ray sensors to detect caries lesions. Furthermore, this technology is expensive for dentists. For these reasons, there is a need for new imaging technologies for the structure and defects of teeth.

THz imaging has the potential to be used in assessing tooth structures without the risk of ionizing the surrounding tissue. Imaging teeth is one of a number of clinical problems that cannot be resolved with simple planar transmission or reflection imaging. Several studies have investigated imaging of the enamel thickness inside teeth. THz pulse imaging (TPI) is capable of distinguishing between different dental tissues [5]. In particular, it is capable of detecting a refractive index change between the tissues in different tooth layers. Another study, made a preliminary assessment of the potential uses of TPI in clinical dentistry, particularly in caries detection and corrosion monitoring. In vitro experiments on whole incisor teeth revealed that TPI was

capable of imaging the enamel in teeth. Imaging capable of displaying enamel thickness in vivo at such high resolution without ionizing radiation would represent a significant breakthrough [30].

In addition, other studies described a TPI system for generating 3D images of dental tissue, capable of making accurately, and reliable, direct measurements of enamel thickness [31]. Some research into THz imaging in diagnosing tooth caries found that a change in the refractive index made it possible to detect lesions smaller than those detectable by the naked eye [32]. In some respects, THz imaging does not yet offer a non-ionizing alternative to X-rays in dentistry. Yookeong et al. [33] investigated the power absorption of dentin and enamel, depending on the frequency increment, and the amplitudes were found to be similar. The refractive index of the enamel was found to be higher than that of dentin. In contrast, Burcu and Hakan. [34] found that THz imaging methods were highly sensitive to structural changes in teeth and thus had the potential to diagnosis them, which is an important factor in detecting and monitoring dental caries. Moreover, Kamburoglu et al. [35], used THz transmission spectroscopy to analyze and characterize permanent and primary carious and healthy teeth. They found that THz waves were sensitive to absorptive changes but refractive index variations were similar between different teeth. In addition, the capability of THz reflection spectroscopy to monitor the curing of dental composition was studied by Michael et al. [36], who found small, but significant, changes in the refractive index and absorption coefficient during series of exposures, correlated with variations in the density of the materials. They also found that sample thickness was a good measurement for monitoring the curing process. Taken overall, these studies and experiments confirmed the usefulness of THz spectroscopy, in both reflection and transmission modes, as a valuable technique for investigating tooth composition, detecting early tooth decay, and clinical applications. On the basis of these results, they also suggested that THz spectroscopy and imaging had the potential to be used in studying dental structure and making early diagnoses of tooth disease.

1.2.3. Terahertz radiation for burn diagnosis

To understand burn wounds, several facts about the skin should be reviewed. Human skin is the outer covering of the body, consisting of mesodermal cells, with pigmentation, such as melanin, provided by melanocytes, which absorb some of the potentially dangerous ultraviolet radiation (UV) in sunlight. The skin is the largest organ in the human body, with a surface area of 1.5- 2.0 m^2 (16.1- 21.5 sq ft.), and the water content of healthy skin is around 70% by weight, depending on environmental conditions [37]. Skin is composed of three primary layers: epidermis, dermis, and hypodermis. The structure of healthy skin is illustrated in Figure 3:

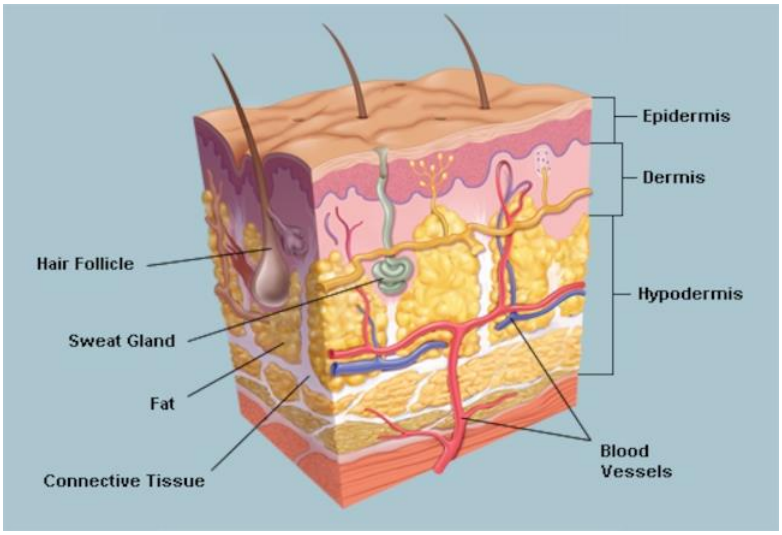

Figure 3: Layer structure of healthy skin.

The epidermis is the outer of the two layers that make up the skin and the inner layer is the dermis. It provides a barrier to infection from environmental pathogens and regulates the amount of water released from the body into the atmosphere through transepidermal water loss (TEWL) [38]. The outer part of the epidermis is composed of stratified layers of flattened cells, arranged perpendicularly. It also contains hair follicles and two types of sweat glands: sebaceous and eccrine. The light absorbance of this tissue is low, but varies due to differences in melanin, blood, and keratin content [39].

The dermis is a skin layer of variable thickness (0.6 -3mm) between the epidermis and subcutaneous tissues [40], which also propagates and absorbs light. The structural components of the dermis are: collagen, elastic fibers, and the extrafibrillar matrix [41]. It also contains mechanoreceptors that provide the sense of touch and thermoreceptors sensitive to heat.

The hypodermis, below the dermis, is used for fat storage. This layer of tissue immediately below the dermis of vertebrate skin consists primarily of connective tissue and fat lobules. It contains larger blood vessels and nerves than those found in the dermis.

Several methods and technologies assist in the clinical assessment of burns, including thermography, using infrared imaging to measure burn wound temperatures as an indicator of their depth [42]. This noncontact imaging modality is capable of distinguish tissues with different thermal conductivities [43].

THz imaging has been developed to identify skin-surface abnormalities, such as burns [44]. There are three primary types of burns: first degree, where the skin is red and non-blistered, second degree, involving blisters and some thickening of the skin, and third degree, characterized by widespread thickness with a white, leathery appearance. Burn depth depends on the temperature and heat capacity of the causative agent, exposure duration, and skin thickness [45].

Assessing burn degree is difficult, especially differentiating between indeterminate and partial-thickness injuries. It is, therefore, interesting that Hassan et al. [46], used THz spectroscopy of second and third degree burns in a survival study over a 72-hour post-injury period to assess their severity. The findings of their in vivo study revealed that the THz response of different-degree burns was not only consistent with presumed water content in the tissue, but also with the density of discrete scattering structures within the skin layers. Other in vivo THz imaging studies by Priyamvada et al. [47], involved burning rat abdomens and imaging them every 15 to 30 min for up to 7H. They found a local increase in the water content of the burned skin, as evidenced by a marked increase in THz reflectivity, which probably correlated to the post-injury inflammatory response. Taylor et al, used THz radiation at a center frequency of 0.5 THz with a bandwidth of 125 GHz to image thermal damage induced by branding previously-frozen porcine skin grafts at 315 $^{\circ}$C for 3 seconds [48]. They concluded that water removal from the burned sections of the excised skin samples resulted in lower terahertz reflectivity compared to the healthy parts.

Terahertz waves are sensitive not only to the post-burn formation of interstitial edema, but also to the density of skin structures, measured by image processing analysis of histological sections. Based on these preliminary results, suggested that the combination of these two effects, as probed by terahertz spectroscopy of the tissue, may ultimately be used to differentiate partial-thickness burns that will heal naturally from those that require surgical intervention.

1.2.4. THz radiation for Eye examination

The eye is a complex biological device that focuses light from external objects in the visual field onto a light-sensitive medium. The visual system is the part of the central nervous system involved in vision. The light that enters the eye is refracted as it passes through the cornea. It then passes through the pupil (controlled by the iris) and is further refracted by the lens. The cornea and lens act together as a compound lens to project an inverted image onto the retina.

The eye has two major focusing components: the cornea, a transparent, dome-shaped layer that covers the front of the eye, is a powerful refracting surface, which provides about two- thirds of the eye focusing power, as well as protecting and shielding the eye from undesirable elements, and filtering out some ultraviolet light. Nearly all of the focusing by the cornea occurs at the front surface, since the aqueous humor is in contact with the back surface and has nearly the same refraction index. There are no blood vessels, but many nerve and a human cornea contains 75% – 80% water [49]. The lens is a transparent, biconvex structure in the eye that, along with the cornea, helps to refract light to be focused on the retina. Most of the light that enters is absorbed by the tissues inside the eye. The aqueous humor fills the space between the lens and the cornea. The vitreous humor, or vitreous body, is a clear, jelly-like substance that fills the large space between the lens and the retina. The sclera

is a tough, white layer covering the entire eye, except the cornea. The sclera is protected by a transparent coating called the conjunctiva. The other key structure in the eye is the retina, a light-sensitive layer, which converts the light image into electrical nerve impulses that are sent to the brain. Figure 4 illustrates the structure of a healthy eye.

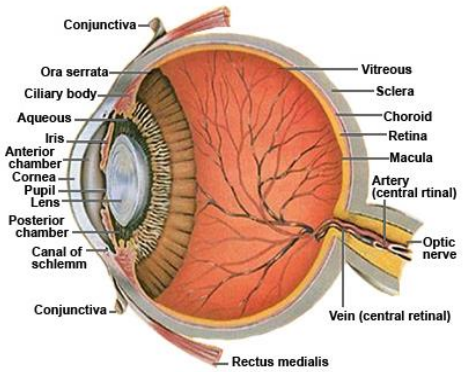

Figure 4: Structure of a healthy eye.

Several laser techniques are used to diagnose and treat eye diseases, such as photodynamic therapy (PDT) and laser photocoagulation. These stop blood vessel growths but cannot reverse damage already done. The risk of laser varies according to the type of surgery, and the most common (LASIK and PRK), designed to treat variation defects, including myopia, hyperopia, astigmatism, and cataract present little risk. In eye cancer, ultrasound uses sound waves to create an image of the eye and computed tomography (CT) scanning creates a three-dimensional picture of the inside of the eye.

One potential application of THz imaging is monitoring corneal graft rejection and distinguishing which grafts are likely to fail and which will recover. Therefore, this technology may be a valuable tool for studying the risk factors, diagnosis, and prognosis of corneal transplant patients [50]. Several research groups have investigated the spectral characteristics of the human cornea, in order to develop non-invasive methods to diagnose the cornea state in the 0.1-2.0 THz frequency range [49]. Shin et al. [51] presented data indicating that exposure to 0.12 THz radiation for 24H had no significant effect on micronucleus (MN) frequency, morphological changes, or the expression levels of heat shock protein (Hsp) in human eye cell cultures. David et al. experimented with terahertz corneal hydration sensing at 100 GHz, which showed promise in ophthalmology and was recently shown to be capable of detecting water concentration changes of about two parts per thousand in ex vivo corneal tissues, thus distinguishing between diseased and healthy tissues [52]. These results suggested that THz imaging can be used as a supplement to central corneal thickness methods for assessing of corneal hydration.

Dae-Cheol et al. [53], demonstrated the polarization of scleral tissues using THz spectroscopy and observed that the polarization- dependent properties are related to the structural characteristics of human scleral tissues, via

the ratio between the difference of the transmission amplitude spectra measured at the polarization angles of 0^o and 90^o. Other studies includes the destructive action of 200 fs laser on human cataract crystalline lens, leading to carbonization, and causing an internal micro explosion, studied by spectral transmission at range 0.2-1 THz, to observe the cataract developed on the lens [54].

1.2.5. THz radiation in oncology

Cancer has proved to be extremely pleomorphic, without a single characteristic common to all neoplastic processes. Cancer is a group of diseases involving abnormal cell growth with the potential to invade other body organs. Not all types of tumors are cancers: benign tumors are not cancerous and do not spread to other parts of the body. Over 100 different cancers are known to affect humans [55]. Cancers are usually named after the organs or tissues where the cancer originally formed [56] and its spread to other regions is called metastasis. Although some types of metastasis are cured with current treatments, they are not effective in all patients [57]. Cancer continues to be a worldwide killer, despite the enormous amount of research and rapid developments in the past decade. According to recent statistics, cancer accounts for about 23% of total deaths in the USA with heart disease as the second most common cause of death [58].

All cancers are staged at the time of the first diagnosis. The cancer stage describes the severity of the cancer, based on the size and/or extent of the primary tumor and whether or not the cancer has spread through the body [59]. Due to increased blood flow in tumors (perfusion), after tissue injury, tumors form new capillaries that facilitate the leakage of bound or unbound proteins into the injury region, leading to further tumors.

Among the different types of tumors, carcinomas, the most widespread, result from altered epithelial cells, which cover the surface of skin and internal organs. Sarcomas result from changes in muscle, bone, fat, or connective tissues. Leukemia is due to malignant white blood cells. Lymphoma is a cancer of lymphatic system cells that derive from bone morrow. Myelomas are cancers of specialized white blood cells that make antibodies. Some tumors increase the patient's metabolic rate and DNA formation, as well as blood flow. These tumors are more successfully imaged by chemical agents. The immune factor mechanism of the body responds to cancer, so chemical agents of specific tumor antibodies are successful in imaging tumors [60].

Techniques used in medical imaging to detect cancer, including X-rays, Magnetic Resonance Imaging (MRI), and fluorescence imaging, have difficulty detecting the exact tumor margin during surgery [61]. Moreover, imaging requires a dye injection into the body to determine the tumor location.

The difference in THz radiation absorbance between tumor and normal tissues may be used for diagnostic purposes [62]. Thanks to its low interference and non-ionizing, non-invasive characteristics, THz radiation has very low photon energy, insufficient to cause chemical damage to molecules or particles of atoms. Thus, it does not cause harmful ionization in biological tissues. THz radiation is very sensitive to polar substances, like water,

and as blood supply usually increases in cancer tissues, their hydration state provides better imaging contrast in soft tissues than X-rays.

Several research groups have been working on detecting the cell structure modifications known to be associated with cancer, with the aim of perfecting THz cancer diagnosis based on the spectral detection of water, since, in all types of cancers, the affected tissues exhibit higher hydration compared to healthy tissues [63].

In the THz domain, many studies focusing on cancer detection found differences in tissue properties. The absorption coefficient and refractive index of fatty tissues are lower than those of cancer tissues, since fatty tissues contain hydrocarbon chains and relatively few polar molecules [26]. Scattering is weak at THz wavelengths, due to the fact that only biological molecules become electronically excited. Thus, THz waves provide better contrast for soft tissues than other imaging techniques [22].

Cancers are visualized by imaging tools, such as THz spectra-imaging. When a THz beam passes through tissue, the reflected THz beam carries information about the optical properties of the tissue being tested and analysis of these properties by THz spectral-imaging is used to detect malignant and nonmalignant disease tissue [2]. Low-energy THz radiation, capable of penetrating deep tissues, provides sufficient information for diagnosing tissue diseases [64]. Tumor imaging using THz radiation was applied to diagnosing dried out cancer samples [65].

The nature of THz waves makes THz imaging techniques useful for detecting and diagnosing various types of cancer in different organs, as demonstrated in many ex vivo and in vivo studies by different groups, for example:

- **Skin cancer**: is the most relevant target for THz spectroscopy and imaging, as it is superficial and consists of thin layers, as illustrated in section 1.2. THz techniques are particularly powerful for detecting skin cancer and estimating its depth. Wallace et al. [8], used THz spectroscopy to study skin cancer (basal cell carcinoma) in freshly excised human tissue. They found a good contrast between normal and diseased tissue, dependent on the relative THz properties of tissue, which vary according to water content. Furthermore, an in vitro study by Kirill et al [64], used THz spectroscopy to diagnose early skin cancer.
- **Brain cancer**: THz spectroscopy with its non-invasive, high-temporal resolution and high sensitivity is useful for studying brain cancer. Yamagushi et al. [66], reported that THz reflection spectroscopy was useful for detecting tumor regions in fresh rat-brain tissue. Both the refractive index and absorption coefficient of cancer tissues were higher than those of normal tissues, due to the higher cell density and water content of the cancerous region. Furthermore, Kun Meng et al.[67], found that THz technology had the potential to distinguish gliomas from normal brain tissues and that THz spectroscopy imaging in the 0.2-2 THz range was valuable for detecting paraffin-embedded brain glioma, by comparing the refractive index, absorption coefficient, and complex dielectric constant of glioma and normal brain tissues. Their results indicated that paraffin-embedded brain glioma had a higher refractive index,

absorption coefficient, and complex dielectric constant than normal brain tissue. They also found that THz waves in the 1.7-2 THz range were suitable for coherent imaging, while the 0.55-0.76 THz range was suitable for intensity imaging.

- **Liver cancer**: Other groups have worked with transmission THz spectroscopy to study liver cancer cells embedded in paraffin and found that the refractive index and absorption coefficient of cancer tissue were less homogeneous than those of normal tissue. Further studies by Stanley et al [68], reported using THz reflection spectroscopy to measure healthy and cirrhotic rat liver tissues, fixed in formalin. They found that the water content and absorption coefficient of cirrhotic tissue were higher than those of normal tissue, even after formalin fixing. Their results showed that THz techniques were effective in discriminating between diseased and healthy tissue due to the difference in absorption of water and tissue structure.
- **Gastric cancer**: the potential of THz spectroscopy and imaging as a useful tool for diagnosing gastric cancer was reported by Young Bin et al [69], who investigated the feasibility of THz reflection spectroscopy for distinguishing between cancer tissue and adjacent normal gastric regions in freshly-excised human tissue. Dibo Hou et al. [70], used THz transmission spectroscopy to examine dehydrated normal and cancerous human gastric tissues. They investigated the THz absorption characteristics of dehydrated normal and cancerous gastric tissue and demonstrated contrast in both the shape and amplitude of spectra between normal and tumor tissues. Further work was reported by Faustino et al. [71], using THz spectroscopy to study a set of paraffin-embedded gastric tissues. They reported that the cancerous regions of all the samples had higher refractive indices and absorption coefficients than the adjacent healthy tissues and also that the higher percentage of water in cancerous tissue was not the only factor contributing to the contrast observed in the refractive index and absorption coefficient. The reported results confirmed the potential of THz waves to discriminate between cancerous and healthy tissue in dried, paraffin-embedded samples and freshly excised tissue.
- **Lung cancer**: several THz spectroscopy and imaging studies focused on lung cancer. Brun et al. [72], used THz reflection spectroscopy to measure and extract the optical properties of 10 μm-thick sections of lung tissue. Their results demonstrated THz spectral differences, not only between tumor and healthy tissues, but also within tumors, thus confirming the potential of THz imaging to provide a first diagnosis of cancer in this region.
- **Colon cancer**: many studies have described the use of THz spectroscopy as a medical imaging technique in diagnosing colon cancer. Leila et al. [73], used THz data to distinguish between normal and abnormal ex vivo colon cancer tissues. Their optimized analysis of THz data indicated the effectiveness of THz reflection imaging in diagnosing colon cancer.

- **Blood cancer**: the continuing development of THz spectroscopy has made it possible to distinguish between signals from different fluids, including blood and its constituents. For example: Reid et al. [74], presented the frequency-dependent absorption coefficient, refractive index, and Debye relaxation times of whole blood, red blood cells, plasma, and a thrombus, identifying small differences in the optical properties and Debye coefficients of blood and its component structures. They suggested using THz technology in vivo during surgical procedures for diagnostic purposes and accurate differentiation of blood and its component structures.
- **Breast cancer**: we will describe more specially this type of cancer since it is the central part of the present work.

1.2.6. Conclusion

THz imaging and spectroscopy techniques are still in the early stages of development, but the many studies using THz spectroscopy and imaging in reflection and transmission mode are indicative of the wide range of possible biomedical applications. THz techniques have an intrinsic advantage over high-frequency power sources ranging from 100 GHz to 10 THz. For all these reasons, our experimental studies used THz techniques and imaging as diagnostic tools for detecting, identifying, and analyzing cancerous and healthy regions in human breast tissue. This is summarized in Figure 5.

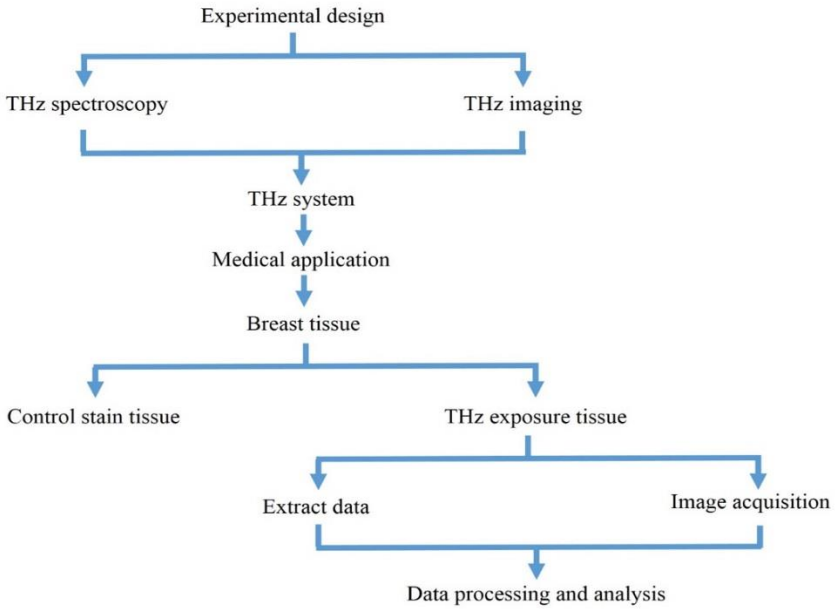

Figure 5: Diagram of data acquisition and analysis in breast tissue using terahertz spectroscopy and imaging.

CHAPTER 2

This Chapter describes the physical basis for the various interactions of electromagnetic radiation with matter, including absorption, scattering, and refraction. In addition, it reviews the theoretical measurements of radiation propagated through matter in transmission and reflection modes.

2. Introduction

2.1. Interaction between electromagnetic radiation and material

Various interaction phenomena occur when electromagnetic radiation is incident on materials. These interactions occur at the surface, reflection and refraction, or in the particles inside the material, resulting in attenuation due to absorption or scattering. Figure 6 shows a typical phenomenon, where the electromagnetic radiation incident on a material interacts with particles inside the medium. The interaction process depends on the energy, wavelength, or frequency of the radiation and the structural nature and concentration of the material. Therefore, all these interaction phenomena provide detailed information about the material. In fact, radiation is used to assess various physical and chemical properties of a wide range of materials. Our experiments on biological tissues and liquids produced important data for calculating the refractive index and absorption coefficient, as a result of the interactions with THz radiation.

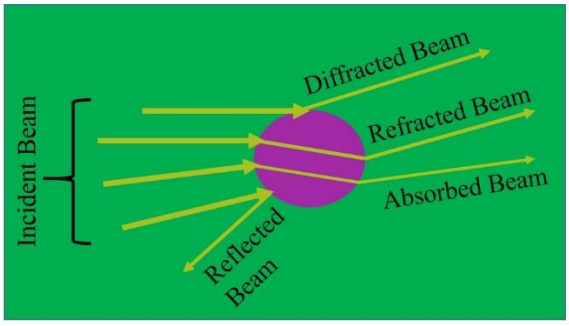

Figure 6: Diagram showing reflection, refraction, absorption, and scattering.

2.1.1. Absorption

Absorption is a reduction in THz beam intensity, affecting all wavelengths as it traverses matter. Materials may absorb all or part of the energy from the incident radiation. Some materials absorb some wavelengths and transmit others. In fact, absorption occurs when the photon frequency incident on the material is equal to the natural frequency of molecules in that material. A number of factors affect the ability of a material to absorb electromagnetic radiation, such as the electronic constitution of the atoms and molecules, radiation wavelengths, the thickness of the absorbing material, and internal parameters, such as the temperature and concentration of the absorbing agent. The attenuation (*A*) of a beam is described by the Beer-Lambert law, equation 2.1, expressing the variation in intensity throughout the medium.

$$A = log_{10}\frac{I_o}{I} \tag{2.1}$$

Or;

$$T_{transmittance} = \frac{I}{I_o} = e^{-\alpha x} = 10^{-A}$$

Where *I* is the intensity of the beam attenuated after traversing a thickness *x* of the medium, I_o is the intensity of the beam at the incident surface and α is the absorption coefficient in cm^{-1}.

2.1.2. Scattering

Photon scattering is the phenomenon produced by direction changes in radiation transmitted inside a medium. An electric field that creates a dipole moment in the molecules in a medium causes resonance and vibration of the particles. The oscillation of the induced dipole moment becomes a source of electromagnetic radiation, resulting in light scattering in all direction except that of the induced dipole moment.

There are two types of scattering:

- Elastic scattering, which occurs when a photon is absorbed and re-emitted at the same frequency. In particular, it occurs when the wavelength of the light is much greater than that of the target and the maximum energy is transferred from the radiation to the target particles through elastic collision. There are two types: Rayleigh and Mie scattering.
- Inelastic scattering occurs when the wavelength of the incident light is the same as that of the scattering target. When light is scattered within an atom, the emitted photon has lower energy than the incident photon.

Scatter direction is random and dependent on scatter size, light wavelength, and the refractive indices of the media it travels through. Attenuation, *A*, due to a single scattering event, is proportional to the number density

of the scattering particles, *N*, the scattering cross-section of the particle, and the particle diameter, *d*. The scattering coefficient μ_s is the probability per unit length of a photon being scattered. Unit is cm^{-1}.

$$A = log \frac{I_o}{I} = N \,.\sigma \,.d = \mu_s \,.d \qquad (2.2)$$

As described above, scattering is a complex interaction between electromagnetic radiation and the molecules in matter.

2.1.3. Refraction

When electromagnetic radiation bends as it passes through an interface medium, this phenomenon is known as refraction. It is the most common phenomenon when radiation and matter interact. Refraction is due to the reduction in phase-velocity of the light wave and occurs even in transparent media with virtually no absorption [25].

Several factors cause electromagnetic radiation to be refracted, including:

- Radiation traveling from a denser to a less dense medium or the reverse.
- Greater difference in density between the interface media produces greater refraction.
- A greater incident angle produces greater refraction.
- A light beam is refracted when it interacts with a medium of a different depth.
- Also, the wavelength of radiation, the nature of the structure, and the surface of the medium.

The refraction effect when a THz beam passes from one transmission medium to another, with incident and refractive indices n_i and n_r at an angle, θ_i, is shown in Figure 7:

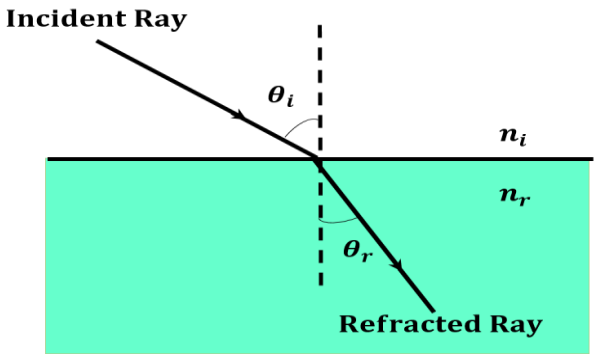

Figure 7: Behavior of light at a boundary between two media with different refractive indices.

The refraction angle is governed by the well-known Snell's law:

$$n_i \ sin\,\theta_i = n_r \ sin\,\theta_r \qquad (2.3)$$

2.2. Theory of light transport in the THz wavelength region

THz waves are detectable in both transmission mode, where THz radiation propagates through a sample, and reflection mode, where the radiation is reflected off the sample. We describe THz beam interaction in both transmission and reflection modes:

2.2.1. Transmission mode measurements

Transmission may be described as a process where THz radiation is transmitted through matter. When THz radiation strikes a medium and is transmitted through it, it is affected as follows:

- Its intensity decreases as the THz radiation penetrates deeper into the medium, due to absorption and scattering [75].
- Its velocity becomes lower in the medium than in air.

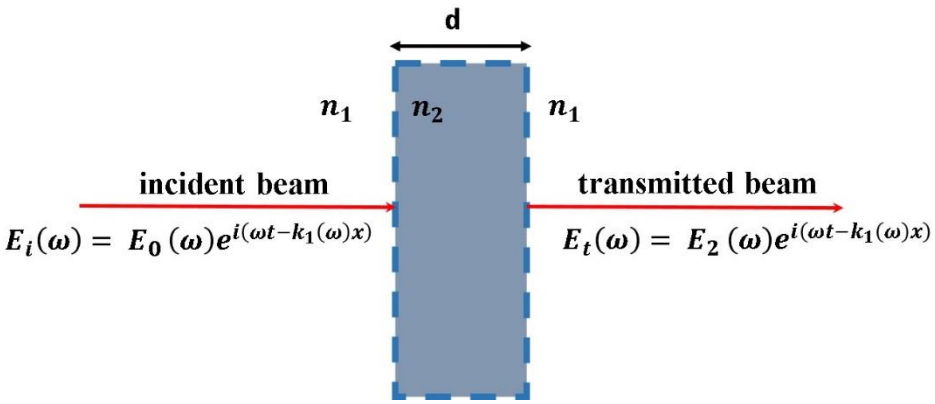

Figure 8: Geometry for Electric Field Transmission of incident waves with amplitude E through a layer of thickness d with refractive index n_2.

Figure 8 shows the transmission model, describing how a radiation beam propagates through the medium. In transmission theory, incident radiation (E_i) with spectrum and n_1 complex refractive index, passes (E_t) in a medium d thick with a complex refractive index n_2. The complex transmission, as a function of frequency ω of the THz pulse in medium 1 and medium 2 after transmission may be expressed as:

$$E_{ref} = E_i(\omega) = E_0(\omega)e^{i(\omega t - k_1(\omega)x)} \quad (2.4)$$

$$E_{sam} = E_t(\omega) = E_2(\omega)e^{i(\omega t - k_1(\omega)x)} \quad (2.5)$$

Where:

E_0 and E_2 are the electric field of the THz pulse in air (medium 1) and sample (medium 2), respectively.

k_1 and k_2 represent the wave numbers in air (medium 1) and sample (medium 2), respectively.

x is the optical path, equal to sample thickness.

The complex transmission for normal incidence is determined using equations (2.4) and (2.5), taking the ratio of the transmission of the sample ($E_{sam}(\omega)$) and reference ($E_{ref}(\omega)$) as;

$$T(\omega) = \frac{E_{sam}(\omega)}{E_{ref}(\omega)} \tag{2.6}$$

To calculate the refractive index and absorption coefficient, the complex refractive index of the sample is given as;

$$\tilde{n}(\omega) = n(\omega) - ik(\omega) \tag{2.7}$$

Where $n(\omega)$ and $k(\omega)$ are the real and imaginary parts of the complex refractive index, $\tilde{n}(\omega)$, respectively.

The extinction coefficient is determined by:

$$k(\omega) = \frac{\alpha(\omega)c}{2\omega} \tag{2.8}$$

Where α represents the absorption coefficient.

In case of normal incident, where the THz pulse is directly transmitted through the medium, the Fresnel transmission coefficients, T_{12} and T_{21}, at each face are determined by: $T_{12} = \frac{2n_1}{n_2+n_1}$ and. $T_{21} = \frac{2n_2}{n_1+n_2}$

Finally, the real part of the refractive index $n(\omega)$ and absorption coefficient $\alpha(\omega)$ of the sample is calculated from equations (2.4), (2.5), and (2.6) [76];

$$n(\omega) = 1 + \frac{c}{\omega d}\left(\varphi_{sam} - \varphi_{ref}\right) \tag{2.9}$$

And;

$$\alpha(\omega) = -\frac{2}{d}\left(\frac{(n(\omega)+1)^2}{4n}\frac{E_{sam}}{E_{ref}}\right) \tag{2.10}$$

Where φ_{sam} and φ_{ref} represent the accumulative phase of the THz pulse propagated along the optical path [77], determined by the complex exponentials $e^{i(\omega t - k_2(\omega)x)}$ and $e^{-i(\omega t - k_1(\omega)x)}$ of the sample and reference, respectively. This is valid for flat homogeneous samples with sufficient thickness to push the different Fabry

Perot echoes far from the main peak. If not, we can take into account the different contributions of each echo and include them into the model.

2.2.2. Reflection mode measurements

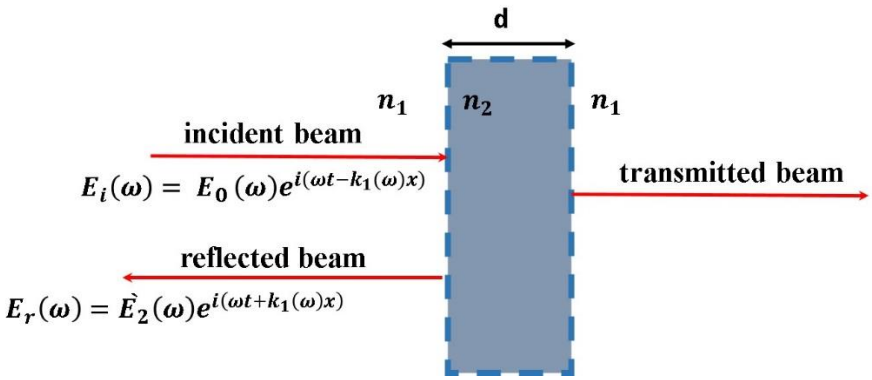

Figure 9 : Reflection geometry for complex-response measurement in a sample with thickness d.

Reflection mode is the second type of measurement. It is difficult to measure the optical properties of many materials, such as biological tissues, in transmission mode, as they are too thick to transmit THz radiation. Reflection mode is, therefore, used to measure these materials. Figure 9 shows reflectance signal measurement in reflection mode.

Calculating the refractive index and absorption coefficient of a material according to reflection theory: normal incident THz pulses are focused onto the surface layer of a sample d thick, with electric field E_i, and refractive index n_1. The THz pulse E_r is reflected at the air/sample interface where the refractive index changes from low to high. Therefore, reflection amplitude R(ω), determined by the ratio of the sample spectrum to the reference spectrum, is:

$$R(\omega) = \frac{E_{sam}(\omega)}{E_{ref}(\omega)} \tag{2.11}$$

$E_{sam}(\omega)$ and $E_{ref}(\omega)$ are given by the following equations:

$$E_{sam}(\omega) = E_r = E_2' e^{i(\omega t + k_1 x)} \tag{2.12}$$

$$E_{ref}(\omega) = E_i = E_1 e^{i(\omega t - k_{1x})} \tag{2.13}$$

Where k_1 represents the wave number of the incident radiation in air (medium 1) and x is the optical path. The wave number may be written as complex parts:

$$k = \frac{2\pi f}{c}\,\tilde{n} \tag{2.14}$$

Where *f* and *c* are the frequency and velocity, respectively, of light in a vacuum.
The Fresnel reflection coefficients R_{12} and R_{21} at each face are determined by;

$$R_{12} = \frac{n_2 - n_1}{n_2 + n_1} \tag{2.15}$$

And

$$R_{21} = \frac{2n_2}{n_1 + n_2} \tag{2.16}$$

Therefore, the complex refractive index of the sample $\tilde{n}_s(\omega)$ as a function of frequency is obtained from equations (2.11), (2.15), and (2.16);

$$\tilde{n}_s(\omega) = \frac{(1-R)\tilde{n}_2^2 + (1+R)\tilde{n}_2\tilde{n}_1}{(1-R)\tilde{n}_1 + (1+R)\tilde{n}_2} \tag{2.17}$$

Finally, the real refractive index, n_s and absorption coefficient α_s of the sample are calculated from equation (2.17) of the complex index of refraction;

$$n_s = real\left(\tilde{n}_s(\omega)\right) \tag{2.18}$$

$$\alpha_s = \frac{2\omega\,.k(\omega))}{c} \tag{2.19}$$

The physical expression could be easily derived for the transverse magnetic or transverse electric cases.

2.3. Spectroscopy at THz wavelengths

Spectroscopy is a technique that uses the interaction of electromagnetic radiation with matter to determine its structure and identify organic compounds. Radiation in various regions of the electromagnetic spectrum, including microwave, terahertz, infrared, near infrared, visible and ultraviolet, as well as X- and gamma-rays, has been used for spectroscopy. In fact, it is possible to obtain different information of molecules when radiation on different wavelengths or frequencies interacts with matter. Radiation energy absorbed by molecules causes different excitation and vibration levels in matter, as shown in Figure 10. The vibration within the molecules depends on the bonds between atoms in the material. The THz frequency range is between the microwave and infrared regions, so THz spectroscopy is a useful tool for probing molecular bonds for gas, specifically vibrational and rotational modes. For example; biomolecules have permanent dipole moments at specific

frequencies, so pure rotation vibration is excited when molecules absorb the energy E, corresponding to the vibrational frequencies, ν, related to the strength of the atoms at either end.

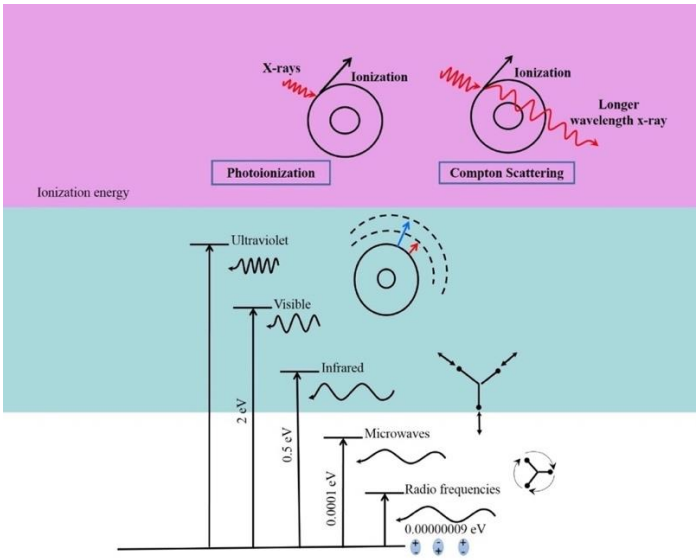

Figure 10: Molecular interaction across the electromagnetic spectrum, starting with radio waves, microwave, terahertz, infrared, near infrared, visible and ultraviolet, as well as x- and gamma-rays. Each portion of electromagnetic spectrum has energy, which is absorbed by molecules causes different excitation and vibration levels in matter.

The vibrational frequency is associated with an intermolecular bond rearrangement, according to the relation $E = h\nu$ (where h is Planck's constant). The rotational spectrum describes the free rotation of a molecule, as illustrated in Figure 11.

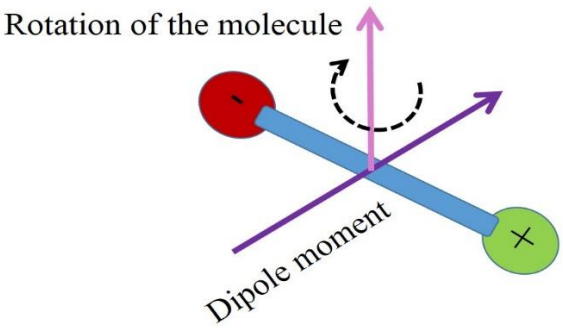

Figure 11: Rotating polar molecule.

A more typical application of the rotational spectrum is to determine information about bond lengths and angles in a molecule. In addition, the spectrum consists of a single line with a frequency used to determine the force constant of the bond. A pure rotational state is only observed in the gaseous phase. In solids or liquids, the

rotational motion is usually hindered by collisions due to the presence of intermolecular force, while, in gas phase, the molecules in pure rotation are in continuous motion and free to rotate unhindered. Furthermore, an increase in the pure rotational motion of gas molecules is due to transitions in discrete rotational energy (frequency). Consequently, a non-polar molecule will not usually exhibit a rotational spectrum. However, electronic excitation may cause an exception to this , leading to a change disturbance in some molecules and creating a net dipole moment of the molecule [78].

Finally, on the basis of these phenomena, THz techniques have been used to measuring the absorption spectra of materials over a range of frequencies. Consequently, in this study, we applied THz spectroscopy to liquids, biological tissues, and solid materials, exhibiting molecule vibrations in the picosecond range, to investigate the optical properties of these materials.

2.3.1. Absorption spectroscopy

Absorption spectroscopy is an important analytical technique used to measure the absorption of a radiation beam by a sample as a function of frequency or wavelength, before and after interaction. The resulting spectrum provides information on the sample's physical and chemical composition, related to the natural molecular structure, thanks to measurements in both transmission and reflection mode. Absorption spectroscopy to determine the absolute concentration of a compound containing various materials, including homogeneous, inhomogeneous, and pure components, is governed by the Beer-Lambert law and requires knowledge of the compound's absorption coefficient.

2.3.1.1. The Beer-Lambert law

Beer-lambert law is used to calculate the concentration of a substance in a sample and its thickness, by determining the spectrum that travels through it. The Beer-Lambert law depends on the intensity of a beam of light of the appropriate wavelength being passed through a layer of a substance, which absorbs a fraction of this light. As the sample absorbs some of the light, the light coming out of the substance has decreased in intensity, proportionally to the concentration of the sample.

The absorption coefficient is independent of the intensity of the light and the thickness of sample. For a purely absorbing medium, the Beer-Lambert law is expressed as;

$$I = I_o\, e^{-\alpha d} \qquad (2.20)$$

Where I is the intensity of light transmitted through a medium of thickness d, I_o is the initial intensity of the light, and α is the absorption coefficient.

For liquid absorbing media, the Beer-Lambert law is expressed as [77];

$$A = -ln(T) = -ln\left(\frac{I}{I_o}\right) = \mu_a\, l = \alpha\, l\, c \qquad (2.21)$$

$$\alpha = -log_{10}(T) = -log_{10}(\frac{I}{I_o}) = \kappa\, l = \varepsilon\, l\, c \qquad (2.22)$$

Where A is the attenuation, κ is the extinction coefficient (in cm^{-1}), ε is the frequency-dependent extinction coefficient, l is the path length, and c is the concentration of the compound in the solution.

Absorbance α as a function of wavelength is useful, since it can be summed for layers of different materials, each with their own ε, l, c.

$$A(\lambda) = c_1\, l_1\, \varepsilon_1 + c_2\, l_2\, \varepsilon_2 + \cdots + c_n\, l_n\, \varepsilon_n \qquad (2.23)$$

Beer's law, A = $\varepsilon\, l\, c$, holds for all optical spectra and, therefore, the intensities of the rotational lines in a vibrational rotation spectrum depend on the fraction of molecules in that rotational state.

Many factors may limit the use of the Beer-Lambert Law, as follows:

- Electrostatic interaction at high concentrations of substance molecules, causes deviation in the absorptivity coefficient, where absorbance increases with concentration.
- The refractive index of a substance changes at high concentrations.
- Light scattering corresponding to the particular nature of the sample.
- Chemical changes as a function of concentration.

Finally, Beer's Law is used in quantitative analysis to determine the concentration of unknown samples from absorbance data.

2.3.2. Dielectric relaxation spectroscopy

Dielectric relaxation spectroscopy (DRS) is a technique used to determine the time-dependent electric polarization processes of various materials placed in a weak electromagnetic field (i.e., the separation of localized molecular charge distributions). At low frequencies, the molecular dipoles orientate in the field (i.e. polarize), thus reducing the electrical potential of the material, which produces the spectroscopic data [79].

The complex dielectric coefficient for liquids and pure components is calculated using the equation (2.7), section 2.2.1. Thus, the imaginary part describing absorption increases with frequency and is referred to as dielectric loss. In addition, the optical constants may be determined from the complex dielectric permittivity. Therefore, the complex refractive index $\hat{n}^2(\omega)$ as a function of frequency is calculated using the equations of real and imaginary parts of the dielectric function are expressed by equations (2.18) and (2.19), section 2.2.2.

Finally, it is possible to describe the interaction of light with various particular materials by determining its optical characterization, corresponding to the complex dielectric constant.

2.3.2.1. The Debye Model

The Debye model [80] is frequently used to explain the dielectric behavior of polar molecules in liquids. When an electromagnetic field is applied, the dipoles are realigned in the direction of the electromagnetic field and relaxed. The relaxation time of the molecules is determined by the following equation;

$$\hat{\varepsilon}(\omega) = \varepsilon_{\infty} + \sum_{j=1}^{n} \frac{\Delta\varepsilon}{1+i\omega\tau} \tag{2.24}$$

$$\Delta\varepsilon = \varepsilon_s - \varepsilon_{\infty} \tag{2.25}$$

Where this equation for the complex dielectric constant ($\hat{\varepsilon}(\omega)$) shows the relation of the dielectric static: ε_s, at low frequency limitation values, ε_{∞} at high frequency limitation values, n the number of relaxation and τ is a characteristic re-orientation time for a single dipole in a material. Therefore, time is required to describe the aligned dipoles in the system. The relaxation time τ is used to calculate the relaxation frequency f_c, as follows;

$$\tau = \frac{1}{\omega} = \frac{1}{2\pi f_c} \tag{2.26}$$

In the case of low-relaxation frequencies, dipoles are able to keep space and response with variations in the field, when the alternating electric field is slow enough, this corresponds to the nature of the chemical bonds in molecules and the localized orientation within the molecules. However, in the case of electric fields with high-relaxation frequencies, dipoles have a limited ability to complete the orientation process and hardly move at all, so energy is dissipated to surrounding molecules, phase difference is exhibited, and permittivity is lost [81]. Consequently, the real ε' and imaginary ε'' parts of the complex permittivity of materials, resulting from the phase differences, can calculated using equations (2.7) and (2.26), as follows:

$$\varepsilon' = \varepsilon_{\infty} + \frac{(\varepsilon_s - \varepsilon_{\infty})}{1+\omega^2\tau^2} \tag{2.27}$$

$$\varepsilon'' = \frac{(\varepsilon_s - \varepsilon_{\infty})\omega\tau}{1+\omega^2\tau^2} \tag{2.28}$$

The real ε' and imaginary ε'' parts of the complex permittivity of pure components are determined by the Cole-Cole equation:

$$\hat{\varepsilon}(\omega) = \varepsilon_{\infty} + \frac{\varepsilon_s - \varepsilon_{\infty}}{1+(i\omega\tau)^{1-\alpha}} \tag{2.29}$$

Where α is the distribution parameter, chosen to give a good fit to measured data [82]. The use of the Cole—Cole diagram in the analysis of dielectric relaxation is proved by showing explicitly that a semicircle in the Cole—Cole diagram corresponds uniquely to a Debye relaxation function.

In fact, the Cole-Cole equation provides information on the real and imaginary permittivity of one or more relaxation processes in a particle distribution. Finally, the Debye and Cole-Cole relaxation data were the best fit for the results of this study, obtained by THz reflection spectroscopy in the 0.2- 2 THz frequency range and 0.15- 100 ps time domain. The results were strongly dependent on the frequency range or time domain of the experiment and the type of materials, as well as the accuracy of the data.

2.4. Structural and THz properties of major tissue constituents

Biological soft tissues vary significantly in their mechanical properties. Tissue structure is the key to this diversity.

2.4.1. Water

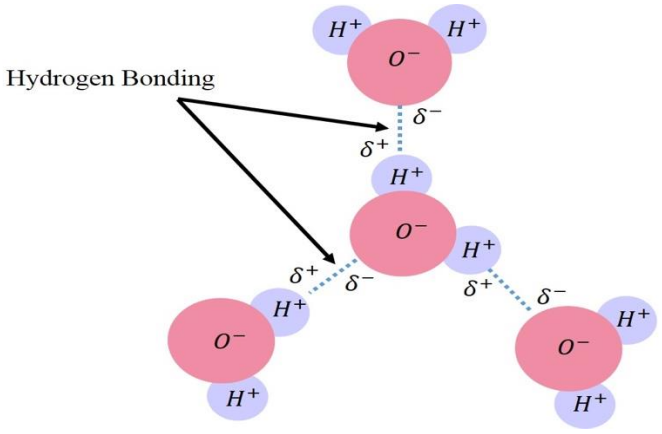

Figure 12: Illustrates the structure of water molecules.

Water, a polar molecule, is highly absorbing in the THz region. Water plays a role in biological molecules, forming larger structures or undergoing chemical transformations. In fact, water itself - or its H^+ and OH^- constituents - participate directly in many biochemical processes. The central O atom forms covalent bonds with two H atoms, leaving two unshared pairs of electrons. Liquid water contains a vast, three-dimensional network of hydrogen bonds, resulting from the attraction between positively-polarized hydrogens and electron pairs on negative oxygens. Each oxygen atom can form two hydrogen bonds, represented by the dotted lines

Figure 12. The water molecule is an asymmetric molecule. Hence the degeneracy in the vibrational and rotational states is lifted, resulting in many possible transitions. This gives rise to spectra with little or no readily discernable vibrations. Vibrational methods have been used to analyze these spectra. In liquid water, each molecule is capable of forming hydrogen bonds with up to four other water molecules, but each bond has a lifetime of only about 10^{-12} s [83]. As a result, the structure of water flickers continually, as water molecules rotate, bend, and reorient themselves.

The absorption spectrum of water molecules covers not only visible light, but also a wide spectrum of electromagnetic radiation, from extremely short γ^{-} and X-rays to long radio waves [84]. The interaction of water molecules with electromagnetic radiation depends closely on its physical properties, as well as its dynamic, electrical, and magnetic properties.

Thanks to its special properties, water is a major compound in biological tissue and biochemical reactions. THz radiation interacts strongly with water due to slow relaxation time of water molecules this is associated with rotational and vibrational of the hydrogen-bonds[85].

Several studies on THz radiation in cancer diagnosis, based on spectral detection of fresh tissues, focused on water, due to its direct effect on the accuracy of the calculated absorption coefficient and refractive index [86], since many cancerous tissues exhibit higher hydration in comparison to healthy (normal) tissue, and, thus, increased absorption in the terahertz spectral region [87]. Moreover, this phenomenon is, also detected by positron emission tomography (PET), near-infrared spectrometry (NIR), and magnetic resonance imaging (MRI) [88], [89]. Other groups have focused their efforts on detecting cell structure modifications known to be associated with cancer [10], [90]. The increase in free water of abnormal vasculature is not the only factor contributing to the noticeable contrast revealed by the THz absorption coefficient, refractive index spectra, and contrast-enhanced THz imaging. The research conducted by S. Joseph et al., aimed at identifying different types of cancers, found that water had a positive effect on contrast in cancer diagnosis [91]. The high-water content in the abnormal tissue region is caused by complex biological tissue, as well as vascularity and body fluid around necrotic regions. These factors are useful not only for detecting cancer, but also for studying qualitative aspects of abnormal regions in bio-tissue, where contributing factors other than water may affect the contrast of THz images at the cellular level [61].

2.4.2. Methanol

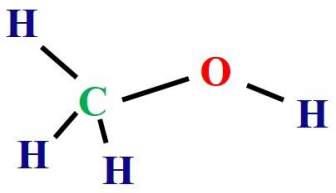

Figure 13: Chemical structure of methanol.

Alcohols are a homologous series containing the functional –OH group, which determines the characteristic reaction of the compounds, and a hydrophobic methyl (CH_3) group [92]. Methanol (methyl alcohol) is an organic compound containing oxygen, hydrogen, and carbon. At room temperature, it is a polar liquid, resulting in significant absorption in the THz region. Methanol vibrates in much the same way as water and, in the liquid phase, the vibrations are damped by the effect of hydrogen bonding.

Several groups have tried to identify organic gases (methanol, acetone, and ethanol) using THz-TDS [93], and found characteristic absorption spectra for these organic gases. Consequently, THz spectroscopy may be used to identify different kinds of organic materials.

Methanol was investigated using terahertz pulse spectroscopy. It exhibited multiple-Debye behavior, making its frequency-dependent dielectric constant a valuable benchmark for dynamic simulations and other theoretical treatments of liquids [94]. A number of methanol studies reported three relaxation times in methanol: T_1, the slowest relaxation of the flexing of chains of molecules, T_2, the rotation of a chain end molecule or a free molecule, and T_3, the fastest relaxation, ascribed to small motions of a methanol molecule between two hydrogen bond sites, which remained the same in solution as in the pure solvent [95]. Finally, as methanol is not found in biological tissue, it was used as a phantom for experimental validation before the technique was applied to tissue.

2.4.3. Lipids

Lipids are a heterogeneous group of compounds, including fats, oils, steroids, waxes, and related compounds, which have similar physical rather than chemical properties. These organic molecules of biological origin may be insoluble or soluble in nonpolar solvents. Lipids have both nonpolar and polar regions. Nonpolar lipids are soluble in nonpolar environments, but not in water, as it is polar.

Lipids are important in biological systems, as they form the cell membrane. Fat is stored in adipose tissue, where it serves as a thermal insulator in the subcutaneous tissues around certain organs, as well as a mechanical cushion, and a source of energy. Nonpolar lipids act as electrical insulators, i.e. do not respond to an electric

field, and completely resist the flow of an electric charge, thus facilitating rapid propagation of depolarization waves along myelinated nerves. Fats and oils are composed of fatty acids bonded to a glycerol molecule, as shown in Figure 14.

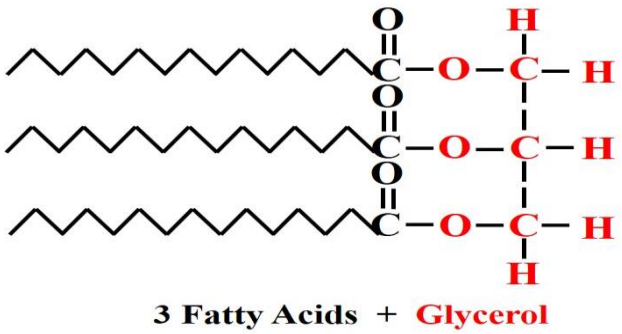

Figure 14 : Structure of a lipid combining glycerol with three fatty acids.

One category of lipid, fatty acids, carbon chains with a methyl group at one end of the molecule and a carboxyl group (COOH) at the other end, form the major component of stored fat. The hydrocarbon chains of these fatty acids are non-polar and are therefore responsible for the behavior of complex lipids and the formation of biological membrane. However, the hydrocarbon chain affects the overall polarity of the molecule by the oxygen molecules, due to charge-cancelling effects: molecules with very short carbon chains are more polar, while longer chains have a non-polar character. Finally, analysis of the dielectric properties of oil at concentrations between 0.3% and 3.3% [96] found that the dielectric behavior of oil complexes was fundamentally different from that of pure oil.

2.5. Conclusion

Thanks to the ability of THz radiation to probe weak interactions with materials and rapid signature acquisition, THz spectroscopy has a number of potential applications. Additionally, several theories have been used to explain and investigate the optical characterization of materials, such as liquids, as well as pure and mixed components, on the basis of their interactions with THz radiation. Subsequently, the ability of THz techniques to measure the dielectric response of polar liquids and biological tissue revealed a number of relaxation processes. Finally, the properties and applications of THz radiation are now clearly understood, making it possible to apply THz spectroscopy to a comprehensive study of the dielectric properties of some types of liquids and biological tissue, including breast cancer.

CHAPTER 3

This Chapter is divided into three parts:

- The first part includes the basic principle of the THz technique, related to the photoconductive emission and detection devices in the THz range.
- The second part presents the Teraview 3000 and Tera Pulse 4000 systems, used in transmission and reflection mode in the experimental work. It also describes the different types of sample-holders used in both transmission and reflection modes.
- Finally, the third part covers the methods for extracting transmission, reflection, and sample properties from the raw data obtained by THz spectroscopy and imaging in the specific experimental configuration.

3. Experimental measurements

3.1. Terahertz generation and detection techniques

3.1.1. Photoconductive systems

Since the 1980s and 1990s, the use of THz spectroscopy has expanded rapidly in the science and technology fields, in a wide variety of applications [97]. Since the first pioneering work by Breshkovsky and coworkers [98], a number of emitter and detector materials and techniques have been investigated and optimized, aimed at producing either maximum pulses or spectrum bandwidth [99]. In general, there are two main ways to generate and detect pulsed THz radiation from femtosecond laser pulses; photoconductive antenna (PCA) and nonlinear optical materials. THz spectroscopy uses two types of photoconductive antenna: a biased PCA to generate THz pulses and an unbiased PCA for detection [100]. There are many reasons to use PCA for THz spectroscopy and imaging. PCA:

1- Operates at room temperature and does not need cooling.
2- Is small in size.
3- Does not require high-voltage power sources.
4- Operates at high THz frequencies.
5- Produces short, high-powered sub-picosecond pulses.

Our main system used photoconductive antennas for generating and detecting THz radiation with a short, high-powered, regular femtosecond laser pulse (Ti: Sapphire laser). It is capable of detecting hot-carrier phenomena in semiconductors on time scales relevant to generating and detecting THz radiation. Finally, before discussing our experimental setup, we introduce the technology for generating THz pulses and detecting them by THz spectroscopy and imaging relative to the PC antenna.

3.1.1.1. Photoconductive emission

In this section, we discuss the physical mechanisms in PCA leading to THz radiation. Several techniques are used to generate and detect coherent THz pulses, using femtosecond lasers, based on PCA excitation of a semiconductor surface, using optical rectification and electro-optic sampling sources for high energy. THz spectroscopy, in either transmission or reflection mode, uses a THz emitter to generate and emit radiation.

A THz emitter is a semiconductor-based PCA. The characteristic structure of PCA is embedded in a semiconductor, such as a low-temperature Gallium arsenide (GaAs) substrate, consisting of two metal electrodes with a small gap as a Hertzian dipole, typically 5 μm, which supports a large electric field across its surface. Diagrams of the PC emitter and emission concept are shown in Figure 15 .

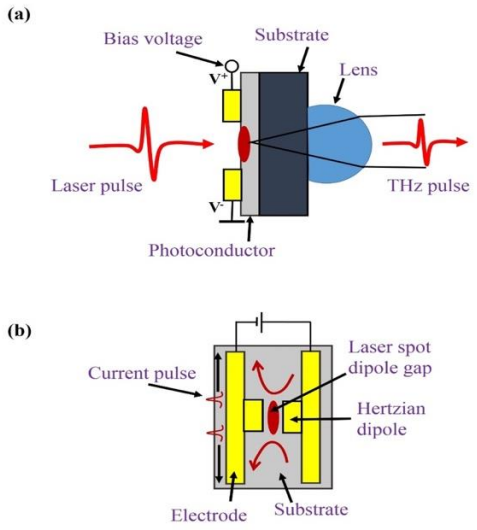

Figure 15: (a) Schematic side view and (b) Top view of PC emitter.

In the THz emitter, operating at room temperature, femtosecond lasers 'pump' pulses (800 nm at 1.5eV) [100], which interact with emitter biased PCA. Consequently, a photocurrent is created with density j and a short, sub-picosecond time scale [101]. Then, the current pulse radiates a THz electric field with a broadband frequency range [100]. The electric field of the THz radiation E_{THz} is proportional to the time derivative dt of the photocurrent dj, described as:

$$E_{THz} \propto \frac{dj}{dt} \quad (3.1)$$

This field depends on two parameters: the pulse width of the femtosecond excitation laser pulse and the decay time of the photocurrent carriers in the active material [102]. The total energy of THz emission depends on the stored energy of the electric field in the PC gap. Unfortunately, increasing the bias voltage may cause a breakdown of the PCA [103]. After generation and emission of the THz pulses, the field is radiated into free space through a lens, like the hyper-hemispherical silicon lens developed by Auston [104], typically placed on the rear of the GaAs substrate. The advantage of the silicon lens is that it reduces the total internal reflection of the THz pulses. Moreover, silicon has a low absorption coefficient and high refractive index (3.42) between 0.2 and 5 THz. Finally, THz pulses propagate to detectors via off-axis paraboloid mirrors through THz lenses and are collected and focused by a silicon lens located on the THz detector.

3.1.1.2. Photoconductive detection

This section will briefly explain how a THz emitted field is detected. A PCA is used to detect the THz radiation. The THz detector is similar in structure to the THz emitter. It consists of two metal electrodes with a small gap, deposited on GaAs BT monolayer. The THz detector gap is excited by a femtosecond laser 'probe' that generates free electrons across the PCA at a given point in time. This generates a photocurrent in the substrate gap proportional to the incident THz electric field. The variation in the optical path between the THz and femtosecond laser pulses via an optical delay enables photoconductive antenna to reconstruct the electric field. The resulting current is amplified and converted to voltage. These extremely weak signals are detected with a lock-in amplifier (LIA) [105], driven by a mechanical chopper wheel localized in the emitter path, providing highly-accurate measurements of the amplitude and phase of the THz electric field signal. The recorded signal is a convolution of the THz pulse by the optical femtosecond pulses, as shown in Figure 16 .

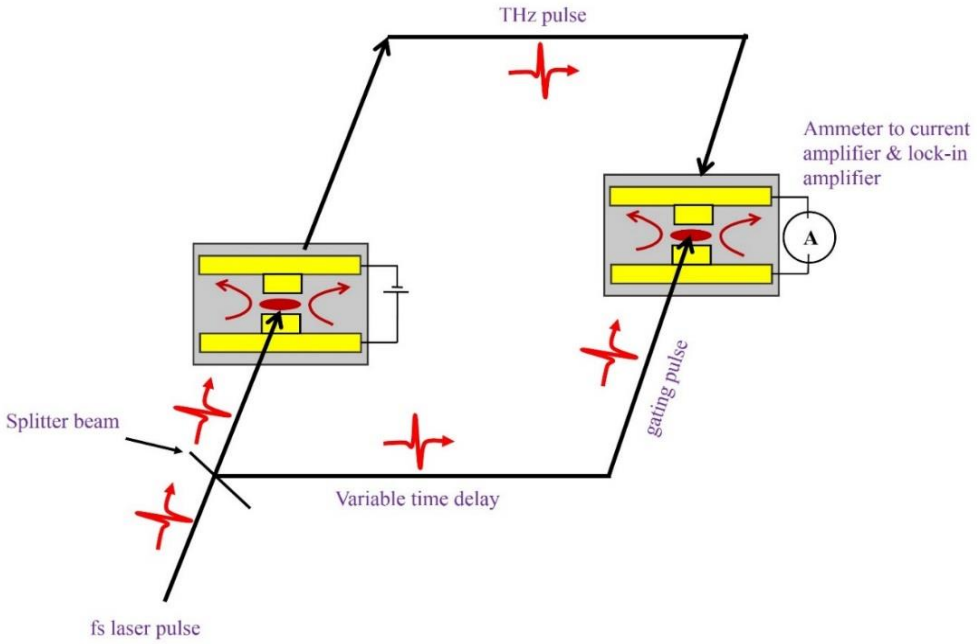

Figure 16: Schematic illustrating the variable optical path between pump-probe pulses.

The THz signal is measured as a function of time by delaying the laser pulse relative to the THz pulse. Since the laser pulse is narrow in comparison to the time duration of the THz pulse, it acts as a gated sampling signal. However, signal intensity depends on the physical characteristics of the emitter and detector, such as the type of substrate materials, active area of the PCA, and the excitation laser pulse [103].

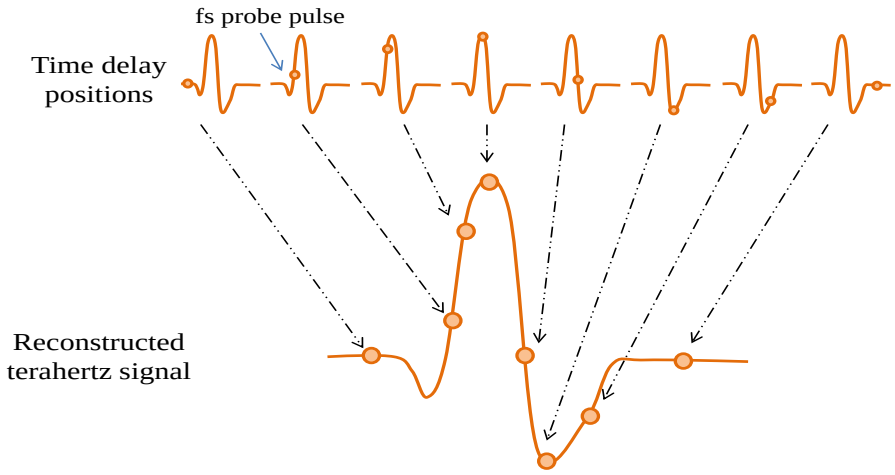

Figure 17: Illustration of the sampling concept of reconstruction of the THz temporal pulse detected by a PC-antenna.

3.2. Teraview THz imaging and spectroscopy systems

This section describes the Teraview 3000 and TeraPulse 4000 THz spectroscopy and imaging systems. These commercial systems were used for all our ex vivo measurements on human breast tissues, performed at the Bergonié institute. Various human tissue structures and their associated diseases were investigated by either THz spectroscopy or imaging. Figure 18(a) and Figure 18(b) show the Terahertz imaging and spectroscopy systems. The Teraview 3000 and TeraPulse 4000 systems provide TDS and spectral imaging in both transmission and reflection modes.

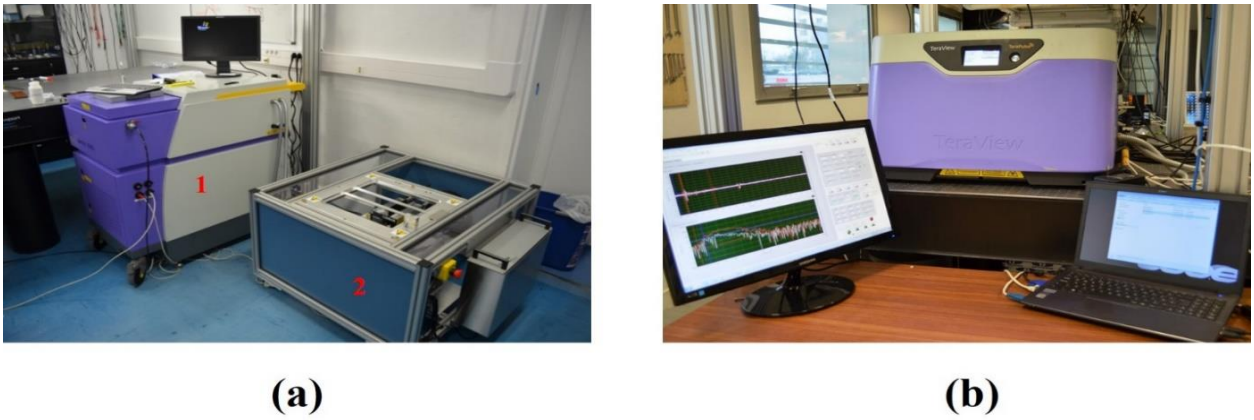

Figure 18: Photograph of (a) Teraview 3000 system, 1) Transmission mode and 2) Reflection mode, and (b) TeraPulse 4000 system, which is more compact and transportable.

In THz spectroscopy and imaging, broadband THz pulses are used to generate images and evaluate the optical properties of a sample from measurements made in both transmission and reflection modes. In THz imaging, measurements are taken on a 2D scan to generate a dataset of time domain waveforms [1]. In both the spectroscopy and imaging techniques, the pulses' time of flight produces depth information and fast Fourier transforms are used to acquire spectral information. In general, the experimental setup for both THz systems uses transmission and reflection geometry, as shown in Figure 18(a) and (b).

Teraview 3000: Figure 18(a1) illustrates the experimental setup for a THz transmission system, using PCAs. The system properties are produced in the 0.2- 3 THz frequency range, with a maximum density of 75dB, a spectral resolution of 0.06 THz, and rapid scan mode (i.e. 30 scans/second).

For measurements in transmission mode, the chamber was purged with dry air or nitrogen during measurements to reduce absorption of the THz spectra measured due to ambient water vapor in the air. All measurements were made at room temperature, around 22 to 23 C°. One of the key considerations for image acquisition is the rate at which the THz waveforms are acquired, since this often determines the time required to form an image.

Typically, spectral imaging is achieved by moving the (X, Y) translating stage with the terahertz beam focused on the sample position. A raster scan with a maximum area of 16×16 mm^2 is performed in the core chamber. Transmitted data for each pixel is acquired and converted from and to the frequency domain by FFT. Time acquisition ranged around from 10 min to 3 hours, depending on the scan parameters, including area of sample scanned and pixel size.

Teraview 3000 in reflection mode: Figure 18(a2) illustrates experimental setup for THz reflection geometry. The geometry is the same as the THz transmission system, with the following main features:

- It is designed as a horizontal system.
- In the optical setup of the mirror, the THz pulse is focused on the sample by a pair of mirrors, and then reflected from the sample to the detector through the same lens.
- Maximum scanning area: 30×30 cm^2.
- During scanning, the sample holder is fixed and the THz emitter and detector move (X, Y) at a maximum speed of 50 mm/second.
- Acquisition time ranges from around 15 min to 7 hours, depending on the scan parameters.

TeraPulse 4000: as shown in Figure 18(b), the THz heads are inserted into an (X, Y, Z) opto-mechanical setup developed in our laboratory for our experimental study on liquids and breast tissues. As shown in Figure 19, this system operates on the same principle and design as the Teraview 3000, with the following differences:

- It is portable, with an 80MHz repetition rate and pulse duration around 80 ps
- Transmission and reflection mode are available in the same box.
- Frequency range from 0.1- 4 THz, supplied by external fibers to provide a flexible configuration for the experimental setup.
- In addition, the sample holder is motorized, giving a maximum scan area of 50×50 mm^2. The setup uses a pair of off-axis planar mirrors.
- In Rapid Scan, the motor moves the sample holder (X, Y) at a maximum speed of 30 mm/second.
- Acquisition time ranges from 15 min to 12 hours.
- Finally, acquisition is performed using the LabVIEW software we developed.

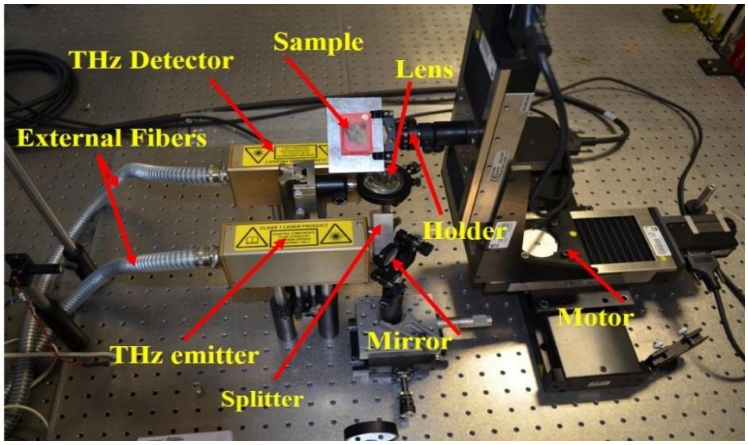

Figure 19: Photograph of the experimental Tera-Pulse 4000 setup developed in the Lab.

3.2.1. Transmission and reflection mode measurements

These experimental measurements used to determine the optical properties of samples and produce 2D images were obtained using THz spectroscopy and imaging in two modes (transmission and reflection), as shown in Figure 18(a), Figure 18(b), and Figure 19. I The reference or sample was placed on the sapphire window. The THz pulses were focused on the detection devices by a pair of optic mirrors (OMs). Finally, different information was extracted by THz spectroscopy of the sample, using either reflection (for strongly absorbing materials) or transmission mode.

3.3. THz imaging and spectroscopy sample holders

3.3.1. Liquid sample cell (transmission)

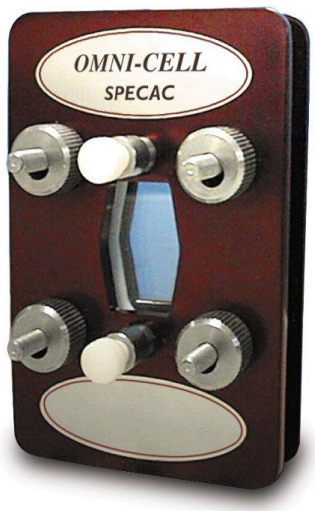

Figure 20: Photograph of liquid sample cell (transmission).

The choice of transparent window materials was suited to THz waves. The space between the cell windows was designed for use with transmission cell holders to obtain the relevant measurements. The THz spectroscopy transmission setup in this study was used to describe the properties of liquid samples. Moreover, the liquid-cell method was used to compare liquid characterization of drops of liquids deposited on the top surface of the sapphire window (reflection spectroscopy). It was essential to check that no gas bubbles were trapped and the liquid was spread in a thin layer between the plates, which were then clamped together. A 1 mm-thick sapphire (or silica) window was adjusted according to the absorbance of the sample liquid by inserting spacers between the double window and rubber rings were placed between the silica window and screws. A reference measurement was made each time using two windows held together. Figure 20 shows a liquid sample holder.

3.3.2. Solid sample cell (transmission)

A solid sample transmission cell, consisting of double sapphire windows with metal spacers, as shown in Figure 21, was used to measure the optical properties of solid biological samples. The sample was placed on top of the sapphire window, positioned at midway of the focal point of the THz transmission beam. A second sapphire window was placed over the sample as a cover and fixed onto the holder to ensure that the sample was securely positioned. The sample could be immersed in physiological serum for preservation purposes. A metal spacer

was used to avoid compressing the tissues, as that would affect their optical properties, while minimizing uneven tissue shrinkage, which may occur during imaging, thus impacting the accuracy of data on the biological tissue extracted from the THz results. A reference measurement was made, using two sapphire windows held together without a sample.

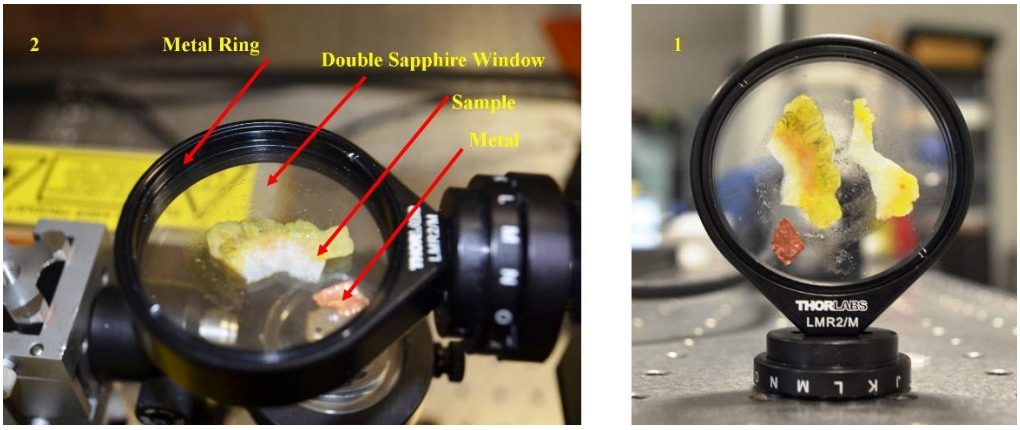

Figure 21: Photograph of solid sample holder 1) Before fixing in system, 2) After fixing in system.

3.3.3. Solid sample cell (reflection)

The same tissue holder was used to extract accurate optical parameters in THz reflection imaging. The method relies on measurements using the reflected signals from the bottom of the sapphire window. These signals may have fluctuations due to tiny variations in window or sample thickness, sublayers of the samples, or the space between the samples and the holder surface. The biological tissue was placed on the sapphire window, positioned at the focal point of the reflected THz waves, and held in place with a metal ring and a sapphire cover window, as previously described. Sample positions were localized by a metal reference point, placed on the sapphire window, visible in the THz images, as shown in Figure 21. Systematic photographs were taken of the samples to correlate with the terahertz images and histopathological report.

3.4. Experimental materials and data analysis methods

In this experiment, pure compounds, liquids, solids, tissue samples, and water were used to determine and validate our data processing, display, and analysis. Furthermore, to obtain analysis data on material properties at the appropriate THz frequencies, samples were created by mixing the pure compounds with water to evaluate the capacity of the THz technique to determine the physical properties of liquids. Finally, section 3.4.1 reviews three compounds used to determine material parameters with the THz setup, including data collection from the

transmission, and reflection measurements. The application of these techniques to tissue is presented in section 3.4.2.

3.4.1. Application to known materials

3.4.1.1. Pure compounds

The term "pure compound" indicates that a substance includes two or more elements in a specific ratio, with a constant chemical composition and characteristic properties in complex mixtures. Pure compounds, such as distilled water and ethanol were used as models for true compounds, to check the predicted response of the validated concentration and compare with the samples studied. Methanol (99.9% pure) was used for this experimental validation, as the interactions of the molecules with water at various concentrations produced different results. It was also essential to include water as one of the components, due to its importance in biological systems [106].

3.4.1.2. Solid materials

The THz spectral response of solid materials is related to lattice vibration, optical phonon-phonon or phonon-electron interactions, and other types of elementary excitation [107]. In this study, THz spectroscopy measurements were used to study and analyze the spectral response of solid materials [106], such as Teflon, glass, and silica. All samples used were smooth and both sides were polished. The optical properties of each sample are shown in Figure 22. Finally, analysis of the THz spectral data provided information on their physical properties. Absorption coefficients indicated that these solid samples had low transmission properties in the 0.2-2 THz region.

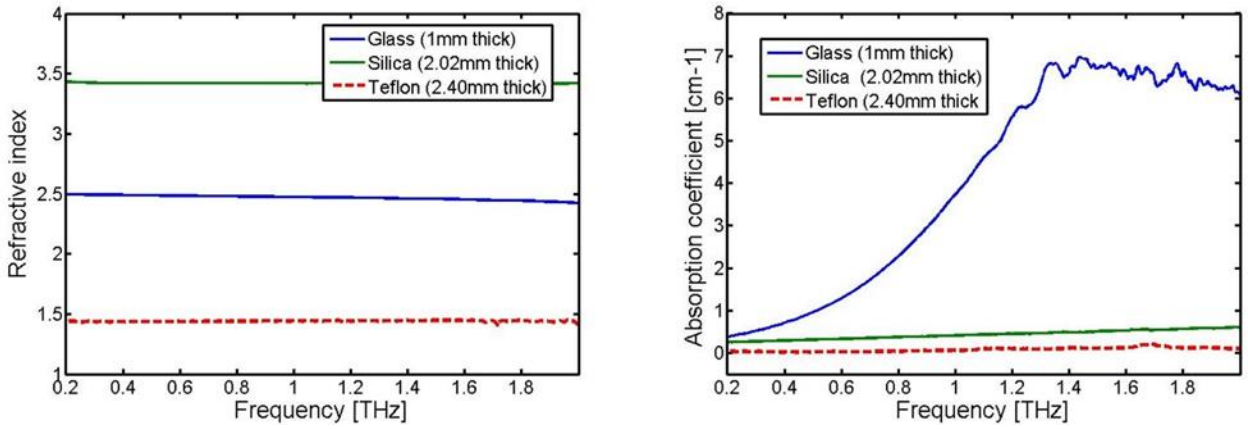

Figure 22: The refractive indices and absorption coefficients of Teflon, glass, and silica were measured by THz spectroscopy.

3.4.1.3. Liquid materials

This section includes the application of THz spectroscopy to the detection and analysis of the dielectric and molecular properties of liquids, depending on their interaction with THz radiation, as well as the relaxation of dipoles within liquids. The dielectric response of the non-polar liquids is due to collision-induced dipole moments [108]. Water and aqueous solutions are considered interesting liquids for biological tissue applications, as illustrated in Chapter 2. Finally, THz spectroscopy has the ability to analyze liquids and liquid-water mixtures, as illustrated in [109].

3.4.1.4. Tissue Samples

Tissue samples were bio-specimens taken from the human body, used for cancer analysis. Medical researchers use tissue to obtain important information that improves cancer detection, diagnosis, and treatment. For THz spectroscopy and imaging, we studied breast cancer tissue samples, prepared according to a histopathological protocol. Pathological assessment was made on the removed tissue to identify diseased locations and healthy tissue for imaging. Figure 23 shows the procedure and a protocol for THz spectroscopy and imaging of human breast tissue. Furthermore, standard operating procedure was followed to obtain human tissue sections from the Bergonié Institute. Finally, these tissues were collected and processed as paraffin blocks. Fresh tissues were also used for characterization in reflection mode.

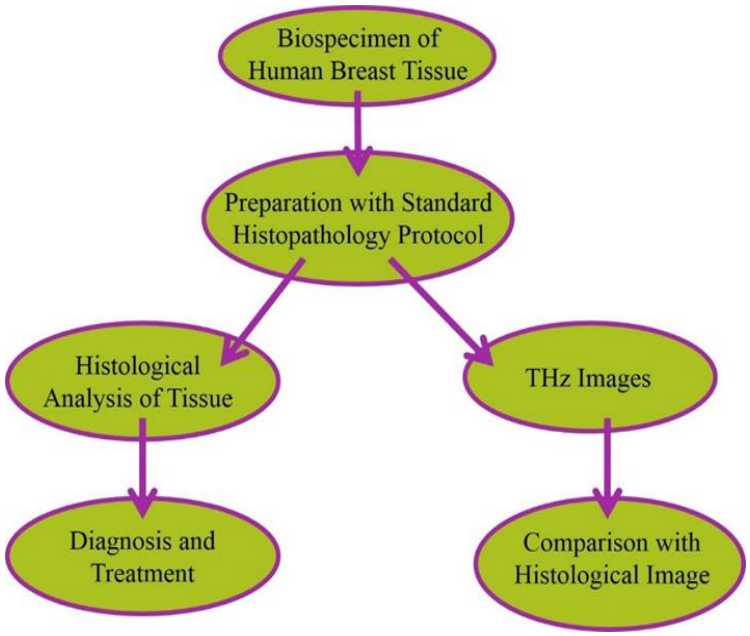

Figure 23: Procedure and protocol for human breast tissue study by THz imaging.

3.4.2. Measurements

3.4.2.1. Transmission Measurements

The intrinsic dielectric parameters of materials were determined by analyzing the complex transfer function in the frequency domain, by the intermediation of a reference sample. Let us consider a sample positioned between the source and detector as shown in Figure 18 (a1). The electric fields transmitted through the reference and the sample, $E_r(w)$ and $E_s(w)$, respectively, are expressed as follows:

$$E_r(w) = A_r e^{i\varphi_r} \tag{3.2}$$

And;

$$E_s(w) = A_s e^{i\varphi_s} \tag{3.3}$$

Where A_r, A_s, φ_r, and φ_s are the amplitude and phase of the electric fields of the reference and sample, respectively. Several approximations were used to calculate the complex transfer function of a sample from its refractive index. The electromagnetic beam was considered to have a plane wave impinging on the sample at normal incidence. Samples were considered:

- homogeneous, planar with parallel sides;
- isotropic, without any surface charge;
- to have a linear electromagnetic response.

In this case, the electric field of the sample is expressed in a function of its reflection, transmission, and propagation coefficients.

$$E_s(w) = T_{air-s}(w).P_s(w,d_s).T_{s-air}(w).E_{inc}(w).FP(w) \tag{3.4}$$

Where $T_{air\text{-}s}$ and $T_{s\text{-}air}$ are the transmission coefficients at the air-sample and sample-air interfaces, respectively, P_s is the propagation coefficient in the sample, E_{inc} is the incident electric field and FP is the Fabry-Perot expression. FP takes into account the multiple reflections at the sample-air interfaces, as follows:

$$FP(w) = \sum_{i=0}^{\infty}\left(R_{air-s}^2(w).P_s^2(w,d_s).T_{s-air}^2(w)\right)^i \tag{3.5}$$

Where R_{s_air}, the reflection coefficient at the air-sample interface is:

$$R_{s-air}(w) = \frac{\tilde{n}_s - \tilde{n}_{air}}{\tilde{n}_s + \tilde{n}_{air}} \tag{3.6}$$

The transmission coefficient at the interface air-sample is:

$$T_{s-air}(w) = \frac{2\,\tilde{n}_s}{\tilde{n}_s + \tilde{n}_{air}} \quad (3.7)$$

The propagation coefficient in the sample is described by:

$$P_s(w) = exp\left[-i\,\frac{\tilde{n}_s.\ w.\ d_s}{c}\right] \quad (3.8)$$

Where d_s is the sample thickness.

Using these equations and one experimental value of the transfer function, it is possible to extract the complex refractive index ($\tilde{n}_s$), is expressed as a function of the real refractive index n and the extinction coefficient k that describes the relative absorption loss at a particular wavelength, as follows:

$$\tilde{n}_s = n - ik \quad (3.9)$$

Thus the absorption coefficient α is calculated from the extinction coefficient as follows:

$$\alpha = \frac{4\pi\, w}{c}\, ik \quad (3.8)$$

Where c corresponds to the speed of light in vacuum. The complex transfer function corresponds to the ratio of the terahertz electric field in a chosen reference (E_r) and after being transmitted through the sample (E_s), simply expressed as follows:

$$Tr(w) = \frac{E_s}{E_r} = \frac{A_s}{A_r}\, exp[\varphi_s - \varphi_r] \quad (3.9)$$

Where the amplitude and phase take into account the reflection, transmission, and propagation coefficients, as well as the Fabry-Perot effect.

Signal processing and noise reduction:

A common way to describe the performance of a particular TDS system is based on its dynamic range (DR) and signal-to-noise ratio (SNR). The DR indicates the minimum detectable signal change and corresponds to the signal-to-noise ratio, expressed in dB. The SNR indicates the extent to which a signal can vary and still be accurately measured; it is the ratio between the largest and smallest measurement. For a system like THz-TDS, which measures both amplitude and phase, several methods are used to define the SNR and DR.

The main definitions of these two values are:

$$DR = \frac{maximum\ value\ of\ the\ signal}{root\ mean\ square\ value\ of\ the\ noise} \quad (3.10)$$

And

$$SNR = \frac{mean\ value\ of\ the\ signal}{standard\ deviation\ of\ the\ signal} \quad (3.11)$$

Several actions were taken to reduce noise and artifacts on the measured spectra:

1- The measurements were made in a chamber purged with dry air to eliminate water vapor. Figure 24 shows the spectra of a measurement made in dry (red), and humid air (blue) by opening the chamber. The blue spectrum represents undesirable absorption bands, corresponding to the absorption of the THz waves by water molecules. A hygrometer was added to the setup for real-time monitoring of the relative humidity level, which was kept below 1% by using a flow of dry air.

2- Each spectrum was average over 1000 repetitions to stabilize the signal fluctuations. System repeatability measurements were performed on the same sample several times over a long period of time. Results showed a signal variance of less than 1% between one measured signal and another one at least one week apart. This variance was considered negligible and the signal was considered as repeatable over a long period.

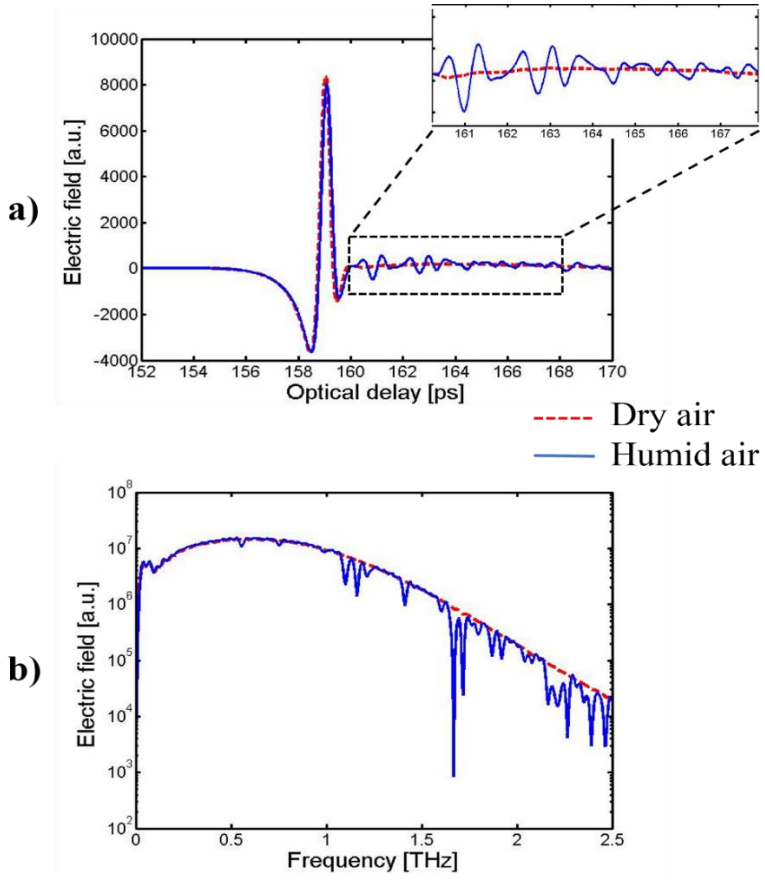

Figure 24: a) Time domain waveforms, b) FFT spectra of these signals in two cases: in dry air (red) and humid air (blue) were measured without samples.

3.4.2.2. Reflection measurements

In this modality, measurements were made using samples positioned on the substrate or sandwiched between double sapphire windows. The sample chamber in THz spectroscopy was purged with nitrogen or air to remove water vapor and all measurements were made at room temperature. The THz beam was then directed at a certain angle, to reflect off the internal surface of the studied sample at a short distance. The THz reflections from sample sublayers created transient waves, which extended beyond the surface into the sample. The sample absorbed the THz beam, resulting in an attenuation of the reflected THz signals, which were compared to those obtained by transmission spectroscopy. A reference was created by focusing the THz beam on the top surface of an empty sapphire window. Finally, data accuracy depended on the sample reflection intensity and characterization of the nature of the sample, as well as experimental system conditions.

To extract the dielectric response of the sample, we implemented a method taken from [110] for processing and reducing the noise from experimental data in the reflection configuration, making four measurements per sample to optimize data extraction. These data are represented on Figure 25. Chiefly, we paid special attention during the calibration procedure, as data extraction in reflection configuration is extremely sensitive to phase mismatch between the reference pulse and the sample reflection. Spectro-imaging was performed to quantify the optical thickness for each image pixel location. Then, using the self-reference method proposed by [17], the phase misalignment, the main remaining error source, which has a major impact on the extracted properties, was drastically reduced [18]. Following this first calibration step, a numerical procedure was applied to calculate and to correct the baseline. Special care was paid to ensure that the sample was firmly held and parallel to the motorized stage. A reference signal was then measured at each pixel position and the dielectric properties were calculated from each pixel signal.

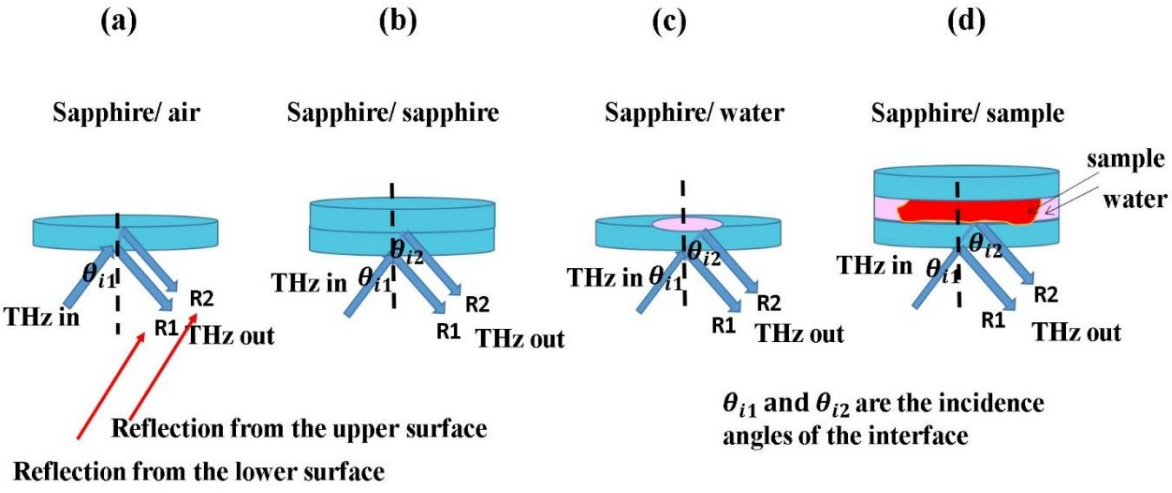

Figure 25: Illustrates the procedure for measuring reflected THz signals.

Figure 25 represents the data in time domain, recorded on a Teraview system in reflection mode. The reflection THz signal was collected from the air-sapphire surface to be used as a reference or air signal, as shown in Figure 25(a), and the reflected THz signal was collected from the sapphire-water interface, as shown in Figure 25(c). Also in this study, a double sapphire (sapphire-sapphire) setup was used to measure the baseline reflection THz pulse (enhancement of the time delay between the 2 peaks), as shown in Figure 25(b). In addition, signals were collected from sapphire-samples but also with other substrates, such as glass, Teflon, and silica as shown in Figure 25(d). All reflection measurements were recorded at 8 deg incident. A 100 ps measurement window was used with 4096 data points collected for each typical sampling time interval of 0.019 ps. These data also contained noise that affected the second peak, if the time delay between them was too small, as shown in Figure 26. The two signals (peaks) were isolated from the data set, by cutting and padding, to facilitate fast Fourier transformation of both signals (R1andR2) with the same time extension and interval. Padding artificially improved the frequency resolution and signal-to-noise ratio in the signals recovered after inverse Fourier transformation.

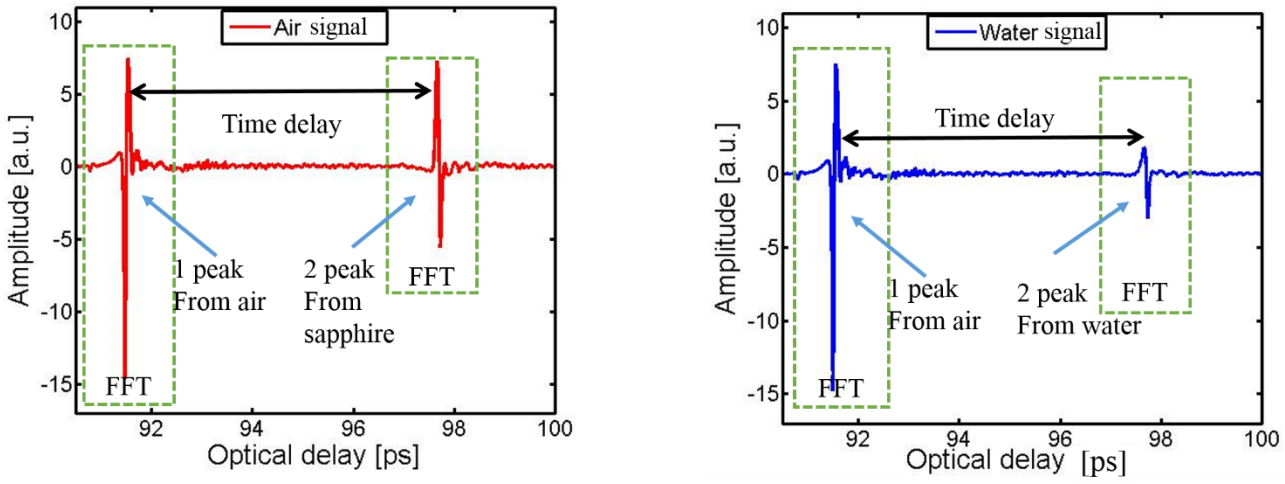

Figure 26: Time domain waveforms of the measured total reflection in air (reference) and water, and the relationship of the transfer function and reflection quotient calculated after signals were cut into two peaks.

After cutting and padding ,(i.e. extending the time domain waveform by additional zero amplitude points on the end of the recorded data series to produce a similar increase in the number of points in the frequency domain), we calculated the transfer function (TF) ratio between the first (1P) and second (2P) peaks of the air-substrate interface. Additionally, we calculated the reflection quotient (RQ) ratio between the second peak of the water signal and the first air peak during the calibration procedure as a function of frequency, as shown in equations (3.14) and (3.15), respectively [110]. This was repeated for all the pixels in the future sample position.

$$TF = \frac{FFT(2P_{air})(x,y,t)}{FFT(1P_{air})(x,y,t)} \quad (3.12)$$

$$RQ = \frac{FFT(2P_{water})(x,y,t)}{FFT(2P_{air})(x,y,t)} \quad (3.13)$$

We then used TF and RQ to process the air $E_{2air}(x,y,t)$ and water $E_{2water}(x,y,t)$ signals at the same spatial point on the window in the time domain using the inverse Fourier transformation (ifft) in equations (3.16) and (3.17);

$$E_{2air}(x,y,t) = ifft\,[\,TF \times FFT\,(E_{1sample}\,(x,y,t)\,] \quad (3.14)$$

$$E_{2water}(x,y,t) = ifft\,[\,RQ \times FFT\,(E_{2air}(x,y,t)\,] \quad (3.15)$$

Consequently, we were able to calculate baseline $E_{baseline}(x,y,t)$ more accurately with equation (3.18) using the FFT command, correcting the errors due to oscillations from the first interface, thus eliminating the noise from the THz baseline signal, as illustrated below in Figure 27.

$$E_{baseline}(x,y,t) = \frac{FFT(E_{2water}(x,y,t)) - M.FFT(E_{2air}(x,y,t))}{1-M} \quad (3.16)$$

Where M represents the ratio between the second water and air peaks for all frequencies. M only depends on the experimental geometry and the material used as substrate. This parameter was calculated and compared with the calibration measurements.

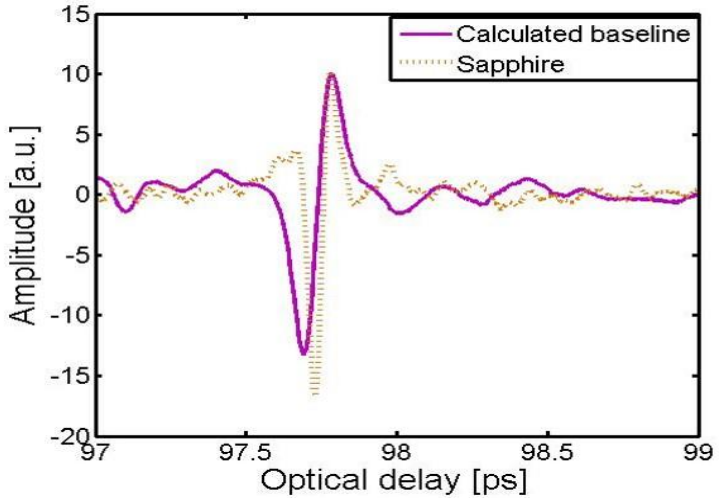

Figure 27: Time domain waveforms of the baseline: measured (Sapphire) and calculated.

Figure 28(a) shows the FFT spectrum of reference (air), water, and second peak sample (fresh tissue) without the baseline method. Figure 28(b) shows the spectrum results of the same second peak samples, corrected using the baseline method. We observed a reduction in oscillations from the spectrum after processing in the frequency range from approximately 0.1 to 2.7 THz. In addition, the spectrum of all samples fell to the noise floor at approximately 3.8 THz, compared with approximately 2.7 THz before processing.

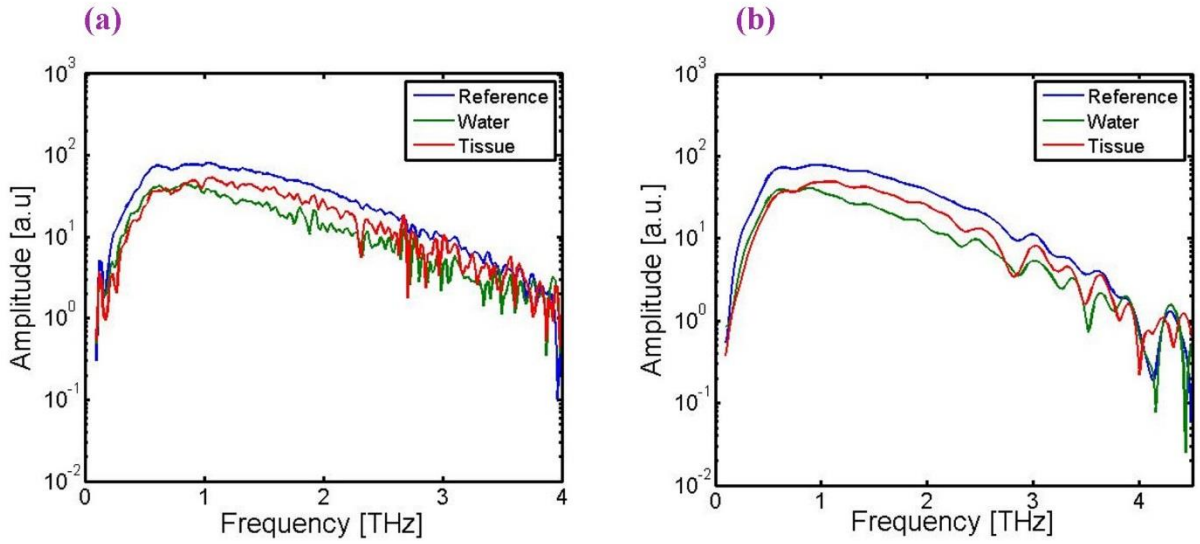

Figure 28: FFT spectra of second peaks of each reference, water, and sample, a) before and b) after data processing.

Consequently, by correcting the baseline, we also improved the data extraction of the THz signals for the sample, water, and reference signals, thus improving the results of the optical properties in the reflection mode. The theory used to calculate the refractive index and absorption coefficient is as follows:

$$M = \frac{(\tilde{n}_{sapphire}\cos\theta_{sapphire} - \tilde{n}_{sample}\cos\theta_{sample})\,(\tilde{n}_{sapphire}\cos\theta_{sapphire} + \tilde{n}_{air}\cos\theta_{air})}{(\tilde{n}_{sapphire}\cos\theta_{sapphire} + \tilde{n}_{sample}\cos\theta_{sample})\,(\tilde{n}_{sapphire}\cos\theta_{sapphire} - \tilde{n}_{air}\cos\theta_{air})} \quad (3.17)$$

Where $\tilde{n}_{sapphire}$, $\tilde{n}_{air}$, *and* $\tilde{n}_{sample}$ represent the complex index of each sapphire, air, and sample, respectively. θ represents the incident angle of the THz beam at the sapphire, air, and sample interfaces, respectively.

From transmission measurements of the refractive and absorption indices of sapphire, we calculated the theta value of sapphire and water using Snell's law, as shown in

Table 1.

$$\tilde{n}_{sapphire}\cos\theta_{sapphire} = \tilde{n}_{air}\cos\theta_{air} \quad (3.18)$$

Table 1: Incident angles calculated from l to 2 interfaces: air and sapphire.

Angle	Sapphire	Air
Deg.	2.93	10
Rad.	0.05	0.17

Then, from equation (3.19) we calculated the complex index ($\tilde{n}_{sample}$) and theta ($cos\theta_{sample}$) of sample, using equation (3.21);

$$\tilde{n}_{sample}\, cos\theta_{sample} = \frac{(1-M)\tilde{n}^2_{sapphire}\, cos\theta^2_{sapphire} + (1-M)\tilde{n}_{sapphire}\, cos\theta_{sapphire}\, \tilde{n}_{air}\, cos\theta_{air}}{(1-M)\tilde{n}_{air}\, cos\theta_{air} + (1-M)\tilde{n}^2_{sapphire}\, cos\theta^2_{sapphire}} = R \qquad (3.19)$$

$$\tilde{n}_{sample} = \sqrt{sin^2\theta_{air} + [real\{R\}]^2} \qquad (3.20)$$

$$cos\theta_{sample} = \frac{real\{R\}}{\sqrt{sin\theta^2_{air} + real\{R\}^2}} \qquad (3.21)$$

Where, the real{R} represents the real part of equation.

Finally, the refractive index and absorption coefficient of the sample were calculated from equations (2.18) and (2.19), as showed in Figure 29. Figure 29(a & b) show the refractive index and absorption coefficient of the microscope slides (glass) investigated. The 1 mm-thick sample was found to have a refractive index of roughly 2.48 to 2.44 at a frequency range between 0.2 and 1.4 THz, with an absorption coefficient of roughly 0.4 to 6.8 cm^{-1} across the same frequency range. Figure 29(c & d) show the refractive index and absorption coefficients of a 2.40 mm-thick Teflon sample, known to have a refractive index of 1.44 in the 0.2 - 2 THz range, with an absorption coefficient of 0.02 to 0.16 cm^{-1} across the frequency range from 0.2 to 1.5 THz. Figure 29(e & f) show the results of the refractive index and absorption coefficient of a 2.02 mm-thick silica sample. The refractive index was 3.44, over a frequency range between 0.2 and 2.2 THz, with an absorption coefficient of 0.3 to 1 cm^{-1} across the frequency range from 0.2 to 1.6 THz. As a result, we observed a marked difference between the corrected and uncorrected optical properties. The shapes of the sample signals obtained from our method after processing were fairly smooth, compared with the shape of the same signal samples before processing, where both the refractive index and absorption coefficient were oscillatory. Therefore, any small amount of measurement noise produced by interference from surface reflections or caused by water vapor significantly affected the calculated optical properties. The baseline processing method was then applied to medical samples to calculate their optical properties with a high degree of accuracy, as shown in Figure 30.

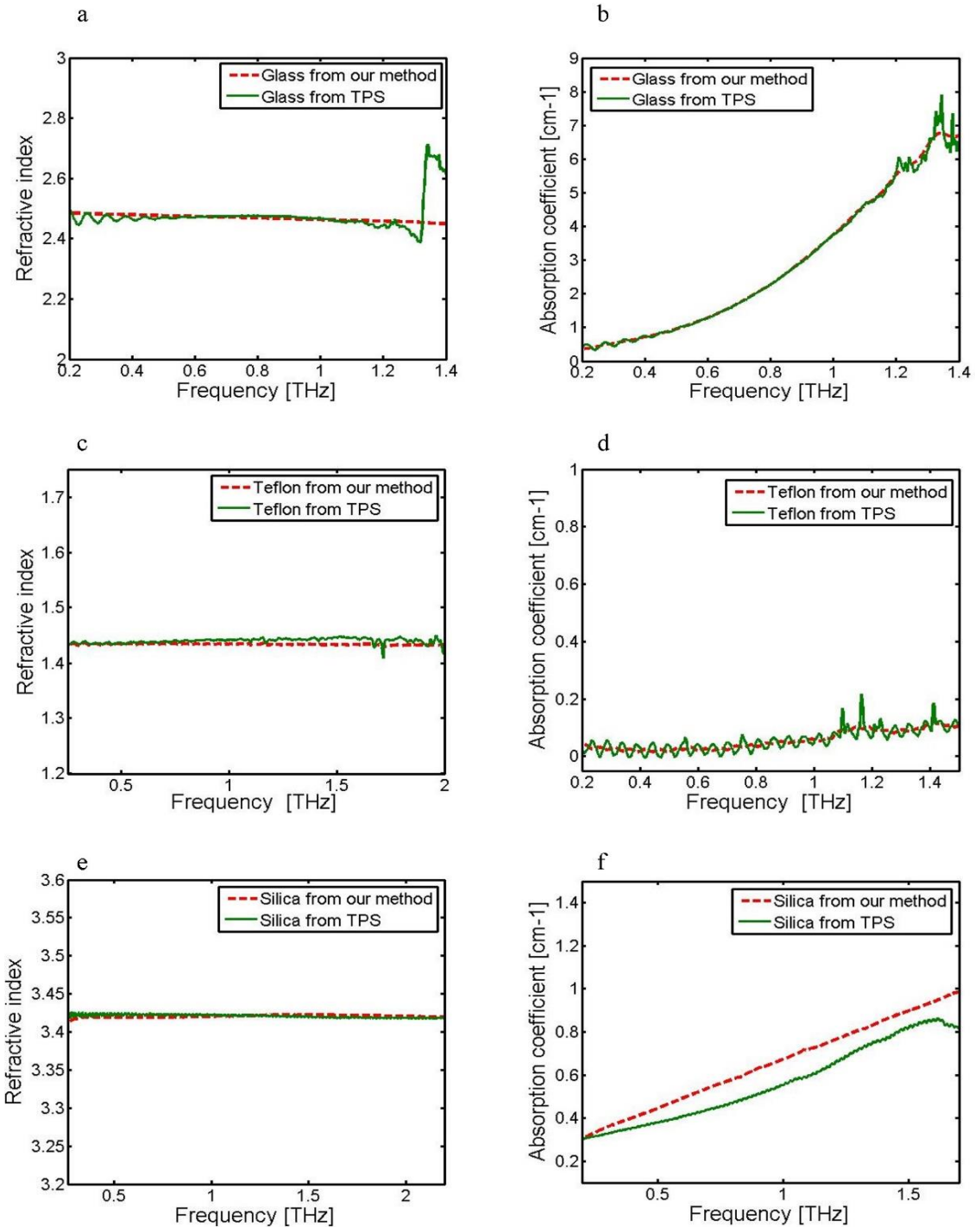

Figure 29: Comparison of the refractive indices and absorption coefficients obtained with the baseline processing method and Terahertz spectroscopy (TPS) measurements of 1 mm-thick glass, 2.40 mm-thick Teflon, and 2.02 mm-thick silica, respectively.

Figure 30 represents the average properties of a 2 mm-thick, fresh breast tissue, taken from a 50-year-old woman diagnosed with grade I invasive carcinoma NST. After processing with the baseline method, we compared

measurements through a 3 mm-thick sapphire window with those obtained without the baseline. The signals were recorded in triplicate. From these plots, we observed that the refractive index and absorption coefficient calculated using the baseline method were smoother than the refractive index and absorption coefficient calculated without using the baseline method. Furthermore, the absorption coefficient and optical indices, with and without baseline, remained close together between 0.35 and 2.1 THz. Moreover, these figures highlighted the differences between the refractive indexes and absorption coefficients of tumor and normal tissue. While the refractive index of tumor regions was around 2.4 at 1 THz, the refractive index of normal tissue was 2.1 at 1 THz. The absorption coefficient of the tumor region was 160cm^{-1} at 1 THz, while that of a normal region was 130 cm^{-1} at 1 THz. However, differences in the refractive index and absorption coefficient values between tumors and normal region may be due to the higher water content in the tumor region than in normal tissue, as the refractive index and absorption coefficient of water at 1 THz are 2.45 and 240 cm^{-1}, respectively for. Therefore, this improvement in THz pulses in the time domain reflected from a sample using the baseline method was important for calculating an accurate refractive index and absorption coefficient in reflection mode at frequency bandwidth, as it removed all low- and high-frequency noise from the reflected signals.

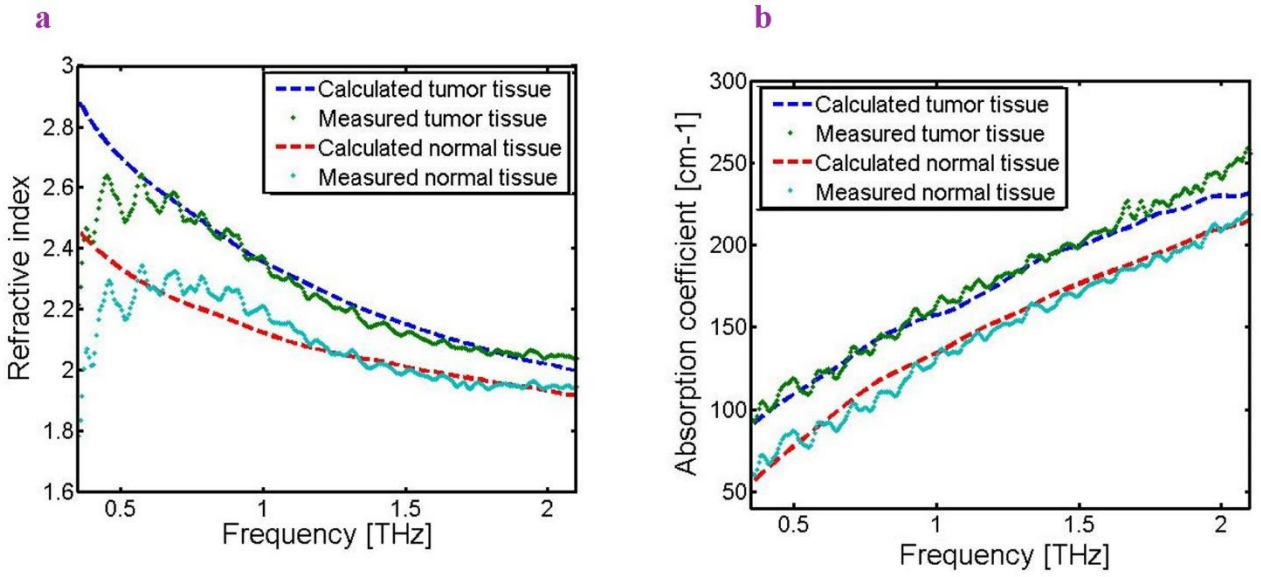

Figure 30: Comparison between a) refractive indices and b) absorption coefficients, calculated by the baseline method and without baseline.

3.4.2.3. Tissue measurements

The human breast cancer samples used in this study were measured in THz spectroscopy and imaging transmission and reflection modes. Our experiments were conducted thanks to cooperation between the laboratory and hospital, enabling us to use tissue specimens. The bio-tissue (embedded, fresh, or block tissue) used for measurement was cut into sections of different thickness. In addition, the preparation time from tissue removal to imaging was typically approximately 30 minutes for fresh samples and any tissue brought from the hospital was kept in physiological serum prior to imaging. Of the 51 samples used in this study, the first 22 were fixed with paraffin and 9 block samples were mounted on transparent materials and imaged by placing on a metal plate. The final 20 fresh tissue sections were measured using scanning and spectroscopy in holding cells. All measurements were made at room temperature. Moreover, samples were imaged using a photographic camera before scanning, to facilitate comparison and correlation between contrast regions on the THz image and features in the photographic image, as shown in Figure 31. After scanning, fresh tissue samples were kept in formalin for 24 hrs. and subjected to further study. Changes in tissue orientation (size, shape, and surface) made accurate image registration difficult for the formalin-treated tissue.

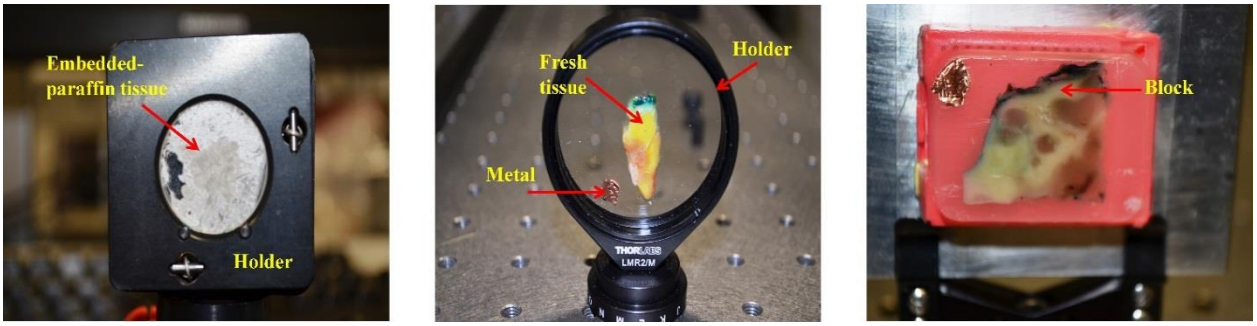

Figure 31: Photograph types: embedded, fresh, and block tissues.

3.5. Summary

The experiments describe above demonstrated the efficiency of THz spectroscopy, for both transmission and reflection geometry. In the 200 GHz-2.5 THz frequency range, we obtained dielectric properties of liquids, solids, and biological tissues. Better results were obtained by studying substances that strongly absorb THz radiation using reflection spectroscopy. The THz absorption and refraction spectra of samples could be used for THz spectroscopy and imaging, to assist in the diagnosis and analysis of biological tissues.

In summary also, the limitations affecting the bandwidth and signal-to-noise of the THz pulse systems were measured. Then, to obtain accurate experimental data with THz , it was necessary to take into account conditions and potential sources of error, such as noise caused by laser fluctuations, imperfect sample surfaces , error

propagation, or multiple reflections, that affect the correct extraction of the absorption coefficient and refractive index and take them into account in the experimental setup.

.

CHAPTER 4

This Chapter presents some experimental data obtained by THz reflection spectroscopy on some phantom materials, with the aim of identifying the THz spectroscopy properties of breast tissue, including lipid, fiber, and cancer. In addition, we tested some models mixing liquids and breast tissues, and then proposed a Debye algorithm to fit the data to a model, and then compared these data with those in the literature to qualify the spectroscopy technique. The goal was to discriminate between breast adipose, fiber, and cancer tissues by their different dielectric responses. Finally, we present a short summary and discussion the results.

4. THz Spectroscopy of Tissue Phantoms

Terahertz spectroscopy and imaging was used to measure all the THz reflection pulses from the interface model [111]. In this part, we determine the complex dielectric properties of pure components to qualify the setup and data processing. The pure components measured in our system included liquid phantoms, such as water, methanol, and formalin, as well as biological tissues. The optical properties and relaxation coefficients of these components in the 0.2- 2 THz range are presented in the following sections. The system was purged with nitrogen to reduce water vapor from spectroscopy and optical path of the spectra prior to measuring. THz radiation interacts with material molecules, causing them to rotate and vibrate, resulting in distinct dielectric spectra, as illustrated in Chapter 2.

Water was interesting to determine, as the complex dielectric properties of the biological tissues were mainly attributable to their high water content. Consequently, water plays an important role in a wide variety of physical and chemical properties of biological tissue [112]. Therefore, the tumors have different water content from fiber and adipose tissues, which modify the contrast mechanism in THz imaging of cancer tissue. In this study, methanol was chosen for experimental study of the THz spectroscopic technique, due to its electric properties, including high absorption in the THz spectrum [113]. However, it has some disadvantages, as it is unstable due to evaporation during scanning. Moreover, biological tissues contain lipids, fibers, and tumors. Lipids are a loose fibrous connective tissue packed with many cells, formed of non-polar molecules containing almost exclusively hydrocarbon chains. Their insolubility in water and solubility in organic materials, and their resulting low-water-content, made them weakly absorbent of THz radiation and demonstrated the potential of providing contrast imaging. Fiber and cancer tissues have a high water content compared to fatty tissues. Biological tissue structures include layers of different cell types, cavities, and vessels containing fluid and

blood, and their typical morphology is altered by disease. In general, it is difficult to obtain tissue with homogenous surfaces for physical measurements with THz spectroscopy.

In order to determine the complex dielectric properties of each pure component (liquids and biological tissues), two-component samples were made, for example, a mixture of water with methanol or water with biological tissue, such as adipose tissue, fibers, and tumors. We used the protocol described in the previous Chapter. The THz beam was focused on the top of a 2 mm-thick sapphire window, where it was reflected at the sapphire-air (reference pulse), sapphire-water (water pulse), and sapphire-sample interfaces (sample pulse). The THz pulse in time domain was acquired at a single, fixed pixel. Consequently, the mean reflected THz pulses from the liquids and biological tissues were compared to water, methanol, and biological tissue data, using the Debye values from the spectroscopy fitting.

Previous studies simulated the interaction of THz radiation in the 0.1-2 THz frequency range with bulk water and skin tissues, using the Debye model [114]. As biological tissues contain mainly water, measurements are only possible in reflection geometry [115], thus Pickwell used a double Debye approach, combined with transmission spectroscopy data, to successfully simulate THz reflection pulses from human skin.

In this study, the absorption coefficients of water, methanol, and various tissues were determined using reflection spectroscopy. The optical properties of the real refractive indices and imaginary absorption coefficients are shown in Figure 33. THz spectroscopy measurements of materials were used to calculate the physical properties of individual materials and mixtures of two pure compounds. We found good agreement between the measured data and some published studies in the frequency range up to 100 GHz with a single Debye model [116]. The Debye [117] and Cole-Cole models [118] are considered efficient for modeling the dielectric properties of human breast tissue [119] and liquids.

4.1. Water and methanol

4.1.1. Absorption coefficient and refractive index

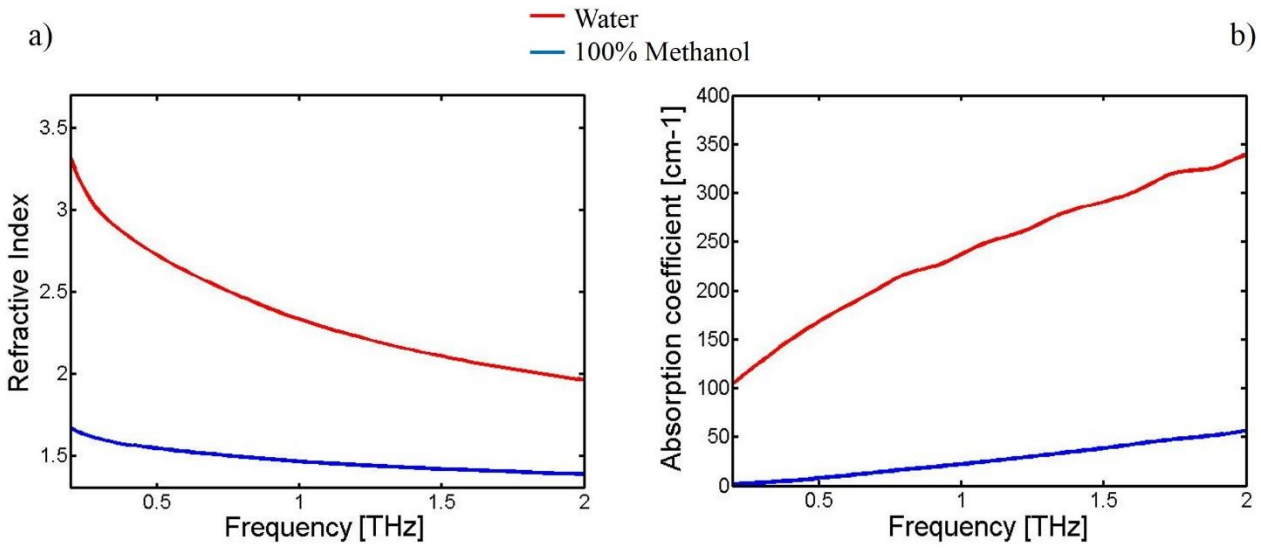

Figure 32: The refractive index (a) and absorption coefficient (b) of distilled water and 100% methanol, measured in TeraPulse 4000 reflection mode.

To calibrate the system, a sapphire water interface measurement was obtained by placing a distilled water droplet on the sapphire window. The sapphire/sample interface was also measured. The baseline was subtracted from both the reference and water pulses to eliminate any back-reflection from the sapphire/air interface by the processing procedure described previously. The refractive index and absorption coefficient were calculated by taking the ratio of the second peak of both the reference and the water in the frequency domain.

The results for the mean refractive index and absorption coefficient of both water and methanol are illustrated in Figure 32 (a) and Figure 32(b), respectively. These plots revealed the variations in the refractive indices and absorption coefficients as a function of frequency in the 0.2-2 THz range. The data for both compounds were calculated by averaging 100 spectra, to offset the high spatial frequency fluctuations. The standard deviations of the absorption coefficients were ($\pm$10.1cm^{-1}) for water and ($\pm$10.3cm^{-1}) for methanol. The average refractive indices were ($\pm$ 0.03) for methanol and ($\pm$ 0.08) for water. Figure 32(a) also shows the dispersive refractive indices of water and methanol, decreasing at higher frequencies. We found that water had a higher refractive index than methanol: while the refractive index of water varied from approximately 3.2 to 2.1, the refractive index of methanol varied from 1.67 to 1.4, as the frequency increased from 0.2 to 2 THz. These plots, also shown in Figure 32(b), confirmed that the absorption coefficients of both water and methanol increased with frequency. The absorption coefficient of methanol ranged approximately from 3-55 cm^{-1} and that of water

from around 107-340 cm^{-1}. The absorption coefficients of water were higher than those of methanol, perhaps due to the polar nature of these compounds. Finally, the refractive index and absorption coefficient of water were approximately in agreement with previously reported values [120].

Our first compound mixture was methanol-water. The mixtures were prepared at various concentrations: 95%/5%, 90%/10%, 75%/25%, 50%/50%, 30%/70%, 20%/80%, and 100% methanol. Figure 33 shows the variations in the refractive indices and absorption coefficients of methanol-water mixtures, in the 0.2-2 THz range. Consequently, the results revealed that the refractive index of methanol at 1THz decreased with increasing water concentrations: from 2.07, 2, 1.9, 1.85, 1.75, 1.64, to 1.47, respectively, as shown in Figure 33(a). Moreover, Figure 33(b) shows the absorption coefficient of the mixture at 1THz, which also decreased with increasing water concentrations: 185, 168, 153, 121.4, 85.8, 78.9, and 51.1cm-1, respectively.

The differences in the refractive indices and absorption coefficients may be due to the direction and strength of the induced dipoles depending on the structure of the materials and the propagation of the electric field [121]. Therefore, Figure 34 presents the results for methanol-water mixtures: the plot shows the changes in the intensity of the mixture of pure compounds as a function of delay time in picoseconds. These changes are due to the fact that light travels slower in materials with a higher refractive index and absorption coefficient, so pulses reflected by the solution will arrive later. This effect is illustrated in Figure 34, as the water peak (higher refractive index) arrives later.

Finally, these results may be due to the dynamic dielectric properties of hydrogen (H) affecting bonding in polar mixtures. This is particularly true of water/methanol mixtures, as both mixture components can serve as donors and acceptors of H bonds, so intermolecular correlations are likely to play an important role in their dielectric relaxation [122]. In addition, these results indicate that the THz reflection technique detects smaller changes in the concentration of the water-methanol mixture.

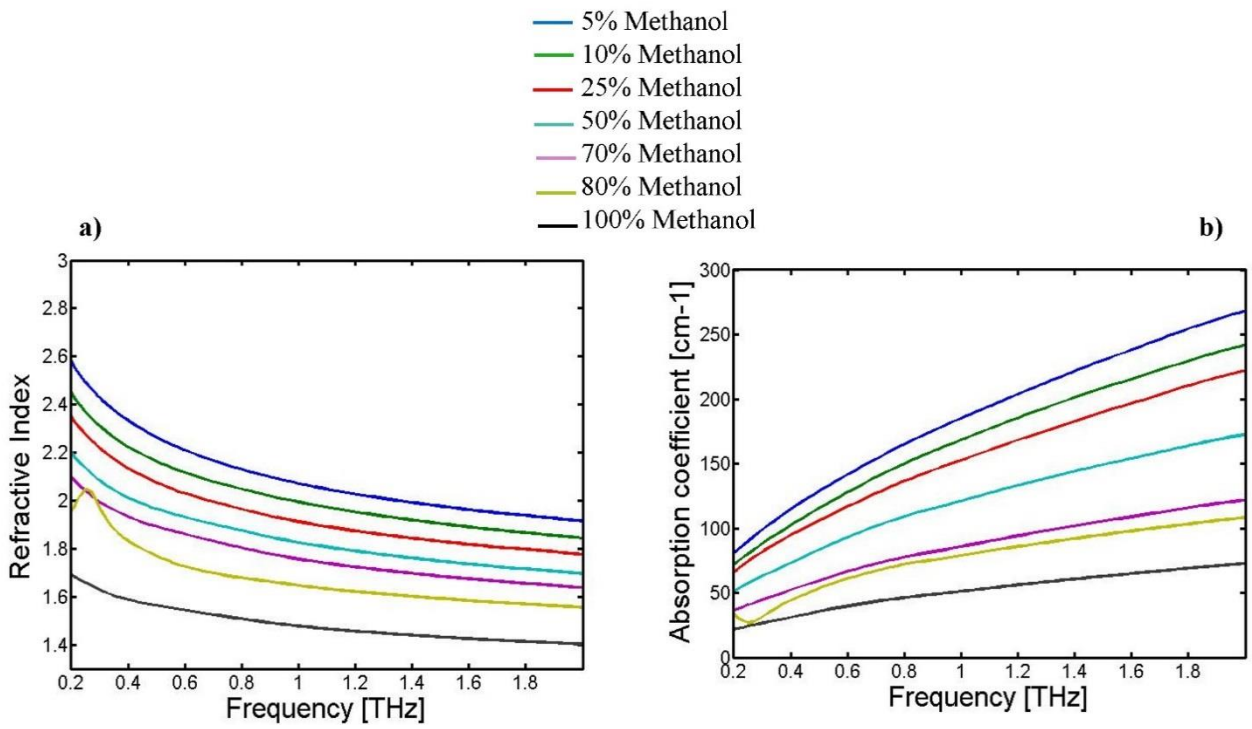

Figure 33: The refractive index of mixtures with varying water/methanol concentrations (a) and absorption coefficient of mixtures with varying water/methanol concentrations.

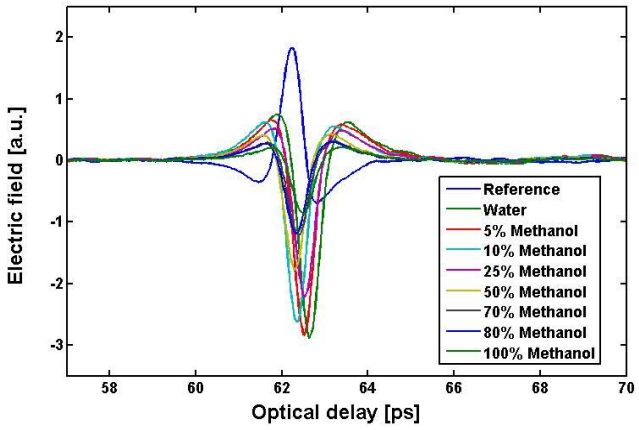

Figure 34: THz reflection spectroscopy impulse function of water/ methanol mixture.

4.1.1. Debye relaxation coefficients

In this section, we studied the behavior of the pure compounds, modeled using two different components: water and methanol. The Debye relaxation coefficient, equation (2.24), and its derivatives were used to analyze the experimental data from the complex dielectric coefficients of both water and methanol, after measuring and extracting the absorption coefficients and refractive indices. The Double Debye relaxation, equation (2.24), was

used to calculate the dielectric coefficients of water and methanol. Figure 35 presents the complex refractive indices, absorption coefficients, and dielectric permittivity. Plots in Figure 35(a) and Figure 35(b) show the Debye model and a Cole-Cole plot of complex permittivity, with imaginary parts plotted against real parts (ε''against ε') of water and methanol, respectively. These plots compare the results of our measurements with Debye model parameters, showing a good agreement. In addition, the plots show that the dielectric permittivity of water was higher than that of methanol. Therefore, the ratio of the imaginary to the real part provides information about the dielectric losses of the materials.

The plots in Figure 35(c) and Figure 35(d) present the complex refractive indices as functions of water and methanol, respectively, over the 0.2-2 THz frequency range. These plots compared measured data obtained from our experiments with the double Debye relaxation model, plotted using parameters such as ε_s at a constant value of 32.63 for methanol and 78.36 for water [94].

The plots in Figure 35(e) and Figure 35(f) show the absorption coefficients as functions of water and methanol, respectively, over a frequency range from 0.2-2 THz. These plots present a comparison between the absorption coefficients obtained from our experiments and the double Debye relaxation model, with the same parameters mentioned above. We found good agreement between the calculated and measured refractive indices of water and methanol, however, slight differences were observed in high or low frequencies for both water and methanol.

Finally, from these results, it is clear that water is more absorbent than methanol, in the frequency range considered. Therefore, the relaxation times of methanol were much slower than those of water, due to stronger methanol bonds and their longer average lifetime. [123], In addition, differences between the Debye relaxation coefficient and measured data may have been due to differences in experimental conditions and fitting methods, as well as systemic errors. This also accounted for differences between measured refractive indices and absorption coefficients. Experimental errors may include the purity of the materials used.

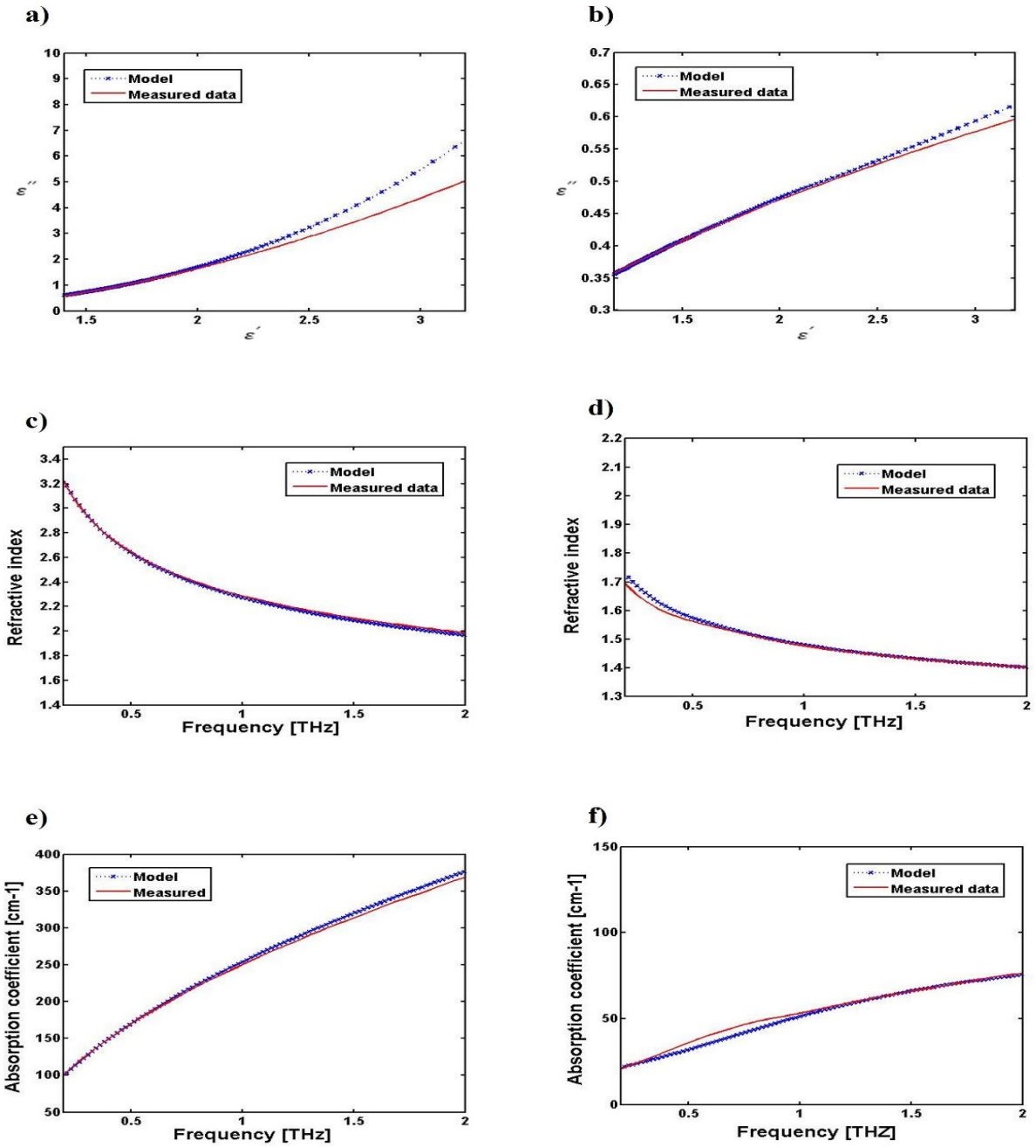

Figure 35: Comparison of experimental data for water and methanol with the Debye relaxation model, a) and b) show Cole-Cole plots of imaginary part ε'' vs real part ε' of water and methanol, respectively. c) and d) show the refractive index as a function of frequency for water and methanol, respectively. e) and f) show the absorption.

We implemented a double Debye fitting and evaluated the global error sources after the total acquisition process and extraction procedure. For example, Figure 36 shows the error bar of the refractive index and absorption coefficient of water, obtained in our experiments after baseline processing [110], compared with the double Debye relaxation model taken from the literature [114]. We propose the optimal value to obtain the best fit.

There was a slight difference with published data. From this figure, the refractive index and absorption coefficient were approximately in agreement with the results for water, Figure 35(c & e).

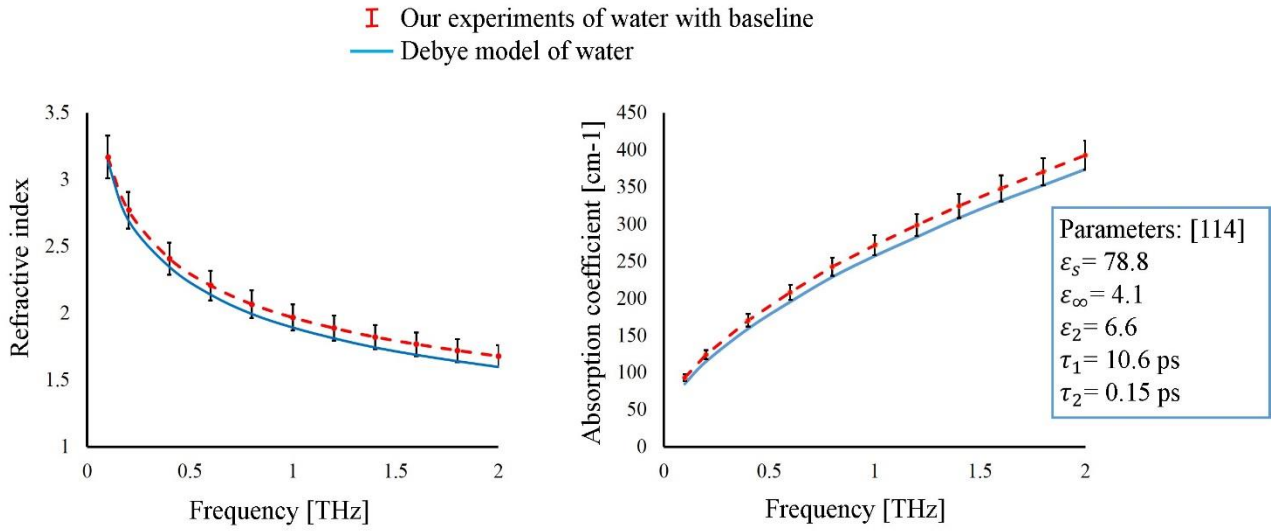

Figure 36: The refractive index (a) and absorption coefficient (b) of distilled water measured with TeraPulse 4000 in reflection mode, showing the error bars calculated from 10 measurements and 30 averaging in a hospital environment.

In conclusion, we analyzed a method for extracting the dielectric function of a sample in the THz region by THz time-domain spectroscopy. We validated the data extraction procedure by comparing our measurements of the dielectric functions of liquid water and ethanol with reported data in the literature.

We then used this method for the determination of liquids, based on the THz dielectric properties of the mixture. The accuracy of the method was found to be highest at low alcohol concentrations. The accuracy was mainly determined by the signal-to-noise level of the spectrometer.

4.1.2. Formalin

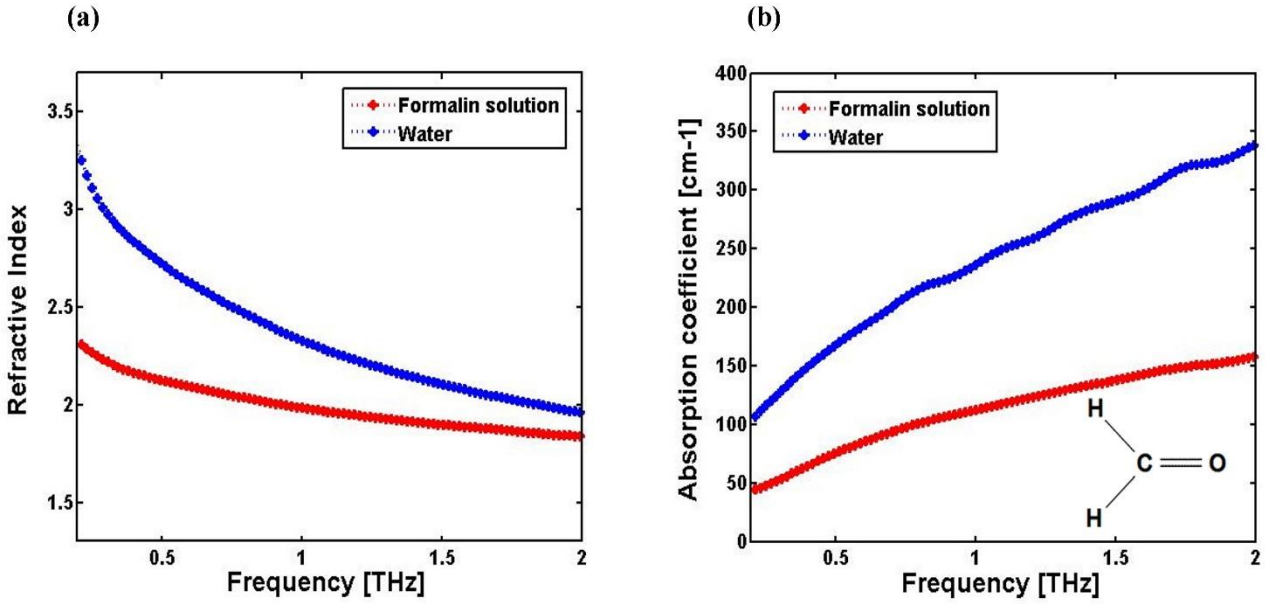

Figure 37: The refractive index (a) and absorption coefficient (b) of distilled water and 30% formalin, measured in TeraPulse 4000 reflection mode.

Formalin is a solution consisting of a mixture of formaldehyde gas and water. The chemical structure of formalin is CH_2O. Formalin solution contains about 30%- 0% formaldehyde gas and a stabilizer to prevent formaldehyde polymerization. The optical properties of formalin solution are represented in Figure 37. The results of formalin data were also measured by THz reflection spectroscopy, and then compared with properties of water. The plot in Figure 37(a) presents the refractive index of formalin, which varied from approximately 2.3 to 1.84 at 0.2-2 THz, i.e. a refractive index lower than of water, which varies from around 3.3 to 1.95. In addition, the refractive index decreased as frequency increased. The plot in Figure 37(b) shows a comparison of the absorption coefficients of formalin and water. The absorption coefficient of formalin varies from around 45 to 158 cm^{-1}, or roughly a factor of three than that of water, across the entire bandwidth.

4.2. Lipids

4.2.1. Refractive index and absorption coefficient

Biological tissue, including human adipose tissue, such as fatty breast tissues, was analyzed using THz reflection spectroscopy, as described in section 3.4.3.2. Figure 38 shows the frequency dependence of the mean of the refractive indices and absorption coefficients for water and 2 mm-thick inhomogeneous adipose (fatty) tissue. The sample consisted of adipose breast tissue from a mammary reduction. The data were processed to remove back-reflections from interface surfaces and minimize inaccuracies [110].

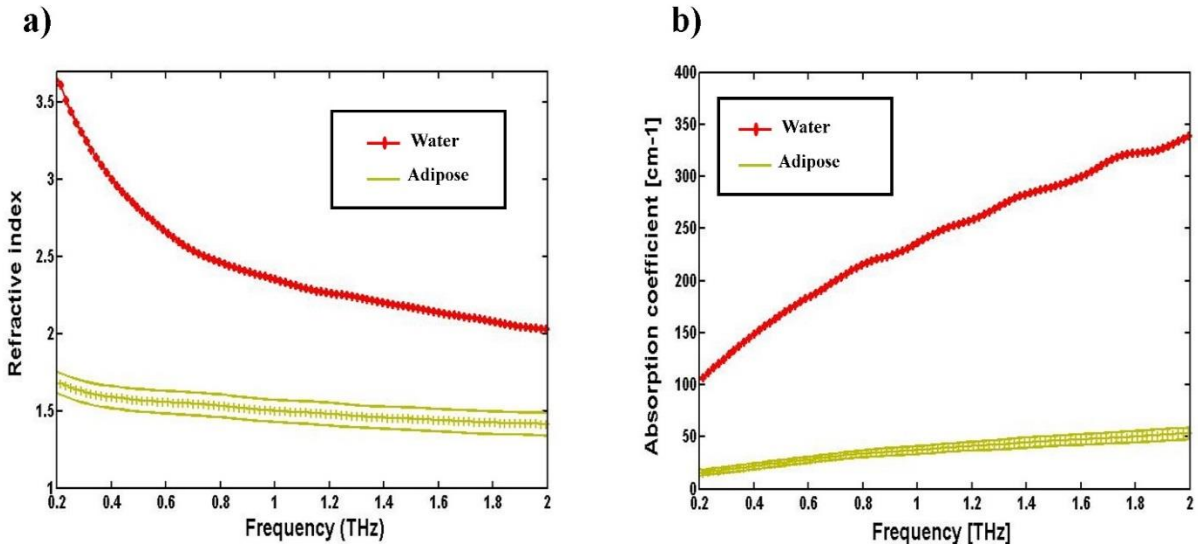

Figure 38: The a) refractive indices and b) absorption coefficients of adipose tissue and water measured in THz reflection mode.

The average of these measurements was ± 0.011 for the refractive index and $\pm 1.1\ cm^{-1}$ for the absorption coefficient. The results for the refractive index and absorption coefficient of water were approximately in agreement with those previously reported [120]. In addition, the refractive index of adipose tissue varied from 1.7 to 1.5 and the refractive index of water varied from approximately 3.56 to 2 over the 0.2 - 2 THz range, as shown in Figure 38(a). Moreover, the refractive indices of both water and lipids decreased as the frequency increased. As shown in the plot in Figure 38(b), the absorption coefficient remained below 50 cm^{-1} .

Finally, these results confirmed that the refractive index and absorption coefficient of adipose tissue were much lower than those of water and closer to the values for methanol. These results may be due to the structural nature of fatty tissues that contain long hydrocarbon chains, as illustrated in section 2.4.3, so there are only a few polar groups per fat molecule.

4.2.2. Debye relaxation coefficient

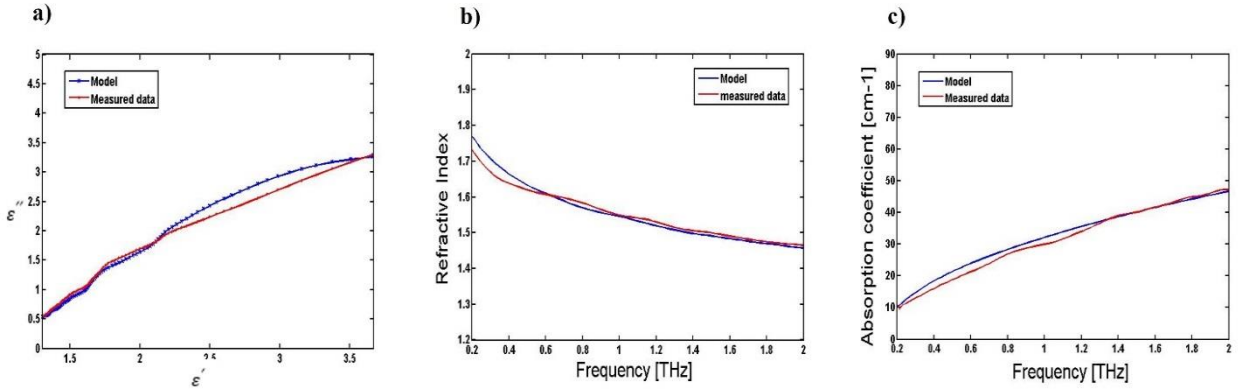

Figure 39: Measured breast lipid data compared to the Debye relaxation model, calculated from Debye parameters: a) shows the Cole-Cole plot of the imaginary part ε'' vs the real part ε' of the lipid; b) shows the refractive index as a function of frequency; and c) shows the absorption coefficient as a function of frequency.

Figure 39(a) shows a Debye model and a Cole-Cole plot of the imaginary part against the real part of the complex dielectric coefficient of the adipose tissue, according to equation (2.24). This plot was compared to the measurement data obtained from our experiments and the results obtained from the Debye relaxation model parameters of the lipid. Moreover, these plots show an increase in both the real and imaginary parts of the dielectric permittivity, due to the complex dielectric properties of lipids.

Figure 39(b) shows a plot of the complex refractive index of the lipid as a function of frequency over the 0.2-2 THz frequency range. This plot compares the measured data of our experiments and the double Debye relaxation coefficients (ε_s, the real part of the complex dielectric coefficient at low frequency, showed a constant value of 3.54 for the lipid [124]). From this plot, we determined that the refractive index of the lipid varied from 1.72 to 1.47 at 0.2-2 THz, but the refractive index calculated from the Debye model parameters, varied from 1.8 to 1.47. Finally, these results confirmed that the Debye model was suitable for fitting the measured dielectric constant of adipose tissue. Figure 39(c) shows the absorption coefficient of the lipid as a function of frequency over the 0.2-2 THz range. We found good agreement between the calculated and measured absorption coefficients of the lipid. The measured and model absorption coefficients of adipose tissue were in close agreement between 10 and approximately 48 cm^{-1} in the 0.2-2 THz range, particularly between 1.35 and 2 THz.

4.3. Breast Fiber

4.3.1. Refractive index and absorption coefficient

The aim of this study was to investigate the dielectric properties of normal breast tissue ex vivo using THz reflection spectroscopy. Fibrous tissues connect the adipose and glandular tissues, as well as balancing the density of the breast. Tissue dielectric properties are structure-dependent and may be used to differentiate between normal and cancerous tissues, including breast tissue [125]. The dielectric properties of fiber over a range of frequencies provide information about the nature of the tissue, including its refractive index and absorption coefficient. This was the first time we had access to this type of complex sample. These results constitute the very first step towards a broader statistical analysis of the measured values of human tissues in the terahertz range.

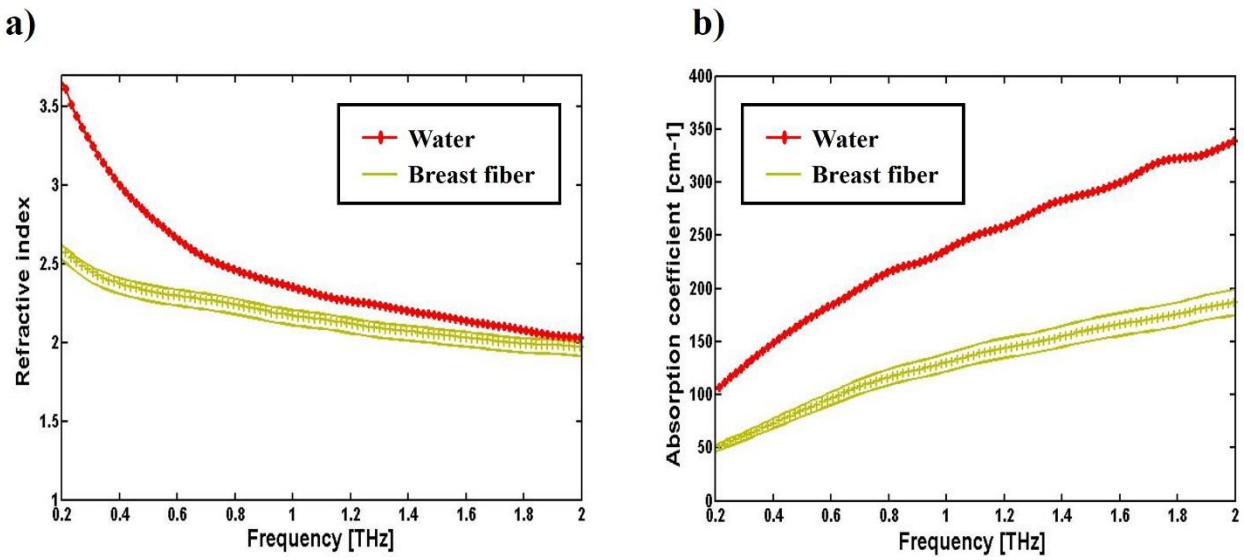

Figure 40: The THz a) refractive indices and b) absorption coefficients of inhomogeneous breast fiber tissue and water measured in reflection mode.

Figure 40 shows the measured mean refractive index and absorption spectrum for 2 mm-thick fiber tissue, compared with those of water. The average standard deviation of these measurements was $\pm$16 cm-1 for the absorption coefficient and $\pm$0.13 for the refractive index. The properties of water are shown in Figure 40(a) and Figure 40(b) for comparison with the fresh fiber tissue. The refractive index and absorption coefficient of inhomogeneous fiber tissue were lower than those of water, but higher than those of lipids. The plot in Figure 40(a) shows that the refractive index of fiber tissue varied from approximately 2.51 to 1.9 over the 0.2-2

frequency range. The plot in Figure 40(b) shows the variation in the absorption coefficient of breast fiber tissue from approximately 50 to 180 cm^{-1} over the 0.2-2 frequency range.

Finally, we confirm that this contrast between different human tissue types is likely to be useful in THz spectroscopy and imaging. The measured data were processed to remove any back reflection from interface surfaces, thus improving the results [110].

4.3.2. Debye relaxation coefficient

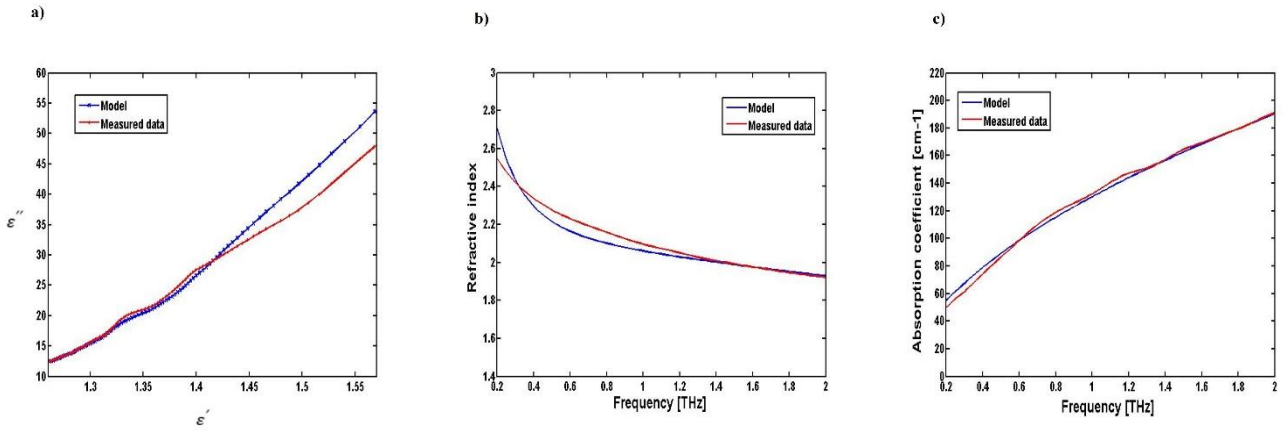

Figure 41: Comparison of measured data for fiber (normal tissue) with the Debye relaxation model, calculated from Debye parameters: a) shows the Cole-Cole plot of the imaginary part ε'' vs $the\ real\ part\ \varepsilon'$ of fiber tissue, b) shows the refractive index as a function of frequency, and c) shows the absorption coefficient as a function of frequency.

Figure 41(a) shows a double Debye model and a Cole-Cole plot of the imaginary part against the real part (ε'' vs ε') of fiber tissue, according to equation (2.24). This plot compares the dielectric permittivity between the measured data obtained from our experiments and those obtained from the Debye relaxation model parameters of the fiber. A clear deviation was found at low frequencies.

Figure 41(b) show a plot describing the behavior of the complex refractive indices of fiber over the 0.2-2 THz frequency range. The refractive index of fiber tissue was extracted from the measured data and compared with the refractive index obtained from the double Debye relaxation parameters. (The double Debye relaxation coefficient , ε_s, was 14.7 for the fiber [120]). Finally, the measured refractive index was a good fit to the Debye relaxation model, particularly in the 1.4- 2 THz range.

Figure 41(c) presents the measured absorption coefficients obtained from our experiments compared with the calculated absorption coefficient fitted from Debye model parameters for fiber tissue, showing that the absorption coefficients increased from 51.5 to 190.9 cm^{-1} over the 0.2-2 THz range. Finally, we found good agreement between the calculated and measured absorption coefficients of fiber tissue.

4.4. Breast cancer

4.4.1. Refractive index and absorption coefficient

This section presents the dielectric properties of breast cancer over a range of frequencies. Figure 42 shows the mean measured refractive index and absorption spectrum for a 2mm-thick section of inhomogeneous breast cancer tissue, compared with the mean data for distilled water as a reference. The measured mean refractive index and absorption spectrum for cancer tissue were $\pm$18 cm-1 and $\pm$0.1, respectively. The measured data were processed to remove any back reflection from interface surfaces, thus improving the results [110].

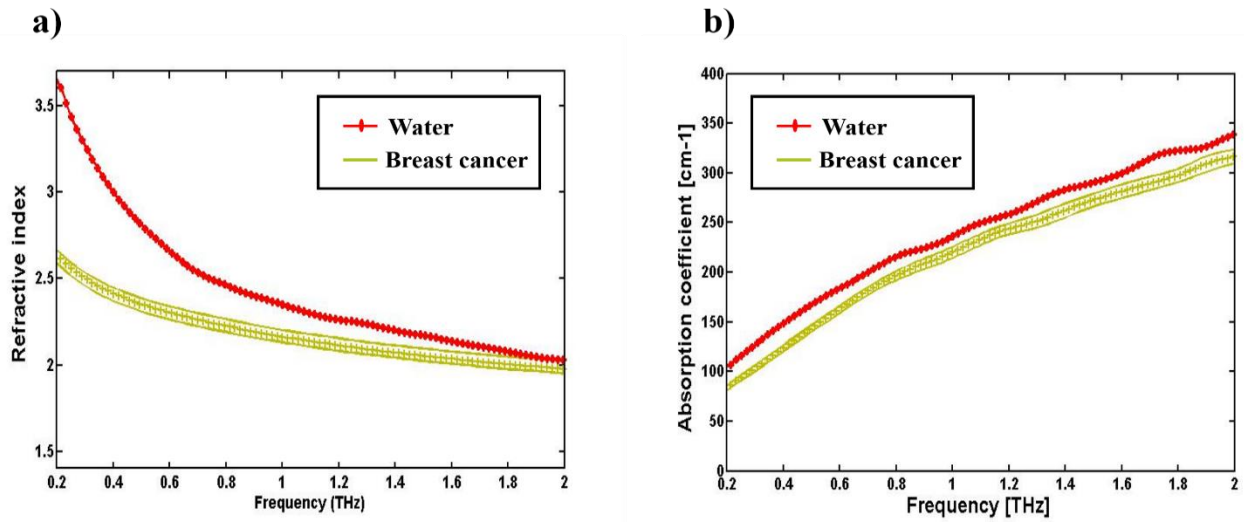

Figure 42: The a) refractive indices and b) absorption coefficients of inhomogeneous cancer tissue and water measured in THz reflection mode.

The properties of water are shown in Figure 42(a) and Figure 42(b) for comparison with the fresh cancer tissue. The refractive index and absorption coefficient of inhomogeneous fiber tissue were lower than those of water, but higher than those of lipid and fiber (see sections 4.2. and 4.3.). From the plot in Figure 42(a), we observe that the refractive index of cancer tissue varied from approximately 2.65 to 2 over the 0.2-2 THz frequency range. The plots in Figure 42(b) show the evolution of the absorption coefficient of breast cancer tissue from approximately 70 to 330 cm^{-1} over the 0.2-2 THz frequency range. This contrast between different human tissue types is well known in THz spectroscopy and very interesting for segmentation purpose.

4.4.2. Debye relaxation coefficient

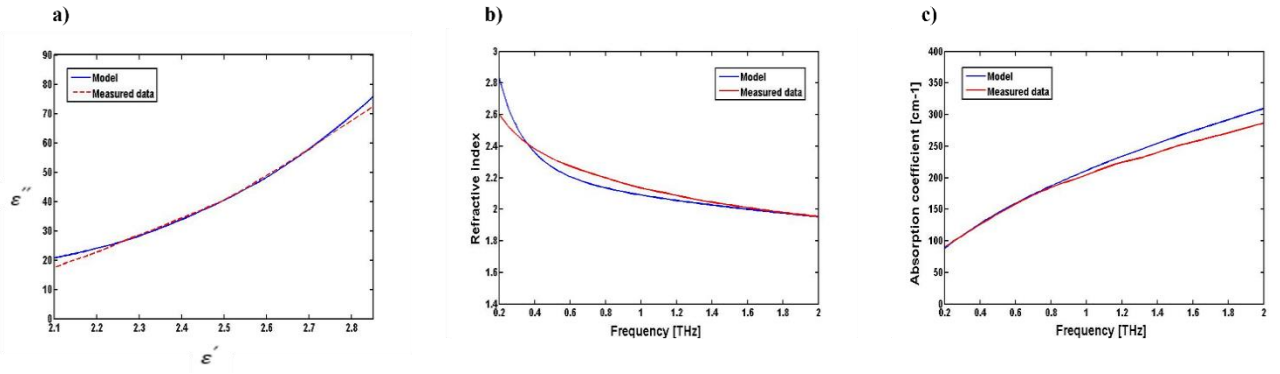

Figure 43: Measured data for breast cancer compared to the Debye relaxation model, calculated from Debye parameters: a) shows the Cole-Cole plot of the imaginary part ε'' vs $the\ real\ part\ \varepsilon'$ of cancer, b) shows the refractive index as a function of frequency, and c) shows the absorption coefficient as a function of frequency.

Figure 43(a) shows a Debye model and a Cole-Cole plot of the imaginary part against the real part (ε'' vs ε') of cancer tissue, according to equation (2.24). This plot compares the dielectric permittivity between the measured data obtained from our experiments and those obtained from the Debye relaxation model parameters of the cancer.

The Debye relaxation coefficient, ε_s, calculated from the complex dielectric coefficient, was 17.6 for cancer tissue [120]. Figure 43(b) shows the behavior of the complex refractive indices of cancer tissue over the 0.2-2 THz frequency range. The refractive index of cancer tissue varied from approximately 2.6 to 1.95 at 0.2-2 THz. A comparison with refractive indices calculated reported in the literature from double Debye relaxation parameters revealed that the measured refractive index was close to the Debye relaxation model, particularly in the 1.4- 2 THz range.

Figure 43(c) shows that the measured absorption coefficient obtained from our experiments compared with the calculated absorption coefficient obtained from the Debye model parameters as functions of frequency ranged from 0.2-2 THz for cancer tissue. This plot shows that the measured absorption coefficient varied from 92.5 to 286 cm^{-1} over the 0.2-2 THz range, giving good agreement between the calculated and measured absorption coefficients and refractive indices of cancer tissue.

Table *2* summarizes the characteristic values of the Debye parameters simulating the dielectric coefficient for human breast tissue, including adipose, fiber (normal), and cancer, as well as liquids, including water and methanol.

Table 2: The extracted THz spectroscopy parameters of human breast tissue and liquids, calculated by model equation (2.24), compared to the double Debye parameters.

Sample	ε_s	t_1 [ps]	ϵ_2	t_2 [ps]	ε_3	t_3 [ps]	ε_∞
Water this work	78.34 $\pm$**5.5**	8.2 $\pm$**2.5**	4.8 $\pm$**1.21**	0.17 $\pm$**0.03**			3.44 $\pm$**0.16**
Water [94]	78.36	8.3	4.93	0.18			3.48
Methanol this work	32.60 $\pm$**3.11**	4.75 $\pm$**1.01**	5.33 $\pm$**1.3**	1.2 $\pm$**0.65**	3.32 $\pm$**0.99**	0.159 $\pm$**0.02**	2.08 $\pm$**0.35**
Methanol [94]	32.63	4.8	5.35	1.25	3.37	0.16	2.10
Lipid this work	3.5 $\pm$**2.1**	9.61 $\pm$**0.55**	1.83 $\pm$**0.4**	0.12 $\pm$**0.02**			2.43 $\pm$**0.21**
Lipid [124]	3.54	9.67	1.89	0.13			2.50
Normal Breast this work	14.54 $\pm$**2.33**	1.44 $\pm$**0.11**	4.15 $\pm$**0.65**	0.0609 $\pm$**0.05**			2.55 $\pm$**0.25**
Normal breast [120]	14.7	1.45	4.16	0.0611			2.58
Cancer breast this work	17.73 $\pm$**3.5**	1.54 $\pm$**0.2**	4.18 $\pm$**0.5**	0.0611 $\pm$**0.02**			2.58 $\pm$**0.12**
Cancer breast [120]	17.6	1.55	4.23	0.0614			2.65

These results revealed that the dielectric properties of cancer tissue, obtained ex vivo by THz spectroscopy in the 0.2-2 THz range, were systematically higher than those of fiber and adipose tissue. In addition, the measured complex dielectric properties of the tissues increased, so we compared the real part ε' and imaginary part ε'' of adipose, fiber, and cancer tissue with those of water. Therefore, using the dielectric data, as indicated above, to investigate and extract the dielectric responses during interactions of THz radiation with various tissues provided valuable information for quantifying the dielectric properties of breast tissue in the THz range.

Moreover, the measured complex dielectric properties of the different breast tissues had different values from the extracted data, depending on their physical properties. The significant difference between heathy breast and tumor tissue indicated that the analysis of THz reflection parameters had the potential to discriminate between cancer and other breast tissues. Details of these THz properties are presented with averaged values and standard errors. Finally, as shown by these findings, THz reflection spectroscopy is capable of measuring the complex dielectric coefficients of adipose, fiber, and cancer tissue, and discriminating among them, due to the different micro- and/or macromolecular structures, especially tumors. In addition, the diagnosis of adipose, fibrous, and cancer tissue in each sample was controlled by a histopathologist, who provided information on the tissue types for evaluating the accuracy of the reflected THz spectroscopy measurements.

4.5. Chemical treatment of tissue sections

Chemical treatment of tissue sections for THz spectroscopy and imaging analysis has a significant impact on the types of structures that are detected and analyzed and is, therefore, an important step in the sample preparation process. This method is used to remove biological salt adducts that may affect the tissue signals observed. On the contrary, chemical treatment may also be used to enhance the signals, depending on the solvent used to dehydrate and fix the tissue. R. Lemaitre et al. [126] found that all the components: signal intensity, signal-to-noise ratio, and number of peaks, were highest for tissue treated with organic solvents, such as xylene or chloroform (44% and 40% increase in signal intensity, respectively), compared with untreated tissue. Seeley et al. [127] found that treating tissue sections with solvents, such as isopropanol, methanol, or ethanol, together with water, extended sample lifetime, as well as reviving previously cut tissue sections, in addition to providing high-quality, reproducible spectral data. They further investigated the impact of solvent treatment of tissue sections on the capacity to distinguish between different structures. Our study revealed that submerging excised tissue sections in formalin, methanol, saline solution, or distilled water had no negative effect on measurements made during THz spectroscopy and imaging, as shown in Figure 44.

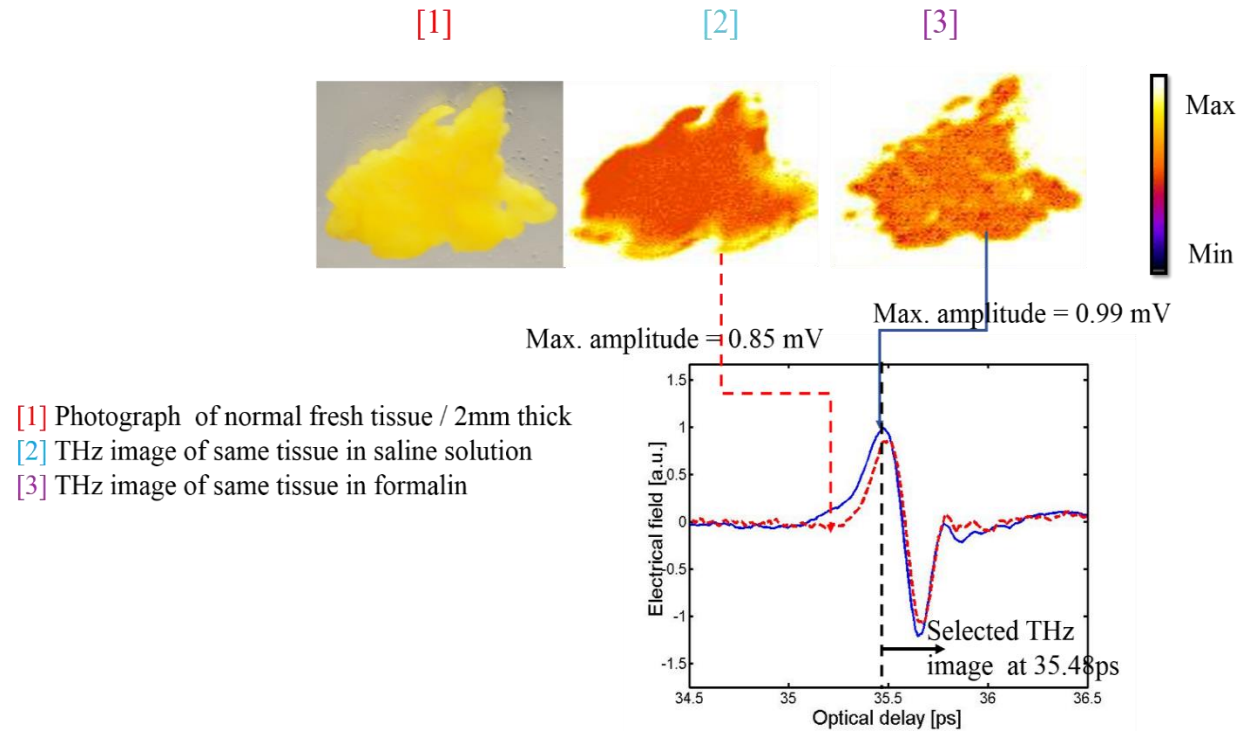

Figure 44: THz measurements of excised tissue sections submerged in formalin and saline solutions.

4.6. Breast changes/tissue aging

Breast tissue and its structure change [128] with age. This is due to a decline in reproductive hormone levels, caused by the natural aging process [129]. As a result of these changes, breasts decrease in size and become less full and elastic. Tissue aging also leads to an increased risk of developing growths in the breast, such as fibroids, cysts, and tumors[130]. The factor that causes tissue aging is the decrease in estrogen hormone that causes the skin and connective tissue of the breast to become less hydrated. In addition, dense breast tissue, including collagen, is replaced by fatty tissue, making it softer, which constitutes another risk factor for breast cancer. Aging thus impacts the number of cells and the quantity of collagen [131]. Several studies on breast tissue aging have also found differences in the proportions of epithelial and stromal cells [132]. N.F. Boyd et al. [133] reported that breast tissue aging was due to the combined effects of two processes: cell proliferation, induced by growth factors and sexual hormones and influenced by reproductive risk factors for breast cancer; and damage to the DNA of dividing cells by mutagens generated by lipid peroxidation. Other factors associated with breast tissue aging included a greater cellularity of breast tissue, as well as higher collagen and protein content [131]. In addition, another factor that causes tissue aging is the high blood level in breast mitogen. Women in the upper 25% of blood levels have a higher risk of breast cancer compared with those in the lower 25% [134].

4.7. Summary and conclusion of this part

4.7.1. Summary

THz reflection spectroscopy measurements from 0.2 to 2 THz used to determine the refractive index and absorption coefficient of liquids and biological tissues. Measurements in reflection mode for all experiments were achieved at one-point locations on material in the center of the imaging window, to calibrate and reduce the influence of any unevenness. Measurements were repeated three times, to obtain accurate data.

In this work, the complex optical coefficients measured by the THz reflection technique were more accurate for the water component, as it has a larger refractive index and absorption coefficient than the other components used. This effect was due to the complex coefficients of methanol, as well as adipose, fiber, and cancer tissues. We found that adipose tissue had a lower refractive index and absorption coefficient than cancer, which, in turn, had a higher value than water. Our measurements confirmed that a significant difference in water content between these measured components resulted in a lower absorption coefficient for adipose tissue, as shown in figures 38, 40, and 42. Breast tissue consists mainly of lipid tissue: normal breast tissue contains around 19% water and tumors slightly more, at 26% [135].

The close agreement between the theoretical and measured data for liquids and biological tissues, demonstrated the accuracy of the THz technique and the measured values were a good fit with a Debye relaxation model. Systemic errors, causing differences between measured refractive index and absorption coefficient data, were found to be responsible for variations between results from different systems.

When the double Debye model was applied to biological tissues, some discrepancies appeared, due to the more complex composition of biological tissues. Biological tissue exhibits a less homogeneous composition, containing normal and cancer cells, and many physical and chemical properties varied from one sample to another. In addition, The THz reflection spectroscopy data used to calculate the refractive indices and absorption coefficients potentially contained measurement and calculation errors. Other challenges, such as parallelism of the imaging window or holder and how positioning the sample, and non-uniform contact of the sample dramatically, may have affected data on optical properties. Therefore, measurements on biological tissue required calibration of the imaging window and applying slight pressure to ensure good contact between the sapphire window and a sample, for a potential source of error in these measurements.

Our measurements were compared with the Debye relaxation model parameters to assess their accuracy in their dielectric behavior. It was possible to determine how variations in THz reflection measurements of liquids and breast adipose, fiber, and cancer tissues differed with tissue composition and different pathology. Finally, spectral performance was measured experimentally for tissue phantoms containing water and water mixture, using THz reflection spectroscopy at room temperature. We optimized the protocol and the data processing to operate a frequency band from 0.2 to 2 THz and analyze biological tissue. Differences in the optical indices in the 300-600GHz bandwidth were clearly observed, as shown in figures 39, 41, and 43.

4.7.2. Conclusion

The results obtained by THz reflection measurements on liquid water, methanol, and biological tissues were in close agreement published papers using the Debye relaxation model. We compared the complex dielectric constant of distilled water with those of methanol and human breast adipose, fiber, and cancer tissues. The double Debye model had some limitations when applied to breast tissue, due to the complex, inhomogeneous nature of biological tissues. The dielectric response at THz frequencies is assumed to be dominated by the picosecond timescale dynamics of water. This comparison of the dielectric properties of methanol, and adipose, fiber, and cancer tissues in the THz region enhances our knowledge of the relationship between these values and the structure of the materials. We used the Debye relaxation model to fit the complex coefficients of liquids and biological tissues, for example: Cole-Cole, combined with a double model to produce a mixed model of human breast tissue, thus enabling us to understand THz imaging contrast mechanisms in biological tissues. We also initiated a data library on this type of tissue and terahertz interaction.

CHAPTER 5

5. Introduction

This Chapter presents the results of the THz spectroscopy and imaging measurements in transmission and reflection mode, focusing on image acquisition for breast cancer determination. Post-processing analysis of the THz images and their optical properties was used to distinguish between cancer, fiber, and fatty tissues, with samples of different thickness that illustrated the effectiveness of the THz technique in biomedical applications.

5.1. Breast Imaging and Spectroscopy

THz spectroscopy and imaging is a rapid, accurate, non-destructive, non-ionizing technique for identifying breast cancer and distinguishing between healthy (adipose or fiber) and cancerous tissues., THz spectroscopy has been used to develop an intra-operative tool for discriminating between breast cancer, tumor margins, and adipose tissue [136]. Many studies have used THz techniques to distinguish between various breast tissues, ex vivo and in vivo. These findings have formed the basis of experimental imaging and characterization of freshly-excised breast cancer tissues [137], [19]. Fitzgerald et al. [10], applied pulsed terahertz imaging in reflection mode to map the margins of tissues excised from 22 breast cancer patients during wide local excision or mastectomy. They measured the maximum and minimum values of the reflected electric field at each point of the scan and identified the potential of pulsed THz imaging using to discriminate cancerous from non-cancerous tissue in excised breast samples. Further work was reported by Ashworth et al. [138], using reflected terahertz pulses in the 0.15-2THz frequency range to measure the physical properties of 20 freshly-excised tissue samples.

Another group explored signal propagation through formalin-fixed and paraffin-embedded breast cancer tissue to determine the depth of objects detected with THz reflection imaging, using time-flight analysis to estimate the three dimensional boundaries of the tumor [139]. The same group used transmission imaging and spectroscopy on 20 and 30 μm slices of breast cancer tissue (formalin-fixed and paraffin-embedded), to determine their properties and define a region of points over which to average the electrical properties from the scan [140]. Tyler Bowman et al. [141] demonstrated the potential of THz spectroscopy in the 0.1 - 4 THz range to characterize cancer, fiber, and normal breast tissue and found that THz technique improved the detection of the margins of excised tissues. These studies enhanced the credibility of THz spectroscopy and imaging for characterizing, analyzing, and identifying human breast cancer tissues. Imaging and extracting the physical properties of the various tissues facilitates identification based on the differential dielectric response. When

THz spectroscopy and imaging was used both transmission and reflection modes to detect breast cancer in fixed and fresh excised tissues, our study revealing if insufficient amounts of tumor tissue had been removed.

To summarize, the THz system, in transmission and reflection mode, provided dielectric contrast for imaging without ionization and was used to detect human breast cancer in ex vivo samples. In addition, THz spectroscopy and imaging of fresh human breast tissue was used to analyze and extract optical properties in order to develop a comprehensive database and identify different types of human breast tissue.

5.2. Image processing

Spectro THz imaging in transmission and reflection mode applied to breast tissue produced several gigabytes per measurement of raw data, which had to be analyzed to extract the information of interest, i.e the capacity of this system to discriminate between benign and malignant tumors could be evaluated. The raw THz profile contained time-varying or spectral information with continuous magnitude. Therefore, the aim of image processing was to represent and transform these input measurements from THz signals, for instance, reducing blur and enhancing image quality, as well as improving contrast. This facilitated to display discrimination between different tissue regions under investigation, such as benign and malignant tumors [142].

In this study, to ensure fast, efficient image processing, we used mathematical operations developed in our team, such as minimum, maximum, divided, multi, derivative, mean, differences, and sum functions, as well as statistical tools, such as Shannon Entropy, to analyze time- and frequency-domain data. Frequency data for each pixel were converted by Fourier transform for analysis [143], as shown in Figure 45. Image processing of the raw data input from THz images was achieved without data loss. In addition, the THz images were proportional to the original size of the tissue section under investigation.

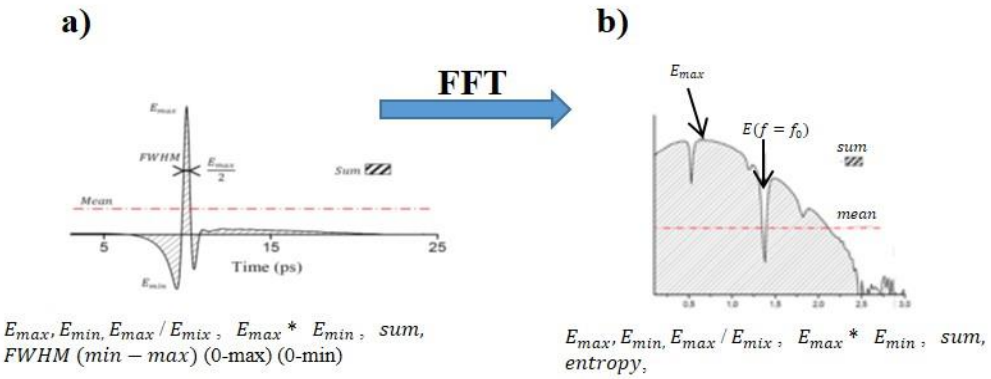

Figure 45: Diagram of image processing operations: a) THz in time domain and b) spectral in frequency domain.

Processing operations thus determined the intensity level of each pixel in the image, so the THz images would provide accurate information about the intensity or energy of THz signal transmitted or reflected from the biological tissue in various positions, over a range of frequencies.

The data registered in 3D (x, y, t) by the THz system for each slice were converted to 2D, to simplify processing [144]. We developed three different methods for processing raw THz imaging data, using different operations, then evaluated and compared the results of each method to identify the approaches that produced the most accurate details in the shortest time.

5.2.1. Slice image method

In this method, we selected the images from the original data obtained at different frequencies and in different positions. It was time-consuming, but produced more accurate, detailed results for each tissue.

5.2.2. Automated image method

This is called the 'automated' method as the images were selected automatically from the original data in both the time and frequency domains. The imaging results varied, depending on the different mathematical operations, but this method produced results very quickly.

5.2.3. Manual image method

Images were selected from the original data manually in the different time and frequency domains. This took longer than the automated method, but produced more consistent results with different operations.

Image processing

Figure 46 show the main steps in processing the THz images of biological tissue:

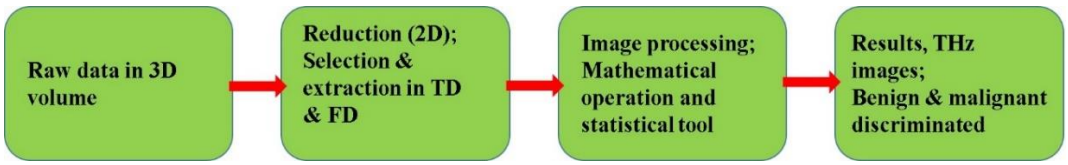

Figure 46: THz raw data processing diagram.

1- Firstly, all imaging data were loaded and converted from 3D to 2D. Then the original image was cropped to reduce file size and facilitate transferring the image for the next step in the analysis. A zero-padding algorithm was applied to the THz signal in the time domain of each pixel as previously

explained. FFT was then applied to obtain the frequency domain parameters, followed by image extraction and processing on raw data, using a mathematical and/or statistical operation.

2- The images were then extracted and processed in the time and / or frequency domains. These images were easily manipulated, enabling us to discriminate between different tissue regions (benign and malignant), thus achieving our aim.

3- Finally, the results of all processing methods are compared to pictures of the samples under investigation.

Mathematical and statistical image processing is described in the following examples: the figures show the processing of the THz imaging input data collected from scans of two fresh excised tissue sections, with different thicknesses, heterogeneities, and uneven surfaces. The parameters for scanning at the second peak interface (quartz/tissue) were applied: averaging: 3; step size: 0.2 mm; area of sample scanned ($-34<x<4$, $2<y<45$) mm, time difference between two points (dt): 0.008 ps; and acquisition time: 13h 30min, corresponding to the step size of the scan and the area of tissue scanned.

Figure 47(a) shows the visible image of two fresh sections (table 3, number3), consisting of cancer, fiber, and fatty regions. Figure 47(c) shows the THz images before processing: the contrast was poor and it was difficult to discriminate between different tissue regions. As shown in Figure 47(b), once the THz images obtained from the slices had been processed in both the time (TD) and frequency domains (FD), it was possible to discriminate between the different regions in the sample at 1.1, 1.2, 1.5, and 1.7 THz in the frequency domain and 26.5, 26.7, 26.9, and 27.2 ps in the time domain. So with different LUT, and an automated contrast adjustment, we can put in light fastly the different area in the sample presenting the same signal intensity.

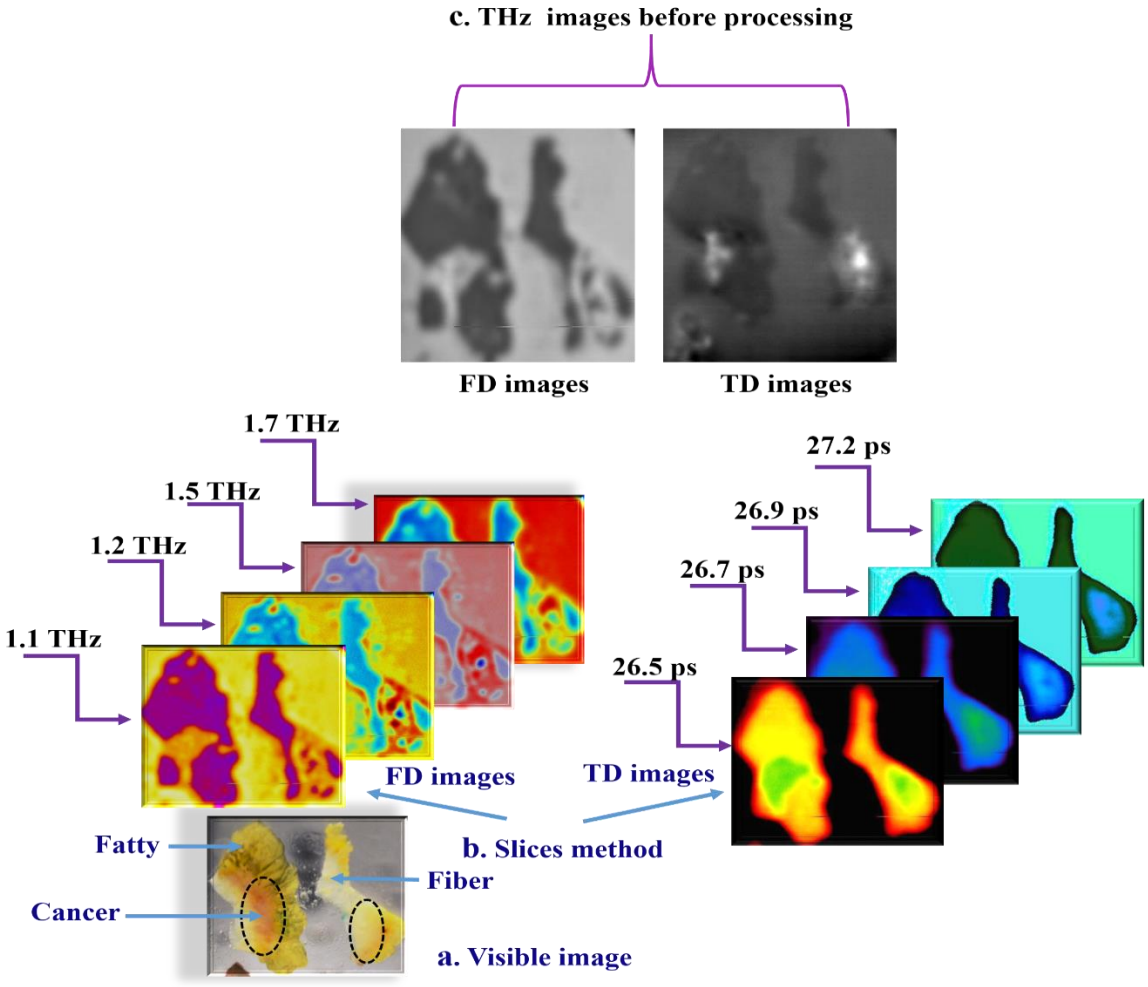

Figure 47: a) visible image of tissue, b) slice method of THz imaging in various time (TD) and frequency domains (FD), and c) THz images before processing.

Figure 48 shows THz images of the same sample obtained by the manual image method, using different operations for both the time and frequency domains, where 1, 2, 3, 4, 5, 6, 7, 8, and 9 represent Diff, Div, derivative, max, mean, min, mult, Entropy-Shannon, and sum operations of the processes, respectively.

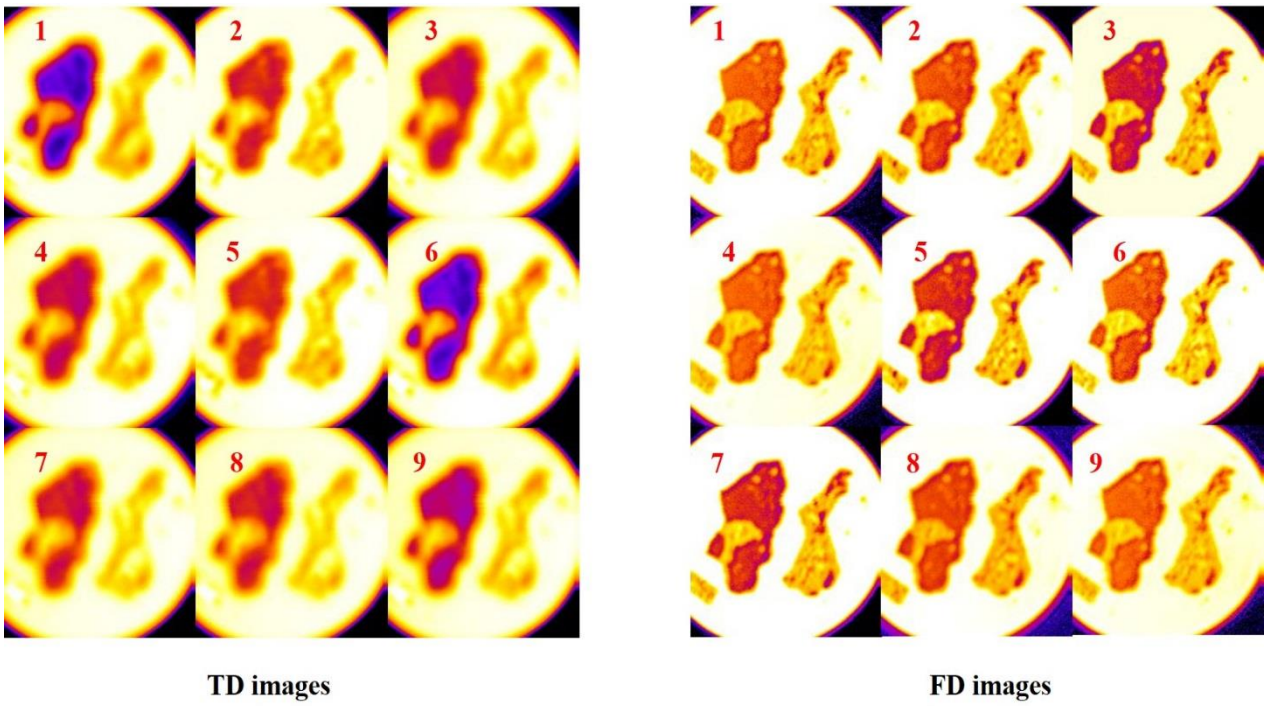

Figure 48: Manual THz image processing method using various mathematical operations in the time domain (TD) at 26.5 ps and the frequency domain (FD) at 1.1 THz.

Finally, Figure 49 shows the THz images obtained by the automatic image method, using different operations in the time domain, where 1, 2, 3, 4, 5, 6, 7, 8, 9, 10, 11, and 12 represent Diff, Div, derivative, energy-entropy, FWHM [0-max] down, FWHM [0-max] up, FWHM [min-max] up, max, mean, min, mult, entropy-Shannon, and sum operation processes, respectively, while 1, 2, 3, 4, 5, 6, 7, 8, and 9 represent the Difference, Div, derivative, max, mean, min, multiplication, entropy-Shannon, and sum process operations in the frequency domain, respectively.

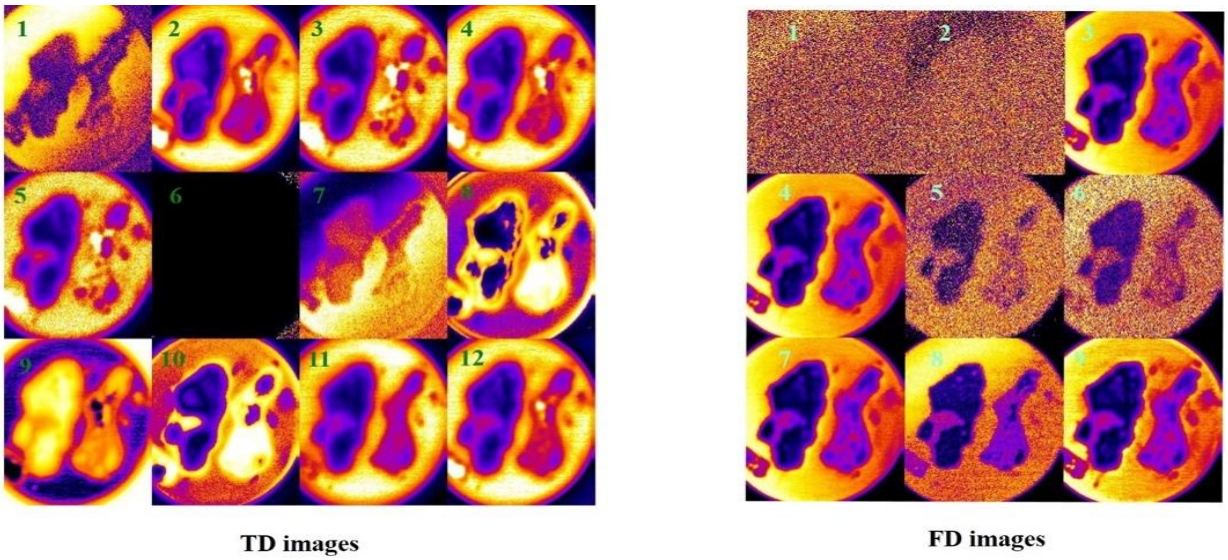

Figure 49: Automatic THz image processing using various mathematical operations in the time (TD) and frequency domains (FD).

For comparison, using manual slice image processing, it was possible to select different THz images for both the time and frequency domains, with better results in terms of evaluation of the various parameters and properties of the tissues observed and discrimination between diseased and healthy tissue, but this approach was more time-consuming.

Manual image processing gave good results with all processing operations applied to the THz images, obtained under the same conditions, such as frequency or time. As shown in Figure 48, the results provided accurate, efficient discrimination between diseased and healthy tissue, but took longer to obtain.

An automatic image processing method was designed, using a mathematical operation to process the results of the THz measurements. This method had both advantages and disadvantages. The image was processed directly, giving rapid results, but all the operations did not produce relevant results, while some operations enabled us to describe or distinguish between diseased and healthy tissue on the basis of the intensity level of each pixel in the image. However, we consider that mathematical analysis applied to THz images is a complementary approach to the pathologist's diagnosis of tissue using an optical microscope to distinguish cancerous areas.

5.3. Results

5.3.1. Patients and specimen preparation

This study was based on 51 tissue samples taken from female human breasts (age range: 35-86 years). Table 3 shows the patient baseline. All samples were collected during breast surgery, between 2015 and 2017, and all cases studied were histologically confirmed by a pathologist. In addition, a pathologist identified diseased and healthy tissue in all samples for diagnosis. The samples consisted of cancer, fiber, and adipose tissues. Samples were taken for analysis after a surgical procedure, to determine whether the diagnosis was accurate. In addition, this method checked that the surgery had removed all cancer tissue with a safe margin of healthy tissue. The fresh tissue samples were processed by the hospital as normal sample after THz imaging.

This study considered three specific factors:

- Different sample thicknesses and types, including fixed and fresh tissues, as well as paraffin block;
- Type and thickness of substrate used to hold the sample sections;
- THz systems in transmission and reflection mode.

Details of the THz systems and sample measurement procedures, in transmission and reflection mode, were described in Chapter 3, while further details on sample preparation were given in annex 2.

Table 3: Patient baseline.

No.	Tumor type	Grade	Age	Body weight (Kg)	Height (cm)	BMI
1	Invasive carcinoma NST	3	85	59	148	26.9
2	Invasive carcinoma NST	3	48	89	163	33.5
3 (2 sections)	Invasive carcinoma NST	2	70	85	165	31.23
4	Invasive carcinoma NST	3	55	59	163	22.21
5	Invasive carcinoma NST	3	86	45	155	18.73
6	Invasive carcinoma NST	2	48	82	162	31.25
7	Invasive carcinoma NST	3	77	88.5	157	35.79
8	Invasive carcinoma NST	2	59	67	163	25.22
9	Invasive carcinoma NST	1	77	75	155	31.22
10	Invasive carcinoma NST	3	37	60	156	24.66
11 (2 sections)	Invasive carcinoma NST	2	57	60	158	31.24
12	Invasive carcinoma NST	3	72	80	167	31.24
13	Invasive carcinoma NST	1	50	90	172	30.4
14	Invasive carcinoma NST	2	39	108	163	41
15 (2 sections)	Invasive carcinoma NST	2	48	80	165	29.39
16	Invasive micropapillary carcinoma	2	53	52	167	18.65
17	Invasive carcinoma NST	2	53	85	160	33.2
18	Invasive carcinoma NST	3	86	58	148	26.48

19	Invasive carcinoma NST	2	77	59	155	24.56
20	Invasive carcinoma NST	3	62	76.5	158	30.65
21 (9 block)	Invasive carcinoma NST	/	/	/	/	/
22 (22 fixed tissue)	Invasive carcinoma NST	/	/	/	/	/

- BMI: body mass index

5.3.2. Data acquisition and analysis

This section describes the significant procedures in data acquisition by THz systems in transmission and reflection mode, as well as statistical analysis of the data.

- **Data acquisition**

A methodology was identified for imaging cancer regions in samples using the 3000 Teraview in both transmission and reflection modes, as well as the 4000 Tera Pulse in reflection mode, as described in Chapter 3. Signals were collected from the quartz-air and quartz-tissue interfaces (second peak). The sample was laid flat between double quartz windows 2 mm or 3 mm thick. THz images were obtained with a raster scanning system using a two-dimensional (2D) movable sample stage with different step size, combined with averaging, to measure the transmitted or reflected signals at each pixel area in an x-y plane on exposure to THz beam. During interaction between the THz pulses and tissue sections, the transmitted or reflected THz signals were subject to temporal delay, attenuation and broadening, with respect to the reference measured without a sample. These variations in signals were due to the incident angle of the THz beams and frequency-dependent physical processes that occur in the biological tissue, like absorption, optical thickness, reflection, refraction, and scattering, which affected the direction of THz propagation, as illustrated in Chapter 2.

All reflection signals recorded from samples were scanned at an incident angle of 10 deg and the 4096 time data points produced a 3-dimensional THz image. In contrast, all transmission signals were measured at a normal incident angle and the 512 or 2024 time data points produced a 2-dimensional THz image. 2D images were acquired from signal amplitudes, by scanning the THz beam at each pixel. Fresh tissues were scanned maximum 2h after excision. Each experiment produced three types of images: a photograph of stained tissue, a photograph of studied tissue, and THz images in the time and frequency domains. To demonstrate, two images, taken with a digital camera, were compared and proved easily distinguishable from THz images. Different volumes of data were acquired, depending on the conditions, such as the scan parameters and sample area. Acquisition times of all the THz images were recorded for times ranging from 30 min to 12 h, depending on the THz system mode, area of breast tissue scanned, and the scanning step size in mm.

- **Data analysis**

The THz images were analyzed in time and frequency domain to identify the internal structure of the samples, detect cancer, and differentiate between healthy and diseased tissues. Statistical analysis was used to calculate the refractive index and absorption coefficient from the sample measurement database, to discriminate between the different tissue regions: cancer, fiber, and adipose. Variable sample quality, due to heterogeneous, complex tissue, uneven surfaces, and tilt, affected THz system measurements, scans and spectra, increasing the scattering effects. Additionally, fresh samples aging affects the chemical tissue structure. In addition, denaturation occurred during storage in saline or formalin, since these solutions penetrate the tissues, affecting the water content, and leading to refraction and absorption effects. Finally, the THz images were used to identify the size, shape, and distribution of the tumor region inside the tissue and also compared with the histopathological image. The statistical analysis results, using many points selected from each region to measure the THz signal reflected in time domain, were averaged to describe the optical properties of each sample region.

5.3.3. Stained tissue slides

Stained tissue was used for comparison with THz images, to identify the optical properties of each tissue region, as well as to correlate the differences between the THz images and the pathologist's diagnosis. Moreover, these slides were used to obtain statistically-significant measurements of breast tissue. Tissue was identified by staining with Hematoxylin and Eosin (H & E): see annex 2, section 7.2.8, for further details. The regions on these slides were identified by microscopic histopathology, followed by analysis of the structures observed to detect diseased and healthy tissue. All stained slides contained three regions: cancer, fiber, and fatty tissue, as shown in the following figures. These regions were marked to align the THz images with the respective photographic images and determine their location and size.

5.4. Medical sample results

The first two sections of this chapter presented the overall and data acquisition methods. The first part of this section presents the analysis results in the form of THz images in time and frequency domain, obtained in transmission and reflection modes, used to discriminate between cancerous and healthy regions. The second part of this section presents statistical analysis of the data, as well as the intrinsic results of the THz imaging and spectroscopy of the following selected samples:

5.4.1. Sample 1: measurements on a glass microscope slide

The Teraview 3000 system was used for transmission and reflection imaging of 20 and 30 µm-thick paraffin-embedded breast tissue, mounted on 1 mm-thick glass microscope slides, with 0.1 mm-thick coverslips. These samples were obtained from 53 and 77 year-old women, weighing 52 and 59 Kg, respectively. The 20µm-thick tissue was diagnosed as grade II invasive micro papillary carcinoma and the 30 µm-thick tissue was diagnosed as grade II invasive carcinoma NST, (table 3).

5.4.1.1. Transmission results

Sections 2.5 × 3.5 cm on tissue/coverslip and tissue/microscope slide were scanned in transmission mode at frequencies of 0.1 to 3 THz, with 10 averages, waveform 2048, and step size 0.5 mm. The breast cancer results are shown in Fig.50 and Figure 51, read from the 3D data file (X,Y,t)

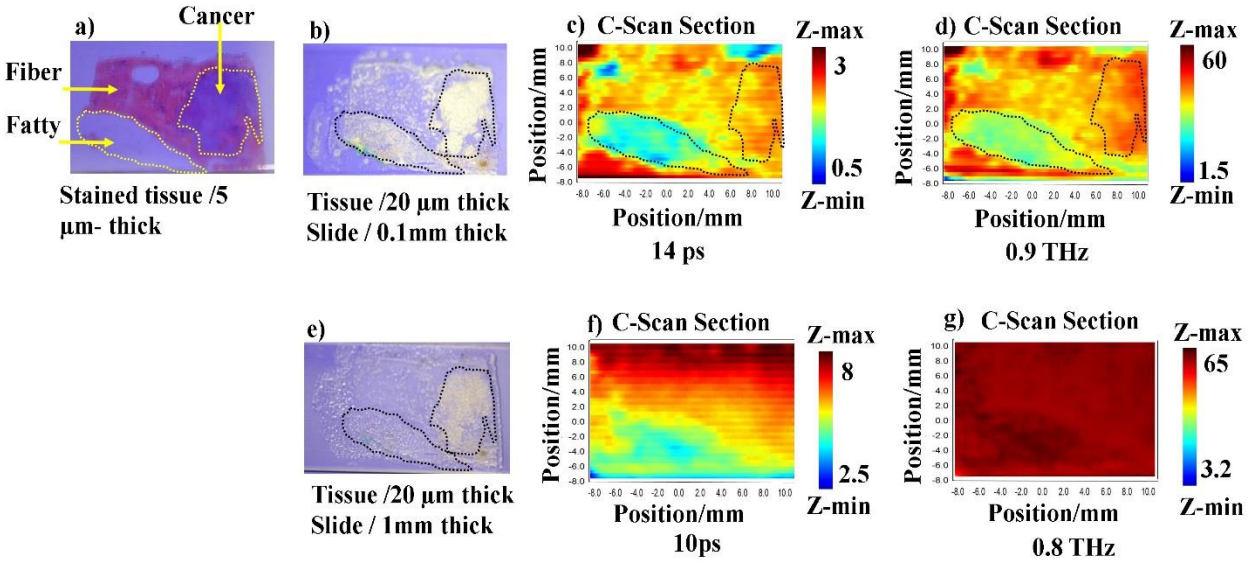

Figure 50: Transmission imaging results for 20 µm-thick samples: (a) photograph of stained tissue; (b & e) photograph of the same tissue embedded in paraffin on a slide and coverslip; (c & f) THz images in time domain at 14 ps & 10 ps, respectively; and (d & g) THz images in frequency domain at 0.9THz & 0.8THz, respectively.

Figure 50(a) shows a photograph of 5 µm-thick stained tissue, where three different regions were diagnosed by the histopathologist: the blue region represents cancer, pink represents fiber, and white represents fatty tissue. The pathology diagnosis was based on increased numbers of cells, changes in their shape, and the coloring of tissue regions. In this figure, the color bars for the time- and frequency-domain images show the electric field amplitude of the THz pulses at each point in each region within the tissue. Figure 50(b & e) show the heterogeneity of the paraffin-embedded tissue sections taken from the same histopathology sample, which made

it more challenging to distinguish between different regions. Additionally, the cancer region observed had a more irregular surface than the fibrous or fatty regions. Figure 50(c & d) show the THz transmission images (20 µm tissue/ 0.1 mm coverslip) selected in the 14 ps time domain and 0.9THz frequency domain. The contrast varied in different regions of the sample, due to dielectric response. This facilitates discrimination between altered regions on the tissue section, compared with the photograph of stained tissue. Consequently, on high-amplitude THz transmission images in time and frequency domains, cancer tissue is defined by a red region, orange/yellow indicates a mixture of fiber and cancer cells, and lower amplitude tissue, indicating a fatty region, appears in blue. On analysis of the THz images, the fiber region appeared more widespread than in the original pathology diagnosis. However, the measurements on the THz images were positively correlated with those on the photograph. In contrast, on Figure 50(f & g), showing the transmission results of THz imaging in the10 ps time domain and 0.8 THz frequency domain, on 20µm-thick tissue mounted on a 1mm thick microscope slide, it was not possible to discriminate between different tissue regions.

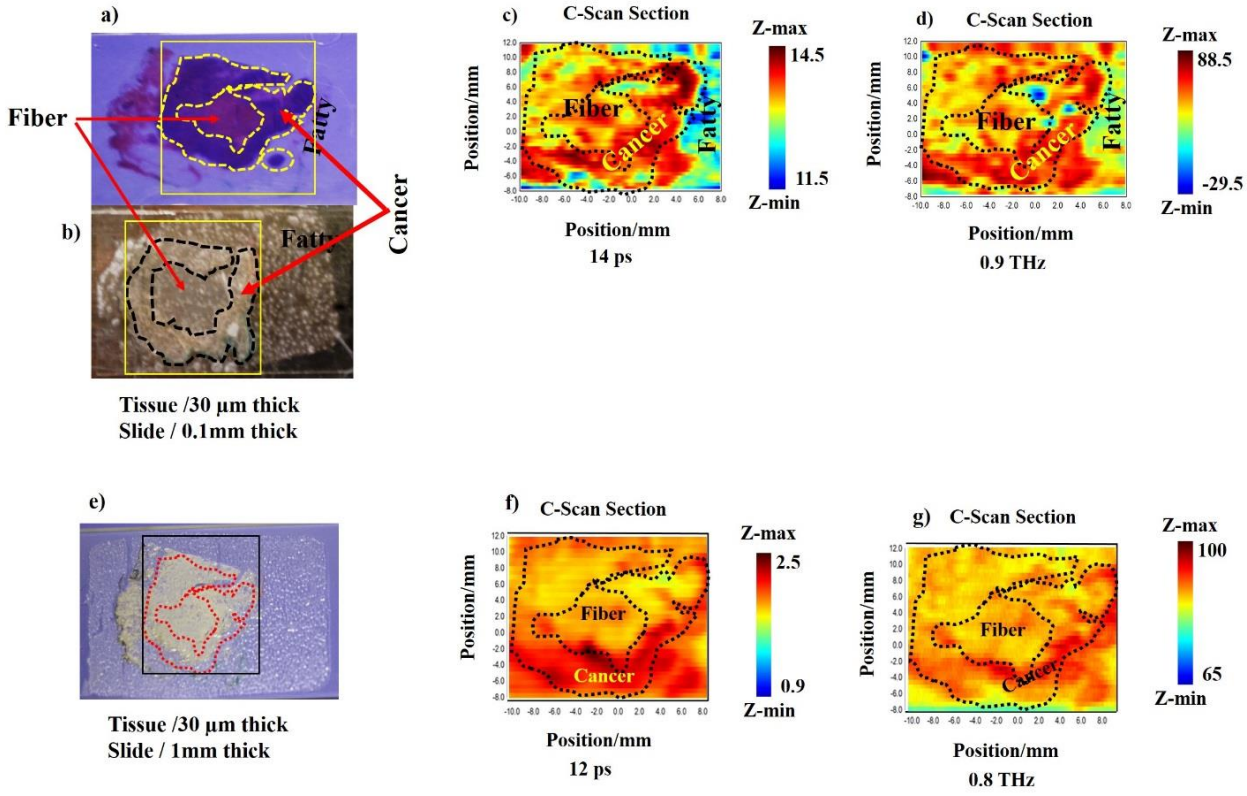

Figure 51: Transmission imaging results for 30 µm-thick samples: (a) photograph of stained tissue; (b & e) photograph of the same tissue embedded in paraffin; (c & f) THz images in time domain at 14 ps & 10 ps, respectively; (d & g) THz images in frequency domain at 0.9THz & 0.8THz, respectively.

Figure 51(a) shows a photograph of 5 µm-thick stained tissue, where three different regions were diagnosed by the histopathologist: the blue region represents cancer, pink represents fiber, and white represents fatty tissue. The pathology diagnosis was based on increased numbers of cells, changes in their shape, and the coloring of tissue regions. Figure 51(b & e) show the heterogeneity of the paraffin-embedded tissue sections taken from the same histopathology sample, which made it more challenging to distinguish between different regions. Additionally, the cancer region observed had a more irregular surface than the fibrous or fatty regions. In these figures, the color bars of the time- and frequency-domain images show the electric field amplitude of the THz pulses at each point in each region within the tissues.

Figure 51(c & d) shows the THz images in transmission mode (30 µm tissue/0.1 mm coverslip) selected in the 14 ps time domain and 0.9THz frequency domain, using peak-to-peak amplitudes of both. The sample regions exhibit significant differences in contrast, due to different amplitudes. It was, therefore, possible to discriminate clearly between different regions in the tissue section, compared with the histopathology results. On high-amplitude THz images in both time and frequency domains, cancer tissue is defined by a dark-red region, red/yellow indicates a mixture of fiber and cancer cells, and lower amplitude tissue, indicating a fatty region, appears blue or yellow.

Figure 51(f & g) show the THz images in transmission mode of a 30 µm thick tissue mounted on a 1 mm microscope slide, at the position selected in the 12 ps time domain and 0.8 THz frequency domain, using peak-to-peak amplitudes. On the same manner, on THz images in both the time and frequency domains, high-amplitude tissue, indicating a cancer region, was dark red and red/yellow or orange indicated a mixture of fiber and cancer cells. However, it was difficult to distinguish a fatty region in THz transmission images in either the time or frequency domains, perhaps due to the lower amplitude of this region. In addition, the THz images on tissue/coverslip clearly discriminated between cancer, fiber, and fatty regions, which was not the case using THz images on tissue/ microscope slide. Consequently, the shape of the cancer region on the THz images matched the histopathology image. In addition, the fiber region appeared more widespread on THz images compared with the histopathology image. However, measurements revealed a positive correlation between the THz images and the original image.

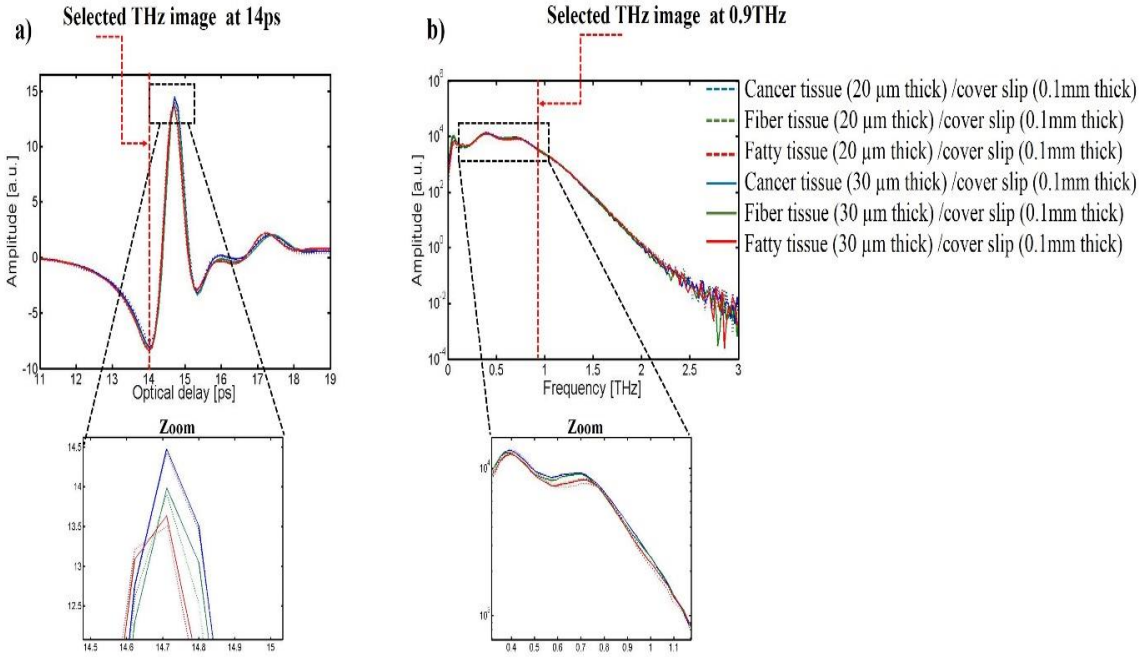

Figure 52: Transmission results on paraffin-embedded tissue (20 & 30 µm thick), mounted on coverslips 0.1 mm thick, a) time domain of signals collected from cancer, fiber, and fatty tissues, and b) FFT spectra of these signals.

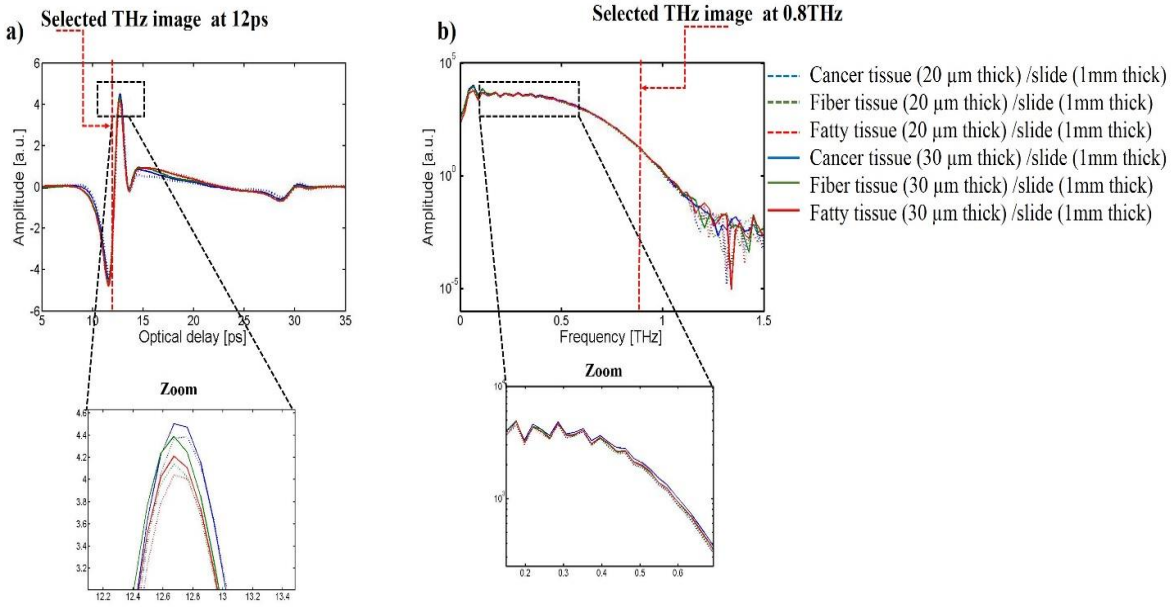

Figure 53: Transmission results on paraffin-embedded tissue (20 & 30 µm thick), mounted on microscope slides 1 mm thick, a) time-domain signals collected from cancer, fiber, and fatty tissues, and b) FFT spectra of these signals.

Figure 52(a & b) show transmitted results of the THz amplitude of waveforms, selected from cancer, fiber, and fatty tissue as a function of optical delay and FFT spectrum, respectively, at frequencies ranging from 0 to 3 THz. These signals were selected from THz images of 20 and 30 µm-thick tissue samples, mounted on coverslips 0.1 mm thick. Little difference was visible between these plots, where the maximum amplitudes on a 30 µm-thick sample were 14.47, 13.98, and 13.63 mV for cancer, fiber, and fatty tissue, respectively. The maximum amplitudes on a 20 µm-thick sample were 14.42, 13.9, and 13.51 mV for cancer, fiber, and fatty tissue, respectively.

Figure 53(a & b) show the transmitted results of the THz amplitude of waveforms selected from cancer, fiber, and fatty tissue as a function of optical delay and FFT spectrum, respectively, at frequencies ranging from 0 to 1.5 THz. These signals were selected from THz images of tissue of 20 and 30 µm thick, mounted on microscope slides 1 mm thick. These plots revealed maximum amplitudes on a 30 µm- thick sample of 4.5, 4.4, and 4.1 mV for cancer, fiber, and fatty tissue, respectively. The maximum amplitudes on a 20 µm-thick sample were 4.4, 4.2, and 4 mV for cancer, fiber, and fatty tissue, respectively. These tiny differences are reproducible.

A comparison of Figure 52 and Figure 53 revealed that there was little difference in time delay between these signals: approximately 14.7 ps for transmitted signals from tissue/coverslip and 12.7 ps for tissue/microscope slide. Furthermore, the spectral plots tracked close together at frequencies ranging from 0.15 to 2.5 THz for tissue/coverslip and 0.15 to 1.1 THz for tissue/microscope slide. All spectra also fell to the noise floor at 2.5 THz for cancer, fiber, and fatty tissue mounted on coverslips and 1.1 THz for the same tissues mounted on microscope slides. Moreover, the fact that the maximum amplitude of cancer, fiber, and fatty tissue was higher on coverslips than microscope slides may explain the difficulty of discriminating between different tissue regions on THz images obtained using microscope slides. Thus, the difference between these measurements may be due to the thickness of tissue and substrate, their optical properties, and the surface nature of both the tissue and the glass substrate.

5.4.1.2. Reflection results

Tissue sections (-10<x>20, -10 <y>10) mm 20µm thick and (-5<x>35, -5<y>15) mm 30µm thick were scanned in reflection mode, at 0.1 to 3 THz and 10 averages, waveform 2048, step size 0.5 mm. The breast cancer results are shown in Figure 54 and Figure 55.

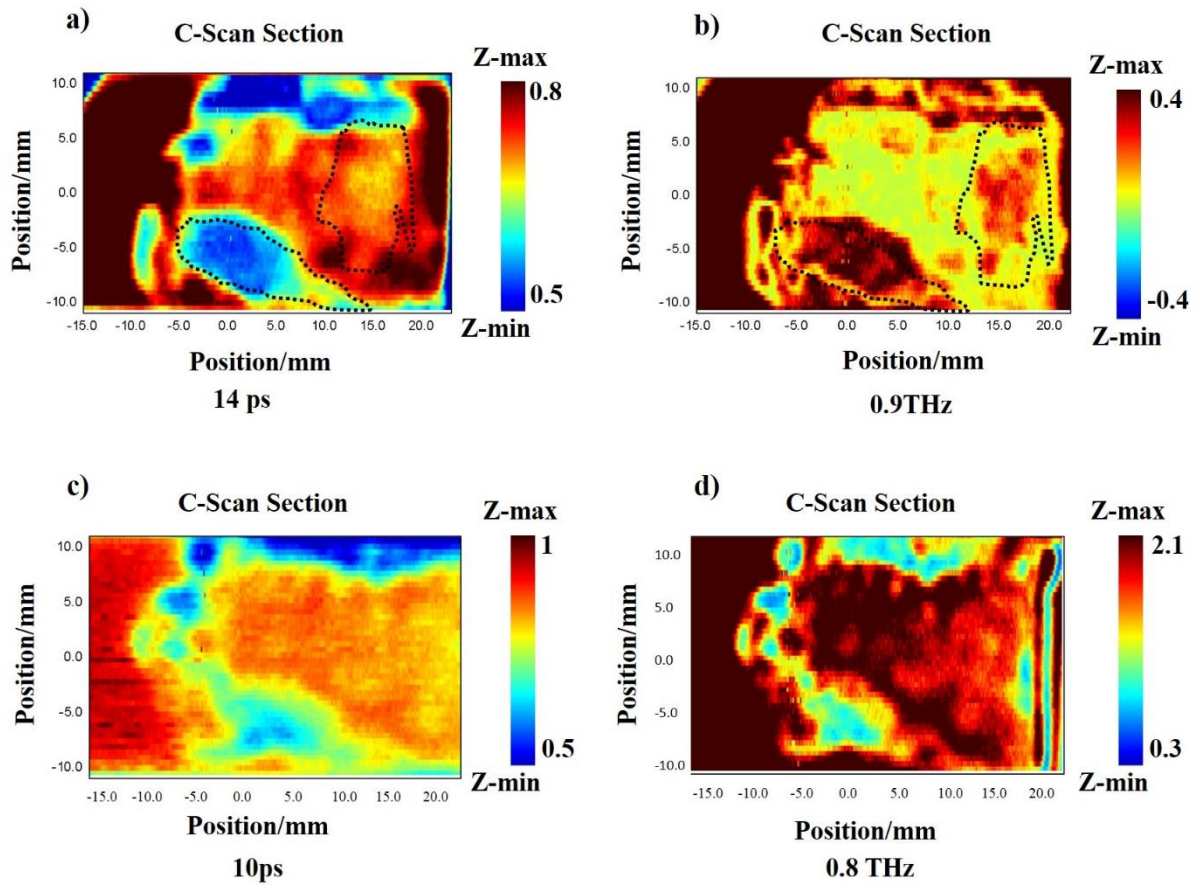

Figure 54: Reflection imaging results for 20µm-thick samples: (a & b) THz images of tissue mounted on coverslips in time and frequency domains at 14 ps & 0.9 THz, respectively; (c & d) THz images of tissue mounted on microscope slides in time and frequency domains at 10 ps & 0.8 THz, respectively.

Figure 54 shows the reflection results of the same 2.5 × 3.5 cm sections used in transmission measurements. Figure 54(a & b) show the THz reflection images (20 µm tissue/0.1 mm coverslip) selected in the 14 ps time domain and 0.9THz frequency domain. In these images, the cancer region had a highly-significant reflection compared to the fiber and fatty regions. In addition, it was easier to discriminate between cancer (red), fiber (yellow), and fatty (black) tissue on THz images in the frequency than in the time domain. Figure 54(c & d) show the THz reflection images (20 µm tissue/ 1 mm microscope slide) selected in the 10 ps time domain and the 0.8 THz frequency domain. These THz images of breast tissue revealed a different contrast due to the different amplitudes of cancer, fiber, and fatty tissue. Thus, it was easier to discriminate between them compared to the photographs of stained tissue. It was also easier to distinguish between cancer (red), fiber (black), and fatty (green) tissue than on THz images in the time domain, possibly due to the different structures of each region or the varying thicknesses of each tissue region. On analysis of the THz images of tissue/coverslip and tissue/microscope slide samples, the fiber region appeared more widespread than in the original pathological

diagnosis. However, measurements on the THz images were positively correlated with those on photographic image.

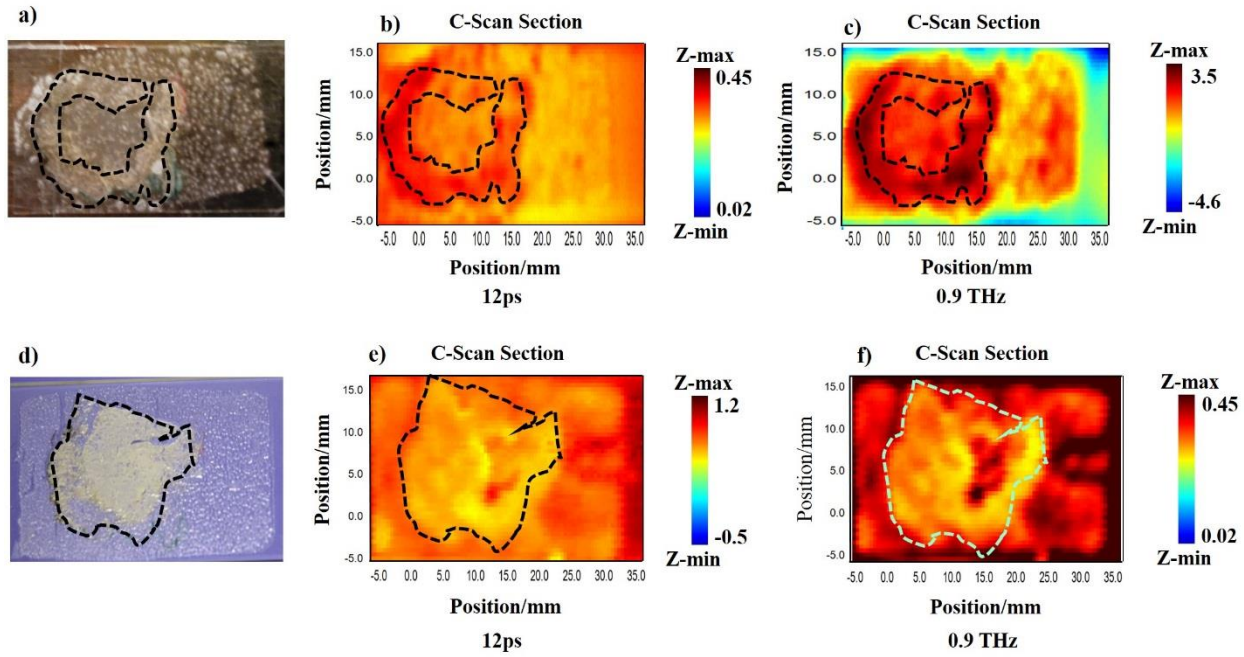

Figure 55: Reflection imaging results for 30 µm samples: (a & d) photograph of paraffin-fixed tissue; (b & c) THz images of paraffin-fixed tissue mounted on coverslips in time and frequency domain at 12 ps & 0.9 THz, respectively; (c & d) THz images of paraffin-fixed tissue mounted on microscope slides in time and frequency domains at 12 ps & 0.9 THz, respectively.

Figure 55 shows the results in reflection mode for the same sections used in transmission measurements, shown in Figure 55(a) and described there in greater details. Figure 55(b & c) represent the THz images in reflection mode (30 µm tissue/0.1 mm coverslip), selected in the 12 ps time domain and 0.9 THz frequency domain, using peak-to-peak amplitudes of both. The sample regions exhibited significant differences in contrast due to different amplitudes. It was, therefore, possible to discriminate between different regions in the tissue section, compared with the histopathology results. The THz image was clearer in the frequency domain than in the time domain. In addition, the high amplitude of cancer tissue is defined by a dark red region, while red/yellow indicates a mixture of fiber and cancer cells. On analysis, the shape of the cancer and fiber region on the THz images matched the histopathology image.

Figure 55(e & f) show the THz images in reflection mode (30 µm tissue/ 1 mm microscope slide), selected in the 12 ps time domain and 0.9 THz frequency domain, using peak-to-peak amplitudes of both. These images exhibited low contrast between different tissue regions, making it difficult to discriminate between cancer and fiber tissue. It was also even more difficult to distinguish the fatty region in both tissue/coverslip and

tissue/microscope slide THz images, due to the very low amplitude. In addition, on the THz reflection image of the tissue/coverslip sample, the cancer and fiber regions were clearly distinguishable, but not on the tissue/ microscope slide image.

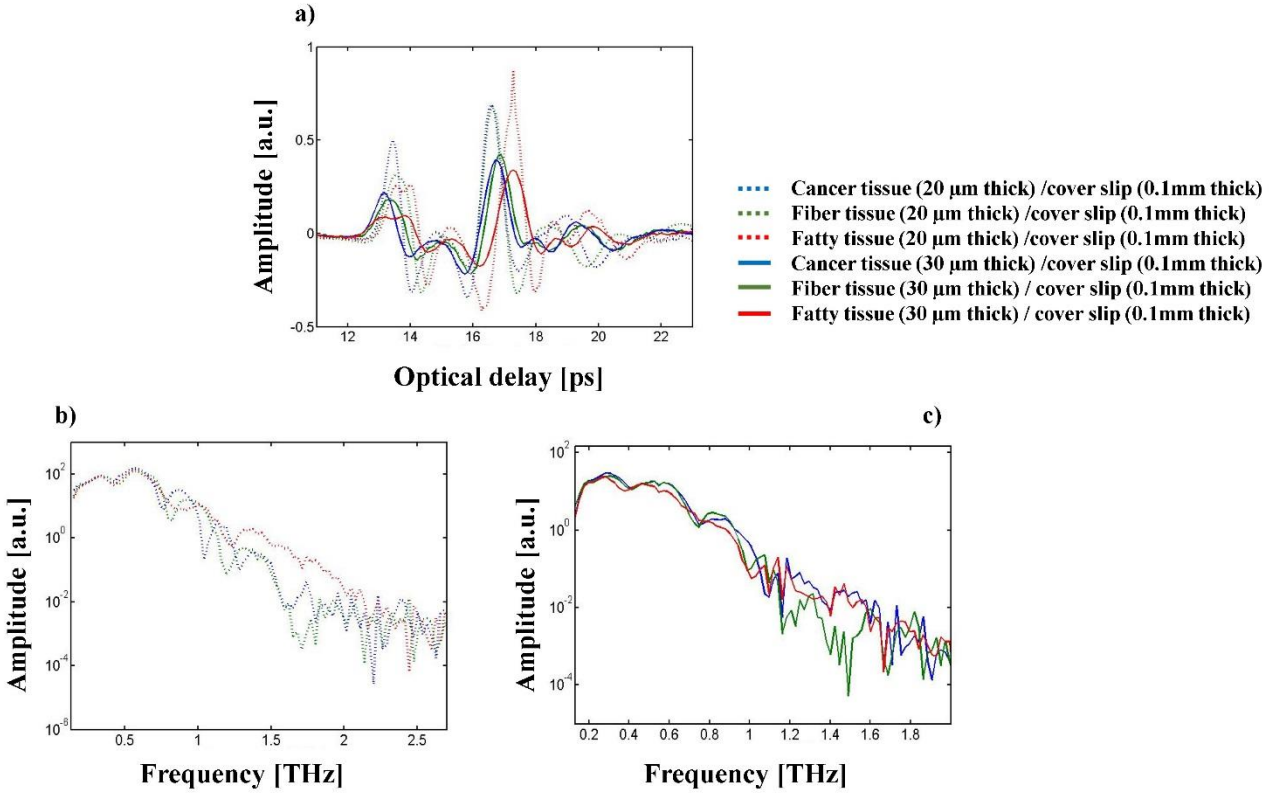

Figure 56: THz reflection results on paraffin-embedded tissue (20 & 30 µm thick), mounted on 0.1 mm-thick coverslips: a) time-domain signals collected from cancer, fiber, and fatty tissues; and b & c) FFT spectra of these signals.

Figure 56(a) shows the position of the time domain of reflected signals selected from cancer, fiber, and fatty regions of paraffin-embedded tissue (20 and 30µm)/0.1 mm coverslip. Different peaks were detected, due to interference from signals reflected from the second surface of the tissue and coverslips. In addition, the amplitudes of all the THz reflected signals from the 20 µm-thick tissue section were higher than those from 30µm-thick samples, with maximum values of 0.5, 0.3, and 0.25 mV for cancer, fiber, and fatty tissue, respectively, on 20µm samples and 0.21, 0.18, and 0.08 mV for cancer, fiber, and fatty tissue, respectively, on 30µm samples. In addition, the maximum reflected THz signal amplitude of breast cancer tissue was higher than that of fibrous and fatty regions, possibly due to each region having a different refractive index, resulting in variations in time delay. The time delay between cancer, fiber, and fatty tissue was 0.11 ps for 20 µm tissue

sections, but 0.2 ps for 30 µm tissue sections, thus explaining the THz beam behavior during progress through each region.

Figure 56(b & c) show the FFT spectrum for each region, used to determine the frequency domain of the THz images. These plots exhibit more spectrum oscillations than expected from the nature of the tissue surface, reflecting differences between the tissue and substrate materials, as well as the tissue-substrate interface. In addition, these plots show the propagation of the THz pulses through the different layers in the tissue. All reflected spectrums from 20µm- and 30µm-thick tissue samples fell to 2THz 1.5 THz, respectively. In contrast, the reflected spectra from these plots tracked close together: between 0.13 and 0.6 THz for 20 µm samples and between 0.15 to 0.3 THz for 30 µm samples. It was possible to discriminate between different tissue regions in 20µm samples in the 0.6 to 1.9 THz frequency range, while the range for 30µm samples was from 0.3 to 1 THz.

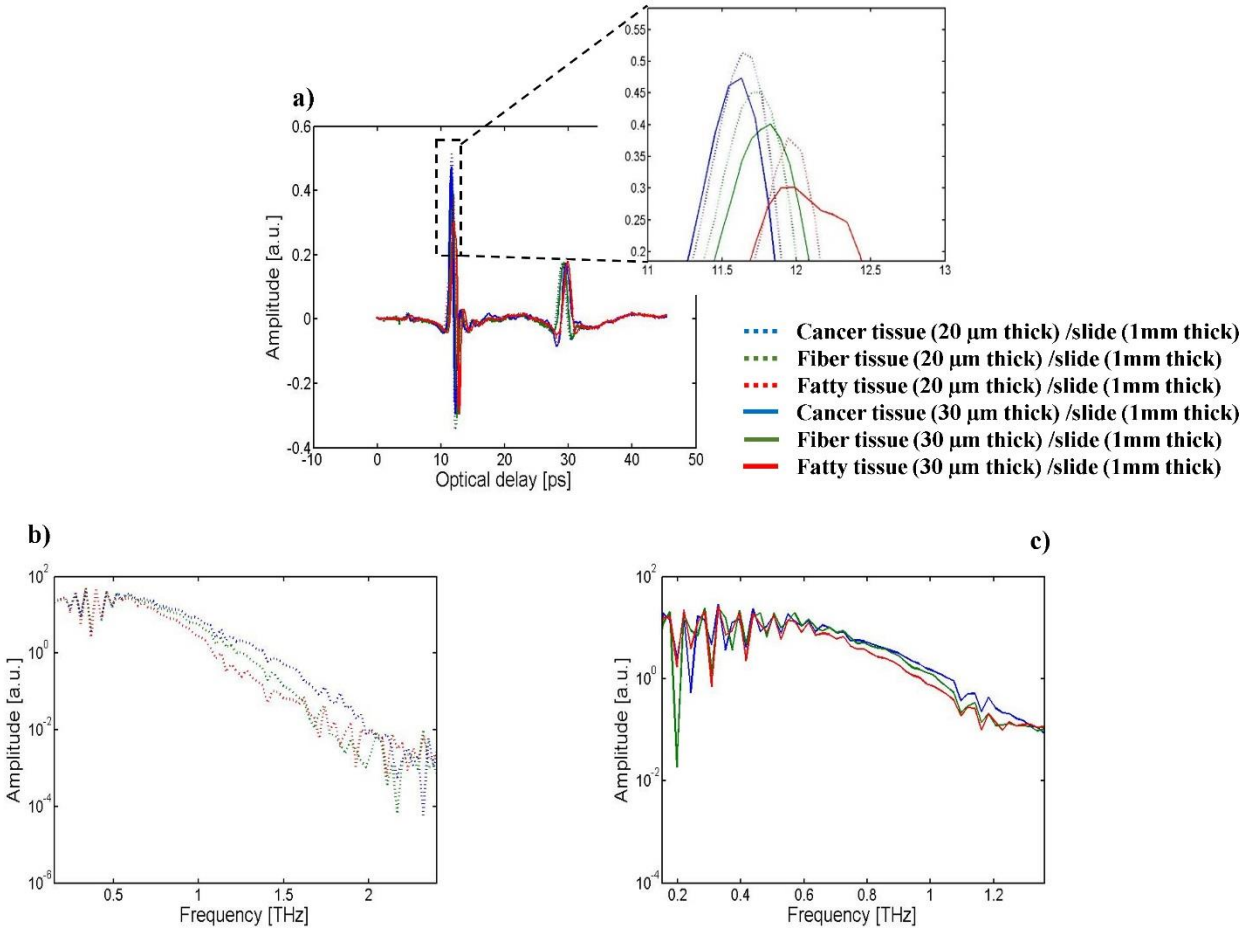

Figure 57: THz reflection results on paraffin-embedded tissue (20 & 30 µm thick), mounted on 1 mm-thick microscope slides: a) time-domain signals collected from cancer, fiber, and fatty tissues; and b & c) FFT spectra of these signals

Figure 57(a) shows the time-domain position of the reflected signals selected from three regions of 20 and 30 µm paraffin-embedded tissue samples on)/1 mm-thick microscope slides. The THz signals were affected by interference, reflecting off the surfaces of the tissue and substrate. The amplitudes of all THz signals reflected from 20 µm paraffin-embedded tissue sections were higher than those from 30µm sections. Maximum amplitudes on 20µm samples were 0.53, 0.45, and 0.4 mV for cancer, fiber, and fatty tissue, respectively, and 0.47, 0.4, and 0.3 mV, respectively, on 30µm sections. In addition, in both 20 and 30 µm breast-tissue sections, the cancer region had a highly-significant reflection compared to the fiber and fatty regions, possibly due to the different refractive indexes of each region. This plot shows that the time delay of THz signals reflected from a fatty region was longer than in the case of cancer and fiber regions: 11.9, 11.6, and 11.8, respectively.

Figure 57(b & c) show the FFT spectrum of each region, used to determine the frequency domain of THz images. These plots reveal that all the spectra tracked closely together, with more oscillations in a frequency range from approximately 0.13 to 0.55 THz than expected from the uneven nature of the tissue surface, as well as the different properties of the tissue and substrate materials. These plots also show the propagation of the THz pulses through different layers in the tissue. All reflected spectra from 20µm and 30µm tissue samples fell to 2THz and 1.3 THz, respectively. In addition, it was possible to discriminate between different tissue regions in 20µm samples in the frequency range between 0.5 and 1.6 THz, while, for the range 30µm samples, was between 0.6 and 1.1 THz.

Consequently, the contrast was more marked on the THz images of 20 and 30 µm tissue samples mounted on 0.1 mm coverslips than those on 1 mm microscope slides, due to the properties and thickness of the tissue and substrate materials. Moreover, the thinner coverslip resulted in higher-amplitude transmission and reflection than the thicker microscope slide, due to its physical properties, including higher absorption. For all samples, the peak amplitudes in transmission and reflection modes were smaller for fiber and fatty tissues than for cancer regions in paraffin-embedded breast tissue, it was the same for the spectral amplitude in the THz frequency range. These variations in amplitude were due to differences in the properties of the tissues. Finally, these results in transmission and reflection and both time and frequency domains may explain the higher absorption and lower refractive index in paraffin-embedded breast tissue samples, mounted on coverslips and microscope slides, represented by their contrast and amplitude. We also want to underline the tissues were embedded with paraffin after chemical treatment, water removal and staining procedure. So the difference of the effective response of these new biological materials (paraffin -fiber, paraffin-adipose, and paraffin cancer) is less pronounced than those observed for freshly excised tissue. The segmentation and the separation between two different tissues in these conditions is much more complicated.

5.4.2. Sample 2: measurements on a sapphire substrate

In this set of experiments, the same the Teraview 3000 transmission and reflection imaging system was used on 30 µm-thick samples of paraffin-embedded breast tissue, mounted on a 5 mm-thick sapphire window. This sample was obtained from a 48-year-old woman and the tissue diagnosis was grade II invasive carcinoma NST (no special tumor).

Image acquisition in transmission mode involved scanning 1.25 × 1.25 cm tissue sections with frequencies in the 0.1 to 3 THz, with 10 averages, waveform 2048, step size 0.1 mm, with an acquisition time of 2 h. The breast cancer results are shown in the figures below, read from the TVL file. Note that it was unconventional to cut paraffin layers and depose it onto a different substrate than microscope slides, and without a cover glass to flatten the paraffin-sample layer.

5.4.2.1. Transmission results

Figure 58(a) shows an image of a 30 µm-thick, paraffin-embedded breast tissue sample, mounted on a 3 mm-thick sapphire window, displaying cancer, fiber, and fatty regions, confirmed by histopathology. It also reveals the more irregular surface of the cancer region to be more irregular, compared to the smoother fiber region. Moreover, the cancer region appears thicker than the fiber and fatty regions.

Figure 58(b & c): the THz transmission image was selected at 6 ps in the time domain and 1 THz in frequency domain. The color bar represents the amplitude of each point on the THz images. The resulting details of the tissue are clearly distinguishable on the THz images in both time and frequency domains, so it was possible to discriminate among the cancer, fiber, and fatty regions. In both images, the cancer region is displayed in dark red, the fiber region in red, and the fatty region in yellow. In addition, differences were observed in pixel amplitudes and distribution on the THz images: the amplitude in the cancer region was higher than in the fiber region, while the fatty region was even lower, thus explaining the contrast in the images, indicating the different densities of cancer, fiber, and fatty tissue. The shape of the cancer region matched that of the histopathology diagnosis.

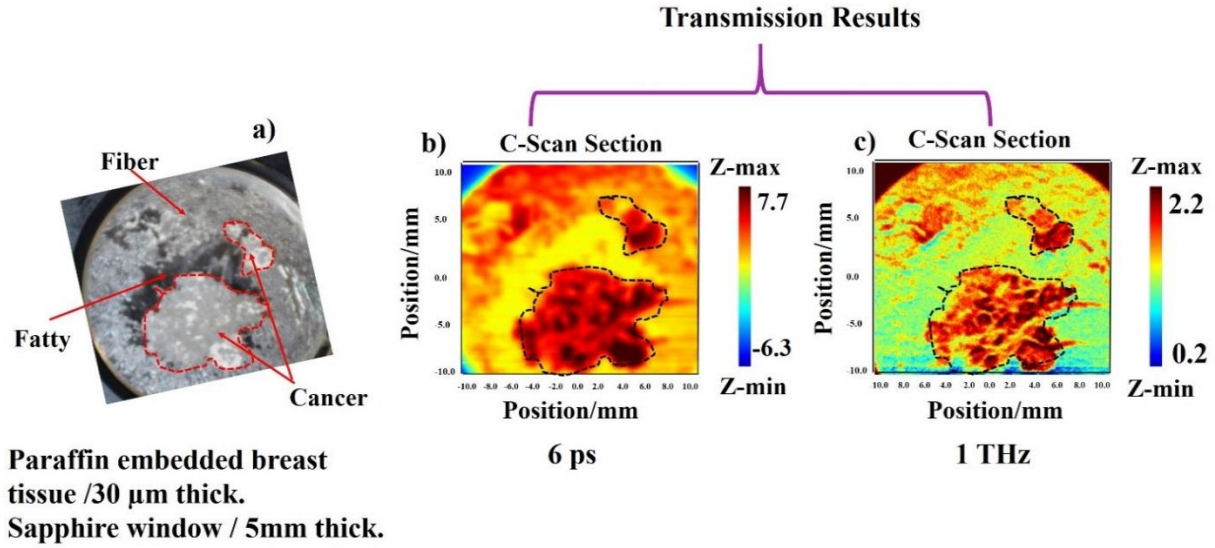

Figure 58: Transmission imaging results: (a) photograph of paraffin-embedded breast tissue, 30 µm thick; b) THz image in time domain at 6 ps, and c) THz image in frequency domain at 1 THz.

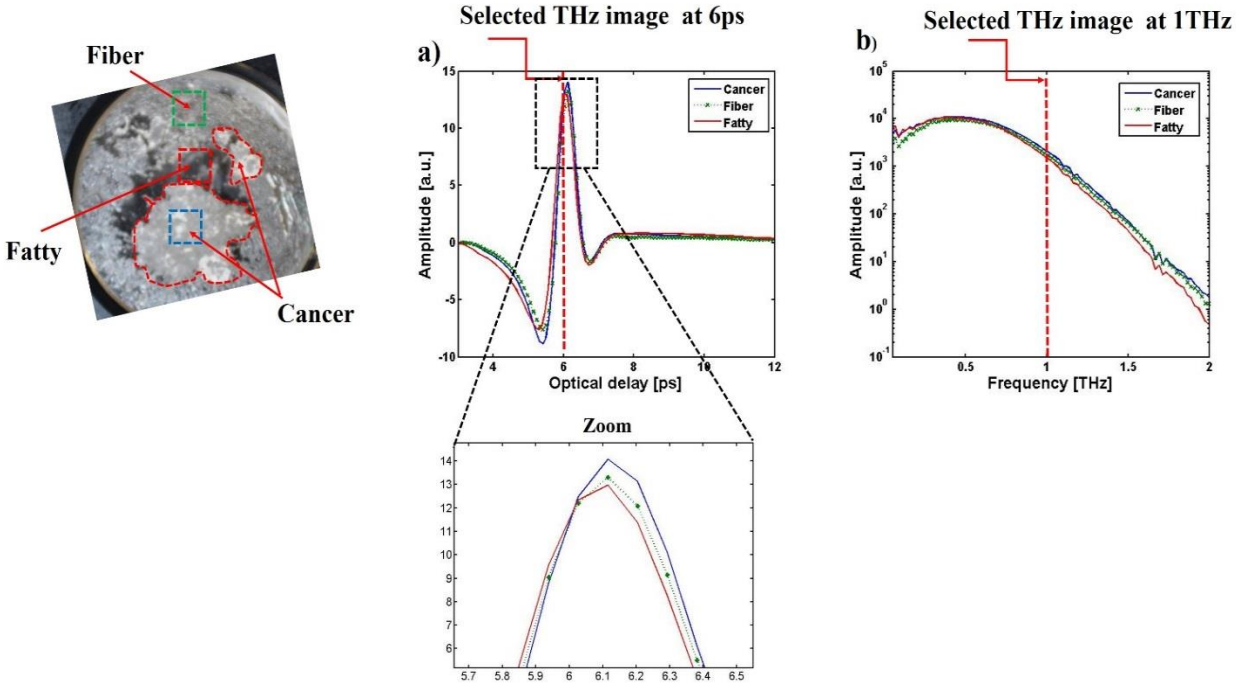

Figure 59: Transmission results of: a) time-domain signals collected from cancer, fiber, and fatty tissues, and b) FFT spectra of these signals.

Figure 59(a) illustrates the position of the time domain in THz transmission signals, collected from heterogeneous areas of paraffin-embedded cancer, fiber, and fatty tissue. These waveform plots, showing that

the cancer region transmitted at higher amplitudes than the other tissue regions, indicate that cancer tissues have a higher structural density than fiber and fatty regions. The maximum amplitudes for cancer, fiber, and fatty tissues were 14.1, 13.3, and 13 mV, respectively. Only a very slight time delay was observed between THz signals transmitted from the three regions, so the plots were very close. Figure 59(b) shows the FFT spectrum of THz transmitted signals, used to determine the frequency domain of THz images. Analysis revealed that the spectra transmitted from all three regions fell to the noise floor at over 2.5 THz. In addition, the tracks of the three spectra remained close together between approximately 0.3 and 0.65 THz and the cancer spectrum tracked the fiber spectrum closely between approximately 0.13 and 0.65 THz. It was possible to discriminate among the three regions in a frequency range of approximately 0.65 to 2 THz. These plots illustrate the behavior of THz pulses in each tissue region.

5.4.2.2. Reflection results

Tissue sections 1.25 × 1.25 cm were scanned in reflection mode for image acquisition at frequencies of 0.1 to 3 THz, 10 averages, waveform 2048, step size 0.5 mm, and an acquisition time of 1 h 15 min. The breast cancer results are shown in Figure 60 below, read from the TVL file.

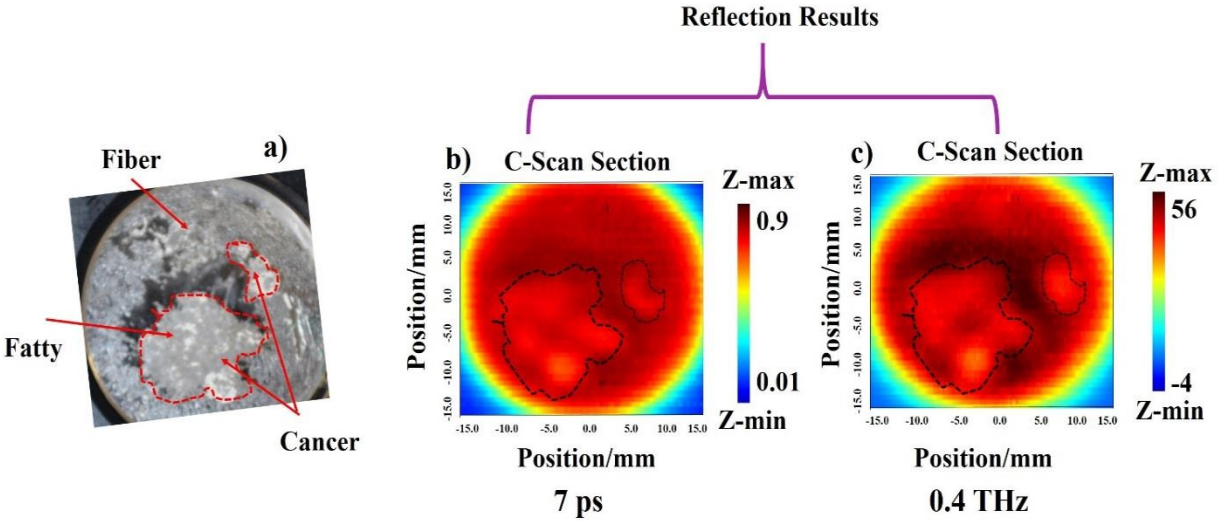

Figure 60: Reflection imaging results for a 30 µm-thick sample: (a) photograph of paraffin-embedded breast tissue; b) THz image in time domain at 7 ps; and c) THz image in frequency domain at 0.4 THz.

Figure 60(a) shows an image of a 30 µm-thick, paraffin-embedded breast tissue sample, mounted on a 3 mm-thick sapphire window, described in greater detail in the transmission results. The color bar represents the amplitude of each point on the THz images. Figure 60(b & c) show the THz reflected images fixed in the time

domain, selected at 7 ps and the frequency domain, selected at 0.4 THz. These results revealed a lack of contrast between the tissues, similar to the uneven contrast in the THz images. It was possible to distinguish the cancer region at 6 ps and 0.4THz, represented by a mixture of red and yellow, but it was difficult to discriminate between fiber and fatty regions, perhaps due to the lower amplitude of their reflected THz signals compared to those of cancer tissues. These results showed that it was possible to identify cancer regions at these values in both time and frequency domains. The shape of the cancer region was in agreement with the original image.

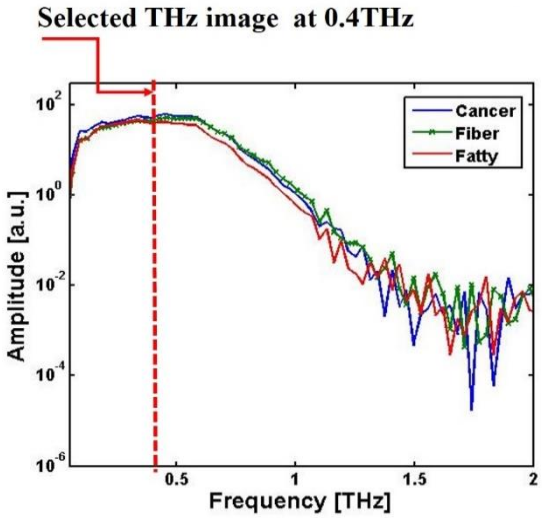

Figure 61: FFT spectra collected from cancer, fiber, and fatty breast tissues.

Figure 61 illustrates the FFT spectra of reflected THz signals to determine the frequency domain of the THz images. The reflected spectra of all three regions also fell to the noise floor at 1.3 THz. In addition, the tracks of the fiber and fatty tissue spectra remained close together between approximately 0.13 and 0.39 THz, while the cancer and fiber spectra remained close together between approximately 0.58 and 0.79 THz. It was possible to discriminate among the three regions in a frequency range of approximately 0.76 to 1.1 THz. These plots illustrated the behavior of THz pulses during progress through each region of paraffin-embedded breast tissue. *To summarize, THz transmission images in both the time and frequency domains offered better contrast and facilitated the margin distinction between different regions of paraffin-embedded tissue. For THz reflected images, the results are less convincing. Moreover, the results from both measurements correlated positively with the original photograph. In addition, these results revealed that THz transmitted signals present a higher contrast than those of the THz reflected signals. We obtained in transmission a very nice correlation with H&E analysis and we can clearly separate the adipose tissue to the fiber ones.*

5.4.3. Sample 3: Reflection imaging on a paraffin block

In the next step, the 3000 Teraview system was used in reflection mode to measure breast tissue embedded in paraffin blocks approximately 3 mm thick. This tissue was heterogeneous, with an uneven surface and irregular thickness. The paraffin block was prepared in the lab at Institut Bergonié and the tissue identified by histopathology and categorized in three regions: cancer, fiber, and fatty. This sample was obtained from a woman with invasive carcinoma NST (no special tumor).

Samples 4 × 2.5 cm were scanned in reflection mode at frequencies of 0.1 to 3 THz and 7volts, 4 averages, waveform 2048, step size 0.05 µm, and an acquisition time of 24 h. The results for the paraffin block samples in reflection mode are shown in Figure 62, read from the TVL file.

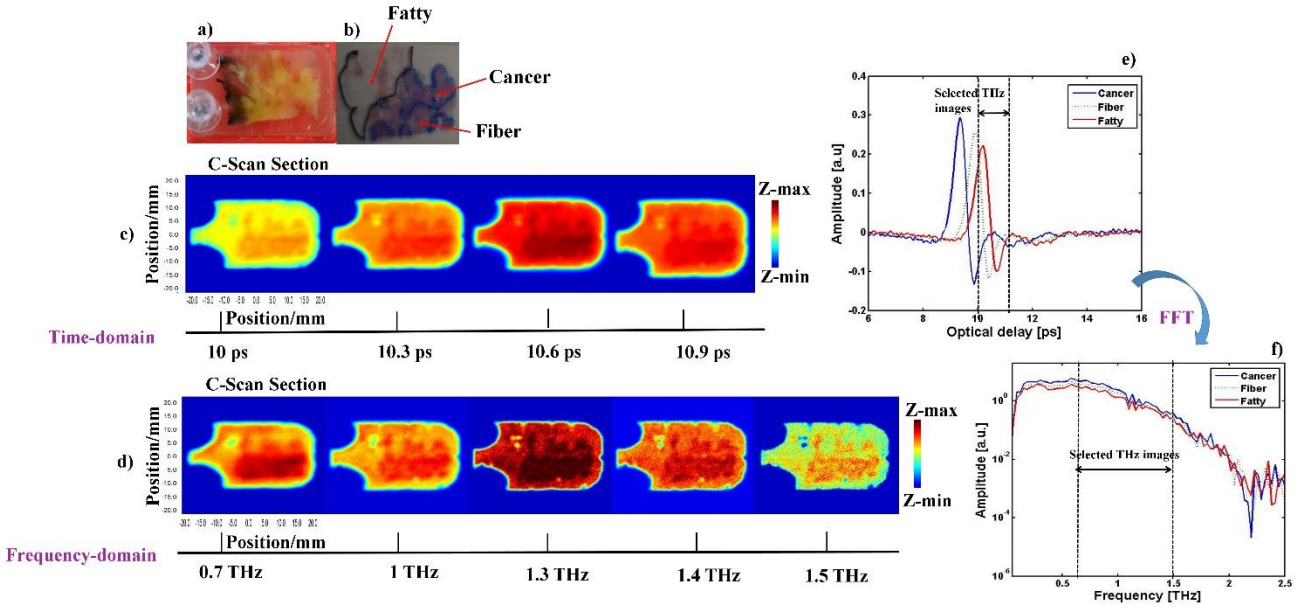

Figure 62: a) photograph of breast tissue inserted in a paraffin block; b) photograph of stained tissue, c & d) THz images in the time and frequency domain, respectively, e) time-domain signals collected from cancer, fiber, and fatty tissues, and f) FFT spectra of these signals.

Figure 62(a) shows a photograph of a breast tissue sample in a paraffin block; Figure 62(b) shows a photograph of a 5µm-thick stained tissue sample. Microscopically, the tissue areas were diagnosed and marked by a histopathologist: blue represents cancer, pink represents fiber region, and white represents the fatty region. Figure 62(c & d) show the processed THz reflected images at a time slice positions within the time domain, selected at 10, 10.3, 10.6, and 10.9 ps. In addition, the THz images of fixed spectra within the frequency domain were selected at 0.7, 1, 1.3, 1.4, and 1.5 THz, respectively. These images were visualized at max amplitude of slice view. In addition, the color bar was scaled based on the maximum and minimum amplitudes of THz

radiation reflected from each pixel of tissue. These images revealed that the cancer region produced the maximum amplitude in both the time and frequency domains, while the fatty region had the minimum amplitude. Therefore, the cancer region was clearly distinguishable at this range in the time domain, as well as in the spectral range in the frequency domain. The cancer region was displayed in highly-contrasted dark red or red, while the fiber and fatty regions were only slightly contrasted. Furthermore, the cancer region was more easily distinguishable on THz images at frequencies ranging from 0.7 to 1.5 THz than in the time domain. The difference of the effective optical index of paraffin embedded tissue is low. Analysis revealed that the cancer tissue was more widespread and mixed with fiber than it appeared to be on the original photograph.

Figure 62(e) shows the time domain of reflected signals, selected from three sample regions, where the cancer region reflected a much higher amplitude (peak amplitude: 0.3) than other tissue regions (peak amplitude for fiber: 0.25, and fatty tissue: 0.2). Figure 62(f) shows the FFT power spectra used to determine the frequency of the THz images. These spectra revealed that all the signals reflected from the three regions fell to the noise floor at approximately 2.2 THz. A clear distinction among the three sample regions was observed between approximately 0.2 and 1.6 THz. Moreover, in this frequency range, the cancer region was reflected at a higher spectrum power than the other regions.

Finally, these THz images and plots in the time and frequency domains indicated the behavior of the THz beam during reflection with the tissue embedded in the paraffin block. These results revealed a positive correlation between the cancer tissues on THz images, compared to the original photograph of stained tissue. Nevertheless, the variation between sane and unsane tissues are very low, leading to a weak contrast in time and frequency domain

5.4.4. Sample 4: Fresh samples

5.4.4.1. Sample immersed in physiologic liquid

The 4000 TeraPulse was also used to scan fresh breast tissues approximately with a 2 to 3 mm thickness. The samples present often heterogeneous texture, and irregular thickness. Samples were prepared in the lab at Institut Bergonié, where the untreated tissue, consisting of two regions, abnormal (tumor) and healthy tissue, was identified by histopathology. Sample preparation is described in an annex. These samples were obtained from women between 39 and 59 years old and the tissue diagnosis was grade II or III invasive carcinoma NST (no special tumor).

Images of 3.5 × 2 cm samples were acquired in reflection mode using a 4000 TeraPulse system at frequencies of 0.1 to 4 THz, 5 averages, waveform 4069, step size 0.1, 0.2, and 0.5 mm, and an acquisition time of 12h, 3h, 2h, and 30 min, respectively, corresponding to the step size. The THz reflection results on fresh tissue are shown

in Figure 63. In the left-hand column, a slide scan of 5 μm-thick stained tissue shows two different regions identified by the histopathologist: the blue region represents tumor tissue, pink represents fiber, and white represents normal tissue. Photographs of fresh breast tissue with tumors are shown in column b of Figure 63, with two regions identified by the histopathologist: a white region representing tumor tissue and a yellow region representing normal tissue. Processed THz images of fixed positions within the time domain were selected at 23, 24, and 25 ps, respectively, as shown in Figure 63, column c. In addition, fixed spectrum THz images were selected in the frequency domain at 0.3, 0.4, and 0.5 THz, respectively, as shown in Figure 63, column d. The THz images were visualized using the peak-to-peak values of the reflected pulses. These selected THz images in the time and frequency domains clearly show the contrast between different tissue regions. The margins of the tumor region are easily distinguished from the normal regions on the THz images in both the time and frequency domains. The tumor region also produced a clear reflection at these frequencies, with a sharper contrast than normal tissue. In addition, the shape and size of the tumor region was similar to the original photograph. Moreover, some regions do not appear uniform on the THz images, possibly mixed regions within the tissue where the tissue composition was not constant.

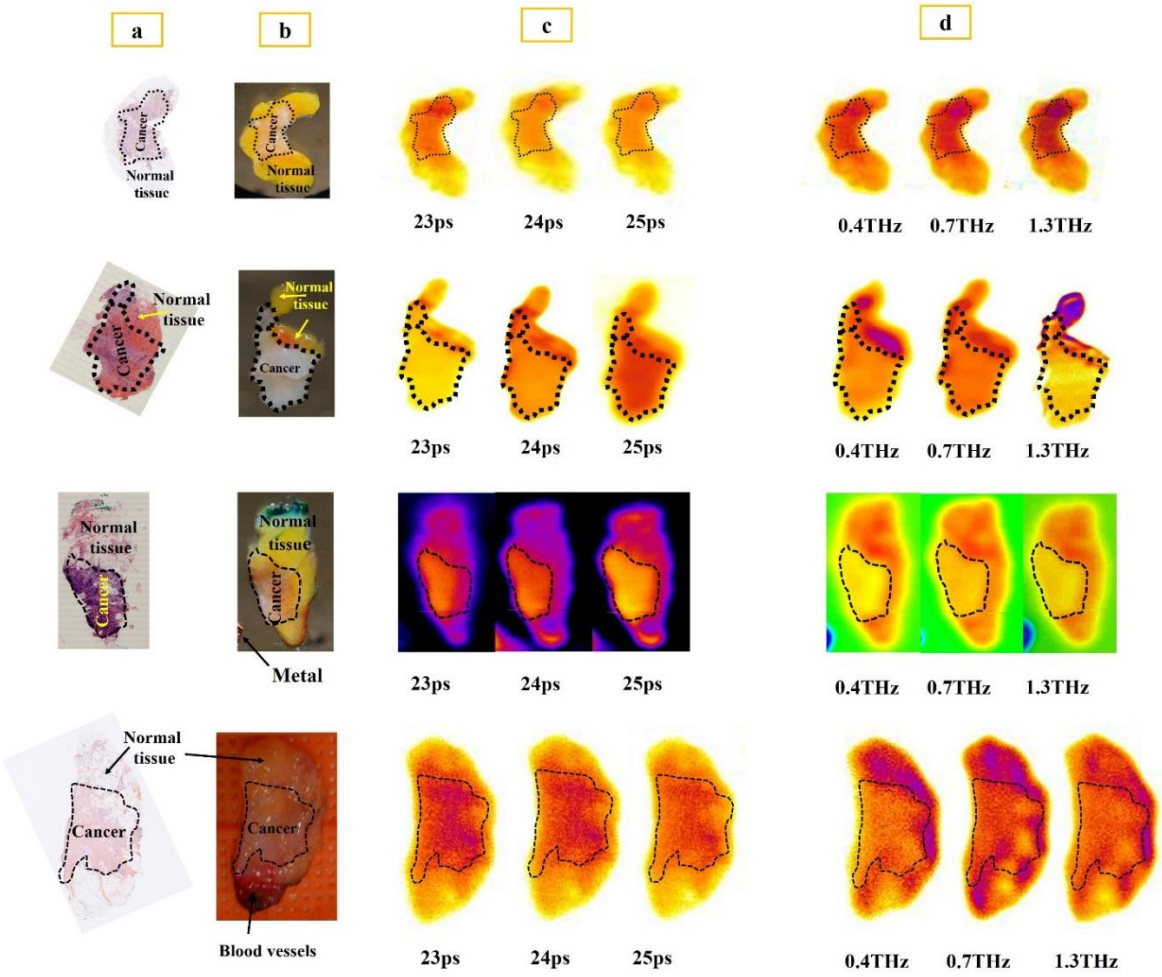

Figure 63: a) Slide scan of 5 µm-thick stained tissue, b) Photograph of fresh tissue and c & d) THz reflected images in time and frequency domains.

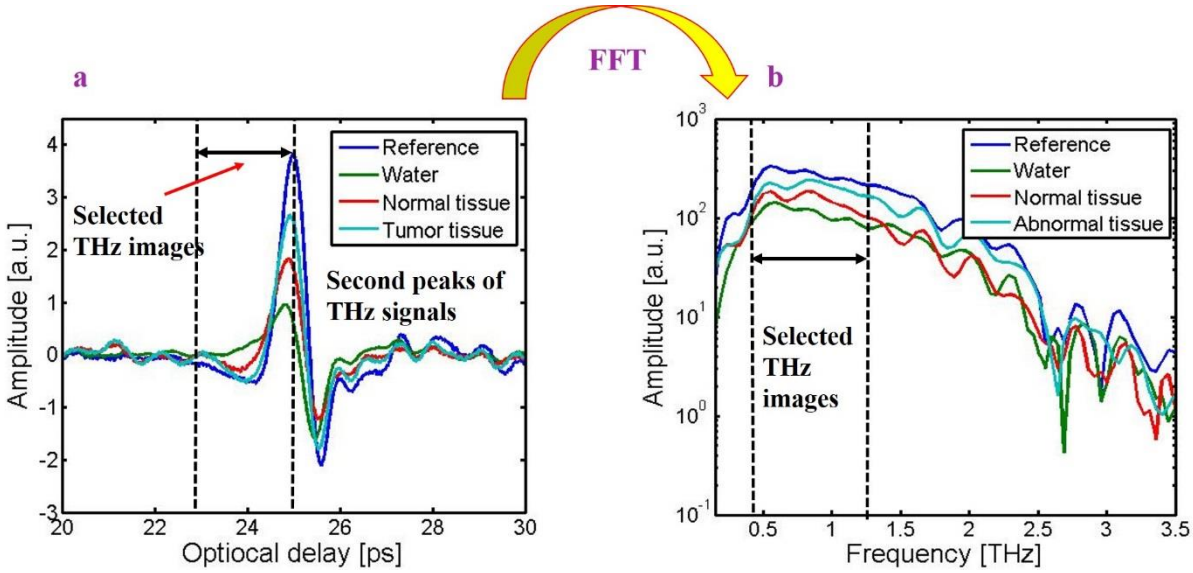

Figure 64: Reflection results: a) time domain of the second THz signal peak collected from reference, water, cancer, fiber, and fatty samples and b) FFT spectra of these signals.

Figure 64(a) shows the second peak of signals measured from one pixel of each reference for alignment, using water for comparison with normal and tumor tissue. Analysis of this plot clearly revealed that each tissue region reflected a different amplitude THz signal compared with the reference THz pulse (4 mV). The peak amplitude reflected from the tumor region (2.8 mV) was higher than that of normal tissue (1.9 mV) and water (0.9 mV), as tumor regions have a higher water content than normal tissue. In addition, these results reflected variations in the structure and optical properties of the various tissue regions. It was, thus, possible to discriminate between tumor and normal regions in fresh tissue, compared with water. The frequency domain provided a more accurate understanding of the behavior of each region. Figure 64(b) shows the FFT spectrum amplitude results for the reference, water, as well as normal and tumor tissue, used to determine the frequency domain of the THz images. On analysis of this plot, there was a clear distinction between tumor and normal tissue, compared with the reference and water, over a range of approximately 0.3 to 2.3 THz. In addition, all the THz signals reflected from the samples fell to the noise floor at 2.5 THz. The frequency range of the power spectrum of the tumor region and normal tissue tracked closely together between approximately 2.2 and 2.5 THz.

We concluded from these results that the THz images representing the amplitude selected in the time and frequency domains can roughly differentiate between tumor and normal tissue. Therefore, the second part of our results includes analysis data used to calculate the refractive index and absorption coefficient of the tissues, making it possible to discriminate between tumor and healthy regions using THz spectroscopy.

5.4.4.2. Results on fresh tissue and tissue fixed with formalin

The last step was to scan fresh breast tissue approximately 2mm thick, before and after fixing in formalin, using a 4000 Tera Pulse system in reflection mode. The sample was obtained from a 57 year-old woman and the tissue diagnosis was grade II invasive carcinoma NST (no special tumor). The sample was prepared in the lab at Institut Bergonié and two regions, abnormal (tumor) and healthy tissue, were identified by histopathology. This untreated tissue had an uneven surface, heterogeneous texture, and irregular thickness.

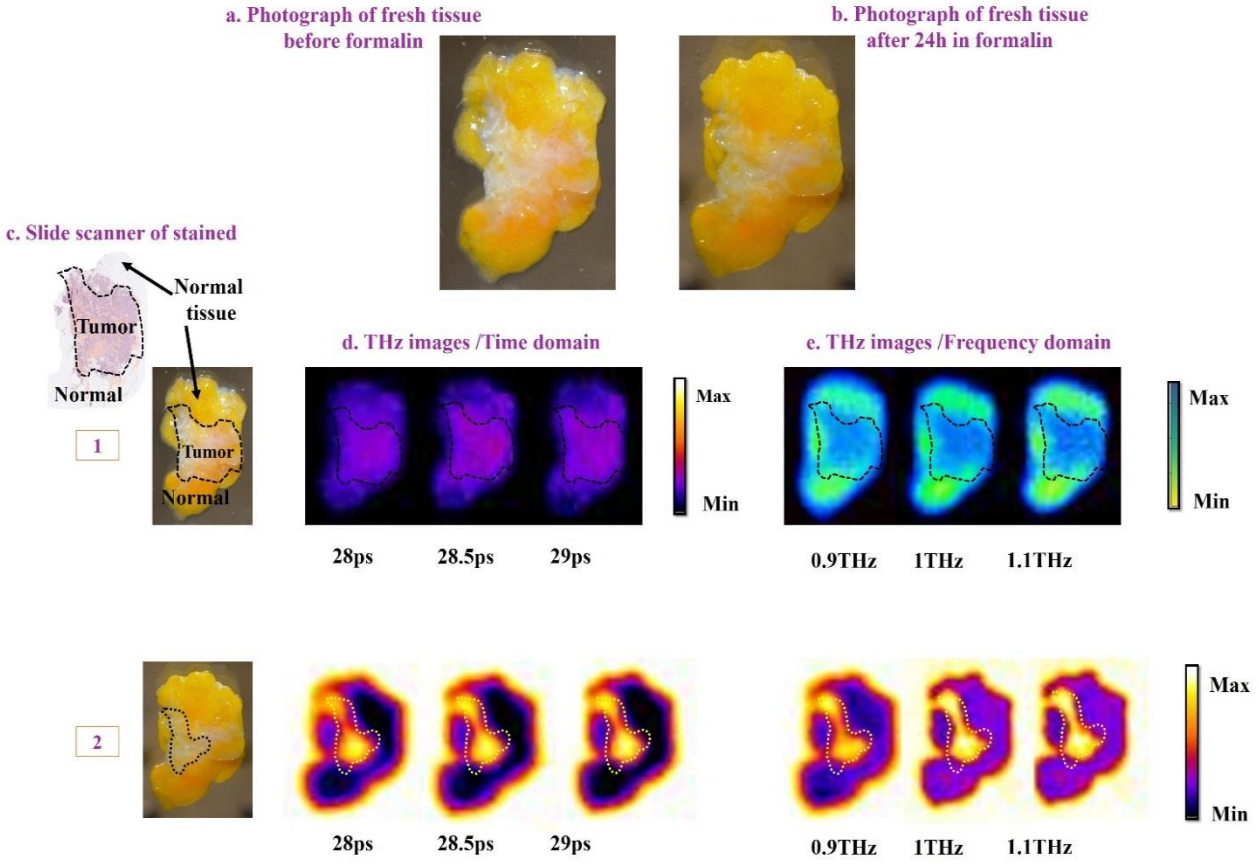

Figure 65: reflection imaging results: a & b) photographs of fresh breast tissue before and after fixing in formalin; c(1 & 2) THz reflected images in the time domain before and after formalin fixing; and d(1 & 2) THz reflected images in the frequency domain before and after formalin fixing.

Figure 65(a & b) show photographs of the fresh breast tissue before and after fixing in formalin for 24h. The white region represents tumor tissue and the yellow region represents normal tissue. These images reveal that formalin affects tissue, leading to shrinkage of the tumor region, possibly due to dehydration. Furthermore, the surface was even more heterogeneous and uneven. On the slide scan of 5 µm-thick stained tissue in Figure

65(c), two different regions were diagnosed by the histopathologist, the blue region represents tumor and white represents normal tissue, showing tumor cells mixed with normal cells

Figure 65(d), rows 1 and 2, show three THz reflected images in fixed positions in the time domain, selected at 28, 28.5, and 29 ps, respectively Figure 65(e), rows 1 and 2, show three THz reflected images of FFT spectrum results, fixed in the frequency domain, selected at 0.9, 1, and 1.1 THz, respectively. The THz time-domain images in row 1 show the fresh tissue before formalin fixing, with two regions: tumor tissue in pink and normal tissue in blue. In the frequency-domain images, blue domain represents tumor tissue and green represents normal tissue. In both images, the amplitude was higher in the tumor region than in normal tissue. The shape of the tumor region was more widespread than in the original photograph. Row 2 shows the THz reflected images of the same fresh tissue, fixed in formalin for 24h. Both time- and frequency-domain images display two colors: tumor tissue in yellow and normal tissue in blue or dark blue. The tumor is in the same location as on the original photograph. Furthermore, the tumor appears smaller in size than on the original photograph. THz images of formalin-fixed tissue show a strong contrast between the tumor and the surrounding normal tissue. As significant amounts of formalin diffuse into the tissue, thus reducing its water content, the dielectric properties of water affect the properties of tumor and normal tissue at frequencies ranging from 0.1 to over 2 THz, as shown in Figure 66 below. This is easily detectable through changes in the THz signal reflected from each region and is largely responsible for the difference in contrast in the reflected THz images of formalin-fixed breast tissues.

5.5. Statistical analysis results: selected THz spectroscopy points on tissue

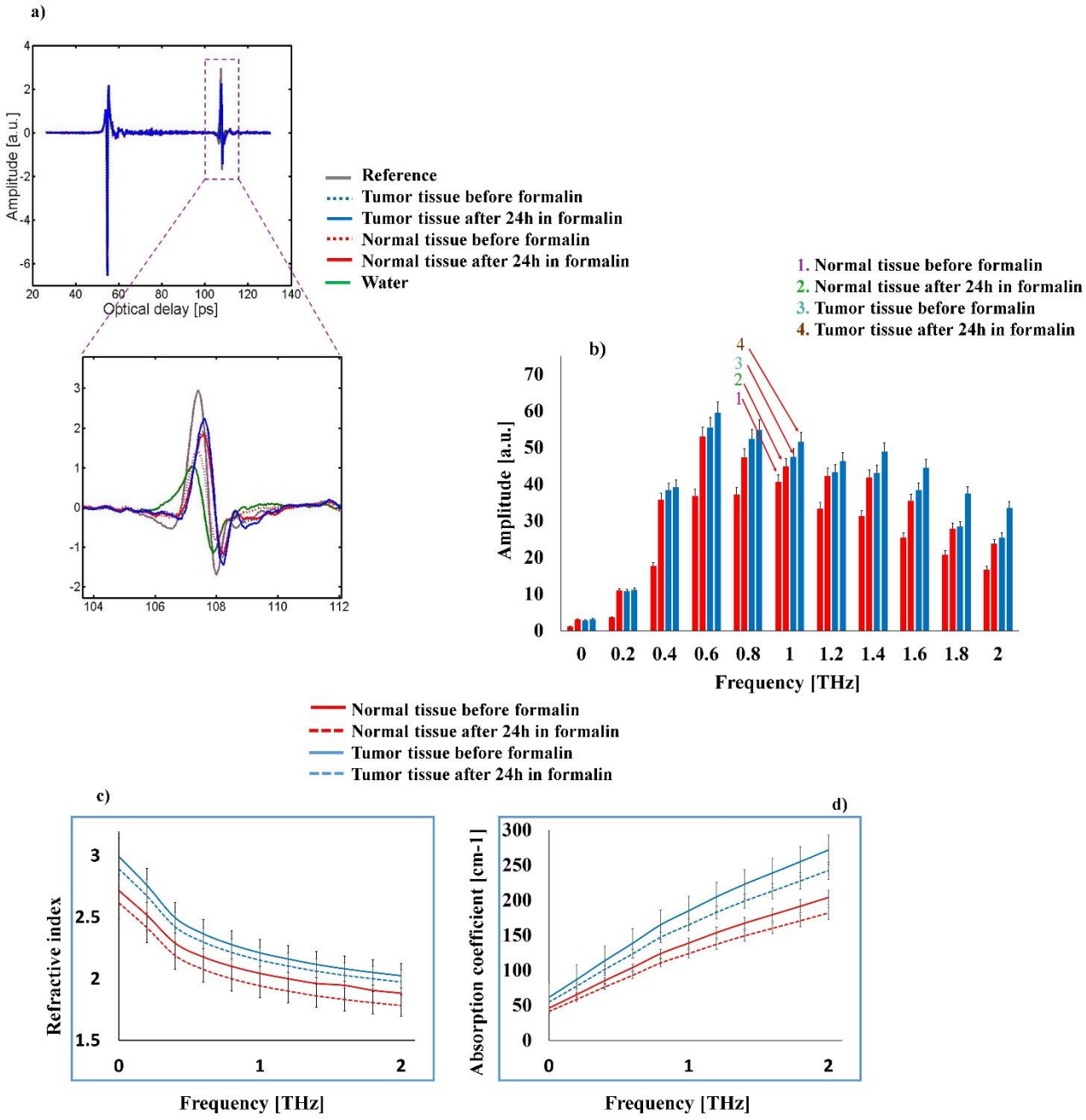

Figure 66: a) THz reflected in time domain; b) average spectrum amplitude with error bar for normal and tumor tissue as a function of frequency; and c & d) average with error bars for refractive index and absorption coefficient of tumor and normal tissue before and after formalin fixing.

Figure 66(a) shows the THz reflected amplitude in the time domain of fresh tissue before and after fixing, compared with the THz reference and water, as a function of time delay, in picoseconds. These pulses were

measured on THz spectra generated by a 4000 Tera Pulse system in reflection mode. The time-domain THz reflected pulses from all samples were collected at three measurement points. The maximum reflected amplitude of the tumor region before fixing was 1.94mV and 2.2mV after 24h in formalin. In normal tissue, the maximum amplitude before formalin fixing was 1.38mV and 1.8mV after 24h in formalin. Furthermore, the amplitudes of both regions were lower compared with the maximum amplitude of the reference, 2.94mV, but higher than that of water, 1.03mV. The time delay differences between the waveforms of fresh and formalin-fixed tissue were similar for all sample regions. For example, the time-delay difference between the normal regions of fresh and formalin-fixed tissue was approximately 0.3 ps, but only 0.1 ps between the tumor regions. These results indicated that the differences in propagation delay between the regions were independent of fixation. In addition, the fixed tissue structure was probed by the THz time-domain signal.

Figure 66(b) shows the average amplitude of tumor and normal tissue before and after fixing in formalin for 24h. Arrows 1 and 3 indicate the normal and tumor tissue before fixing, respectively, and arrows 2 and 4 indicate the normal and tumor tissue after 24h in formalin. A significant difference in amplitude was clearly observed at frequencies ranging from 0.6 to 2 THz. The average values for normal tissue before and after fixing, measured at 1 THz, were 40.6 mV $\pm$ 0.21 and 44.9 mV $\pm$ 0.24, respectively, while the values for tumor tissue before and after fixing, were 47.4 mV $\pm$ 0.26 and 51.5 mV $\pm$ 0.27, respectively. Consequently, the amplitudes of both tumor and normal tissue were lower before than after fixing.

Figure 66(c & d) show the refractive index and absorption coefficient of tumor and healthy tissue over frequencies ranging from 0 to 2 THz, calculated by averaging the data obtained from one pixel in each region, in triplicate. The average data are plotted as error bars. These plots revealed that the refractive index and absorption coefficient of tumor tissue were higher than those of normal tissue. In addition, the refractive index and absorption coefficient of both tumor and normal tissues were lower after fixing. At 1 THz, the refractive index of normal tissue decreased from 2.28 $\pm$ 0.13 to 2.02 $\pm$ 0.06 and the absorption coefficient from 140.6 $\pm$ 10 cm^{-1} to 120 $\pm$ 9 cm^{-1}. The refractive index of tumor tissue decreased from 2.38 $\pm$ 0.15 to 2.1 $\pm$ 0.10 and its absorption coefficient from 190 $\pm$ 10 cm^{-1} to 164 $\pm$ 11 cm^{-1}, possibly due to the dehydrating effect of formalin. The significant differences between these data in this frequency range explain the variations in THz signals reflected from tumor and normal tissue before and after fixing, making it possible to discriminate between them. This is illustrated in Figure 67(a & b) below, which presents a quantitative analysis of the refractive index and absorption coefficient at 1 THz of tumor and normal tissue.

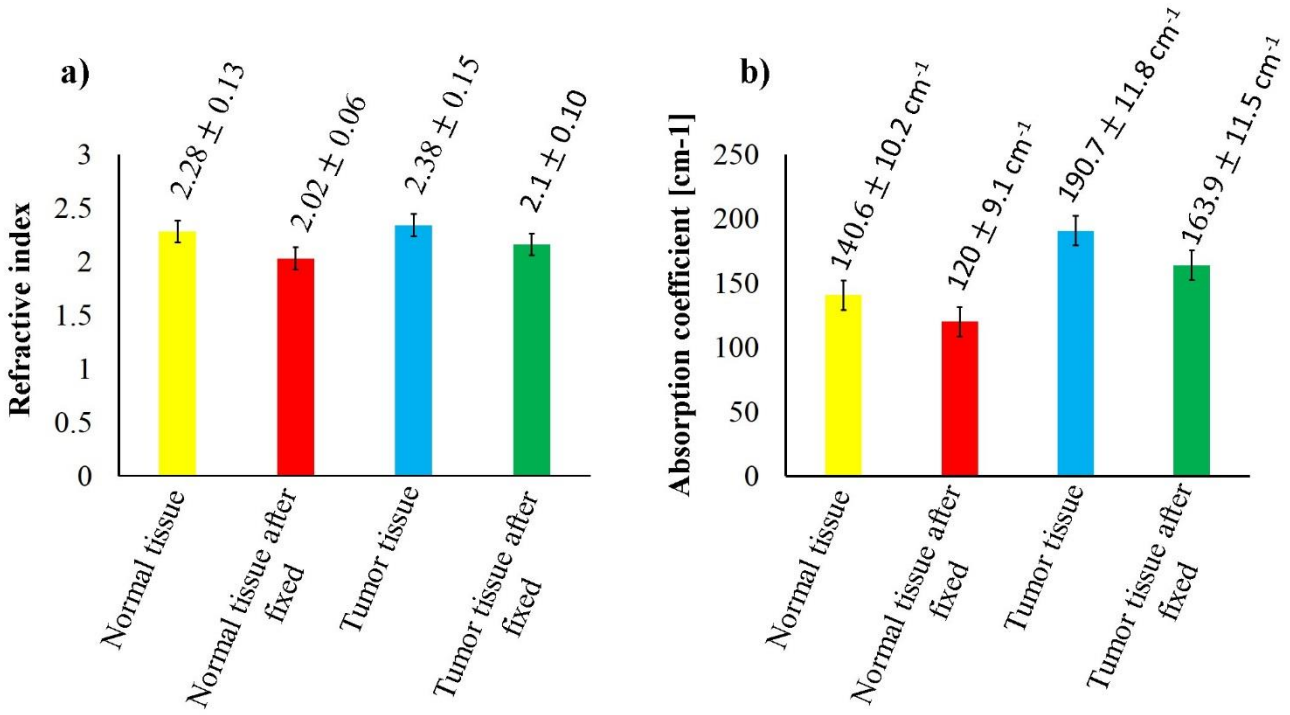

Figure 67: Comparison of average results, with error bar, for normal and tumor tissue, before and after formalin fixing: at 1 THz; a) refractive indices and b) absorption coefficients.

5.6. Comparison of results from paraffin-fixed, fresh, and formalin-fixed tissue

The differences in contrast on THz images of paraffin fixed, fresh, and formalin-fixed tissue in the time and frequency domains were more marked in transmission than reflection mode. In addition, the time delay in THz reflected waveforms from different sample regions varied according to the thickness and properties of the tissue and substrate.

Finally, these results revealed significant differences in contrast between the spectroscopic information from stained and non-stained tissue that had been subjected to a histological process and unprocessed, fresh tissue. However, not all results were significant: in reflection mode, 20 µm-thick paraffin-fixed tissue on a 1 mm-thick microscope slide did not produce any response, as shown in Figure 50 (f & g). If one have only paraffin embedded samples, its preferable to image in transmission thick samples (more than 30µm) deposited on a transparent material such as silica or sapphire.

5.7. Summary and discussion

5.7.1. Summary

In summary, THz images of paraffin-embedded, formalin-fixed, and fresh breast cancer tissues were made and analyzed, using the experimental results from the 3000 Teraview and 4000 Tera Pulse in transmission and reflection modes. Fifty-one sections of breast cancer tissue with different tumor grades were investigated, in view of their histologic background, over the 0.2- 2 THz range.

- The results revealed that 20 µm, 30 µm, 1 mm, 2 mm, and 3 mm thick tumors were detectable with a margin of normal tissue.
- Using the THz system in reflection mode on the fresh tissue provided clearer images than paraffin-embedded tissue. In addition, when the formalin-fixed tissue was compared to fresh tissue, the THz images showed stronger contrast in time- and frequency-domain amplitude, indicating that the breast tissue became more transparent to THz radiation after fixing in formalin. For example, at 1 THz, the reflected amplitude after fixation was 54% higher for normal regions and 56% for tumor regions, as shown in Figure 66(b). The tumor location was still clearly indicated, although its size had decreased compared to measurements on fresh tissue, due to the effect of formalin, (shown in Figure 65 row 2).
- Formalin diffusion into the tissue section deteriorated the tissue structure, causing cell shrinkage and distortion of the breast tumor. This is unfortunate, as tumor size is important in breast cancer staging. Although most pathologists report tumor size after histopathological processing (fixation) or microscope examination, breast cancer staging should be based on fresh tissue measurements, especially for small tumors.
- A comparison of microscopic data on stained tissue and THz images of paraffin-embedded tissue in the time and frequency domains also clearly revealed significantly stronger contrast between cancer, fiber, and fatty tissue in the latter. Moreover, tumor size and location in paraffin-embedded tissue qualitatively matched those on the stained tissue image. This confirmed the feasibility of using paraffin-embedded tissues for cancer detection by THz imaging (with minor practical interest).
- Transmission imaging was more effective than reflection imaging for distinguishing between tissue regions, perhaps due to low-amplitude differences in their response. Furthermore, the contrast between different tissue regions reflected the dispersion properties of the tissue and substrate. In addition, reflected imaging was highly sensitive to the experimental procedure and protocols (sample positioning, parallelism onto the substrate etc).
- The THz reflection imaging results for paraffin-block (breast tissue) presented above revealed small variations in contrast between different tissue regions over the frequency range. In addition, the tumor

location was possible to distinguish from fatty and fiber tissue, as shown in Figure 62(c & d). In reflection mode, the images did not show a clear distinction between regions with heterogeneous thickness in the same sample, due to weak THz reflection.

- From the THz images, it was concluded that it is difficult to discriminate between the normal and tumor regions of breast tissue in either the time or frequency domains.
- Consequently, the optical properties of fresh normal and tumor tissue were also examined before and after formalin fixing, using broadband THz radiation, as shown in Figure 66(c & d), and a number of measurements were proposed. At 1 THz, the refractive index and absorption coefficient after fixation decreased significantly from 55% to 48% for normal regions and 57.2% to 50% for tumor regions.
- Finally, the measured response of a sample depends on its own properties and those of the substrate. Tumor and normal tissue have different dielectric properties in the THz bandwidth, producing different natural responses, and this factor is important for discriminating between them. Therefore, these results confirmed that the THz technique was effective for detecting tumors, despite the challenges presented by the complex structure, heterogeneous thickness, and uneven surface of breast tissue. This encouraged us to develop and the implement a THz technique for medical application to understand the effect of different breast tissue regions on THz propagation.

Analysis of the breast tissue rely on the measurements of complex dielectric response such as refractive indices, and absorption coefficients. We can determined them and compared the different breast tissue regions on the THz images. We should be noted that data calibration is crucial to achieve accurate results. Consequently, these results confirmed that spectroscopy and imaging using THz radiation at the bandwidth of frequencies tested were capable of producing sufficient contrast to distinguish cancer regions from fiber and fatty regions. This is significant, as the cancer margin detected may influence a histopathological decision on patient surgery, or even result in a missed cancer.

5.7.2. Discussion

In conclusion, we presented the development and the use of a THz spectroscopy and imaging technique in both transmission and reflection modes for breast cancer detection and compared the results with the slide-mounted tissue samples. The parameters selected for measuring by the THz technique were dependent on system and sample type, acquisition time, step size, and scan area.

The accuracy of THz spectroscopy and imaging varied among the different types of complex excised breast tissues and substrate materials used in this study. These differences may be due to scattering effects or the interaction of THz radiation with samples and substrates (Chapter 2). However, THz spectroscopy and imaging has several potential advantages:

- After a quite long acquisition time, data extraction is rapid (30 min) and easy compared with the preparation of clinical reports.
- The technique does not involve contact with the excised biological tissue.

THz spectroscopy was capable of discriminating between diseased and healthy tissue, with a margin for breast tissue depending on the wavelength. However, some remaining problems, limitations, and challenges in applying THz spectroscopy and imaging to breast tissue were due to:

- The complex composition of breast tissues, with less homogenous, uneven surfaces, and dielectric properties that varied from one sample to another, as well as between different regions in the same section.
- Ageing of tissues during acquisition.
- The type of substrates used.

Our findings provide proof of concept on the use of THz spectroscopy and imaging to measure the physical properties of breast samples and discriminate between healthy and diseased tissue. In addition, they demonstrate how complex breast tissue, with its uneven surface and subsurface, can be imaged and detected in THz transmission and reflection modes. We also assessed the effectiveness of each mode for identifying cancerous regions and distinguishing them from fiber and adipose tissues. THz beams penetrate excised breast tissue to submillimeter depths without contact, providing more detailed information about the characteristics of various tissue regions. It is possible to analyze samples of different thicknesses and types (fresh, fixed, and block), as well as heterogeneous samples, using the THz technique, and extract relevant data. Furthermore, it is also useful for evaluating whether an excised tissue region has been chemically or physically altered by measuring its dielectric complex, refractive index, and absorption coefficient spectrum.

It was more difficult to measure the samples in reflection than transmission mode, due to a number of factors, including:

- Sample thickness: measurement was more difficult with thinner samples, as scanning affected their refractive index and absorption coefficient.
- THz scattering and the front and back reflection produced weak, oscillating signals (artefact).
- Accurate positioning of the sample with respect to the reference signal

The effectiveness of this technique on tissue was determined by recording THz signals from different regions of excised breast tissue and using the data to calculate the refractive index and absorption coefficient of each region. The next step was to estimate where high absorption on the THz spectrum coincided with high refractive indices for breast tissue regions.

Sections of breast tissue (fresh, paraffin-embedded, and formalin-fixed) containing cancer, fiber, and adipose regions were examined using both THz transmission and reflection techniques. Tumor regions in breast tissue

were also detected in the time domain by measuring the THz amplitude reflected through the thickness of a breast tissue section, as shown in Figure 64, section 5.4.4.

Finally, the THz technique was used to extract and compare the results of cancer, fiber, and adipose tissues, with and without water, and detect breast cancer, by analyzing fresh tissue and samples fixed in formalin, which contained water. This confirmed that the refractive indices and absorption coefficients of cancer regions were higher than those of other regions in all samples, as cancer regions propagated THz radiation more efficiently than fiber or adipose regions. This was due to the higher water content of cancerous tissues, which provided clearer contrast in the THz images, thus confirming the refractive index and absorption coefficient findings.

As the biological architecture of breast tissue is different from one sample to the other, the light-tissue interaction is complex and difficult to physically quantify. Also, the heterogeneity of the tissue and the varying beam size with frequency are both additional complications. Nevertheless, the effective refractive index has been extracted and averaged from different tissues over several locations and has been reported. Approximately 34,000 waveforms have been collected from the samples analyzed. The results are shown considering the mixture of tissue presented by the measurement area and are compared with both the optical view and the histology slide. After correlation with the optical image and the stained slice, we have estimated a deviation of +/- 2 pixels with respect to the step sizes in X and Y directions. Then, we selected the pixels where there was no ambiguity about the nature of the tissue. Interesting results indicate that in the 300 – 600 GHz range, the refractive index of Cancer / Fiber regions differs from adipose / fibers regions and pure fatty tissue. The refractive index resulting from a spectroscopic measurement is always higher than the one extracted for other tissue mixtures. A significant difference can be observed in the 300 – 600 GHz band. The extracted optical indices are in good agreement with published data. There is no clear evidence that the cancer type and grade play a significant role on the refractive index value. We are currently investigating a solution to propose for each sample a linear equation describing the contribution of each tissue response, on the basis of Bruggeman distribution. However, results may suggest the ability of THz spectroscopy to differentiate the margins from surrounding fibro glandular tissue and fat within the 300 – 600 GHz. A wider set of tests is however needed to draw further conclusions. Similar tendencies were also observed for assessing breast carcinoma in excised paraffin-embedded human breast tissue in both transmission and reflection imaging. However, one should highlight that the histology slides used to correlate the THz images with tissue regions are 5 µm thick. The opto-biological interaction depth is assumed to range between 20 µm and 50µm. Thus, another approach considering the whole histology slide stack along the penetration depth would be beneficial to assess tissue heterogeneity in depth.

CONCLUSION

6. General conclusion and perspectives

This chapter presents a summary of the findings presented in the previous chapters and provides some suggestions for future work, indicating the potential to develop efficient biomedical applications based on THz reflection and transmission techniques in the time and frequency domains.

This study used THz spectroscopy and imaging to detect breast cancer tissue and discriminate between tumor and normal tissue, thus helping surgeons to remove the cancer with a precise margin of normal tissue. The THz reflection and transmission techniques described in Chapter 2 revealed the high potential of THz radiation, a non-contact, non-ionizing technique, for analyzing biological tissue. The imaging and spectral data obtained, especially for breast cancer samples, confirmed its potential for tumor detection, compared to the technologies currently used, such as X-ray and MRI examinations.

The potential of terahertz technology in breast cancer detection was highlighted by performing THz spectroscopy and imaging in reflection and transmission modes, a basic experimental method using time-domain waveform acquisition and frequency-domain by Fast Fourier Transform, in the 0 - 3 THz frequency band using the 3000 Tera-View and 0 - 4THz using the 4000 Tera-Pulse system. This technique demonstrated its sensitivity to cancer tissue, by providing sufficiently-accurate, automated THz images to assist the histopathologist in diagnosing breast cancer and reducing the time required, compared with the usual histopathology report.

An ex-vivo study was performed, applying THz spectroscopy and imaging analysis to several types and grades of breast cancer tissue. Paraffin-embedded tissues, blocks, fresh, and formalin-fixed tissues, including tumors adjacent to healthy tissue, were subjected to THz spectroscopy and imaging. The results indicated that it was possible to analyze these types of specimens at acquisition frequencies from 0.1 to 2 THz, successfully obtaining THz images in the time and frequency domains, and demonstrating the significant contrast of the THz images. The breast cancer tissue images obtained, using the appropriate tissue sections and image processing tool, clearly revealed the cancer margin. The results presented above clearly demonstrated the applicability of THz imaging and spectroscopy to biomedical analysis. This THz technology provided highly-sensitive cancer margin identification, using electromagnetic waves in the THz range.

Cancer was detected in breast tissue by THz imaging thanks to the contrast between THz waves transmitted or reflected from tumor regions in breast tissue, compared to fiber and fatty tissue. This THz technique successfully provided data on breast cancer, fiber, and fatty tissue (both fixed in formalin and fresh, containing

water) to create the first database in France on THz responses of biological tissue. In addition, THz imaging was used to obtain reflection and transmission measurements on the same paraffin-embedded tissue samples (without water), distinguishing between different tissue regions mounted on different types of substrate: coverslip, sapphire window, and silica. The results of both modes were in good agreement. In addition, it was possible to distinguish a cancer region in a tissue block (with difficulty), as well as obtaining sufficiently accurate reflection imaging on fresh and formalin-fixed tissue, mounted between double sapphire windows, to distinguish between tumor and normal tissues. Thanks to the Bergonié Cancer Institute, we had the opportunity to use reflection THz imaging and spectroscopy in the Department of pathology to study ex-vivo human breast tissue at [0.1- 4THz]. Automated Image processing reduced the time to display the best contrasted image as possible, facilitating cancer detection. Three image processing methods were used (slice, automated, and manual) to visualize the data and apply discriminant analysis to the image. This revealed greater detail in the cancer, fiber, and fatty tissue regions, as illustrated in Chapter 5.

Furthermore, we demonstrated that THz spectroscopy analysis was capable of detecting breast cancer in samples from patients of different ages and weights, as well as different tumor grades, distinguishing it from normal tissue by its higher refractive indices and absorption coefficients. The tissue measurements were very sensitive and could vary with time: The repeatability is altered with biomedical samples: We observed that a variation in tissue measurements occurred when the measuring location was moved from one point to another in the same region, leading to a change in signals and spectra.

In addition, the differences in refractive indices and absorption coefficients compared to measurements from each region of tissue were due to the varying densities and uneven surfaces of the samples. This led to big variance in results, even considering the average of repeated measurements taken at several points.

Hence, this study presents the fundamental physics behind the complex dielectric of liquids and biological tissues, measured using the THz technique. The data were supported by a fit with the Debye relaxation coefficient model. In this model, the real and imaginary parts were calculated and experimental data fitted by making broadband measurements using water, methanol, lipid, fiber, and cancer samples. The purpose of this study was to determine whether THz spectroscopy was sufficiently accurate to determine the dielectric behavior and optical properties of biological tissues and liquids over a broad range of frequencies. These experiments revealed that the THz system was sufficiently sensitive to measure THz signals and analyze the composition of the liquids and biological tissues by the spectral average of their optical properties, dielectric complexes, and Debye relaxation coefficient model. Furthermore, THz reflection spectroscopy was found to have great potential in measuring the reflected spectra and dielectric properties of liquids at different concentrations.

In this pilot study we also focused on the ability of the under-exploited 300-600 GHz frequency band to differentiate between breast tissue types. To do so, a far-field reflection geometry THz imaging system was

situated in the Department of Pathology at Bergonié Institute, the oncology laboratory partner. Freshly excised breast tissue samples have been collected and analyzed in view of their responses within the 300 – 600 GHz narrow frequency window. The refractive index of these tissues was calculated and compared between each other at several frequencies. Our results confirm the tendency for tissue matrices containing malignant cells to exhibit a higher mean refractive index than the ones consisting of healthy tissues. Such a difference is observed over the studied frequency band. THz-images have also been produced; in the majority of them, a quite good optical correlation between histology slides and THz-delimitated area is observed. However in order to increase the efficiency of such measurements, a THz near-field imaging matrix array is under study and will be deployed to assess, with greater resolution, higher speed and lower cost breast tissue classification.

Overall, terahertz technology performed well in medical applications for breast cancer detection and these successful dielectric measurements may be used to determine the cancer cell concentration in the samples. In addition, these non-destructive dielectric measurements at terahertz frequencies may be complementary to low-frequency measurements of cancer cell concentrations. Furthermore, THz images of breast tissue in a comparative study with MRI, X-ray, and fluorescence microscopy study are likely to provide complementary information for identifying breast cancer.

Concerning future perspectives, terahertz spectroscopy is clearly not ready to be implemented in a clinical tool. More work is needed to clarify the interaction of terahertz radiation with biological tissues at micro and macro levels. Moreover, our studies showed that we could find statistical differences even in healthy tissue. One of the next steps could be the qualitative and quantitative extraction of the different parts of a tissue such as fibrosis and adipose. This could be initially developed with tissue phantom spectroscopy and chemometric tools.

Secondly, further knowledge is required of the interaction of THz radiation with tissue, possibly by analyzing the response at the cell level. To achieve this aim, we are working on the development of near-field sensor capable of distinguishing cells from fibers and the means to implement this new type of imaging sensor.

REFERENCES

[1] J. P. Guillet, B. Recur, L. Frederique, B. Bousquet, I. Manek-hönninger, P. Desbarats, P. Mounaix, J. P. Guillet, B. Recur, L. Frederique, B. Bousquet, and L. Canioni, "Review of Terahertz Tomography Techniques," *J. Infrared, Millimeter, Terahertz Waves*, vol. 35, no. 4, pp. 0–30, 2014.

[2] F. Zhang, H. W. Wang, K. Tominaga, M. Hayashi, T. Hasunuma, and A. Kondo, "Application of THz Vibrational Spectroscopy to Molecular Characterization and the Theoretical Fundamentals: An Illustration Using Saccharide Molecules," *Chem. - An Asian J.*, vol. 12, no. 3, pp. 324–331, 2017.

[3] D. K. George, A. Charkhesht, and N. Q. Vinh, "New terahertz dielectric spectroscopy for the study of aqueous solutions," *Rev. Sci. Instrum.*, vol. 12, no. 86, pp. 123105–6, 2015.

[4] P. H. Siegel, "Terahertz Technology in Biology and Medicine," vol. 52, no. 10, pp. 2438–2447, 2004.

[5] D. D. Arnone, C. M. Ciesla, A. Corchia, S. Egusa, M. Pepper, J. M. Chamberlain, C. Bezant, E. H. Linfield, R. Clothier, and N. Khammo, "Applications of terahertz (THz) technology to medical imaging," vol. 3828, no. June, p. 209, 1999.

[6] K. Kawase, "Terahertz imaging for drug detection and large scale integrated circuit inspection," *Opt. Photonics News*, vol. 15, no. October, pp. 34–39, 2004.

[7] R. M. Woodward, B. E. Cole, V. P. Wallace, R. J. Pye, D. D. Arnone, E. H. Linfield, and M. Pepper, "Terahertz pulse imaging in reflection geometry of human skin cancer and skin tissue.," *Phys. Med. Biol.*, vol. 47, no. 21, pp. 3853–3863, 2002.

[8] V. P. Wallace, A. J. Fitzgerald, E. Pickwell, R. J. Pye, P. F. Taday, N. Flanagan, and H. A. Thomas, "Terahertz pulsed spectroscopy of human basal cell carcinoma," *Appl. Spectrosc.*, vol. 60, no. 10, pp. 1127–1133, 2006.

[9] Y. Miura, A. Kamataki, M. Uzuki, T. Sasaki, J. Nishizawa, and T. Sawai, "Terahertz-wave spectroscopy for precise histopathological imaging of tumor and non-tumor lesions in paraffin sections," *Tohoku J. Exp. Med.*, vol. 223, pp. 291–296, 2011.

[10] A. J. Fitzgerald, V. P. Wallace, M. Jimenez-linan, L. Bobrow, R. J. Pye, and A. D. Purushotham, "Terahertz Pulsed Imaging of human breast tumors," *Radiology*, vol. 239, no. 2, pp. 533–540, 2006.

[11] P. Haring Bolivar, M. Brucherseifer, M. Nagel, H. Kurz, A. Bosserhoff, and R. Büttner, "Label-free probing of genes by time-domain terahertz sensing.," *Phys. Med. Biol.*, vol. 47, no. 21, pp. 3815–3821, 2002.

[12] D. B. B. Zachary D. Taylor, Rahul S. Singh and W. S. G. Priyamvada Tewari, Colin P. Kealey, Neha Bajwa, Martin O. Culjat, Alexander Stojadinovic, Hua Lee, Jean-Pierre Hubschman, Elliott R. Brown, "THz Medical Imaging : in vivo Hydration Sensing THz Medical Imaging : in vivo Hydration Sensing," *IEEE Trans. Terahertz Sci. Technol.*, vol. 1, no. 1, pp. 201–219, 2011.

[13] C. B. Reid, A. Fitzgerald, G. Reese, R. Goldin, P. Tekkis, P. S. O'Kelly, E. Pickwell-MacPherson, A. P. Gibson, and V. P. Wallace, "Terahertz pulsed imaging of freshly excised human colonic tissues.," *Phys. Med. Biol.*, vol. 56, pp. 4333–4353, 2011.

[14] M. Tonouchi, "Cutting-edge terahertz technology," *Nat. Photonics*, vol. 1, no. March, pp. 97–105, 2007.

[15] J. B. Jackson, M. Mourou, J. F. Whitaker, I. N. Duling, S. L. Williamson, M. Menu, and G. A. Mourou, "Terahertz imaging for non-destructive evaluation of mural paintings," *Opt. Commun.*, vol. 281, no. 4, pp. 527–532, 2008.

[16] J. M. Delagnes and P. Mounaix, "Non-invasive investigation of art paintings by terahertz imaging," *Appl. Phys. A*, 2010.

[17] M. R. Leahy-Hoppa, "Terahertz for weapon and explosive detection," *WIT Trans. State Art Sci. Eng.*, vol. 54, pp. 1–14, 2012.

[18] K. Kawase, Y. Ogawa, and Y. Watanabe, "Non-destructive terahertz imaging of illicit drugs using spectral fingerprints," *Opt. Express*, vol. 11, no. 20, pp. 2549–2554, 2003.

[19] T. Y. B. Owman, M. A. E. L. Henawee, and L. U. K. C. Ampbell, "Terahertz transmission vs reflection imaging and model-based characterization for excised breast carcinomas," *Biomed. Opt. Express*, vol. 7, no. 9, pp. 7587–7596, 2016.

[20] S. R. Tripathi, E. Miyata, P. Ben Ishai, and K. Kawase, "Morphology of human sweat ducts

observed by optical coherence tomography and their frequency of resonance in the terahertz frequency region," *Sci. Rep.*, vol. 5, no. 1, pp. 1–7, 2015.

[21] E. Curry, S. Fabbri, P. Musumeci, and A. Gover, "THz based phase space manipulation in a zero-slippage IFEL," *physics.acc-ph*, vol. 18, no. 11, pp. 1–18, 2016.

[22] G. J. Wilmink and J. E. Grundt, "Invited review article: Current state of research on biological effects of terahertz radiation," *J. Infrared, Millimeter, Terahertz Waves*, vol. 32, pp. 1074–1122, 2011.

[23] H. Z. Zhanke Yan, Yibin Ying and H. Yu, "Research progress of terahertz wave technology in food inspection," *Soc. Int. Eng. Opt.*, vol. 6373, pp. 63730R–1–63730R–10, 2006.

[24] B. T. Kearney, "Enhancing microbolometer performance at terahertz frequencies with metamaterial absorbers," Naval Postgraduate school, 2013.

[25] M. Walther, "Modern Spectroscopy on biological molecules," 2003.

[26] C. Yu, S. Fan, Y. Sun, and E. Pickwell-Macpherson, "The potential of terahertz imaging for cancer diagnosis: A review of investigations to date," *Quantitative imaging in medicine and surgery*, vol. 2. pp. 33–45, 2012.

[27] R. H. Clothier and N. Bourne, "Effects of THz exposure on human primary keratinocyte differentiation and viability," *J. Biol. Phys.*, vol. 29, no. 2–3, pp. 179–185, 2003.

[28] O. Zeni, G. P. Gallerano, A. Perrotta, M. Romano, A. Sannino, M. Sarti, M. D???Arienzo, A. Doria, E. Giovenale, A. Lai, G. Messina, and M. R. Scarf, "cytogenetic observations in human peripheral blood leukocytes following in vitro exposure to thz radiation: a pilot study," *Health Phys.*, vol. 92, no. 4, pp. 349–357, 2007.

[29] B. Şenel, K. Kamburoğlu, O.¨ Üçok, S. P. Yüksel, T. Özen, and H. Avsever, "Diagnostic accuracy of different imaging modalities in detection of proximal caries," *Dentomaxillofacial Radiol.*, vol. 39, no. 8, pp. 501–511, 2010.

[30] C. Longbottom, D. A. Crawley, B. E. Cole, D. D. Arnone, V. P. Wallace, and M. Pepper, "Potential uses of terahertz pulse imaging in dentistry: caries and erosion detection," *Proc. SPIE*, vol. 4610, p. 109, 2002.

[31] D. Crawley, C. Longbottom, V. P. Wallace, B. Cole, D. Arnone, and M. Pepper, "Three-dimensional terahertz pulse imaging of dental tissue," *J. Biomed. Opt.*, vol. 8, no. 2, pp. 303–

7, 2003.

[32] Y. Sun, M. Y. Sy, Y.-X. J. Wang, A. T. Ahuja, Y.-T. Zhang, and E. Pickwell-Macpherson, "A promising diagnostic method: Terahertz pulsed imaging and spectroscopy," *World J. Radiol.*, vol. 3, no. 3, pp. 55–65, 2011.

[33] Y. C. Sim, I. Maeng, and J. H. Son, "Frequency-dependent characteristics of terahertz radiation on the enamel and dentin of human tooth," *Curr. Appl. Phys.*, vol. 9, no. 5, pp. 946–949, 2009.

[34] B. Karagoz, H. Altan, and K. Kamburoglu, "Terahertz pulsed imaging study of dental caries," *SPIE Proc. Laser Treat. Monit. Feed. Control*, vol. 9542, pp. 95420N–8, 2015.

[35] K. Kamburoğlu, N. Ö. Yetimoĝlu, and H. Altan, "Characterization of primary and permanent teeth using terahertz spectroscopy," *Dentomaxillofacial Radiol.*, vol. 43, pp. 1–6, 2014.

[36] M. Schwerdtfeger, S. Lippert, M. Koch, A. Berg, S. Katletz, and K. Wiesauer, "Terahertz time-domain spectroscopy for monitoring the curing of dental composites," *Biomed. Opt. Express*, vol. 3, no. 11, pp. 1–9, 2012.

[37] E. Pickwell, B. E. Cole, A. J. Fitzgerald, M. Pepper, and V. P. Wallace, "*In vivo* study of human skin using pulsed terahertz radiation," *Phys. Med. Biol.*, vol. 49, no. 9, pp. 1595–1607, 2004.

[38] A. Baroni, E. Buommino, V. De Gregorio, E. Ruocco, V. Ruocco, and R. Wolf, "Structure and function of the epidermis related to barrier properties," *Clin. Dermatol.*, vol. 30, no. 3, pp. 257–262, 2012.

[39] T. Lister, P. A. Wright, P. H. Chappell, T. Lister, P. A. Wright, and P. H. Chappell, "Optical properties of human skin," *J. Biomed. Opt.*, vol. 17, no. 9, pp. 1–16, 2012.

[40] R. R. Anderson and J. A. Parrish, "The Optics of Human Skin," *J. Invest. Dermatol.*, vol. 77, no. 1, pp. 13–19, 1981.

[41] M. a Hurt, "'Animal-type Melanoma' and 'Entities' Related to It: Exegesis of a Subject Until Now Incomprehensible. Contrary View on Behalf of Patients," *Am. J. Dermatopathol.*, vol. 29, no. 6, pp. 597–598, 2007.

[42] M. I. Liddington and P. G. Shakespeare, "Timing of the thermographic assessment of burns," *Burns*, vol. 22, no. 1, pp. 26–28, 1996.

[43] N. J. Prindeze, P. Fathi, M. J. Mino, N. A. Mauskar, T. E. Travis, D. W. Paul, L. T. Moffatt, and J. W. Shupp, "Examination of the Early Diagnostic Applicability of Active Dynamic Thermography for Burn Wound Depth Assessment and Concept Analysis," *J. Burn Care Res.*, vol. 36, no. 6, pp. 626–635, 2015.

[44] R. Bogue, "Terahertz imaging: a report on progress," *Sens. Rev.*, vol. 29, no. 1, pp. 6–12, 2009.

[45] R. Gómez and L. C. Cancio, "Management of Burn Wounds in the Emergency Department," *Emerg. Med. Clin. North Am.*, vol. 25, no. 1, pp. 135–146, 2007.

[46] M. H. Arbab, D. P. Winebrenner, T. C. Dickey, A. Chen, M. B. Klein, and P. D. Mourad, "Terahertz spectroscopy for the assessment of burn injuries in vivo," *J. Biomed. Opt.*, vol. 18, no. 7, pp. 77004–7, 2013.

[47] P. Tewari, C. P. Kealey, D. B. Bennett, N. Bajwa, K. S. Barnett, R. S. Singh, M. O. Culjat, A. Stojadinovic, W. S. Grundfest, and Z. D. Taylor, "In vivo terahertz imaging of rat skin burns," *J. Biomed. Opt.*, vol. 17, no. 4, pp. 40503–3, 2012.

[48] A. C. M. Hassan Arbab, Trevor C. Dickey, Dale P. Winebrenner, M. B. Klein, and and P. D. Mourad, "Terahertz reflectometry of burn wounds in a rat model," *J. Surg. Res. Biomed. Opt. EXPRESS IEEE Trans. Microw. Theory Tech. J. Phys. D Appl. Phys. Biol. Phys. Appl. Phys. Lett. Phys. Med. Biol. Appl. Phys. B Reflective J. Phys. Chem*, vol. 40, no. 10024, pp. 475–481, 2011.

[49] M. I. Sulatsky, E. A. Strepitov, O. A. Smolyanskaya, M. K. Khodzitskiy, I. V Prozheev, E. L. Odlyanitskiy, A. G. Zabolotniy, and I. A. Geyko, "Analysis of Spectral Characteristics of the Human Cornea Obtained in the Terahertz Frequency Range," *PIERS Proceedings, Guangzhou, China, August 25–28*, pp. 1532–1535, 2014.

[50] D. B. Bennett, Z. D. Taylor, P. Tewari, R. S. Singh, M. O. Culjat, W. S. Grundfest, D. J. Sassoon, R. D. Johnson, J.-P. Hubschman, and E. R. Brown, "Terahertz sensing in corneal tissues," *J. Biomed. Opt.*, vol. 16, no. 5, pp. 57003–7, 2011.

[51] S. Koyama, E. Narita, Y. Shimizu, T. Shiina, M. Taki, N. Shinohara, and J. Miyakoshi, "Twenty four-hour exposure to a 0.12 THz electromagnetic field does not affect the genotoxicity, morphological changes, or expression of heat shock protein in HCE-T cells," *Int. J. Environ. Res. Public Health*, vol. 13, no. 793, pp. 1–9, 2016.

[52] D. Bennett, M. Culjat, J. Hubschman, and E. Brown, “Assessment of corneal hydration sensing in the terahertz band : in vivo results at 100 GHz,” *J. Biomed. Opt.*, vol. 17, no. 9, pp. 97008–7, 2012.

[53] D. C. Shin, J. M. Park, G. B. Jung, J. H. Shin, C. S. Kee, C. Kang, and J. W. Lee, “Polarization-dependent properties of human scleral tissues at terahertz frequencies,” *Opt. Soc. Am.*, vol. 3, no. 27p, pp. 1–2, 2016.

[54] S. N. Sakhnov, E. V. Leksutkina, O. a. Smolyanskaya, a. V. Usov, S. E. Parakhuda, Y. V. Grachev, and S. a. Kozlov, “Application of femtotechnologies and terahertz spectroscopy methods in cataract diagnostics,” *Opt. Spectrosc.*, vol. 111, no. 2, pp. 257–261, 2011.

[55] The free encyclopedia Cancer - Wikipedia, “Cancer - Wikipedia, the free encyclopedia.” 2012.

[56] National Cancer Institute, “What Is Cancer? - National Cancer Institute.” .

[57] National Cancer (NCI), “Metastatic Cancer Fact Sheet - National Cancer Institute.” .

[58] P. Anand, A. B. Kunnumakara, C. Sundaram, K. B. Harikumar, S. T. Tharakan, O. S. Lai, B. Sung, and B. B. Aggarwal, “Cancer is a preventable disease that requires major lifestyle changes,” *Pharm. Res.*, vol. 25, no. 9, pp. 2097–2116, 2008.

[59] American Cancer Society, “Cancer Staging Fact Sheet - National Cancer Institute.” 2013.

[60] A. M. Scott, J. P. Allison, J. D. Wolchok, and H. Hughes, “Monoclonal antibodies in cancer therapy,” *cancer Immun.*, vol. 12, pp. 1–8, 2012.

[61] S. J. Oh, S.-H. Kim, Y. Bin Ji, K. Jeong, Y. Park, J. Yang, D. W. Park, S. K. Noh, S.-G. Kang, Y.-M. Huh, J.-H. Son, and J.-S. Suh, “Study of freshly excised brain tissues using terahertz imaging,” *Biomed. Opt. Express*, vol. 5, no. 8, pp. 2837–42, 2014.

[62] H. Hoshina, S. Nakajima, M. Yamashita, C. Otani, and N. Miyoshi, “Terahertz imaging diagnostics of the cancer tissues with chemometrics technique,” *IRMMW-THz 2006 - 31st Int. Conf. Infrared Millim. Waves 14th Int. Conf. Terahertz Electron*, p. 195, 2006.

[63] F. Wahaia, G. Valusis, L. M. Bernardo, A. Almeida, J. a. Moreira, P. C. Lopes, J. MacUtkevic, I. Kasalynas, D. Seliuta, R. Adomavicius, R. Henrique, and M. Lopes, “Detection of colon cancer by terahertz techniques,” *J. Mol. Struct.*, vol. 1006, no. 1–3, pp. 77–82, 2011.

[64] K. I. Zaytsev, K. G. Kudrin, S. a Koroleva, I. N. Fokina, S. I. Volodarskaya, E. V Novitskaya, A. N. Perov, V. E. Karasik, and S. O. Yurchenko, "Medical diagnostics using terahertz pulsed spectroscopy," *J. Phys. Conf. Ser.*, vol. 486, pp. 1–5, 2014.

[65] R. Sudo, A. Noda, K. Takagi, K. Fukui, K. Yamamoto, M. Tani, Y. Fukunaga, and N. Miyoshi, "Pathological diagnosis of an experimental tumor using THz time-domain spectroscopy," *34th Int. Conf. Infrared, Millimeter, Terahertz Waves, IRMMW-THz 2009*, pp. 9–10, 2009.

[66] S. Yamaguchi, Y. Fukushi, O. Kubota, T. Itsuji, T. Ouchi, and S. Yamamoto, "Brain tumor imaging of rat fresh tissue using terahertz spectroscopy," *Sci. Rep.*, vol. 6, no. 30124, pp. 1–6, 2016.

[67] K. Meng, T. Chen, T. Chen, L. Zhu, Q. Liu, Z. Li, F. Li, S. Zhong, Z. Li, H. Feng, and J. Zhao, "Terahertz pulsed spectroscopy of paraffin-embedded brain glioma," *J. Biomed. Opt.*, vol. 19, no. 7, pp. 77001–6, 2014.

[68] S. Sy, S. Huang, Y.-X. J. Wang, J. Yu, A. T. Ahuja, Y. Zhang, and E. Pickwell-MacPherson, "Terahertz spectroscopy of liver cirrhosis: investigating the origin of contrast," *Phys. Med. Biol.*, vol. 55, no. 24, pp. 7587–7596, 2010.

[69] Y. Bin Ji, C. H. Park, H. Kim, S. Kim, G. M. Lee, S. K. Noh, T. Jeon, J. Son, Y. Huh, S. Haam, S. J. Oh, S. K. Lee, and J. Suh, "Feasibility of terahertz reflectometry for discrimination of human early gastric cancers," vol. 6, no. 4, pp. 1413–1421, 2015.

[70] D. Hou, X. Li, J. Cai, Y. Ma, X. Kang, P. Huang, and G. Zhang, "Terahertz spectroscopic investigation of human gastric normal and tumor tissues," *Phys. Med. Biol.*, vol. 59, no. 18, pp. 5423–5440, 2014.

[71] F. Wahaia, I. Kasalynas, D. Seliuta, G. Molis, A. Urbanowicz, C. D. Carvalho Silva, F. Carneiro, G. Valusis, and P. L. Granja, "Study of paraffin-embedded colon cancer tissue using terahertz spectroscopy," *J. Mol. Struct.*, vol. 1079, no. December, pp. 448–453, 2015.

[72] M. A. Brun, F. Formanek, A. Yasuda, M. Sekine, N. Ando, and Y. Eishii, "Terahertz imaging applied to cancer diagnosis," *Phys Med Biol*, vol. 55, no. 16, pp. 4615–4623, 2010.

[73] L. H. Eadie, C. B. Reid, A. J. Fitzgerald, and V. P. Wallace, "Optimizing multi-dimensional terahertz imaging analysis for colon cancer diagnosis," *Expert Syst. Appl.*, vol. 40, no. 6, pp. 2043–2050, 2013.

[74] C. B. T. T.-D. S. of H. B. Reid, G. Reese, A. P. Gibson, and V. P. Wallace, "Terahertz Time-Domain Spectroscopy of Human Blood," *IEEE Trans. Terahertz Sci. Technol.*, vol. 3, no. 4, pp. 363–367, 2013.

[75] F. A. Jenkins and H. E. White, *FUNDAMENTAL OF OPTICS*, 4th ed. United States of America: Quebecor World, 1937.

[76] G. Peter, "Propagation of Terahertz Radiation in Non- Homogeneous," 2008.

[77] G. P. Kniffin and L. M. Zurk, "Model-based material parameter estimation for terahertz reflection spectroscopy," 2012.

[78] N. Vanhaecke and O. Dulieu, "Precision measurements with polar molecules: The role of the black body radiation," *Mol. Phys.*, vol. 105, no. 11–12, pp. 1723–1731, 2007.

[79] G. Smith, A. P. Duffy, J. Shen, and C. J. Olliff, "Dielectric relaxation spectroscopy and some applications in the pharmaceutical sciences," *J. Pharm. Sci.*, vol. 84, no. 9, pp. 1029–1044, 1995.

[80] F. Buckley and A. A. Maryott, "Influence of molecular shape on the dielectric constant of polar liquids," *J. Res. Natl. Bur. Stand. (1934).*, vol. 53, no. 4, pp. 229–244, 1954.

[81] T. H. Basey-fisher, "Biosensing with Microwave Debye Relaxation Analysis," Imperial Collage London, 2013.

[82] S. H. and S. NEGAMI and In, "A Complex Plane Representation of Dielectric and Mechanical Relaxation Processes in Some Polymers," 1967.

[83] L. Eisley, "Water: The Medium of Life," pp. 30–50, 2011.

[84] J. D. Bogdan Wozniak, "Light Absorption by Water Molecules and Inorganic Substances Dissolved in Sea Water," vol. 33, 2007.

[85] S. Y. Huang, Y. X. J. Wang, D. K. W. Yeung, a T. Ahuja, Y.-T. Zhang, and E. Pickwell-Macpherson, "Tissue characterization using terahertz pulsed imaging in reflection geometry," *Phys. Med. Biol.*, vol. 54, no. 1, pp. 149–60, 2009.

[86] G. M. Png, J. W. Choi, B. W.-H. Ng, S. P. Mickan, D. Abbott, and X.-C. Zhang, "The impact of hydration changes in fresh bio-tissue on THz spectroscopic measurements," *Phys. Med. Biol.*, vol. 53, pp. 3501–17, 2008.

[87] M. He, A. K. Azad, S. Ye, and W. Zhang, “Far-infrared signature of animal tissues characterized by terahertz time-domain spectroscopy,” *Opt. Commun.*, vol. 259, pp. 389–392, 2006.

[88] T. U. Br-bromide and J. Missimer, “Measurement of the Extracellular Space in Brain,” vol. 44, pp. 1210–1218, 2003.

[89] J. E. Downing, W. M. Christopherson, and W. L. Broghamer, “Nuclear Water Content During Carcinogenesis,” *Natl. Inst. Heal*, vol. 15, pp. 1176–1180, 1961.

[90] A. Manuscript, “NIH Public Access Molecular and Functional MRI of the Tumor Microenvironment,” *Control*, vol. 49, no. 5, pp. 687–690, 2011.

[91] C. S. Joseph, A. N. Yaroslavsky, M. Al-arashi, T. M. Goyette, C. Jason, A. J. Gatesman, B. W. Soper, C. M. Forgione, T. M. Horgan, E. J. Ehasz, R. H. Giles, and W. E. Nixon, “Terahertz spectroscopy of intrinsic biomarkers for non-melanoma skin cancer .,” *SPIE 7215, Terahertz Technol. Appl. II*, pp. 1–10, 2009.

[92] T. Ishiyama, V. V Sokolov, A. Morita, and T. Ishiyama, “Molecular dynamics simulation of liquid methanol. I. Molecular modeling including C – H vibration and fermi resonance Molecular dynamics simulation of liquid methanol. I. Molecular modeling including C – H vibration and fermi resonance,” vol. 24509, 2011.

[93] L. Chen and S. Oishi, “Terahertz Time-Domain Spectroscopy of Organic Gasses,” *Rev. Laser Eng.*, vol. 34, no. 3, pp. 251–254, 2006.

[94] J. T. Kindt and C. A. Schmuttenmaer, “Far-Infrared Dielectric Properties of Polar Liquids Probed by Femtosecond Terahertz Pulse Spectroscopy,” vol. 3654, no. 96, pp. 10373–10379, 1996.

[95] M. L. T. Asaki, A. Redondo, T. A. Zawodzinski, A. J. Taylor, M. L. T. Asaki, A. Redondo, T. A. Zawodzinski, and A. J. Taylor, “Dielectric relaxation of electrolyte solutions using terahertz transmission spectroscopy Dielectric relaxation of electrolyte solutions using terahertz transmission spectroscopy,” vol. 8469, no. 2002, 2014.

[96] S. Gorenflo, R. Buchner, and H. Helm, “Dielectric properties of oil – water complexes using terahertz transmission spectroscopy,” vol. 421, pp. 494–498, 2006.

[97] M. S S Dhillon1, M S Vitiello, E H Linfield, A G Davies, Matthias C Hoffmann, John Booske,

Claudio Paoloni, M Gensch, P Weightman, G P Williams, E Castro-Camus10, D R S Cumming, F Simoens, I Escorcia-Carranza, J Grant, Stepan Lucyszyn, "The 2017 terahertz science and technology roadmap," *J. Phys. D. Appl. Phys.*, vol. 50, no. 4, pp. 1–49, 2017.

[98] N. Katzenellenbogen and D. Grischkowsky, "Efficient generation of 380 fs pulses of THz radiation ' on by ultrafast pulse excitation of a biased metal-semiconductor interface," *Am. Inst. Phys.*, vol. 58, no. 3, pp. 222–224, 1991.

[99] D. M. Daniel R. Grischkowsky, *Sensing with Terahertz Radiation*, 1st ed. Springer-Verlag Berlin Heidelberg, 2003.

[100] J. A. Fülöp, L. Pálfalvi, G. Almási, and J. Hebling, "High energy THz pulse generation by tilted pulse front excitation and its nonlinear optical applications," *J. Infrared, Millimeter, Terahertz Waves*, vol. 32, no. 5, pp. 553–561, 2011.

[101] V. N. Trukhin, A. V. Andrianov, and N. N. Zinov'ev, "Generation of terahertz radiation by a photoconductive antenna," *Acta Phys. Pol. A*, vol. 113, no. 3, pp. 921–924, 2008.

[102] M. Tani, K. Yamamoto, E. S. Estacio, C. T. Que, H. Nakajima, M. Hibi, F. Miyamaru, S. Nishizawa, and M. Hangyo, "Photoconductive emission and detection of terahertz pulsed radiation using semiconductors and semiconductor devices," *J. Infrared, Millimeter, Terahertz Waves*, vol. 33, no. 4, pp. 393–404, 2012.

[103] X. C. Zhang and J. Xu, *Introduction to THz wave photonics*. 2010.

[104] D. H. Auston, K. P. Cheung, and P. R. Smith, "Picosecond photoconducting Hertzian dipoles," *Appl. Phys. Lett.*, vol. 45, no. 3, pp. 284–286, 1984.

[105] Q. Wu, M. Litz, X. C. Zhang, Q. Wu, M. Litz, and X. Zhang, "Broadband detection capability of ZnTe electrooptic field detectors," vol. 2924, no. 1996, pp. 1–4, 2012.

[106] J. El Haddad, B. Bousquet, L. Canioni, P. Mounaix, J. El Haddad, B. Bousquet, L. Canioni, P. Mounaix, J. El Haddad, B. Bousquet, L. Canioni, P. Mounaix, B. Bousquet, and L. Canioni, "Review in terahertz spectral analysis," *Trends Anal. Chem.*, vol. 44, pp. 98–105, 2013.

[107] B. Hou, Y. Wang, Y. Wu, H. Chen, L. Wang, P. Fu, and F. Liu, "THz spectra of five borates crystals," *Chinese Sci. Bull.*, vol. 53, no. 1, pp. 155–158, 2008.

[108] J. E. Pedersen and S. R. Keiding, "Thz Time-Domain Spectroscopy of Nonpolar Liquids," *IEEE J. Quantum Electron*, vol. 28, no. 10, pp. 2518–2522, 1992.

[109] K. N. Woods and H. Wiedemann, “The influence of chain dynamics on the far-infrared spectrum of liquid methanol,” *J. Chem. Phys.*, vol. 123, no. 13, pp. 1–21, 2005.

[110] S. Fan, E. P. J. Parrott, B. S. Y. Ung, and E. Pickwell-macpherson, “Calibration method to improve the accuracy of THz imaging and spectroscopy in reflection geometry,” *Photonics Res.*, vol. 4, no. 3, pp. 29–35, 2016.

[111] K. Shiraga, Y. Ogawa, T. Suzuki, N. Kondo, A. Irisawa, and M. Imamura, “Determination of the complex dielectric constant of an epithelial cell monolayer in the terahertz region,” *Appl. Phys. Lett.*, vol. 102, no. 5, pp. 53702–3, 2013.

[112] M. Takahashi, “Terahertz Vibrations and Hydrogen-Bonded Networks in Crystals,” *Crystals*, vol. 4, no. 2, pp. 74–103, 2014.

[113] D. M. Slocum, T. M. Goyette, R. H. Giles, and W. E. Nixon, “Experimental determination of terahertz atmospheric absorption parameters,” *Proc SPIE*, vol. 9483, p. 94830O–12, 2015.

[114] E. Pickwell, B. E. Cole, A. J. Fitzgerald, V. P. Wallace, and M. Pepper, “Simulation of terahertz pulse propagation in biological systems,” *Appl. Phys. Lett.*, vol. 84, no. 12, pp. 2190–2192, 2004.

[115] R. Woodward, V. Wallace, B. Cole, R. Pye, D. Arnone, E. Linfield, and M. Pepper, “Terahertz Pulse Imaging in reflection geometry of skin tissue using time domain analysis techniques,” *Proc. SPIE*, vol. 4625, pp. 160–169, 2002.

[116] U. Kaatze and V. Uhlendorf, “The Dielectric Properties of Water at Microwave Frequencies,” *Zeitschrift für Phys. Chemie*, vol. 126, no. 2, pp. 151–165, 1981.

[117] P. Debye, “Polar Molecules,” *Chenical Cat. Company, Inc., New York*, vol. 18, pp. 89–95, 1929.

[118] K. S. Cole and R. H. Cole, “Dispersion and Absorption in Dielectrics I. Alternating Current Characteristics,” *J. Chem. Phys.*, vol. 9, no. 4, pp. 341–351, 1941.

[119] S. Alshehri and S. Alam, “Homogeneous and Heterogeneous Breast Phantoms for UWB Imaging,” *Kiv*, pp. 1–5, 2011.

[120] E. Pickwell-MacPherson, “Biological applications of terahertz pulsed imaging and spectroscopy,” p. 171, 2005.

[121] W. J. Topf, M. E. Thomas, and T. J. Harris, “Optical and Physical Properties of Materials Crystals and Glasses,” 1995, pp. 33.1-33.101.

[122] B. M. Ladanyi and M. S. Skaf, “Wave Vector-Dependent Dielectric Relaxation of Methanol - Water Mixtures,” pp. 1368–1380, 1996.

[123] J. B. Asbury, T. Steinel, and M. D. Fayer, “Vibrational echo correlation spectroscopy probes of hydrogen bond dynamics in water and methanol,” *J. Lumin.*, vol. 107, no. 1–4, pp. 271–286, 2004.

[124] C. Q. Bao Truong, “DIELECTRIC MODELLING OF HUMAN SKIN AND BREAST TISSUE IN TERAHERTZ FREQUENCIES: POTENTIAL APPLICATION TO CANCER DETECTION,” 2015.

[125] R. J. Halter, A. Hartov, J. A. Heaney, K. D. Paulsen, and A. R. Schned, “Electrical impedance spectroscopy of the human prostate,” *IEEE Trans. Biomed. Eng.*, vol. 54, no. 7, pp. 1321–1327, 2007.

[126] R. Lemaire, M. Wisztorski, A. Desmons, J. C. Tabet, R. Day, M. Salzet, and I. Fournier, “MALDI-MS Direct Tissue Analysis of Proteins: Improving Signal Sensitivity Using Organic Treatments,” *Anal. Chem.*, vol. 78, no. 20, pp. 7145–7153, 2006.

[127] E. H. Seeley, S. R. Oppenheimer, D. Mi, P. Chaurand, and R. M. Caprioli, “Enhancement of Protein Sensitivity for MALDI Imaging Mass Spectrometry After Chemical Treatment of Tissue Sections,” *J. Am. Soc. Mass Spectrom.*, vol. 19, no. 8, pp. 1069–1077, 2008.

[128] R. G. Abramson, A. Mavi, T. Cermik, S. Basu, N. E. Wehrli, M. Houseni, S. Mishra, J. Udupa, P. Lakhani, A. D. A. Maidment, D. A. Torigian, and A. Alavi, “Age-Related Structural and Functional Changes in the Breast: Multimodality Correlation With Digital Mammography, Computed Tomography, Magnetic Resonance Imaging, and Positron Emission Tomography,” *Semin. Nucl. Med.*, vol. 37, no. 3, pp. 146–153, 2007.

[129] C. Fitzgerald, A. E. Zimon, and E. E. Jones, “Aging and reproductive potential in women,” *Yale J. Biol. Med.*, vol. 71, no. 5, pp. 367–381, 1998.

[130] P. D. Richard J. Santen, M.D., and Robert Mansel, M.D., “Benign Breast Disorders,” *Obstet. Gynecol. Clin. North Am.*, vol. 40, no. 3, pp. 459–473, 2013.

[131] T. Li, L. Sun, N. Miller, T. Nicklee, J. Woo, L. Hulse-smith, M. Tsao, R. Khokha, L. Martin,

and N. Boyd, “The Association of Measured Breast Tissue Characteristics with Mammographic Density and Other Risk Factors for Breast Cancer The Association of Measured Breast Tissue Characteristics with Mammographic Density and Other Risk Factors for Breast Cancer,” *Cancer Epidemiol. Biomarkers Prev.*, vol. 14, pp. 343–349, 2005.

[132] D. M. Gertig, I. E. Stillman, C. Byrne, D. Spiegelman, S. J. Schnitt, J. L. Connolly, G. A. Colditz, and D. J. Hunter, “Association of age and reproductive factors with benign breast tissue composition,” *Cancer Epidemiol. biomarkers Prev.*, vol. 8, pp. 873–879, 1999.

[133] N. F. Boyd, G. A. Lockwood, J. W. Byng, D. L. Tritchler, and M. J. Yaffe, “Mammographic densities and breast cancer risk,” *Cancer Epidemiol. Biomarkers Prev.*, vol. 7, pp. 1113–44, 1998.

[134] S. E. Hankinson, W. C. Willett, D. S. Michaud, J. E. Manson, G. A. Colditz, C. Longcope, B. Rosner, and F. E. Speizer, “Plasma Prolactin Levels and Subsequent Risk of Breast Cancer in Postmenopausal Women,” *JNCI J. Natl. Cancer Inst.*, vol. 91, no. 7, pp. 629–634, 1999.

[135] A. Cerussi, N. Shah, D. Hsiang, A. Durkin, J. Butler, and B. J. Tromberg, “In vivo absorption, scattering, and physiologic properties of 58 malignant breast tumors determined by broadband diffuse optical spectroscopy.,” *J. Biomed. Opt.*, vol. 11, no. 4, p. 44005, 2015.

[136] S. K. Yngvesson, B. St. Peter, P. Siqueira, P. Kelly, S. Glick, A. Karellas, and A. Khan, “Feasibility demonstration of frequency domain terahertz imaging in breast cancer margin determination,” *Proc SPIE Int Soc Opt Eng*, pp. 1-19, 2012.

[137] J. Jossinet, “The impedivity of freshly excised human breast tissue,” *Physiol. Meas.*, vol. 19, no. 1, pp. 61–75, 1998.

[138] P. C. Ashworth, E. Pickwell-MacPherson, E. Provenzano, S. E. Pinder, A. D. Purushotham, M. Pepper, and V. P. Wallace, “Terahertz pulsed spectroscopy of freshly excised human breast cancer.,” *Opt. Express*, vol. 17, no. 15, pp. 12444–12454, 2009.

[139] T. Bowman, M. El-shenawee, and L. Campbell, “Time of flight estimation for breast cancer margin thickness using embedded tumors,” *Proc. SPIE*, vol. 9706, p. 97061V 6, 2016.

[140] T. Bowman, M. El-shenawee, and L. Campbell, “Regional spectroscopy of paraffin-embedded breast cancer tissue using pulsed terahertz transmission imaging,” *Proc. SPIE*, vol. 9706, p. 97061W–6, 2016.

[141] T. Bowman, S. G. Sharma, and L. Rock, “Terahertz Spectroscopy for the Characterization of Excised Human Breast Tissue,” *IEEE*, pp. 1–4, 2014.

[142] A.Al. Amel, J. Bou-Sleiman, C. Quentin, G. Macgrogan, H. Balacey, Z. Thomas, P. Mounaix, and J.-P. Guillet, “Terahertz Biomedical Imaging: From Multivariate Analysis and Detection to Material Parameter Extraction,” *Prog. Electromagn. Res. Symp.*, pp. 2756–2765, 2017.

[143] P. M. H. Ballacey, A.Al-Ibadi, G.Macgrogan, JP.Guillet, E.MacPherson, “Automated data and image processing for biomedical sample analysis,” *IEEE*, pp. 2–3, 2016.

[144] H. Balacey, B. Recur, J. B. Perraud, J. B. Sleiman, J. P. Guillet, and P. Mounaix, “Advanced Processing Sequence for 3-D THz Imaging,” *IEEE Trans. Terahertz Sci. Technol.*, vol. 6, no. 2, pp. 191–198, 2016.

[145] Carol DeSantis, R. Siegel, and A. Jemal, “Breast Cancer Facts and Figures 2017-2018,” *Am. Cancer Soc. Inc.*, pp. 1-44, 2017.

[146] P. N.-J., C. Y., B. C., C. Y., D. N.E., V. L. G.J., F. R., W.-S. S., S. M.L., and C. R., “Cardiovascular disease outcomes after breast cancer in postmenopausal women: Results from the women’s health initiative,” *PLoS One*, vol. 12, no. 9, pp. 1–20, 2017.

[147] L. Caplan, “Delay in Breast Cancer: Implications for Stage at Diagnosis and Survival,” *Front. Public Heal*, vol. 2, pp. 1–5, 2014.

[148] Breastcancer.org, “Surgical Margins.” 2017.

[149] T. Fujisawa, T. Hirakata, Y. Yanagita, M. Iijima, H. Horikoshi, K. Takeuchi, and Y. Saitoh, “The detection of pCR after PST by contrast-enhanced ultrasonography for breast cancer,” *Breast Cancer*, vol. 20, no. 1, pp. 75–82, 2013.

[150] R. D. Macmillan and S. J. McCulley, “Oncoplastic Breast Surgery: What, When and for Whom?,” *Curr. Breast Cancer Rep.*, vol. 8, no. 2, pp. 112–117, 2016.

[151] A. C. Lind, C. Bewtra, J. C. Healy, and K. L. Sims, “Prospective peer review in surgical pathology,” *Am J Clin Pathol*, vol. 104, no. 5, p. 560–6., 1995.

[152] J. M. Granholm and J. Olszewski, *What You Need to Know Before Writing Your RFP*. 2008.

[153] Syed K. Mohsin, “Assessment of the Surgical Margins,” in *Frozen Section Library: Breast*, Illustrate, vol. 9, Springer Science and Business Media, 2011, pp. 33–55.

[154] J. Q. Brown, T. M. Bydlon, L. M. Richards, B. Yu, S. A. Kennedy, J. Geradts, L. G. Wilke, M. Junker, J. Gallagher, W. Barry, and N. Ramanujam, "Optical assessment of tumor resection margins in the breast," *IEEE J Sel Top Quantum Electron*, vol. 16, no. 3, pp. 530–544, 2010.

[155] A. S. Y. Leong, S. Braye, and B. Bhagwandeen, "Diagnostic 'errors' in anatomical pathology: Relevance to Australian laboratories," *Pathology*, vol. 38, no. 6, pp. 490–497, 2006.

[156] N. Masciadri and C. Ferranti, "Benign breast lesions: Ultrasound," *J. Ultrasound*, vol. 14, no. 2, pp. 55–65, 2011.

[157] W. A. Berg, A. G. Sechtin, H. Marques, and Z. Zheng, "Cystic Breast Masses and the ACRIN 6666 Experience," *Radiol Clin North Am.*, vol. 48, no. 5, pp. 931–987, 2011.

[158] W. D. Kerridge, O. N. Kryvenko, A. Thompson, and B. A. Shah, "Fat Necrosis of the Breast: A Pictorial Review of the Mammographic, Ultrasound, CT, and MRI Findings with Histopathologic Correlation," *Radiol. Res. Pract.*, vol. 2015, pp. 1–8, 2015.

[159] S. Ganau, L. Tortajada, F. Escribano, F. J. Andreu, and M. Sentís, "Fat Necrosis," in *Mammography - Recent Advances*, Spain, 2012, pp. 374–388.

[160] F. Taşkin, K. Köseoğlu, A. Ünsal, M. Erkuş, S. Özbaş, and C. Karaman, "Sclerosing adenosis of the breast: Radiologic appearance and efficiency of core needle biopsy," *Diagnostic Interv. Radiol.*, vol. 17, no. 4, pp. 311–316, 2011.

[161] H. Berment, V. Becette, M. Mohallem, F. Ferreira, and P. Chérel, "Masses in mammography: What are the underlying anatomopathological lesions?," *Diagn. Interv. Imaging*, vol. 95, no. 2, pp. 124–133, 2014.

[162] G. Sallustio, "Sclerosing Adenosis of the Breast: Report of Two Cases and Review of the Literature," *Polish J. Radiol.*, vol. 80, pp. 122–127, 2015.

[163] M. Guray and A. A. Sahin, "Benign Breast Diseases: Classification, Diagnosis, and Management," *Oncologist*, vol. 11, pp. 435–449, 2006.

[164] J. H. Chen, O. Nalcioglu, and M. Y. Su, "Fibrocystic change of the breast presenting as a focal lesion mimicking breast cancer in MR imaging," *J. Magn. Reson. Imaging*, vol. 28, no. 6, pp. 1499–1505, 2008.

[165] D. C. Allred, "Ductal carcinoma in situ: Terminology, classification, and natural history," *J. Natl. Cancer Inst. - Monogr.*, no. 41, pp. 134–138, 2010.

[166] J. Makki, “Diversity of breast carcinoma: Histological subtypes and clinical relevance,” *Clin. Med. Insights Pathol.*, vol. 8, no. 1, pp. 23–31, 2015.

[167] M. Rick Alteri, MD; Tracie Bertaut, APR; Louise A Brinton, PhD; Stacey Fedewa, MPH; Rachel A Freedman, MD, MPH; Ted Gansler, MD, M. L. A. N. Mia M Gaudet, PhD; Joan Kramer, MD; Chun Chieh Lin, MBA, PhD; Marji McCullough, SCD, RD; Kimberly Miller, P. MD, MPH; Dearell Niemeyer, MPH; Anthony Piercy; Cheri Richards, MS; Ann Goding Sauer, MSPH; Scott Simpson; Robert Smith, and M. Dana Wagner; and Jiaquan Xu, “Breast Cancer Facts and Figures 2015-2016,” *Am. Cancer Soc. Inc.*, vol. 404, no. 861015, pp. 1–38, 2015.

[168] D. Pape-zambito, Z. Jiang, H. Wu, K. Devarajan, C. M. Slater, K. Q. Cai, A. Patchefsky, M. B. Daly, and X. Chen, “Identifying a Highly-Aggressive DCIS Subgroup by Studying Intra-Individual DCIS Heterogeneity among Invasive Breast Cancer Patients,” vol. 9, no. 6, pp. 1–10, 2014.

[169] D. M. Carraro, E. V. Elias, and V. P. Andrade, “Ductal carcinoma *in situ* of the breast: morphological and molecular features implicated in progression,” *Biosci. Rep.*, vol. 34, no. 1, pp. 19–28, 2014.

[170] A. Soran, “Ductal carcinoma in situ: Current concepts,” *Pathology*, vol. 48, no. 3, pp. 180–193, 2010.

[171] G. J. Logan, D. J. Dabbs, P. C. Lucas, R. C. Jankowitz, D. D. Brown, B. Z. Clark, S. Oesterreich, and P. F. McAuliffe, “Molecular drivers of lobular carcinoma in situ.,” *Breast Cancer Res.*, vol. 17, no. 76, pp. 1–10, 2015.

[172] S. P. Bagaria, J. Shamonki, M. Kinnaird, P. S. Ray, and A. E. Giuliano, “The Florid Subtype of Lobular Carcinoma In Situ: Marker or Precursor for Invasive Lobular Carcinoma?,” *Ann. Surg. Oncol.*, vol. 18, no. 7, pp. 1845–1851, 2011.

[173] H. Buerger, E. C. Mommers, R. Littmann, R. Diallo, C. Brinkschmidt, C. Poremba, B. Dockhorn-Dworniczak, P. J. Van Diest, and W. B??cker, “Correlation of morphologic and cytogenetic parameters of genetic instability with chromosomal alterations in in situ carcinomas of the breast,” *Am. J. Clin. Pathol.*, vol. 114, no. 6, pp. 854–859, 2000.

[174] D. Butler Dr. and M. Rosa Dr., “A morphologically and clinically distinct variant of lobular

carcinoma," *Arch. Pathol. Lab. Med.*, vol. 137, no. 11, pp. 1688–1692, 2013.

[175] B. Zhang, X. Cao, J. Chen, J. Chen, L. Fu, X. Hu, Z. Jiang, N. Liao, D. Liu, O. Tao, Z. Shao, Q. Sun, S. Wang, and Y. Wang, "Guidelines on the diagnosis and treatment of breast cancer (2011 edition)," *Gland Surg.*, vol. 1, no. 1, pp. 39–61, 2012.

[176] B. Zengel, U. Yararbas, A. Duran, A. Uslu, N. Elıyatkın, M. A. Demırkıran, F. Cengiz, C. Şimşek, H. Postacı, E. Vardar, and R. Durusoy, "Comparison of the clinicopathological features of invasive ductal, invasive lobular, and mixed (invasive ductal + invasive lobular) carcinoma of the breast," *Breast Cancer*, vol. 22, no. 4, pp. 374–381, 2013.

[177] C. H. FOX, F. B. JOHNSON, O. WHITING, and P. P. ROLLER, "Formaldehyde Fixation," *Stud. Second Lang. Acquis.*, vol. 33, no. 8, pp. 845–853, 1985.

[178] M. Lazebnik, L. McCartney, D. Popovic, C. B. Watkins, M. J. Lindstrom, J. Harter, S. Sewall, A. Magliocco, J. H. Booske, M. Okoniewski, and S. C. Hagness, "A large-scale study of the ultrawideband microwave dielectric properties of normal breast tissue obtained from reduction surgeries.," *Phys. Med. Biol.*, vol. 52, no. 10, pp. 2637–56, 2007.

[179] S. Moscato, G. Matrone, M. Pasian, A. Mazzanti, M. Bozzi, L. Perregrini, F. Svelto, G. Magenes, P. Arcioni, and P. Summers, "A mm-wave 2D ultra-wideband imaging radar for breast cancer detection," *Int. J. Antennas Propag.*, vol. 2013, 2013.

Annex

6.1. Annex 1: Table 4: All fresh tissue, fixed tissue, and block.

Nearsense number	Type	Grade	Patient's age	Body weight (Kg)	Height (cm)	BMI	Photo
1	Invasive carcinoma NST	3	85	59	148	26.9	\\\\
2	Invasive carcinoma NST	3	48	89	163	33.5	\\\\
3	Invasive carcinoma NST	2	70	85	165	31.23	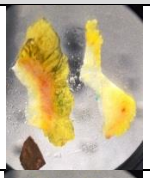
4	Invasive carcinoma NST	2	70	85	165	31.23	
5	Invasive carcinoma NST	3	55	59	163	22.21	
6	Invasive carcinoma NST	3	86	45	155	18.73	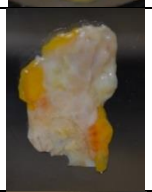
7	Invasive carcinoma NST	2	48	82	162	31.25	
8	Invasive carcinoma NST	3	77	88.5	157	35.79	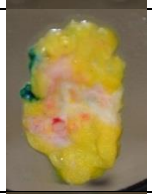
9	Invasive carcinoma NST	2	59	67	163	25.22	

10	Invasive carcinoma NST	1	77	75	155	31.22	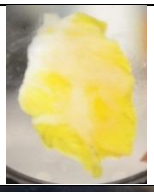
11	Invasive carcinoma NST	3	37	60	156	24.66	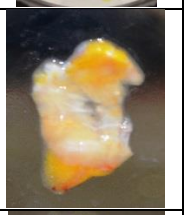
12	Invasive carcinoma NST	2	57	60	158	31.24	
12	Invasive carcinoma NST	2	57	60	158	31.24	
13	Invasive lobular carcinoma	3	72	80	167	31.24	
14	Invasive carcinoma NST	1	50	90	172	30.4	
15	Adipose tissue colon	benign	64	58	165	21.3	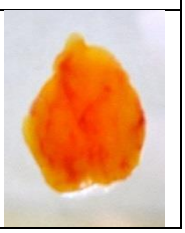

16	Colon adenocarcinoma	Low grade	64	58	165	21.3	
17	Invasive carcinoma NST	2	39	108	163	41	
18	Leiomyoma uterus	benign	77	46	150	20.45	
19	Invasive carcinoma NST	2	48	80	165	29.39	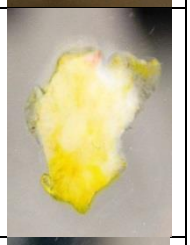
20	Invasive carcinoma NST	2	48	80	165	29.39	
Tissue – paraffin/slide (no: 3 samples)	Invasive micropapillary carcinoma	2	53	52	167	18.65	
Tissue – paraffin/slide (no: 3 samples)	Invasive carcinoma NST	2	53	85	160	33.2	
Tissue – paraffin/slide (no: 3 samples)	Invasive carcinoma NST	3	86	58	148	26.48	
Tissue – paraffin/slide (no: 3 samples)	Invasive carcinoma NST	2	77	59	155	24.56	
Tissue – paraffin/slide (no: 3 samples)	Invasive carcinoma NST	3	62	76.5	158	30.65	
Block (no: 9 samples)	/	/	/	/	/	/	

Tissue-paraffin/on silica, no: 5 samples)	/	/	/	/	/	/	
Tissue-paraffin/on sapphire, no: 2 samples)	/	/	/	/	/	/	

6.2. Annex 2: Breast Cancer Imaging

This part presents a brief background on human breast tissue structures and types of cancer, as well as an overview of imaging techniques used to detect breast cancer. We also review the various methods for preparing breast cancer samples for THz imaging and microscope histopathology. The next section is a short review of breast cancer stages. Finally, we present processing sequences of the various methods for 3D THz imaging of excised human breast tissue for cancer detection.

6.2.1. Introduction

Breast cancer is a long-term research area with tremendous public health implications. In 2017, an estimated 252,710 women and 2,470 men will be diagnosed as new breast cancer cases in the United States. In addition, an estimated 63,410 new cases of in situ breast lesions will be diagnosed in women, and 41,070 people will die from this disease (40,610 women and 460 men) [145]. Recent studies have found that breast cancer is the second cause of death in women after heart disease [146].

Early diagnosis of breast cancer before it spreads is essential to improve the survival rate of women [147]. It is, therefore, important to provide high-sensitivity diagnostic tools to detect breast cancer with a high degree of accuracy to avoid false-positive results and prevent repeat surgery of the patient.

In breast surgery, surgeons remove malignant tissue, together with a margin of healthy tissue around it, to ensure that all the cancer has been removed [148]. Detecting breast cancer while minimizing the margin of normal tissue may be quite difficult [149] and this remains an important area for improving surgery, optimizing breast cancer treatment, and avoiding repeat surgery. Clinical follow-up is conducted using various instruments, data analysis methods, and standard preparation protocols, but the results from different tissue regions may be difficult to compare. Additionally, the amount of healthy tissue removed by surgery must be minimized to avoid any significant effect on the patient [150]. Moreover, obtaining the full examination results may require several days[151], [152], only to determine that a second surgery is necessary.

The pathologist classifies the excised tissue as follows: positive, with cancerous tissue extending to the cut edge of the excised tissue, negative, indicating no cancerous tissue within at least 2 mm of the cut edge, or close, with cancerous tissue within 2 mm of the cut edge [153], as shown in Figure 68.

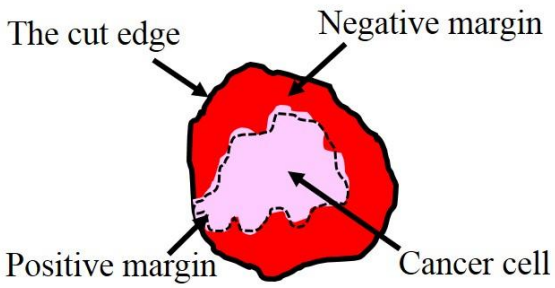

Figure 68: Negative and positive margin of excised breast cancer tissue.

Detection of cancer cells in the margin tissue typically results in a second surgery (re-excision surgery), to remove the remaining cancerous tissue in the surgical cavity, as a precaution to prevent local recurrence [154]. For this reason, a full pathology analysis of the excised tissue may take several days to complete. This time delay may have a significant impact on the patient, in cases where a positive margin requires repeat surgery. Finally, there is a potential for human error in relying solely on a pathology assessment [155]. It is, therefore, necessary to devise a highly-accurate, pre-surgical analysis method.

Details of THz techniques developed for breast cancer diagnosis, are presented in the following sections.

6.2.2. Tumor types

6.2.2.1. Benign breast tumors

Benign breast tumor refers to noncancerous changes in the breast and alterations in the ducts and lobules. In addition, benign breast tumors develop from a combination of connective tissue and epithelial cells. This type of tumor is circumscribed, due to the absence of infiltration, rarely spreads to other parts of the body, and can be removed by surgery. In this section, we present and describe several types of benign breast tumors:

Fibroadenomas of the breast:

Fibroadenomas are common benign (non-cancerous) breast tumors, made up of both glandular and stromal (connective) tissues, that form a solid lump [156]. They are more frequently found in women between the ages of 20 and 30, but occur for women of any age. Sometimes, this type of tumor may stop growing or even shrink on its own, without treatment. On MRI, fibroadenomas are rounded and smooth with clear-cut borders. They are sometimes accompanied by coarse calcification, or they may appear like cysts or well-contained tumors, as shown in Figure 69.

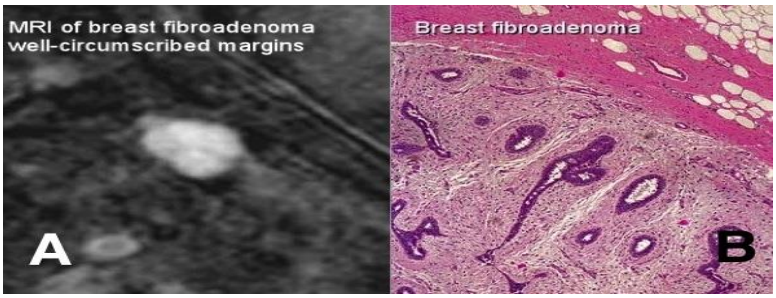

Figure 69: A) MRI image of a breast mass, B) photomicrograph of the histology of the excised mass confirmed a benign breast fibroadenoma, consisting of irregular, well-formed glands in varying amounts of fibrous stroma. http://breast-cancer.ca/3c-fibroadenoma/.

Cysts:

Most breast cysts, identified as simple cysts by ultrasound, are benign and never become cancerous [157]. Breast cysts develop from lobules (milk-production glands) and ducts (tubes that carry milk to the nipple), surrounded by glandular, fibrous, and fatty tissue. Typically, these fluid- or blood-filled sacs develop in women aged from 25 to 45. Breast cysts may be any size, from a few millimeters to several centimeters, and are usually well-circumscribed masses with round or ovoid shapes.

Fat necrosis:

Fat necrosis of the breast is a benign inflammatory process that damages adipose tissue [158]. In addition, it may occur after breast surgery or radiation treatment. Fat necrosis does not lead to the development of breast cancer [159]. Moreover, fat necrosis may be difficult to diagnose by imaging, as;

- Masses consisting of breast fat necrosis resemble malignant breast tumors on diagnostic imaging;
- The dense mass has an irregular shape, a spiky border, and a collection of microcalcifications;
- Fat necrosis may also resemble a typical lipoma or liposarcoma, which are rarely found in breast tissue.

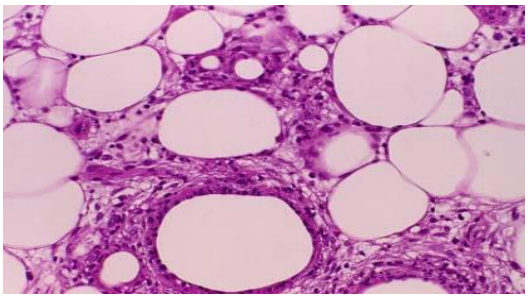

Figure 70: Irregular fat necrosis (H&E).

Adenosis:

Figure 71 shows adenosis of the breast, a non-malignant mass made up of lobules (milk-producing glands) and ducts [160]. Breast adenosis are surrounded by glandular, fibrous, and fatty tissue [161]. They are often found in biopsies of women, who have fibrosis or cysts in their breasts. Breast adenosis may mimic cancer, mass, and microcalcifications [162] and develops in women aged between 20 and 40. Breast adenosis is diagnosed by mammography or ultrasound imaging, but is not easily distinguished in these images, due to the emotional distress caused by the fear of breast cancer.

Fibrocystic Change:

Fibrocystic breast change (FCCs) is a noncancerous condition, caused by the proliferation of hormone-dependent mesenchymal and epithelial structures, that occurs in women aged between 20 and 50 [163]. FCC is referred to by several names: fibrocystic disease, fibrocystic changes, cystic disease, and mammary dysphasia. In addition, FCCs comprise both cysts and some solid breast lesions, such as sclerosing adenosis, epithelial hyperplasia with or without atypia, apocrine metaplasia, diffuse papillomatosis, and radial scar [163]. However, FCCs sometimes make it more difficult to detect a hidden cancer with imaging techniques [164], due to the breast density associated with fibrocystic breast eclipsing the breast cancer on the mammography film or ultrasound image.

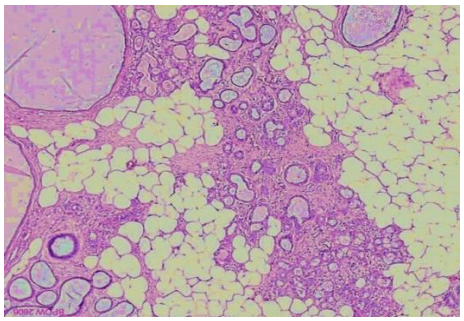

Figure 71: Sclerosing adenosis around glands in fibrous and fatty tissue (H&E).

6.2.3. Malignant breast disease

This type of tumor is cancerous and may spread to other parts of the body. Types of malignant breast tissue include noninvasive and invasive cancer, as follows:

6.2.3.1. Noninvasive types:

1- Ductal Carcinoma in situ (DCIS):

Ductal Carcinoma in situ (DCIS) occurs when abnormal cells replace the normal epithelial cells of the breast ducts and may expand into the ducts and lobules [165]. DCIS is referred to as a noninvasive form of breast cancer, as the abnormal cells have not grown through the layer of the milk ducts, where they originated, or spread to other organs in the body [166]. Some of these tumors do not affect a woman's health, as they grow very slowly, even without treatment. DCIS may evolve into an invasive breast cancer. In 2008-2012, DCIS represented an estimated 83% of new in situ cases diagnosed in women[167]. However, among women who had surgery for DCIS, may were left untreated, as the tumor was originally misclassified as benign, and approximately 20%-53% were diagnosed with an invasive breast cancer over the next 10 or more years [167]. As there is no certain method for accurately determining with the development potential of a DCIS lesion, a diagnosis is usually followed by surgery, radiation and/ or hormonal therapy. In addition, there is active ongoing research aimed at identifying the molecular characteristics of DCIS, in order to predict its recurrence or progression to invasive forms [168].

DCIS is classified into three types, based on cellular morphology, size and shape, architectural pattern, and nuclear atypia : low, intermediate, and high grade, each associated with different clinical outcomes, dependent on accurate diagnosis [169].

1- **Low grade- DCIS (LG-DCIS):** refers to a cancer with a low growth rate. It is characterized by monomorphic cell proliferation, uniform nuclear size, approximately that of normal ductal cells, a variety of architectural patterns, cribriform and micropapillary, as well as solid and papillary growth [170]. In addition, cells are well-polarized, and mitotic figures are rare. Moreover, punctate necrosis is more common than focal in LG-DCIS. Small laminated calcifications may also be present.
2- **High grad-DCIS (HG-DCIS):** these DCIS cells grow more quickly, forming a population of atypical cells with marked nuclear pleomorphism of cells, arranged in variable architectural patterns, including micro-papillary, or, more frequently solid and cribriform types, although amorphous calcification with comedo necrosis is often present. In addition, a single layer of atypical cells is sufficient to diagnose high grade-DCIS [169].
3- **Intermediate grade-DCIS:** consists of a combination of LG-DCIS and HG-DCIS.

2- Lobular carcinoma in situ (LCIS)

Lobular carcinoma in situ is also known as a lobular neoplasia. LCIS of the breast refers to an uncommon lesion with a distinctive histological appearance, characterized by masses of loosely-adherent (atypical) cells with

small round, monotonous, hyperchromatic nuclei that distend acini in the lobular unit of the breast. These atypical cells do not spread beyond the lobule walls. In addition, untreated LCIS is not thought to be a precursor of invasive lobular cancer. Typically, LCIS is often found in breast biopsies that have been carried out for other reasons, such as removing benign lesions. In 2008-2012, LCIS was estimated to represent approximately 13% of women's in situ breast tumors. LCIS develops in women ages between 40 and 50. There are three main histological classifications of LCIS:

1- Classical (CLCIS)

CLCIS is histologically classified by a uniform growth of small round cells with a ring of clear cytoplasm, loosely adherent, distended acini of the lobular unit of the breast, mitotic figures, and necrosis, as well as calcification. These atypical cells do not spread beyond the lobule walls. In addition, CLCIS is subdivided into: A-CLCIS, which is generally low-grade, with small nuclei and inconspicuous nucleoli, and B-CLCIS, with large grade cells and larger, slightly irregular, nuclei and small nucleoli [171].

2- Florid (F-LCIS)

Florid LCIS (F-LCIS) is a rare architectural subtype of LCIS. F-LCIS is histologically characterized by solid type ductal carcinoma [172] and is, therefore, considered a precursor to invasive lobular carcinoma (ILC). In addition, F-LCIS is often associated with necrosis and calcification. Moreover, F-LCIS shows greater genetic instability, unlike C-CLIS, including a higher fraction of genomic alterations, associated with either size, hormone receptor status, or subsequent or concurrent invasive lobular carcinoma [173].

3- Pleomorphic (P-LCIS)

Histologically, P-LCIS is defined as a carcinoma with a lobular growth pattern similar to that of invasive lobular carcinoma: moderately large nuclei, coarse chromatin, prominent nucleoli, not uncommon mitotic figures, and central necrosis. In addition, P-LCIS cells and nuclear atypia are more consistent with invasive ductal carcinoma [174]. Moreover, P-LCIS exhibits genetic alteration, with similarities in molecular alteration to C-CLIS, so it is better classified as a variant of invasive lobular carcinoma [174].

6.2.3.2. Invasive Breast Cancer

Breast cancer cells that have grown beyond the ducts and spread into surrounding breast tissues and nodes is defined as invasive breast cancer or malignant tumor. Types of invasive breast cancer include invasive ductal carcinoma (IDC), invasive lobular carcinoma (ILC), and mixed ductal/lobular mammary carcinoma (MDLC), as shown in Figure 72. The most common is invasive carcinoma of no special type (NST), known as invasive infiltrating ductal carcinoma not otherwise specified (IDC-NOS). IDC can affect women at any age and

represents approximately 80% of all breast cancer diagnoses [175]. Possible symptoms of invasive breast cancer include: a lump or thickness in an area of the breast, variations in breast size and shape, dimpling of the skin, or changes in nipple shape. Other possible symptoms include bloody discharge from the nipple and a swelling or lump in the armpit. Invasive breast cancer may be diagnosed by a mammogram or ultrasound imaging, and a small tissue biopsy is taken for diagnoses under a microscope.

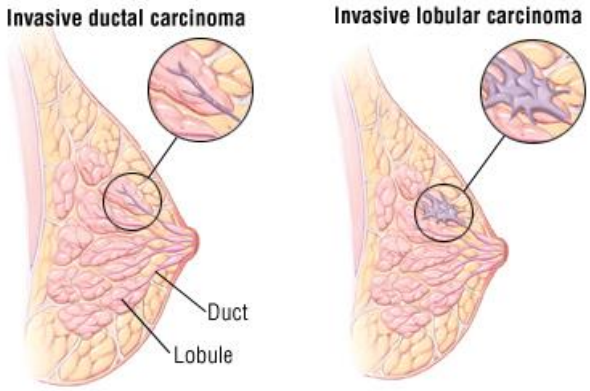

Figure 72: Side view of invasive breast cancer (ductal and lobular).

Invasive breast carcinoma is associated with various clinical diagnoses, concerning histopathological characteristics, including: age, tumor size, nodal involvement, disease stage and grade, hormone therapy, and cell proliferation rate, as well as estrogen receptors (ER), and survival rate [176].

Histological examination;

1- Invasive ductal carcinoma (IDC) is defined as a variety of patterns, single-cell infiltration, and foci of poorly-formed glands, as well as a glandular pattern revealed by a single lesion.
2- Invasive lobular carcinoma (ILC) is characterized by: uniform dispersion of the infiltrating cancer cells, classified as solid, alveolar variant, pleomorphic, tubulolobular variant, or variant lesions.
3- MDLC is defined as a tumor that infiltrates ductal (IDC) components, often diagnosed at an advanced stage, accounting for 10 to 49% of a tumor, the rest being of a recognized lobular type.

6.2.4. Cancer stages

Cancers break through the walls of the glands or ducts, then spread and grow into surrounding breast tissue. Breast cancer metastasis is influenced by the stage of the disease, and early diagnosis is important to prevent the cancer from developing and spreading. Tumors are classified in stages, according to their size and the extent to which they have spread within the breast and to other tissue, nearby lymph nodes, or distant metastases. Stages are classified from 0 to IV, the most advanced, summarized as follows:

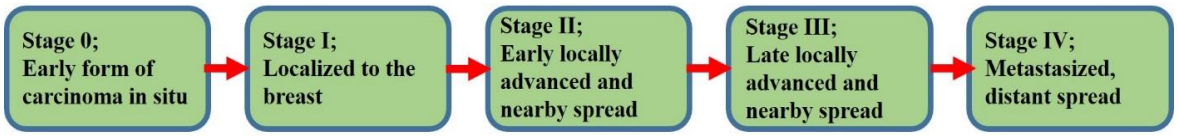

Figure 73: Cancer stages of breast tissue.

1- **Stage 0** refers to non-invasive breast cancer, with no breakaway cells or extension to neighboring normal tissue.
2- **Stage I** refers to tumors confined to the breast and is divided into two groups: stages IA and IB, according to tumor size (approximately 2 cm or smaller) and lymph nodes (approximately 0.2 mm to 2mm).
3- **Stage II** refers to tumors that have spread to surrounding breast tissue or nearby lymph nodes. This stage is divided into two groups: stages IIA and IIB, depending on size (approximately 2-5 cm), not yet spread to the lymph nodes, as well as lymph node involvement (approximately 0.2 mm to 2mm).
4- **Stage III** refers to metastasized cancer, where the cancer cells have spread to nearby lymph nodes and muscle, but not distant organs in the body. Stage III is divided into three groups: stages IIIA, IIIB, and IIIC, according to size (larger than 5 cm), as well as the nearby lymph nodes (cancer found in approximately 4 to 9 axillary lymph nodes).
5- **Stage IV** refers to metastatic cancer, which has spread to distant organs in the body, such as brain, liver, lung, and bones or lymph nodes above the collarbone.

6.2.5. Sample preparation and on site protocol

In this study, all samples were obtained during breast cancer surgery from women patients diagnosed with infiltrating ductal carcinoma (IDC). The following protocol was used to prepare the sample for microscopy examination and THz imaging: fixation, embedding, sectioning, and staining. The procedure was carried out by pathologists and laboratory technicians, as follows:

6.2.5.1. Fixation

Preparing a sample for examination typically starts after surgery. The tissues are fixed in aqueous solutions containing the following chemicals:

1- Formaldehyde for biological tissue. Formaldehyde binds (by cross-linking) the proteins, amino acids, peptides, and some lipids in the tissue that contain sulfhydryl groups. Cross-linking stops autolysis and preserves the cellular structure of the tissue [177], which is important in classifying cancer cells. For optimal fixation, harvested tissues should be approximately 3 mm thick and 15 mm wide, to insure that

the formaldehyde penetrates the tissue, cross-links the proteins, and stops autolysis as quickly as possible. Specimens should be fixed in 10% buffered formaldehyde for 20 to 30 min at room temperature before they are processed.

2- After formaldehyde fixation, the tissue is transferred to 70% ethanol for 15 min, but tissues may become very brittle and difficult to section after prolonged storage in ethanol.

3- The tissues are then transferred to 100% and 95% alcohol for 15 min in each solution.

4- The tissue is then immersed in 10% formalin solution.

6.2.5.2. Embedding and sectioning

After chemical fixing, the tissues are embedded in paraffin wax to remove the water from the breast tissue and replace it with paraffin. In addition, this process provides a stable base for cutting sections using a microtome tool for examination and study. These blocks may be stored and used for decades. Another advantage of paraffin wax as an embedding agent is that sections stick together as they are cut, forming a ribbon of sections. For microscopy examination, paraffin sections are cut at a thickness of 3-5 µm, as the diameter of red blood cells is about 7 µm, so the section only contains a single layer of these cells. For THz imaging, paraffin sections are cut at a thickness of 20-30 µm and mounted on glass slides (1 mm and 0.1 mm thick), silica 2 mm thick, sapphire windows 5 mm thick, and UVFS windows 5 mm thick. Sections are placed in warm water to flatten them and mounted on the transparent materials. After thorough drying, they are ready for staining prior to microscopy examination. The sections prepared for THz study were not stained.

6.2.5.3. Staining and Microscopy

Hematoxylin and eosin (H & E) were used to stain 3-5 µm slices, mounted on glass slides, for microscopic examination by a pathologist. H & E staining is included in many steps in the process, using hematoxylin to stain nucleic and cytoplasmic RNA dark blue or purple and eosin to stain proteins red or pink and dark-red, as red blood cells are strong absorbers of eosin staining. Staining a sample takes a minimum of 75 min. Reagents used for staining include: 100% alcohol, 95% alcohol, and xylene to clear the sample, hematoxylin, eosin, safranin, and distilled water. The options for staining thin slices are as follows:

1- Dewax sections in xylene for 3 min.

2- Rehydrate in 100%, 95%, and 70% alcohol for 3min each.

3- Immersed the section in hematoxylin for 30 sec.

4- Wash the section with distilled water for 15 min.

5- Stain the section with eosin for 10 sec.

6- Rinse the section in distilled water to remove the excess stain.

7- Finally, immerse the section in 70% ethanol for differential staining of the tissue matrix and cellular components. Cover the slide with a glass coverslip and leave it to dry.

Stained tissues were examined under a microscope, by a pathologist, to identify the normal structure of the tissues and the diseased structures, as well as to determine whether cancer was present in the tissue section and identify the type. Corresponding changes occur in the chemical and physical structure of the tissue, visible under microscopic examination, which can be used to characterize the diseased tissues by their typical structure and abnormalities compared to those of normal cells. Although, this technique offers excellent resolution, it takes time to prepare the sample for sectioning, staining, and examination, so obtaining results by this technique may take from hours to several days. In addition, the steps required to prepare the sections are technically complicated, requiring specialized equipment and expertise. Moreover, microscopic examination requires a skilled pathologist to make a diagnosis on the basis of stained tissue. Finally, these H & E stained slides were taken for standard histopathology diagnosis, in order to identify any differences correlate with the findings of the THz image, obtained by transmission and reflection imaging of these sections.

6.2.5.4. Fresh tissue

Fresh excised sections of both normal and tumor tissue were prepared for this study, without fixing, sectioning, or staining, which only required a few minutes, as follows:

1- Cut the tissue in different thickness: 100, 200, and 300 µm. These sections were inhomogeneous, with uneven surfaces, and complex tissue.

2- Immerse them in saline solution for THz imaging.

3- Finally, after imaging, the tissues were kept in 30% buffered formalin.

6.2.6. Conclusion

In conclusion, THz images of biological tissues will be measured by THz spectroscopy and imaging in transmission and reflection mode, followed by direct or indirect processing. These THz images will be then correlated with histopathological images given by Bergonié institute in Bordeaux. As sample preparation to ensure the accurate detection of tumor margins and discriminate between benign and malignant regions requires several hours, the fact that this automated or manual test, using fresh-tissue slices is capable of identifying cancer regions rapidly is of great interest. Therefore, as well as efficiently extracting data from THz images, it is also possible to extract dielectric properties of the sample from signal processing, such as its refractive index and absorption coefficient, as described in detail in the next chapter.

6.3. Annex 3: Results of fresh tissue _serum

Tissue No.1

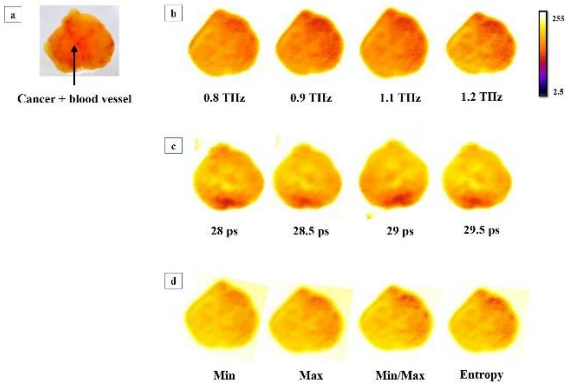

Tissue No. 2

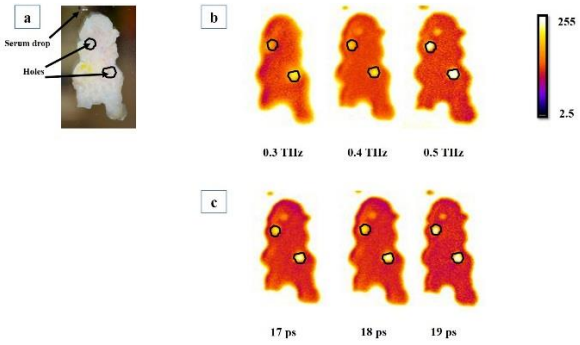

Tissue No. 3

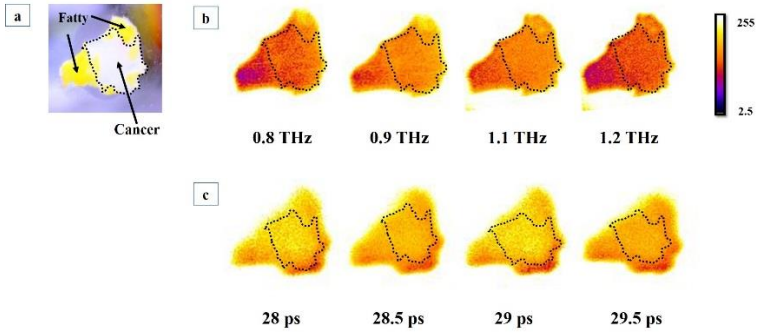

Tissue No. 4

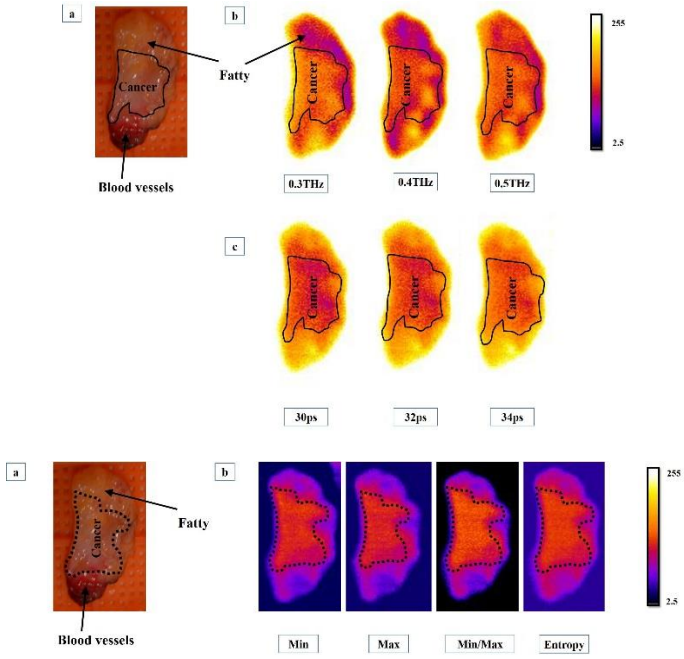

Tissue No. 5

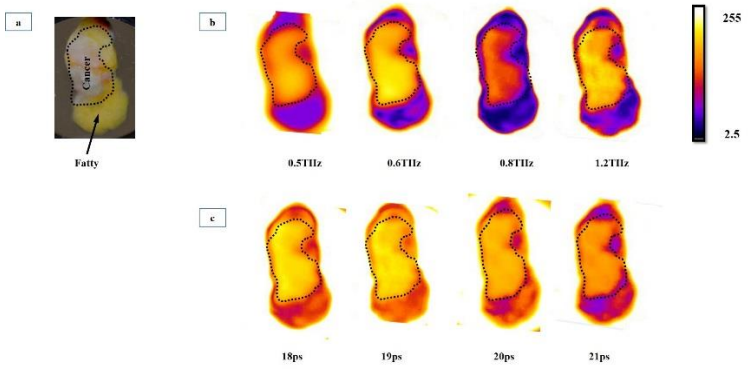

Tissue No. 6

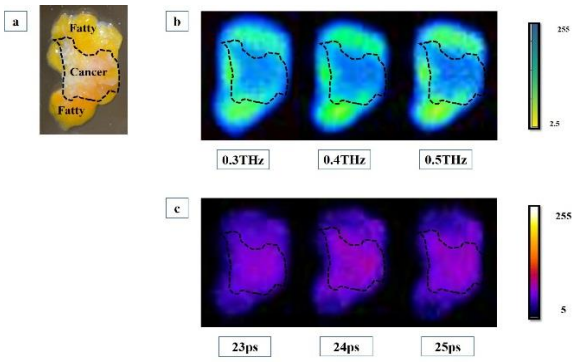

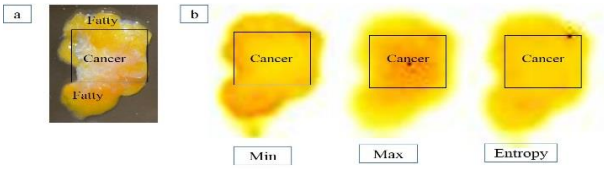

Tissue No. 7

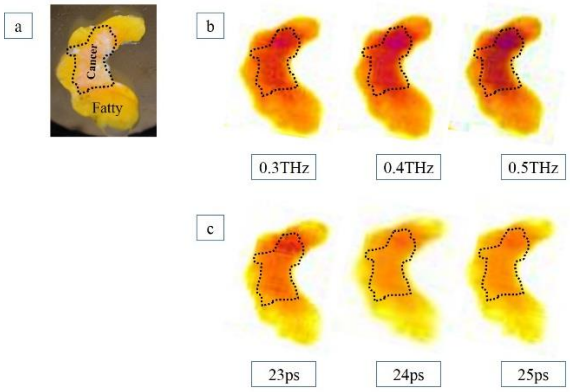

Tissue No. 8

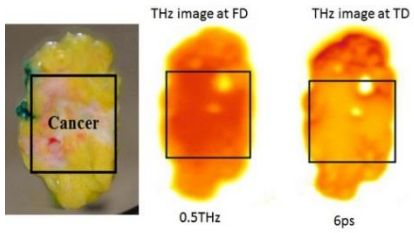

Tissue No. 9

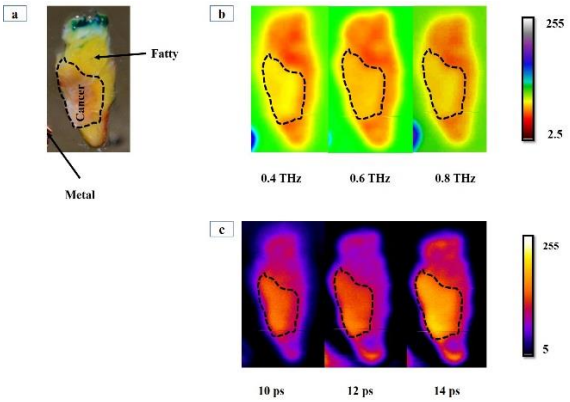

Tissue No.10

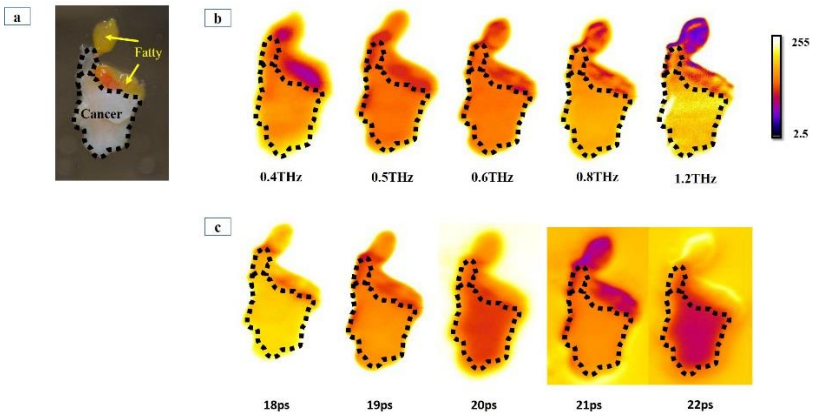

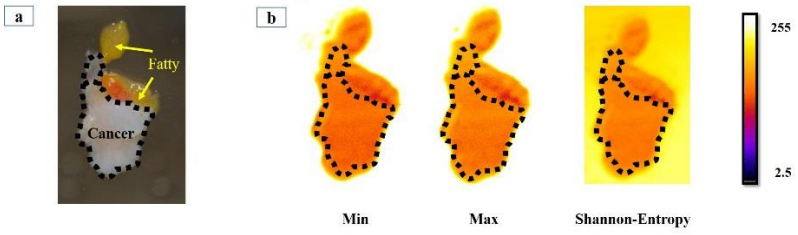

6.4. Annex 4: Data Extraction

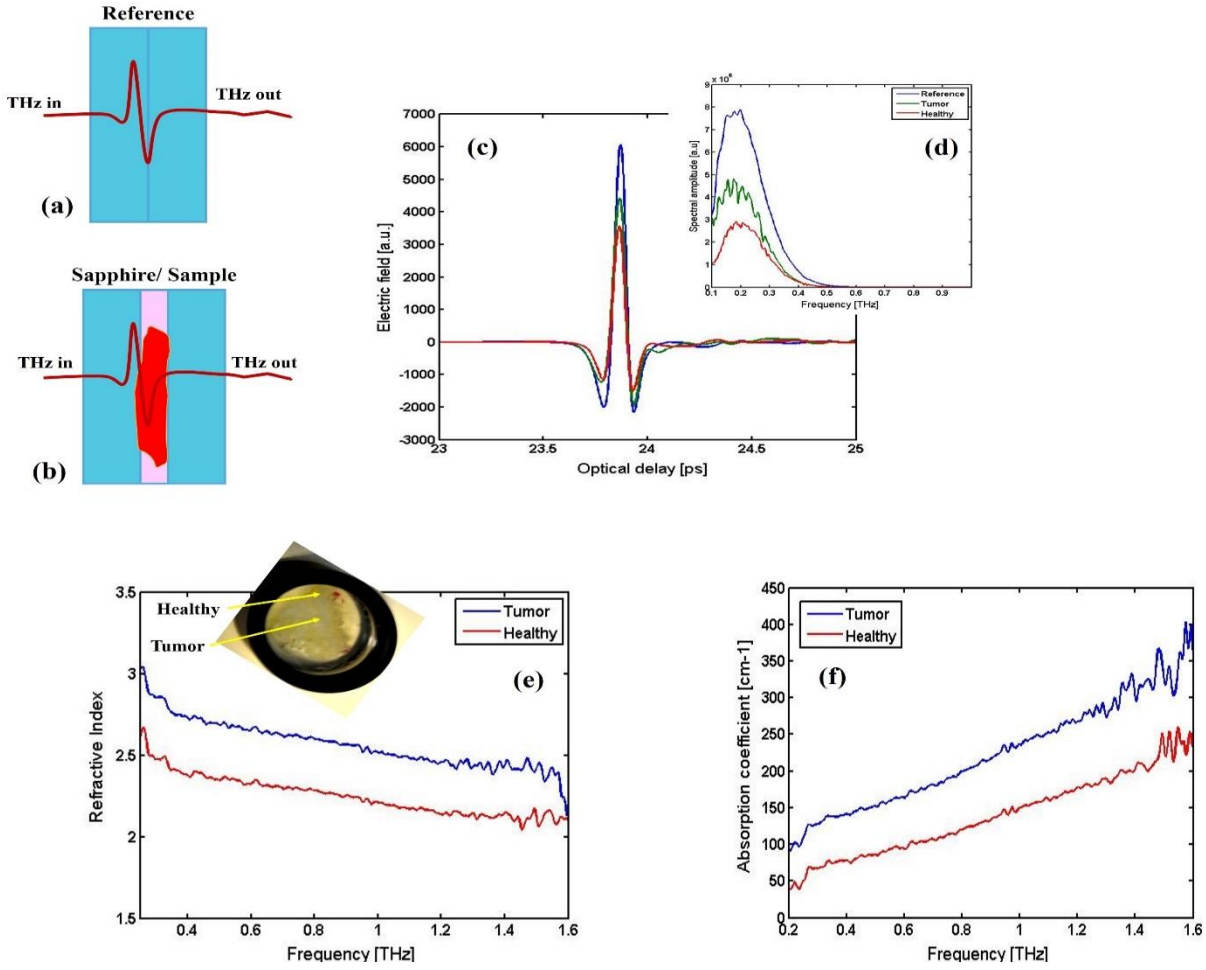

THz transmission spectroscopy of 200 µm-thick breast tissue: (a) sapphire window reference, (b) sample measurement of tissue in sapphire holder, (c) electric field of THz signals as a function of the time delay, (d) spectral amplitude in the frequency domain, (e) spectra of the refractive index of tumor and healthy tissue, (f) spectra of the absorption coefficient of tumor and healthy tissue.

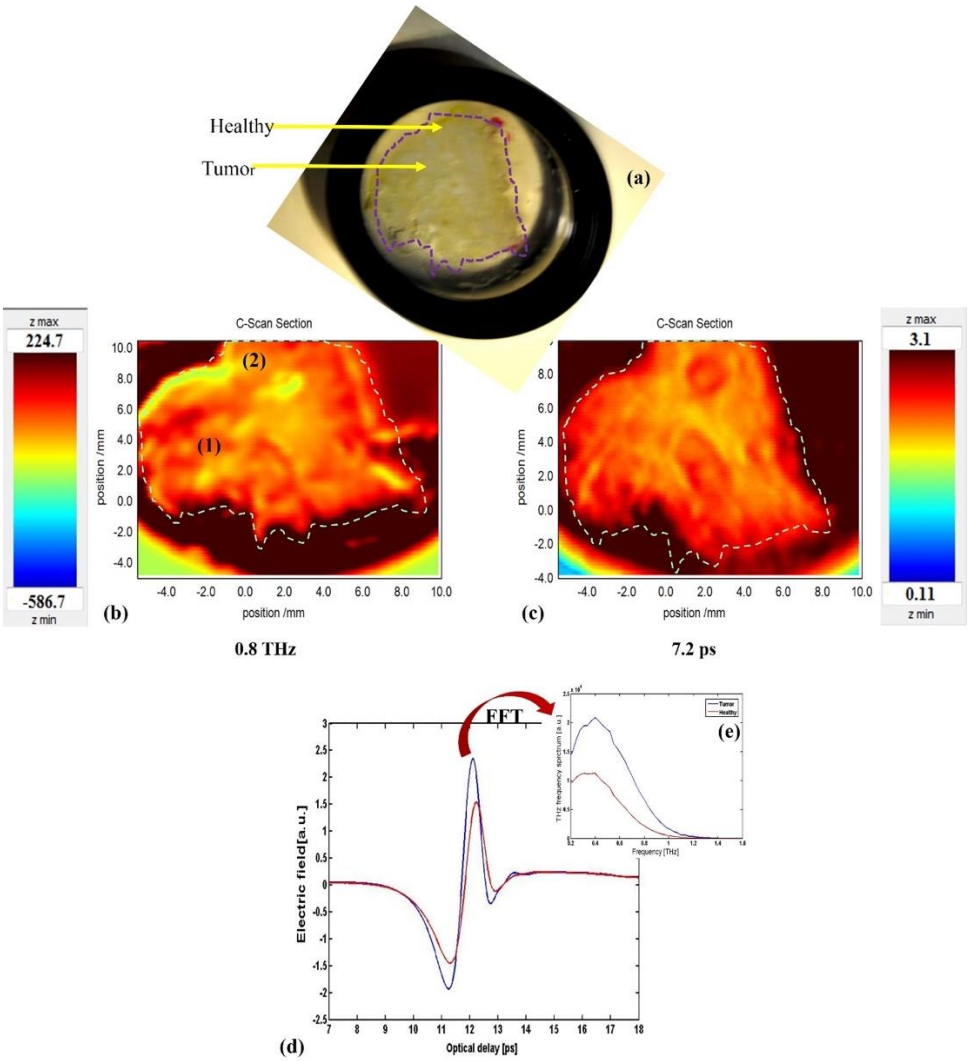

THz transmission imaging of fresh breast tissue, (a) visible image of 200 µm-thick paraffin gel-embedded breast tissue (tumor and healthy), (b) Image at 0.8 THz, (c) THz image at 7.2 ps. (d) THz signals were selected from two tissue regions (1. tumor, 2. healthy), (e) THz spectra of the same regions in the frequency domain.

Several physical properties of the samples affected the values of the parameters. Certain parameters were more dependent on particular physical properties (refractive index and absorption coefficient) significant to image generation, as shown in figures (d) and (e). Each dataset acquired generated a set of parametric images from the extracted data.

In transmission- acquisition mode, the parameters are:

- All the THz time- and frequency-domain spectra are collected for each pixel, by changing the time delay between the pump and probe beams.

- As well as the sample's physical position in space, resulting in detection of the THz electric field amplitude and phase.
- In addition, variations in amplitude of the THz radiation at that fixed time delay are required to acquire an image.

Reflection

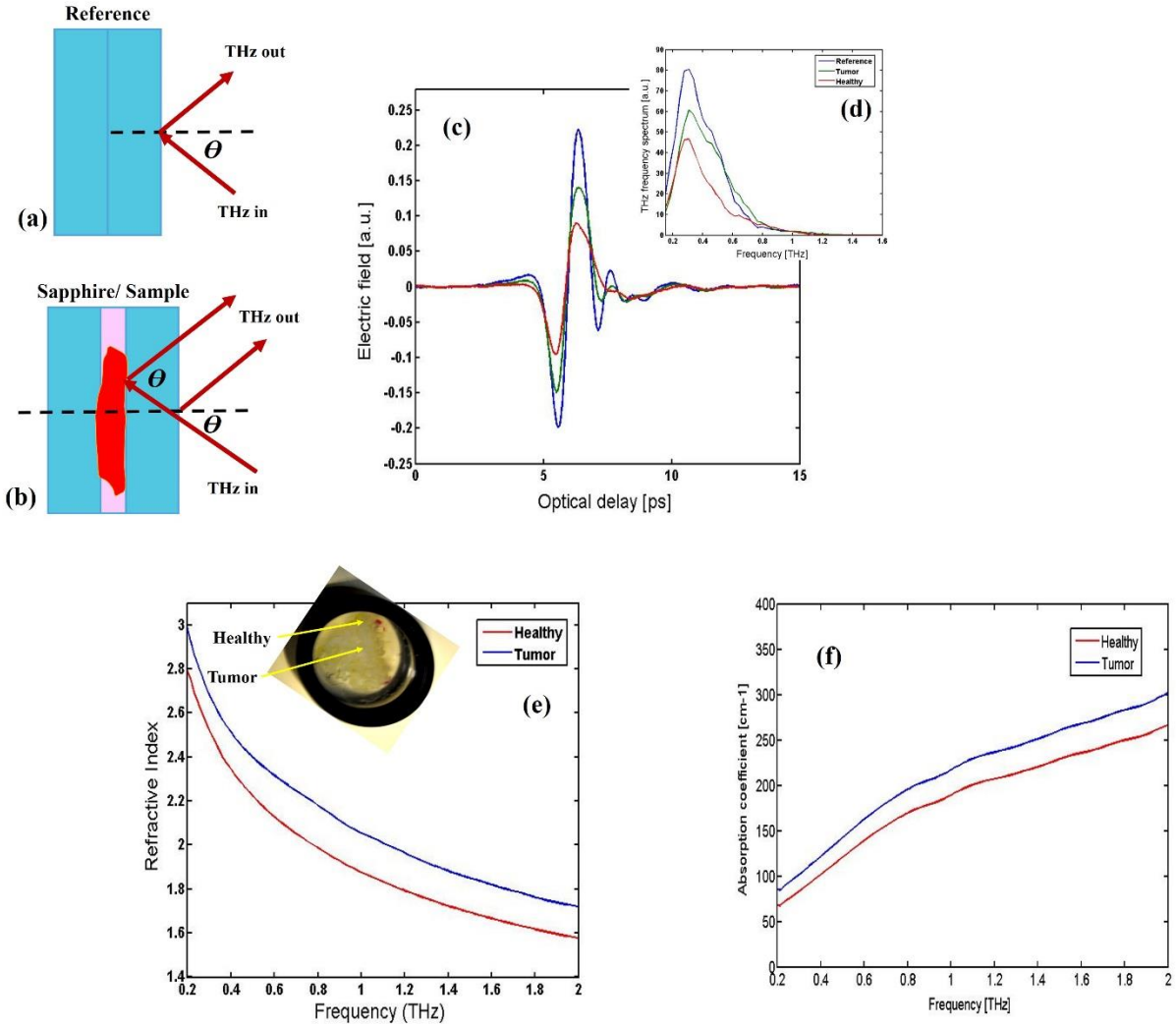

THz reflection spectroscopy of 200 µm-thick breast tissue: (a) the sapphire window reference, (b) sample measurement of tissue in sapphire holder, (c) electric field of THz signals as a function of the time delay, (d) spectral amplitude in the frequency domain, (e) spectra of the refractive indexes of tumor and healthy tissue, (f) spectra of the absorption coefficients of tumor and healthy tissue.

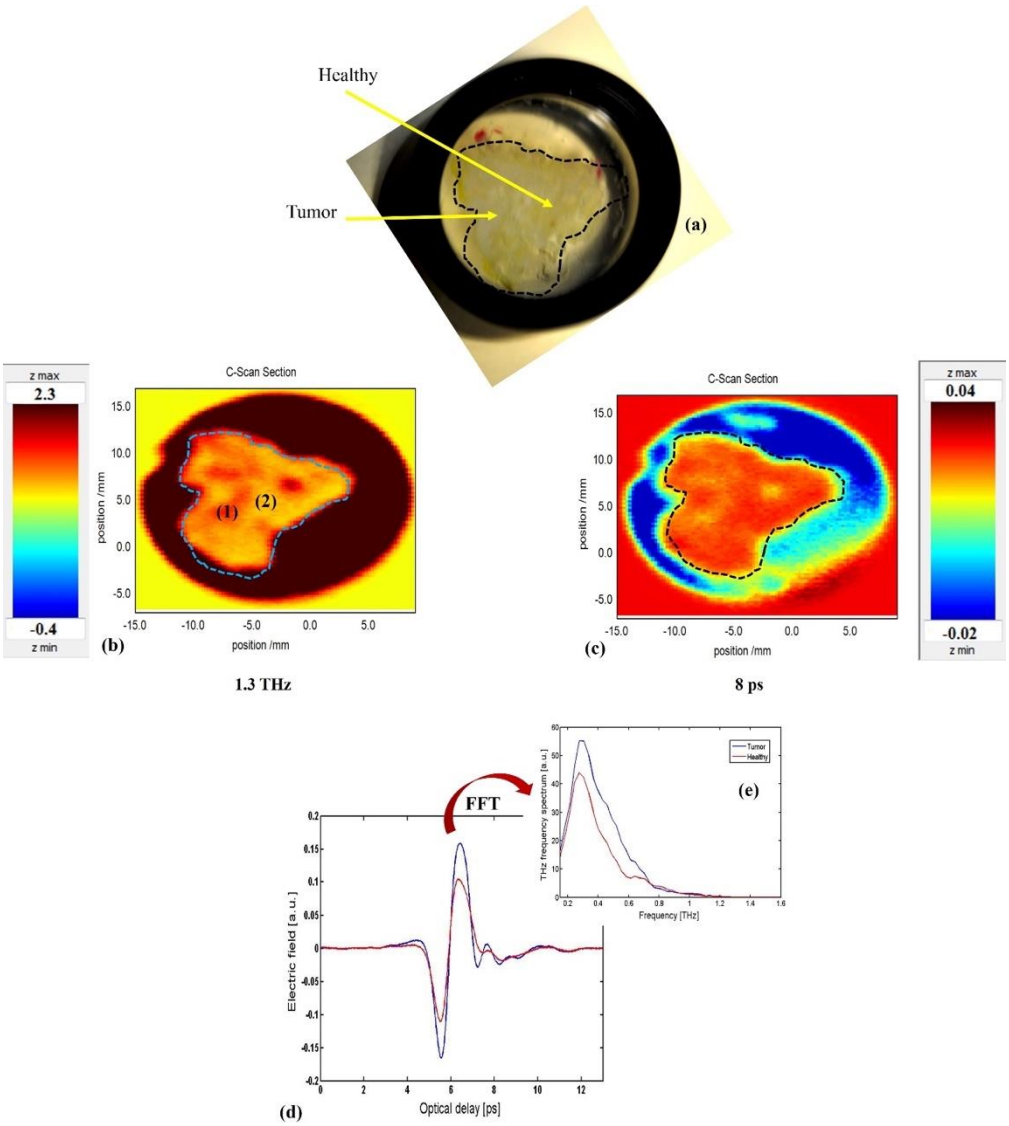

THz reflection imaging of fresh breast tissue, (a) visible image of 200 µm-thick paraffin gel-embedded breast tissue (tumor and healthy) with step size of 0.25 mm, (b) Image at 1.3 THz, (c) THz image at 8 ps. (d) THz signals were selected from two tissue regions (1. tumor, 2. healthy), (e) THz spectra of the same regions in the frequency domain.

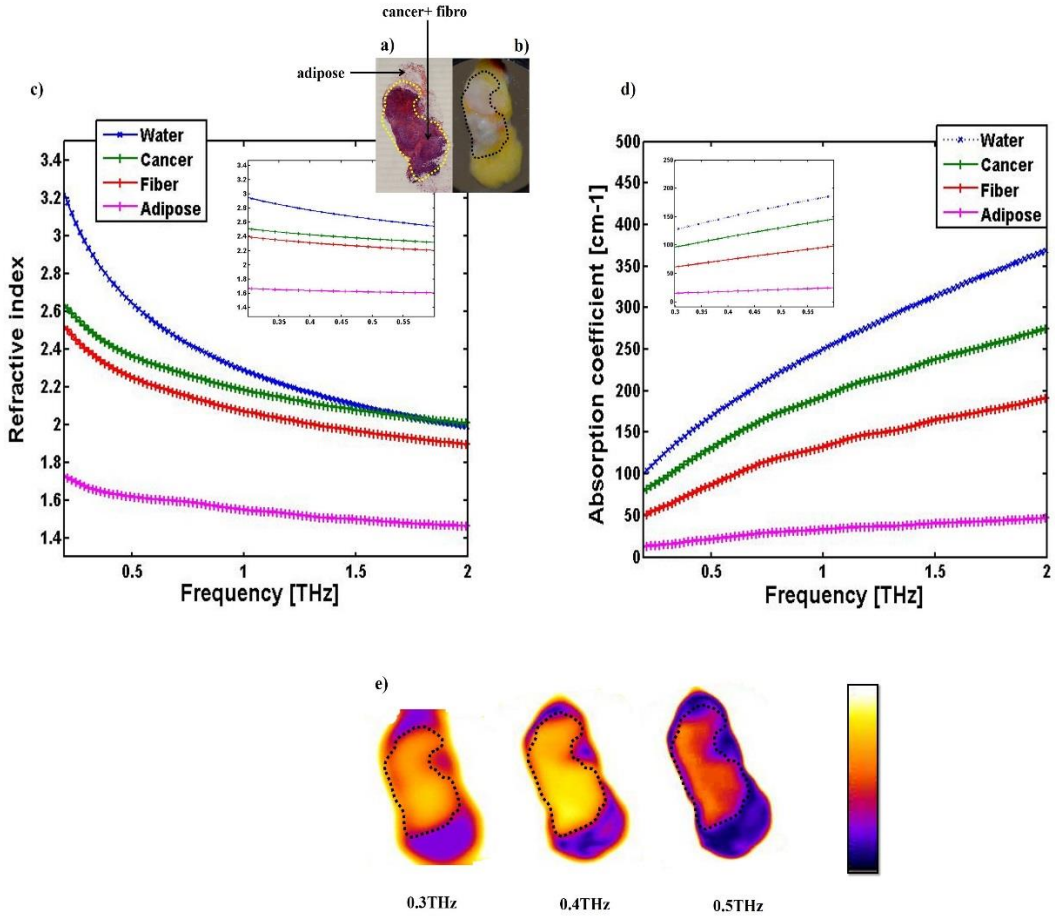

Figure: The complex properties of water and breast cancer, fiber, and adipose tissues. a) photograph of stained tissue 5 µm thick, b) photograph of 2 mm-thick fresh tissue, c) refractive index, d) absorption coefficient. c) THz images at 0.3, 0.4, and 0.5 THz.

This study examined adipose, fiber, and cancer tissues, using frequencies ranging from 300-600 GHz. Some groups characterized human breast tissues, investigating the dielectric properties of freshly excised samples over the frequency range from 0.5 to 20 GHz [178]. Another group studied the dielectric characterization of biological tissues over an extended frequency range, from 20 to 40 GHz, using millimeter-wave (mm-wave) imaging systems, as a possible means of increasing spatial resolution for near-surface tumors, where a limited penetration depth is required [179].

Figures (a & b) show photographs of stained tissue 5 µm thick and fresh tissue 2 mm thick, respectively. Each section consisted of three regions: adipose, fiber, and cancer, corresponding to a histopathological diagnosis. Figures (c & d) show two data extracts of the refractive indices and absorption coefficients of water and biological tissues, respectively, in the 300-500 GHz range. Figure (e) shows THz reflection images of raw data

for fresh tissue/water, exhibiting sufficient dielectric contrast between cancer, fiber, and adipose tissues to image breast cancer at an interesting tradeoff in the 300-600 GHz range.

Table 2: Double Debye model parameters and measured data for human breast tissues and water in the 300 to over 500 GHz range.

Material	0.3 THz		0.4 THz		0.5 THz	
	Index	Absorption (cm-1)	Index	Absorption (cm-1)	Index	Absorption (cm-1)
Water-Debye parameters	2.93	127.7	2.7.1	157.4	2.58	178
Water-this work	2.93 ±0.38%	128.3 ±1.3%	2.72 ±0.36%	157 ±1.7%	2.59 ±0.35	178.6 ±2.2%
Abnormal-Debye parameters	2.5	110.2	2.36	134	2.23	152.4
Abnormal-this work	2.44±0.35%	109 ±1.08%	2.36 ±0.34%	133 ±1.4%	2.28 ±0.31	149.9 ±1.6%
Normal-Debye parameters	2.42	68.2	2.3	82.9	2.16	95.8
Normal-this work	2.41 ±0.34%	66.9 ±0.66%	2.33±0.33%	78.9 ±0.97%	2.2 ±0.32%	94.7 ±1.02%
Adipose-Debye parameters	1.7	15.1	1.64	18.45	1.6	21.76
Adipose-this work	1.66 ±0.26%	15.43 ±2.2%	1.62 ±0.27%	18.46 ±2.7%	1.6 ±0.26%	22.01 ±3.1%

6.5. Annex 5: other samples

Sample 3

This study used the same Teraview 3000 system with transmission and reflection imaging to scan 30 µm-thick, paraffin-embedded, breast tissue, mounted on 2.04 mm-thick transparent silica material. The tissue section consisted of cancer, fiber, and fatty regions, identified by histopathology diagnosis.

The sample, 3 × 3 cm, was scanned in transmission mode at frequencies of 0.1 to 3 THz and 7 volts, 3 averages, waveform 2048, step size 0.25 µm, subsampling 4, and an acquisition time of 1h 15min. The results are shown in the figures below, read from the TVL file.

➢ Transmission results

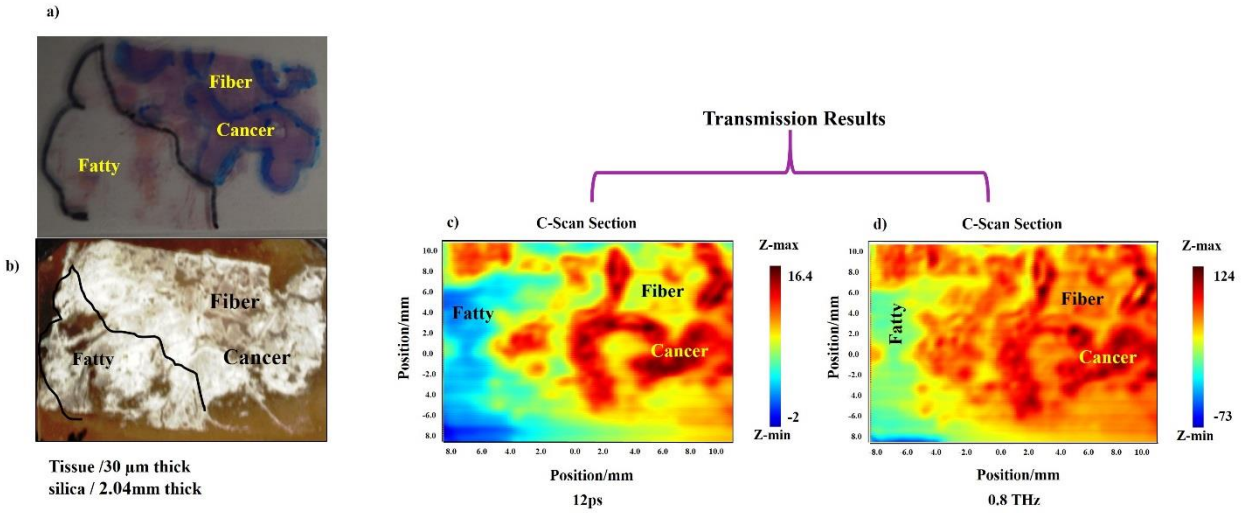

Transmission imaging results: (a) a photograph of 5µm-thick stained tissue, b) 30 µm-thick paraffin embedded breast tissue, c) THz image in time domain at 12 ps, and c) THz image in frequency domain at 0.8 THz.

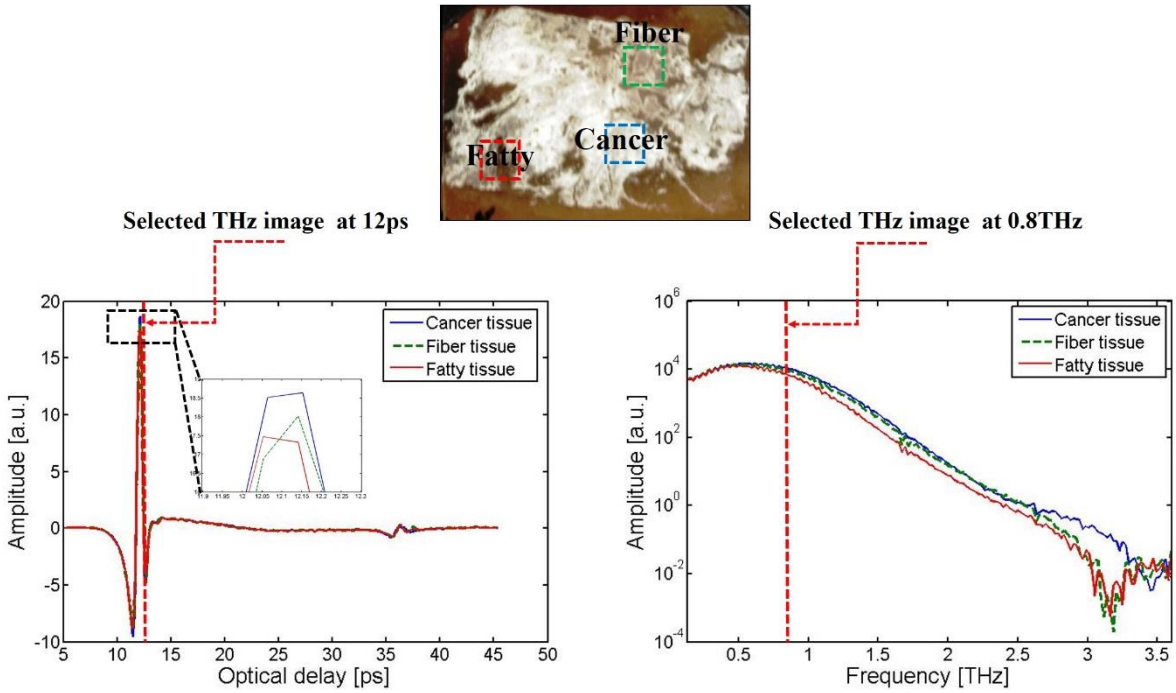

Transmission results of: a) time-domain signals collected from cancer, fiber, and fatty regions, and b) FFT spectra of these signals.

- **Reflection results**

The same 3 × 3 cm section was scanned in reflection mode, at frequencies of 0.1 to 3 THz and 7 volts, 3 averages, waveform 2048, step size 0.1 µm, subsampling 4, and an acquisition time of 2h 30min. The results for breast cancer are shown in the figures below, read from the TVL file.

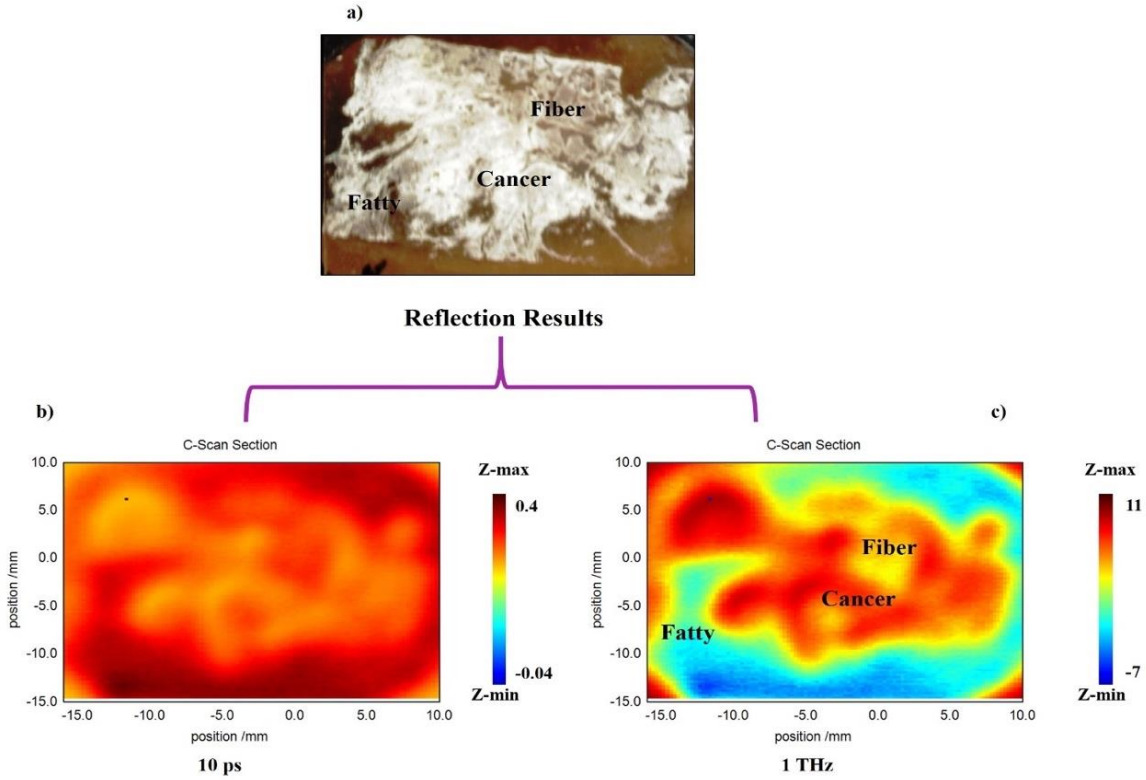

Reflection imaging results, (a) photograph of 30 µm-thick paraffin-embedded breast tissue; b) THz image in time domain at 10 ps; and c) THz image in frequency domain at 1THz.

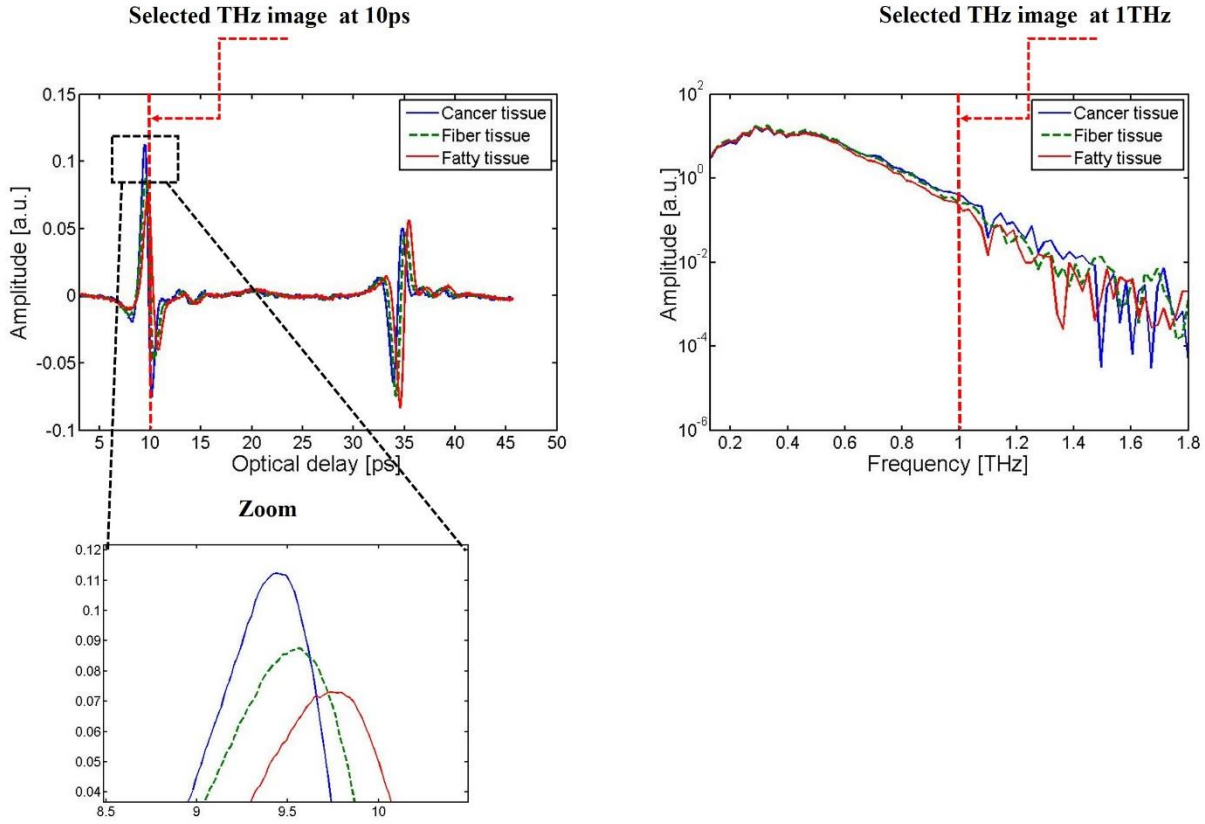

Reflection results: a) time-domain signals collected from cancer, fiber, and fatty regions and b) FFT spectra of these signals.

LIST OF PUBLICATIONS

Journal papers

- H. balacey, **A. Al-Ibadi**, G. MacGgrogan, JP. Guillet, E. Macpherson, and P. Mounaix. **Automated data and image processing for biomedical sample analysis**. (2016) IEEE.

- **A. Al-Ibadi**, Q. Cassar, T. Zimmer, G. MacGgrogan, JP. Guillet, and P. Mounaix. **THz spectroscopy and imaging for breast cancer detection in the 300-500GHz range.** IRMMW **(**2016).

- **A. Al-ibadi**, J. Bou Sleiman, Q. Cassar, G. MacGgrogan, H. Balacey, T. Zimmer, P. Mounaix, and JP. Guillet. **Terahertz biomedical imaging: From multivariate analysis and detection to material parameter extraction.** Progress In Electromagnetics Research, 2017.

- Laven Mavarani, Philipp Hillger, Thomas Bucher, Janusz Grzyb, Quentin Cassar, Amel Al-Ibadi, Thomas Zimmer, Gaétan MacGgan, Jean-Paul Guillet, Patrick Mounaix, and Ullrich R. Pfeiffer. **NearSence- Advance towards a silicon- based terahertz near-field imaging sensor for ex vivo breast tumor identification.** FREQUENZ 2018.

Conference presentation and proceedings

- **A. Al-ibadi**, J. Bou Sleiman, Q. Cassar, G. MacGrogan, H. Balacey, T. Zimmer, P. Mounaix, and JP. Guillet. **Terahertz biomedical imaging: From multivariate analysis and detection to material parameter extraction,** oral presentation, international conference of progress in electromagnetic research symposium-spring (PIERS), russia March 22-25, 2017.

- A.Al-ibadi, Q. Cassar, T. Zimmer, G. MacGrogan, JP. Guillet, P. Mounaix, L. Mavarani, J. Grzyb, U. Pfeiffer, **THz Spectroscopy and Imaging for Breast Cancer Detection in the 300-500 GHz range,** oral presentation at the 9th THz Day, Dunkerque, France, June, 2017.

Posters

- A. Al-Ibadi, J.P. Guillet, G. MacGrogan J. Bou Sleiman, P. Mounaix, **THz Spectroscopy Imaging for Cancer Detection,** GPU – Environnements / SIS, IMS laboratory , France, 2017. Awarded Prize for the best poster.

- Q. Cassar, A.Al-ibadi, G. MacGrogan, L. Mavarani, P. Hillger J. Grzyb, U. Pfeiffer, T. Zimmer, JP. Guillet, P. Mounaix, Breast tumor margin detection in the 300-600 GHz, University of Bordeaux, France, 2017.

- A. Al-Ibadi, J.P. Guillet, G. MacGrogan, P. Mounaix, **THz Spectroscopy Imaging for Cancer Detection,** University of Bordeaux, france, 2016.